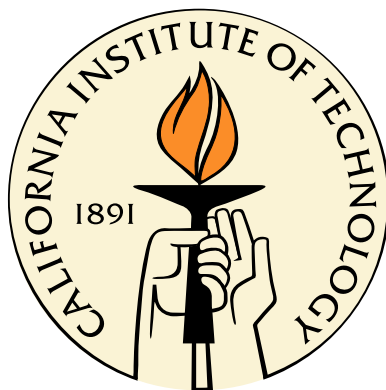


Non Invasive *In Vivo* Molecular Imaging of Cancer Nanotherapy Uptake and Response with PET/MRI

Thesis by
Thomas Sheung Chee Ng

In Partial Fulfillment of the Requirements
for the Degree of
Doctor of Philosophy



California Institute of Technology
Pasadena, California

2012
(Defended June 12, 2012)

© 2012

Thomas Sheung Chee Ng

All Rights Reserved

To my family; past, present, and future.

“It’s wanting to know that makes us matter. Otherwise we’re going out the way we came in.”

–Tom Stoppard, *Arcadia*

Acknowledgments

First and foremost I must express my sincere gratitude to my advisor, Russell Jacobs, for letting me work in his lab and on this project. He afforded me great latitude to explore, learn, and explore some more while providing me with patient support and timely advice throughout the way. Thank you for trusting in me. His unflappable demeanor, breadth of knowledge, work ethic, and enthusiasm to explore new ideas inspired and will continue to inspire me.

I have had the opportunity to work with several terrific advisors during my time here. Scott Fraser welcomed me into his lab from the first day; never failing to provide insightful advice during our meetings and motivating me with his infectious enthusiasm for science. Andrew Raubitschek treated me like his surrogate son; indulging in my explorations, yet always reminding me to never lose sight of the end goal: the patient's well-being. Simon Cherry opened his lab and engineering expertise to me and was always only a phone call or email away. Thank you all.

My thanks also to my committee, Paul Patterson, Grant Jensen, and Mark Davis, for their support throughout my time here.

No project can succeed on a single individual's effort alone. At Caltech, I must thank colleagues at the Caltech Brain Imaging Center and Fraser lab for their support and advice, especially Xiaowei Zhang, Sonia Collazo, Adriana Perles-Barbacaru, Andrey Demyanenko, Benoit Boulat, Elaine Bearer, Mike Tyszka, Sharon Lin, David Koos, Alex Lin, Lin Zhao, Erika Martinez, Aura Keeter, and Mary Martin. Haick Issian and Andre Jefferson at the Radiation Safety Office provided expert help for all the PET studies. David Colcher, Desiree Crow, Junie Chea, and Kofi Poku, amongst others, at the City of Hope facilitated studies between the two institutions. Ciprian Catana gave birth to the first-generation MR-compatible PET insert. It was a privilege to work with Angie Louie's group at UC Davis. Kazuki Sugahara, Tabet Teesalu from Erkki Ruoslahti's lab at the Sanford-Burham Institute provided guidance for the iRGD work. I also thank Peter Conti for

allowing me to work in the Molecular Imaging Center at USC.

I had the pleasure of working directly with great people. Hargun Sohi and Daniel Procissi shared the same basement with me for a large part of my graduate career. Their camaraderie and support has been immense. Yibao Wu worked diligently and patiently with me to push the PET/MRI instrumentation to “version 1.1” and also pushed up my spiciness tolerance. David Wert taught me the art of immunohistochemistry. Jim Bading and Ryan Park spent many nights with me in a basement at USC developing the PET/MRI to autoradiography system; fortunately finding the time to share delightful meals at Dino’s. Thank you Jim for keeping me accountable. Jose Reyes and Jinha Park worked with me to translate our protocols to the clinic, teaching me the unique challenges of clinical MRI. Tom Tu and Adrian House enlightened me on the intricacies of PET/MRI nanoparticle development. Thank you all for your friendship.

My academic career here would not have begun without two fortunate events. My time working with Thomas Budinger, Jonathan Maltz, and Henry Van Brocklin at Berkeley inspired me to pursue translational research and molecular imaging. I am grateful to them for exposing me to this field. The USC–Caltech MD/PhD program gave me the chance to learn medicine at a top medical school and to discover science at an extraordinary and unique place; I am very lucky to have this opportunity.

Too many friends, colleagues, and soccer teams have supported me outside the lab for me to name them all here. Without you, I would only have fun inside the lab! Thanks to each of you for standing by me through thick and thin.

Michelle has brought me much joy and happiness since we first met. Her kindness and love keeps me going; thank you for being in my life.

Finally, none of this would be possible without my family. My parents sacrificed a lot to move to Australia to build a new life for my brothers and me. Their love, support and guidance made me who I am today. I am eternally appreciative for all that they have done for me; I try to make them proud. I am also indebted to my brothers Heinz and Anthony for their support and the sacrifices that they have made since I left the antipodean shores. Mum, Dad, Heinz, and Anthony, I love you all; this is for you.

Abstract

Although researchers have made great strides toward understanding the biological processes underlying cancer pathology, this has not led to major improvements in the management of the disease. Development of new treatments to combat cancer remains imperative. Nanosized therapies show promise to improve tumor treatment response by localizing therapy while reducing treatment-related toxicity. Understanding how nanotherapies are taken up and cause their effects at the intact tumor level *in vivo* will complement *ex vivo* histological and *in vitro* biochemical studies and facilitate the translation of nanotherapy treatments to the clinic. Currently, few *in vivo* methods exist to study nanotherapy uptake and response at the intact tumor scale. Magnetic resonance imaging (MRI) and positron emission tomography (PET) are imaging methods that provide different but complementary information about the tumor microenvironment and nanotherapy uptake/response. Direct spatiotemporal correlation of PET and MRI data via their simultaneous acquisition has the potential to be powerfully synergistic, especially for the study of physiological processes that are time sensitive or where good spatial coregistration of the multimodal data is important. As the field of hybrid PET/MRI is still in its infancy, with only a handful of active systems worldwide, it is vital that continued PET/MRI technology development be pursued to realize its full potential.

The objective of this thesis is to develop noninvasive, multimodal PET/MRI methods to study the uptake and response of cancer nanotherapies. Three studies were pursued toward this goal. First, we describe the development of a quantitative, small animal simultaneous PET/MRI system that is capable of dynamic, intratumoral imaging. The results show that the system provides quantitative images that are highly correlated with *ex vivo* autoradiography. The system was able to follow the uptake of a radiolabelled antibody inside the tumor over time, visualizing antibody movement from the vascular space to the tumor mass. Second, we adapted a functional MRI technique, diffusion MRI, to monitor treatment response of the cancer nanotherapy CRLX101. CRLX101-treated ani-

mals showed a significant diffusion MRI response within 2 days of treatment, before significant size changes were observed. Modeling of the diffusion MRI data was able to predict the potent antiproliferative effect of CRLX101, commensurate with histological data. Finally, we developed MRI and PET/MRI methods to study the tumor response to the tumor-penetrating peptide iRGD, which has shown good potential to improve cancer nanotherapy uptake. The results show that iRGD can have a variable tumor response, which may be dependent on the tumor microenvironment.

The primary contributions of this thesis work is the development of small animal hybrid PET/MRI technology to enable multimodal intratumoral studies and the development of clinically-applicable imaging methods to monitor the uptake and response of cancer nanotherapies.

Contents

Acknowledgments	v
Abstract	vii
List of Figures	xiii
List of Tables	xvi
Abbreviations	xviii
1 Introduction	1
1.1 The Fight against Cancer	1
1.2 Personalized Non Invasive Molecular Imaging to Improve Cancer Treatment	3
1.3 Outline and Scope of Thesis	6
2 Background and Review	8
2.1 Targeted Cancer Nanotherapies	8
2.2 Modulation of the Tumor Microenvironment to Enhance Drug Uptake	10
2.3 Imaging in Oncology	11
2.3.1 PET Basics	11
2.3.2 MRI Basics	14
2.3.3 Combining PET and MRI	20
2.3.4 Digital Whole-body Autoradiography	22
2.3.5 Imaging of Targeted Nanotherapy Uptake	24
2.3.6 Imaging of Targeted Nanotherapy Response	25

3	Development of Simultaneous PET/MRI Technology for Robust <i>In Vivo</i> Studies	26
3.1	Further Considerations of PET Insert Effects on <i>In Vivo</i> MRI Performance	26
3.1.1	Materials and Methods	26
3.1.2	Results	30
3.1.3	Discussion	36
3.2	A Robust Coregistration Method for <i>In Vivo</i> Studies Using a First Generation Simultaneous PET/MRI Scanner	39
3.2.1	Abstract	39
3.2.2	Introduction	40
3.2.3	Materials and Methods	42
3.2.4	Results	47
3.2.5	Discussion	52
3.2.6	Conclusions	55
3.2.7	Supplemental Data	56
3.3	Phantom Designs for Robust <i>In Vivo</i> Coregistration of Hybrid Imaging Systems: Comparison of Semiautomatic and Automatic Approaches	60
3.3.1	Introduction	60
3.3.2	Materials and Methods	61
3.3.3	Results	64
3.3.4	Discussion	65
3.4	Quantitative, Simultaneous PET/MRI for Intratumoral Imaging with a MR-compatible PET Scanner	67
3.4.1	Abstract	67
3.4.2	Introduction	68
3.4.3	Materials and Methods	70
3.4.4	Results	76
3.4.5	Discussion	82
3.4.6	Conclusions	87
3.4.7	Supplemental Data	87

3.5	Synchronization of PET/MRI Hardware	92
3.5.1	Materials and Methods	93
3.5.2	Discussion	93
3.6	MR Gradient Effects on the PET Insert	95
3.6.1	Materials and Methods	95
3.6.2	Results	96
3.6.3	Discussion	99
3.7	PET/MRI Informatics Considerations	103
3.7.1	Image Generation	103
3.7.2	Storage	103
3.7.3	Integration	103
3.7.4	Discussion	105
4	Serial Diffusion MRI to Monitor and Model Early Treatment Response to the Targeted Nanotherapy CRLX101	107
4.1	Abstract	107
4.2	Translational Relevance	108
4.3	Introduction	109
4.4	Materials and Methods	111
4.5	Results	114
4.6	Discussion	121
5	Imaging the Tumor Response to the Tumor-penetrating Peptide iRGD	126
5.1	Introduction	127
5.2	Materials and Methods	129
5.3	Results	137
5.4	Discussion	144
6	Summary and Future Work	153
6.1	Summary	153
6.2	Future Work	154

A	A Study of the Timing Properties of Position-sensitive Avalanche Photodiodes	159
B	Receptor-targeted Iron Oxide Nanoparticles for Molecular MR Imaging of Inflamed Atherosclerotic Plaques	185
C	Cooccurrence Matrices to Compare Multimodal Image Datasets: Further Considerations	199
D	Synchronous PET/MRI Software Code	208
E	MATLAB Implementation of a Unique Identifier for Multimodal Data Linkage	215
	Bibliography	217

List of Figures

1.1	Therapeutics targeting different hallmarks of cancer.	2
1.2	Five year cancer survival rates, 2001–2007.	4
2.1	Enhanced permeability and retention.	9
2.2	A basic pulsed gradient SE sequence for diffusion MRI imaging.	16
2.3	DCE-MRI can infer tissue vascular function.	19
2.4	Real-time paradigm for PET/MRI studies.	21
2.5	PSAPD-based MR-compatible PET insert.	22
3.1	B_0 comparisons with and without the PET insert for the spherical phantom.	31
3.2	B_0 fieldmaps in the presence of the PET insert for the spherical phantom.	32
3.3	B_0 fieldmaps in the presence of the PET insert for the cylindrical phantom.	33
3.4	B_0 comparisons with and without the PET insert for the cylindrical phantom.	34
3.5	Relative B_1 maps with and without the PET insert.	34
3.6	B_{1u} comparisons with and without the PET insert.	35
3.7	Dynamic MRI time traces with and without the PET insert.	37
3.8	Signal drift quantification with and without the PET insert.	38
3.9	PET/MR FOV alignment phantom.	44
3.10	PET/MR FOV alignment strategy registers other phantom sets robustly.	45
3.11	Different spatial resolution of the PET and MR images.	48
3.12	PET/MR images of tumor and heart.	50
3.13	PET/MR alignment using different geometries.	50
3.14	PET guided MRS assay of MC38.CEA tumor.	51
3.15	MR images with PET on/off.	57

3.16 Schematic of automatic phantom.	61
3.17 Semiautomatic and automatic alignment phantom renderings.	62
3.18 Automatic phantom rod delineation.	63
3.19 Automatic axial alignment of images.	64
3.20 Alignment phantom PET/MRI images.	65
3.21 Quantitative PET/MRI evaluation phantoms.	71
3.22 PET/MRI scanner accuracy and stability within an imaging session.	77
3.23 Linearity and stability of the PET/MRI scanner across multiple imaging sessions.	78
3.24 Multimodal imaging of radiotracer uptake in tumors.	79
3.25 Pixel-based similarity across PET/MRI scanner (frozen specimens), microPET and autoradiography images.	80
3.26 Structure-based similarity among PET/MRI scanner (frozen specimen), microPET and autoradiography images.	81
3.27 <i>In vivo</i> simultaneous diffusion MRI/radiolabeled antibody PET reveals phases of antibody uptake.	83
3.28 Cooccurrence matrix analysis of functional PET and MRI data offers insight into tumor antibody uptake.	84
3.29 Resolution differences between autoradiography and PET.	85
3.30 Linearity of PET/MR scanner, microPET R4 and autoradiography.	90
3.31 Scatter plot of simultaneous diffusion MRI and PET antibody measurements at two different times after injection of ^{64}Cu -labeled antibody.	91
3.32 Synchronous PET/MRI strategy.	92
3.33 Fast kinetics of small molecular agents necessitate synchronous PET/MRI.	94
3.34 MRI gradient effects on count rates.	96
3.35 MRI gradient effects on count rates for the PET insert.	97
3.36 MRI gradient effects on count rates for individual detectors.	98
3.37 Orientation of PET detector modules in MRI.	98
3.38 Energy spectra for different gradient conditions.	100
3.39 PET/MRI database setup.	104

4.1	Diffusion MRI is sensitive to early CRLX101 response.	115
4.2	Histogram analysis of diffusion MRI.	116
4.3	ADC changes over treatment week show efficacy of CRLX101.	117
4.4	Tumor volume size changes over treatment week.	118
4.5	A logistic model of tumor growth can be applied to ADC data.	119
4.6	Cellular proliferation rates for different treatment groups were calculated by applying ADC data to a logistic model of tumor growth.	120
4.7	Boxplots of cellular proliferation rates for different treatment groups.	120
4.8	Histological assessment of CRLX101 and CPT-11 response.	122
5.1	Study design for iRGD MRI.	131
5.2	AIF, tumor time curves and model fits from Magnevist injection.	134
5.3	Study design for Diffusion MRI/PET.	135
5.4	Heterogeneity of tumor CA uptake.	137
5.5	Vascular parametric maps for a single mouse over multiple days.	138
5.6	Mean percentage change from baseline, sorted by tumor K_{trans} value.	140
5.7	Mean percentage change from baseline, sorted by distance from tumor edge.	141
5.8	PET/MRI of radiolabelled-Herceptin uptake 1 hour post injection.	142
5.9	PET/ Diffusion MRI of radiolabelled-Herceptin uptake 3 and 20 hours post injection.	143
5.10	Immunofluorescence of antibody uptake with saline.	145
5.11	Immunofluorescence of antibody uptake with iRGD.	146
5.12	Distribution of antibody immunofluorescence with iRGD.	147
6.1	Simultaneous PET/MRI data can analyzed with image-based models.	156
C.1	Voxel-by-voxel comparisons between images with different spatial resolutions.	203
C.2	Correlation of baseline and blurred data at different FWHM.	204
C.3	Cooccurrence matrix comparison.	204
C.4	Concordance correlation coefficients for cooccurrence matrices compared to the control matrix.	205

List of Tables

2.1	Common positron-emitting isotopes	13
2.2	MRI contrast agents.	17
2.3	Comparison between PET and MRI	20
2.4	Current state of hybrid PET/MRI systems	23
3.1	Relative B_{1u} values with and without the PET insert	30
3.2	T_1 measurements with and without the PET insert	36
3.3	Centroid alignment error of phantoms using the PET/MR transformation scheme over multiple days.	49
3.4	Centroid alignment error as a function of location within the transaxial field of view.	51
3.5	^{18}F -FDG-PET-guided ^1H MRS.	52
3.6	Alignment displacements by different pulse sequences.	57
3.7	Alignment error using 2D transformation.	58
3.8	Alignment error using 3D transformation.	59
3.9	Alignment error comparison between automatic and semiautomatic alignment meth- ods.	65
3.10	Image similarity metrics used to compare PET image quality with autoradiography.	75
3.11	Count rate differences across different gradient conditions for individual detectors.	99
5.1	Vascular parameters for whole ROI	139
5.2	Percentage change of vascular parameters from baseline for whole ROI	139
5.3	Area under curve for whole ROI.	141
5.4	Percentage change of vascular parameters from baseline for whole ROI	141
5.5	Mean ADC values at 3 and 20 hours post iRGD treatment	144

5.6 Mean PET uptake values at 3 and 20 hours post iRGD treatment 144

5.7 Maximum PET uptake values at 3 and 20 hours post iRGD treatment 144

Abbreviations

^{18}F -FLT	^{18}F -3'-fluoro-3'-deoxy-1-thymidine
^{18}F -FDG	^{18}F -fluoro-deoxyglucose
ACR	Activity concentration recovery
ADC	Apparent diffusion coefficient
AIF	Arterial input function
ANOVA	Analysis of variance
APD	Avalanche photodiode
AUC	Area under the curve
BL	Burkitt's lymphoma
BOLD	Blood oxygen level dependent
CA	Contrast agent
CCC	Concordance correlation coefficients
CEA	Carcinoembryonic antigen
CoV	Coefficients of variation
CPT	Camptothecin
CT	Computer tomography
CWSSIM	Complex wavelet structural similarity index

DCE-MRI	Dynamic-contrast enhanced MRI
DOI	Depth of interaction
DOTA	1,4,7,10-tetraazacyclodecane-1,4,7,10-tetraacetic acid
DTPA	Diethylene triamine pentaacetic acid
DWBA	Digital whole-body autoradiography
EPI	Echo planar imaging
EPR	Enhanced permeability and retention
FA	Flip angle
FLASH	Fast low-angle shot MRI
fMRI	Functional MRI
FOV	Field of view
FWHM	Full width at half maximum
GUI	Graphical user interface
i.p.	Intraperitoneal
i.v.	Intravenous
ID	Inner diameter
LSO	Lutetium oxyorthosilicate
LV	Left ventricle
MAP	Maximum <i>a posteriori</i>
MR	Magnetic resonance
MRI	Magnetic resonance imaging

MRS	MR spectroscopy
NIM	Nuclear instrumentation module
NMR	Nuclear magnetic resonance
OD	Outer diameter
OSEM	Ordered-subset expectation maximization
PAF	Platelet activating factor
PCC	Pearson's correlation coefficients
PET	Positron emission tomography
PMT	Photomultiplier tubes
PSAPD	Position-sensitive avalanche photodiode
PSF	Point spread function
PSNR	Peak signal-to-noise ratio
QAR	Quantitative autoradiography
RARE	Rapid acquisition with relaxation enhancement
RF	Radiofrequency
RMSE	Root mean squared error
ROI	Region of interest
SD	Standard deviation
SE	Spin echo
SEM	Standard error of the mean
SiPM	Silicon photomultiplier

SNR	Signal to noise ratio
SPECT	Single-photon emission computer tomography
SSIM	Mean structural similarity index
TE	Echo time
TR	Repetition time
TRT	Treatment related toxicity
TTL	Transistor transistor logic
TUNEL	Terminal nucleotidyl transferase-mediated nick end labeling
VEGF	Vascular endothelial growth factor
VOI	Voxel of interest

Chapter 1

Introduction

1.1 The Fight against Cancer

Cancer is a set of diseases characterized by the uncontrolled growth and spread of abnormal cells. Great advances have been made in understanding the underlying biology of cancer [1, 2]. Apart from the discovery of an ever-increasing number of genetic abnormalities and signalling-pathway defects stemming from proliferating cancer cells themselves, recent research has also highlighted the complex interplay between cancer cells and their tumor microenvironment [3]. *In situ* cancer tumors are heterogeneous, consisting not only of cancer cells (which themselves are not homogeneous inside the tumor, as demonstrated by the recent discovery of cancer stem cell populations [4]), but also various types of stromal support cells [5], blood vessels [6], and immune cell populations. How these different components interact and support the growing tumor can greatly affect tumor progression. The large number of potential therapeutic targets within the tumor generated from these discoveries have led to the development of many novel drugs targeting specific components of tumors (figure 1.1) . In particular, nanotherapy, which describes the class of agents with a size range of ~1–100 nm, is a promising drug design strategy that is being actively investigated. Cancer nanotherapies show great promise for oncological treatment, since they can be engineered to overcome barriers of uptake posed by the tumor microenvironment [7]. Additionally, nanotherapies can reduce treatment-related toxicity by concentrating delivery of drugs into the tumor mass.

Translating this basic biological understanding and engineering progress to effective clinical endpoints (i.e.increased patient survival) remains a challenge. Survival rates from several types of cancer remain low (figure 1.2, [8]). A major issue contributing to this is the fact that our un-

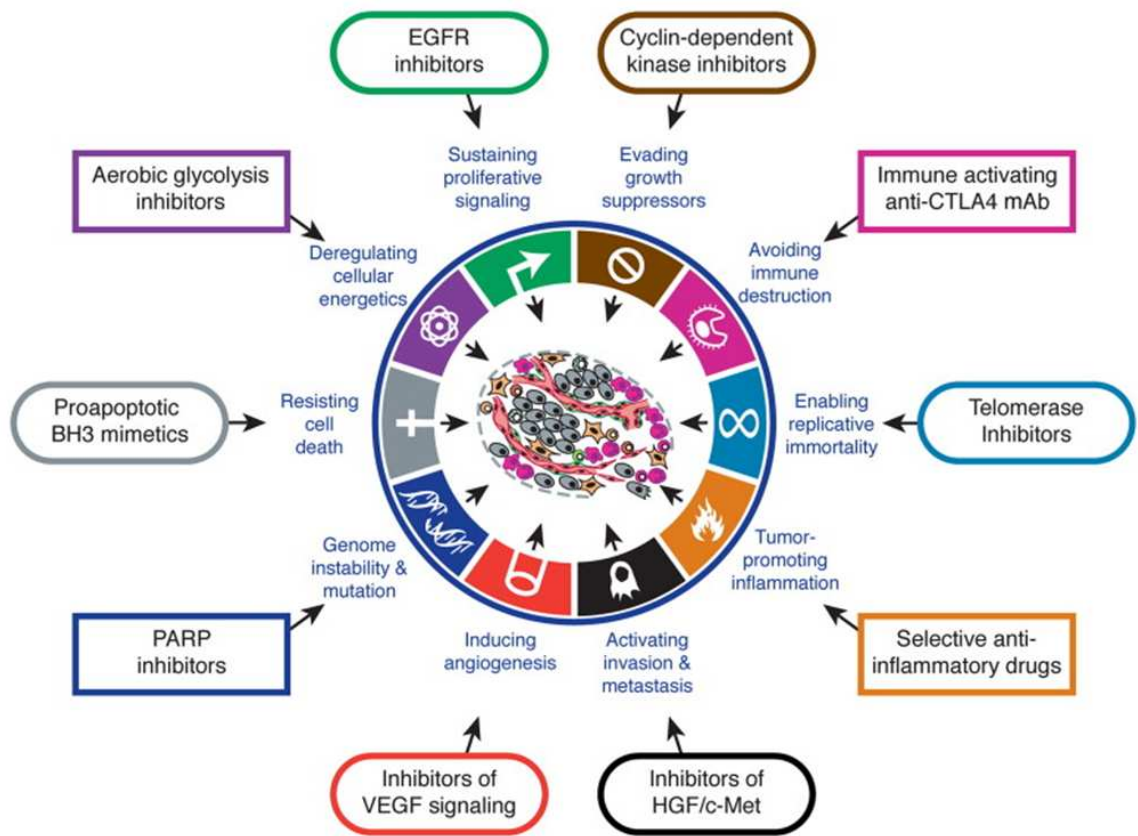


Figure 1.1: Therapeutics targeting different aspects of cancer growth are under development (adapted from [1]).

derstanding and evaluation of tumor progression and response to treatment in individual patients remain limited. For example, consider a tumor type studied in this work, Burkitt's lymphoma (BL). The genetic profiles of well-defined BL are known; however patients often present a phenotype intermediate between BL and other aggressive lymphomas, making diagnosis difficult [9]. Although the disease has been shown to be quite chemosensitive, no consensus treatment exists [10]. Often, a high-intensity chemotherapy regimen is administered to the patient over 3–6 cycles, which can take 3–6 months to complete. Treatment evaluation is then documented 4–8 weeks posttreatment. The criteria for treatment response is based mainly on anatomical reduction of tumor burden, complemented by laboratory tests and tissue biopsies to confirm response *after* completion of therapy [11]. While recent response rates are quite good, even close to 100%, some variants of BL in adolescents and young adults have poor prognosis. If cancer nanotherapy is to be successfully translated to the clinic to treat diseases such as BL, tools that enable us to understand the causes of poor tumor treatment response and identify individual patients that do not respond well early in the treatment regimen will be highly desirable. noninvasive molecular imaging is one such tool.

1.2 Personalized Non Invasive Molecular Imaging to Improve Cancer Treatment

Noninvasive imaging has become indispensable for both research and clinical management of cancer during the past 20–30 years. Visualization of the tumor mass with high-resolution anatomical imaging modalities such as x-ray, computer tomography (CT), and magnetic resonance imaging (MRI) enables cancer diagnosis and staging. This has been augmented by the availability of ^{18}F -fluorodeoxyglucose (^{18}F -FDG) positron emission tomography (PET) to locate tumors. These imaging modalities now play a vital role in forming the criteria for tumor response [11].

Advances in the field of molecular imaging are enabling researchers to address questions about the complex dynamics between various components of the tumor and the therapies used to treat them. Studies with the imaging modalities mentioned above are moving beyond mere size measurement and tumor staging. Imaging techniques and imaging probes are being developed to monitor specific molecular aspects of tumor growth [12]. The imaging modalities mentioned are noninva-

Five-year Relative Survival Rates* (%) by Stage at Diagnosis, 2001-2007

	All Stages	Local	Regional	Distant		All Stages	Local	Regional	Distant
Breast (female)	89	99	84	23	Ovary	44	92	72	27
Colon & rectum	64	90	69	12	Pancreas	6	22	9	2
Esophagus	17	37	18	3	Prostate	99	100	100	29
Kidney [†]	70	91	63	11	Stomach	26	62	28	4
Larynx	61	77	42	33	Testis	95	99	96	73
Liver [‡]	14	27	9	4	Thyroid	97	100	97	56
Lung & bronchus	16	52	24	4	Urinary bladder [§]	78	71	35	5
Melanoma of the skin	91	98	61	15	Uterine cervix	69	91	57	19
Oral cavity & pharynx	61	82	56	34	Uterine corpus	82	96	67	16

*Rates are adjusted for normal life expectancy and are based on cases diagnosed in the SEER 17 areas from 2001-2007, followed through 2008.

†Includes renal pelvis. ‡Includes intrahepatic bile duct. §Rate for in situ cases is 97%.

Local: an invasive malignant cancer confined entirely to the organ of origin. **Regional:** a malignant cancer that 1) has extended beyond the limits of the organ of origin directly into surrounding organs or tissues; 2) involves regional lymph nodes by way of lymphatic system; or 3) has both regional extension and involvement of regional lymph nodes. **Distant:** a malignant cancer that has spread to parts of the body remote from the primary tumor either by direct extension or by discontinuous metastasis to distant organs, tissues, or via the lymphatic system to distant lymph nodes.

Source: Howlader N, Krapcho M, Neyman N, et al. (eds). *SEER Cancer Statistics Review, 1975-2008*, National Cancer Institute, Bethesda, MD, www.seer.cancer.gov/csr/1975_2008/, 2011.

American Cancer Society, Surveillance Research 2012

(a) Five year cancer survival rates, stratified by stage at diagnosis.

Trends in 5-year Relative Survival Rates* (%) by Race, US, 1975-2007

	All races			White			African American		
	1975-77	1987-89	2001-2007	1975-77	1987-89	2001-2007	1975-77	1987-89	2001-2007
All sites	49	56	67 [†]	50	57	69 [†]	39	43	59 [†]
Brain	22	29	35 [†]	22	28	34 [†]	25	31	40 [†]
Breast (female)	75	84	90 [†]	76	85	91 [†]	62	71	77 [†]
Colon	51	60	65 [†]	51	61	67 [†]	45	53	55 [†]
Esophagus	5	10	19 [†]	6	11	20 [†]	3	7	13 [†]
Hodgkin lymphoma	72	79	86 [†]	72	80	88 [†]	70	72	81 [†]
Kidney & renal pelvis	50	57	71 [†]	50	57	71 [†]	49	55	68 [†]
Larynx	66	66	63 [†]	67	67	65	59	56	52
Leukemia	34	43	57 [†]	35	44	57 [†]	33	36	50 [†]
Liver & intrahepatic bile duct	3	5	15 [†]	3	6	15 [†]	2	3	10 [†]
Lung & bronchus	12	13	16 [†]	12	13	17 [†]	11	11	13 [†]
Melanoma of the skin	82	88	93 [†]	82	88	93 [†]	58 [†]	79 [†]	73 [†]
Myeloma	25	28	41 [†]	25	27	42 [†]	30	30	41 [†]
Non-Hodgkin lymphoma	47	51	70 [†]	47	52	71 [†]	48	46	62 [†]
Oral cavity & pharynx	53	54	63 [†]	54	56	65 [†]	36	34	45 [†]
Ovary	36	38	44 [†]	35	38	43 [†]	42	34	36
Pancreas	2	4	6 [†]	3	3	6 [†]	2	6	4 [†]
Prostate	68	83	100 [†]	69	85	100 [†]	61	72	98 [†]
Rectum	48	58	68 [†]	48	59	69 [†]	45	52	61 [†]
Stomach	15	20	27 [†]	14	19	26 [†]	16	19	27 [†]
Testis	83	95	96 [†]	83	95	97 [†]	73 [†]	88 [†]	86
Thyroid	92	95	97 [†]	92	94	98 [†]	90	92	95
Urinary bladder	73	79	80 [†]	74	80	81 [†]	50	63	64 [†]
Uterine cervix	69	70	69	70	73	70	65	57	61
Uterine corpus	87	83	83 [†]	88	84	85 [†]	60	57	61

*Survival rates are adjusted for normal life expectancy and are based on cases diagnosed in the SEER 9 areas from 1975-77, 1987-89, and 2001 to 2007, and followed through 2008. †The difference in rates between 1975-1977 and 2001-2007 is statistically significant (p < 0.05). ‡The standard error is between 5 and 10 percentage points. §Survival rate is for cases diagnosed in 1978-1980.

Source: Howlader N, Krapcho M, Neyman N, et al. (eds). *SEER Cancer Statistics Review, 1975-2008*, National Cancer Institute, Bethesda, MD, www.seer.cancer.gov/csr/1975_2008/, 2011.

American Cancer Society, Surveillance Research, 2012

(b) Five year cancer survival rates, stratified by race.

Figure 1.2: Five year cancer survival rates in the United States, 2001–2007. Adapted from [8].

sive, allowing real-time studies of the intact tumor during growth and/or therapy. They are also quantitative, which enable comparisons intra- and intersubjects across multiple time points. There is also increasing recognition that studies integrating information from multiple modalities can be synergistic, providing information not available in unimodal situations. The most spectacular example of this synergy is the widespread adoption of PET/CT systems. CT gives high-resolution anatomical context to the PET data, and the combination has demonstrated clear clinical benefit [13]. Recent developments in hybrid PET/MRI promises to offer even more synergistic value [14]. MRI not only provides high-resolution anatomical images, but can also provide functional information that is complementary to PET. The field of hybrid PET/MRI is still in its infancy; continued development of PET/MRI technology is necessary to realize its full potential.

Progress in the design and development of cancer nanotherapies are informed by their interactions with the tumor microstructure *in situ*. Most investigations to understand the interaction of nanotherapies and the tumor microenvironment are done *in vitro* [15, 16], *ex vivo* [17], or invasively [18], which may not always simulate *in situ* situations well. Noninvasive imaging modalities, such as PET/MRI, will be very useful to study cancer nanotherapy uptake and response. Researchers have begun to use noninvasive imaging to study the uptake of nanotherapies, mostly focusing on examining the gross uptake of therapies into the tumor mass [19, 20].

The goal of this thesis is to develop clinically applicable, noninvasive imaging technologies, specifically PET and MRI, to understand the uptake and response of cancer nanotherapies beyond simple tumor size measurements and the gross uptake of nanotherapies into tumors. We first describe the development and evaluation of a small animal hybrid PET/MRI system to study the heterogeneous uptake of antibodies into the tumor. The second part of the thesis concerns the development of a functional imaging technique, diffusion MRI, to model and follow the early response of a nanotherapy currently in clinical trials. The final part of the thesis describes work to develop PET/MRI methods to study the effects of the tumor modulating peptide iRGD, which has the potential to significantly improve the uptake of nanotherapies into the tumor.

1.3 Outline and Scope of Thesis

This thesis describes work developing and validating a first-generation small animal, simultaneous PET/MRI imaging system and the application of both PET and MRI (individually or together) techniques to study the uptake and response of different targeted cancer nanotherapies.

1.3.1 Review of Targeted Cancer Nanotherapies, Tumor-modulating Peptides and Multimodal Noninvasive Imaging

Chapter 2 first reviews the current status of targeted nanotherapies for cancer. We describe the different design approaches being investigated to improve targeting of drugs into the tumor site. Tumor microenvironmental factors which may affect the kinetics and biological activity of targeted therapies are described. Next, we review recent attempts to improve tumor drug uptake by modulating the tumor microenvironment. Treatments which attenuate barriers to drug access in the tumor may act synergistically with carefully designed targeted therapies to enhance therapeutic response.

The second half of the chapter reviews the application of noninvasive imaging to study cancer therapy uptake and tumor response. The basic physics of PET, MRI, and DWBA, as well as their use in imaging cancer nanotherapy are reviewed. Advances in the nascent field of hybrid PET/MRI imaging are outlined.

1.3.2 Developing Simultaneous PET/MRI for Robust *In Vivo* Studies

Hybrid PET/MRI systems are being built. However, thorough characterization and verification of such systems are required before being used in meaningful *in vivo* studies. Chapter 3 describes the characterization and development of a first-generation small animal PET/MRI system to enable robust physiological studies. First, we examine potential interference effects of the PET insert on MRI image quality with direct regards to *in vivo* studies that we wish to pursue. Next, we present work on the development of a reliable image coregistration strategies between simultaneously acquired PET and MRI images.

Making believable physiological inferences from high-resolution PET and MRI datasets requires that the images are faithful to real contrast distributions in the imaged tissue. We describe

work that validated the imaging ability of the PET/MRI system to reveal intratumoral uptake patterns as compared to a commercial PET system and DWBA.

To enable robust physiological studies, complete integration of the PET and MRI hardware and software is necessary. In the last part of the chapter we describe our efforts to streamline the hybrid PET/MRI system technology and consider MRI interference effects on the PET insert that need to be addressed in next generation systems.

1.3.3 Serial Diffusion MRI to Monitor and Model Early Treatment Response to the Targeted Nanotherapy CRLX101

Successful translation of targeted cancer nanotherapies to the clinic requires robust tools to evaluate effective patient response. noninvasive imaging techniques show great promise in this regard and can be directly translated from preclinical studies to clinical trials. Chapter 4 describes work on the evaluation of a functional MRI method, diffusion MRI, to monitor the response of CRLX101 in a preclinical murine model of Burkitt's lymphoma. We also applied the diffusion MRI data to a logistical model of tumor growth to evaluate the model's ability to predict CRLX101's activity.

1.3.4 Imaging the Tumor Response to the Tumor-penetrating Peptide iRGD

iRGD is a tumor-penetrating peptide that has been shown to improve tumor delivery of drugs by modulating the tumor microenvironment. Translation of this peptide to the clinic requires a robust assay of its efficacy. Chapter 5 describes preliminary results in developing noninvasive (PET and MRI) assays of iRGD response.

1.3.5 Summary and future work

Future directions raised by the current work are presented in chapter 6.

Additional information and studies related to work described in this thesis are presented in the appendices.

Chapter 2

Background and Review

2.1 Targeted Cancer Nanotherapies

Therapies such as chemotherapy or small molecule molecularly targeted therapeutics (e.g. kinase inhibitors) are powerful anticancer treatments and form the standard of care in current clinical management of cancer. However, these agents distribute non-specifically in the body, and since cancer targets are often the overexpression of normally expressed markers, these agents can cause toxicity to both cancer and normal cells. Treatment-associated toxicity (TRT) can limit achievable dosage within the tumor and result in suboptimal treatment. Furthermore, many tumor types can develop resistance to these small molecule therapies.

Nanotherapies, which describes the class of agents with a size range of ~1–100 nm, are being actively explored to overcome the issues of small molecule therapies [21, 4, 22]. Often, small molecule therapies are directly attached or encapsulated within a “carrier” nanostructure for drug delivery. Structures being explored range from polymers [23, 24] and carbon nanotubes [25] to liposomes [26] and viral protein cages [27]. Gold nanorods can be delivered to the tumor to provide localized photothermal heating. This can cause direct tumor toxicity or improved uptake of a complementary drug carrier [7]. Alternatively, existing peptides and protein constructs can be modified to improve their targeting efficacy. An example of this is the development of immunocytokines, whereby cytokine peptides are engineered onto antibodies to target their effects locally to the tumor site [28, 29].

Nanotherapies overcome toxicity and resistance issues by several mechanisms. First, size and surface characteristics of nanotherapies can be tuned to extend their circulation time in the body

by reducing reticuloendothelial and renal clearance. Next, the nanotherapies can target the tumor by harnessing the properties of the tumor environment. The most characterized property is the enhanced permeability and retention effect (EPR). The fast growing tumor requires a continuous nutrient supply and thus releases factors to recruit and grow blood vessels. Imbalance of angiogenic signals lead to highly disorganized and leaky tumor blood vessels. This, along with compromised tumor lymphatics, allow macromolecules above ~50 kDa to accumulate in the tumor interstitium. The nanotherapy considered in this work, CRLX101 [30], has been postulated to accumulate via EPR (see chapter 4 for further discussion).

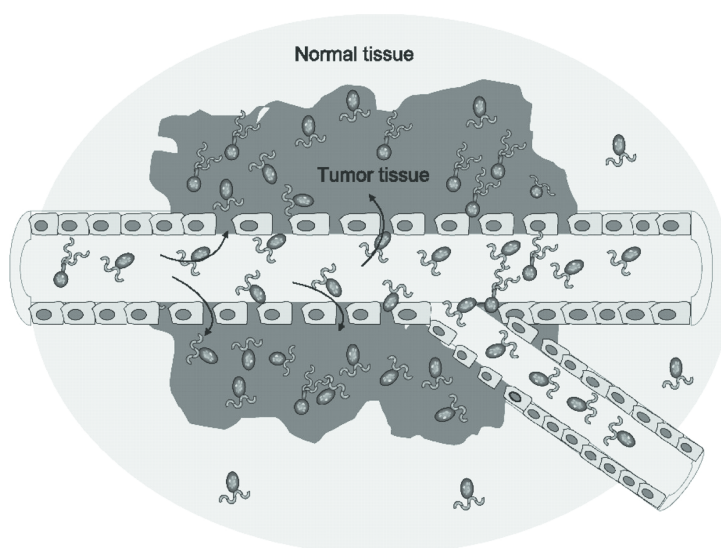


Figure 2.1: Enhanced permeability and retention. Dysregulation of the angiogenic signals within tumors lead to immature and leaky blood vessels in the tumor. This enables macromolecules and nanoparticles to enter the tumor interstitium. This, along with compromised lymphatics, lead to retention of these large-sized particles in the tumor (adapted from [4]).

Tumor targeting can be further improved. Specific targeting of cell populations via receptor targeting can be achieved by the attachment of receptor ligands or antibody fragments onto the nanotherapy surface. Transferrin or folate receptors, which are often over-expressed in tumors, are common targets [31, 32]. Targets along the tumor endothelium (e.g. $\alpha_v\beta_3$ integrin receptors) have also been explored for antivascular agents [33]. Other properties, such as the pH of the tumor [34] and the overexpression of enzymes [35] in the tumor have also been explored as tumor localizing targets. Recent work suggests that combining several of these targeting mechanisms into a single nanotherapy system is synergistic [7].

Tumors can become chemoresistant via multiple mechanisms. The best known is the P-glycoprotein efflux pump pathway [36]. Nanotherapies can potentially overcome these effects since they uptake into cancer cells via different pathways compared to conventional therapies [37].

2.2 Modulation of the Tumor Microenvironment to Enhance Drug Uptake

Improved tumor targeting is the primary rationale behind the development of cancer nanotherapies [38]. However, nanotherapies currently in clinical trials show modest improvements over conventional treatment [39]. Studies exploring the factors preventing enhanced efficacy have highlighted the heterogeneity of nanotherapy uptake within the complex tumor microenvironment. Although leaky blood vessels form the basis of EPR, their vessel-wall structure are often abnormal, leading to vessel collapse and thus heterogeneous delivery [40]. Similarly, lymphatic drainage is also compromised in tumors with a result of fluid retention within the tumor mass and tumor interstitial hypertension [41]. This may impede penetration of nanotherapies throughout the tumor. Moreover, the tumor microenvironment consists not only of tumor cells, but support matrix such as collagen fibers and glycosaminoglycan [15, 42]. Depending on the size and structure of nanotherapies these structures (which are also heterogeneous within the tumor) can impede nanotherapy penetration and limit their efficacy [18].

Strategies have been investigated to modulate the tumor in order to improve nanotherapy penetration. Judicious use of antiangiogenic agents have been used to “normalize” tumor blood vessels [43]. This improves vascular perfusion within the tumor and reduces interstitial fluid pressure. However, these effects may be transient and actually remove the leakiness desired from EPR. The leakiness of the blood vessel have also been modulated via other means, such as the application of VEGF or metronomic chemotherapy regimens [44, 45]. The tumor matrix can also be modulated via degradation of the collagen matrix and decreasing the levels of glycosaminoglycans, improving the uptake of antibodies and viral particles [46, 42].

Another strategy to improve therapy uptake in the tumor is the use of cell-penetrating peptides. Peptides are generated with specific targets such as tumor blood vessels or the cell nucleus, most

often via phage display [47]. These peptides are then often fused to a cargo of interest, such as nanoparticles or siRNA to improve the drug or particle uptake [48]. Interestingly, a recent paper reports that a tumor-penetrating peptide (iRGD) can improve the uptake of a variety of drug therapies ranging from small molecules to nanoparticles into tumors without direct conjugation to the agent of interest [49]. This suggests that iRGD has tumor modulating effects beyond pure tumor homing. Although the exact mechanism of action *in vivo* remains elusive, iRGD is purported to target the tumor via the α_v integrin receptors on tumor blood vessels. A cleavage mechanism then occurs, exposing a peptide motif (the CendR motif [50]) which interacts with the neuropilin-1 receptor and mediates downstream effects leading to drug tumor penetration [48, 49, 50]. Neuropilin-1 is associated with the VEGF pathway suggesting that modulation of tumor blood vessels may play a role in this process. The imaging of iRGD effects were investigated in this work. Further discussion of iRGD is found in chapter 5.

2.3 Imaging in Oncology

The research and clinical management of cancer has been revolutionized by imaging [12]. Currently, several imaging modalities are being developed and used. For successful translation of imaging assays from the benchtop to bedside, it is imperative that all aspects of the imaging assay be considered, ranging from the biological process being considered, the chemistry of the probes and the imaging hardware, to the methods of image analysis [51].

Here, we review imaging considerations with regards to the two modalities considered in this work: PET and MRI.

2.3.1 PET Basics

PET is an imaging technique that relies on the emission of coincident annihilation photons emitted indirectly from positron emitting radionuclides [52]. Attachment of radionuclides to specific biological molecules or compounds can provide highly sensitive assays of many physiological processes [51]. The biodistribution of these molecules in the body are dependent on their pharmacokinetics and pharmacodynamics. PET images showing their biodistribution allow us to infer the mechanism of specific physiological processes in a dynamic and noninvasive manner. Radiolabelled compounds

have been developed to monitor many processes including metabolism [53, 54], receptor binding [55, 56], antibody trafficking [57], gene expression [58], and perfusion [59].

As the unstable radionuclide attached to the molecule of interest decays, positrons are emitted as byproducts. The positron travels a short distance (*the positron range*), losing its kinetic energy, and then annihilates with an electron. The annihilation process converts the masses of the positron and electron into two 511 keV photons emitted in coincidence almost simultaneously (~nanoseconds, ns). Detection of these photons defines a line volume (*line of response*) along which the annihilation process occurred. Detection of these photons at multiple angles around the object allows the definition of multiple line integrals of activity distributions. Image reconstruction algorithms [60, 61] can be applied to this information to create images of radioactivity distribution (and hence the molecules attached). The spatial resolution of PET systems is on the order of ~1–5 millimeters and is a function of the positron range, deviations from colinearity of emitted coincidence photons, and the effectiveness of the detector to resolve lines of response.

With proper correction and calibration of the line integral data and reconstructed image data, the pixel intensities of resultant images should be proportional to the radioactivity present at the pixel location and thus would provide implicitly the concentration of the radiolabelled probe of interest. For further discussion of both hardware and software calibration required for well-calibrated PET, we refer the reader to [52, 51] and chapter 3.

As discussed earlier, successful PET studies require prudent integration of hardware, software, biology and chemistry. Of interest to the work described herein is the need to choose the correct radioisotope to explore the physiological processes of interest. Several positron-emitting isotopes are currently routinely used in PET (table 2.1). Three important factors need to be considered in choosing the isotope for any study:

1. *Chemistry*: Different radioisotopes are linked to the molecule of interest with a variety of methods. Halogens such as ^{18}F and ^{76}Br are covalently linked to the molecule, while radiometals such as ^{64}Cu and ^{68}Ga [62] are conjugated to the molecule via a chelate (such as DOTA) [63]. Careful consideration needs to be made to determine whether the molecule of interest can be labeled with the isotope, and whether chemistry of the labelling will affect the pharmacokinetics or biological interpretation of the PET signal. Moreover, while the

chemistry of radioisotopes are the same as the non-radioactive isotopes, the radiolabelling process needs to be well within the half-life of the isotope of interest to allow enough signal for imaging.

2. *Half-life*: The half-life of the isotope needs to be fitted to the physiological question of interest. For example, the kinetics of nanotherapies are on the order of hours to days. If the question at hand is to determine the kinetics of the agent, then a relatively long half-life isotope such as ^{64}Cu or ^{124}I would be desirable. However, a short half-life isotope such as ^{18}F or ^{11}C may be more applicable for fast acting physiological processes or diagnostic purposes, where radiation overexposure becomes a critical concern.
3. *Branching fraction*: The branching fraction for a isotope defines the fraction of particles which will decay via a particular decay mode. Specifically, we are concerned with the percentage of positron emission. One may need to design imaging protocols, the injected dose or make alterations to the calibration to account for the lower sensitivity of certain isotopes during PET imaging. This is particularly relevant for ^{64}Cu , as only 17% of all decays are positrons.

Table 2.1: Common positron-emitting isotopes

Isotope	Half-life (hours)	β^+ decay fraction (%)	β^+ energies (keV)
^{68}Ga	1.13	90	1899
^{11}C	0.34	99	960
^{15}O	0.034	99	1732
^{18}F	1.83	100	634
^{64}Cu	12.7	17.4	653
^{61}Cu	3.3	62	1220
^{76}Br	16.2	6.3	871
		5.2	990
		25.8	3382
		6	3941
^{89}Zr	78.4	22.7	897
^{86}Y	14.7	11.9	1221
		5.6	1545
^{124}I	100.3	11.8	1535
		10.9	2138

2.3.2 MRI Basics

MRI leverages the quantum mechanical phenomenon whereby nuclei with non-zero magnetic spin quantum numbers achieve splitting of spin energy levels when placed in an external magnetic field. Classically, one can visualize this spin property as a charge rotating about an axis. This rotation creates a small magnetic moment (dipole) that can be characterized by a vector. In the absence of an external magnetic field, the dipoles are randomly orientated and the vector sum of the dipoles within a region (e.g. an imaging voxel) is zero. When placed in an external magnetic field, the dipoles align to the field parallel or antiparallel to the field, corresponding to different energy levels. An excess of spins align in the lower energy state, resulting in a net magnetization vector aligned with the external B_0 field. The aligned spins precess about the field axis with a fixed angular frequency ω and is related to B_0 by the Larmor equation:

$$\omega = \gamma B_0, \quad (2.1)$$

where γ is the gyromagnetic ratio for the nuclei in question.

When aligned, the magnetization “signal” from any population of spins cannot be differentiated with the stronger B_0 field. To detect the magnetization signal, spins need to be “tipped” from the longitudinal to the transverse plane. This can be achieved by excitation of the spins with RF pulses at the Larmor frequency ω . Energy released as excited spins relax back to the longitudinal plane can be detected using receiver coils to generate a MR signal.

Differentiation of different types of nuclei and substances are determined by their frequency of precession about B_0 , and their characteristic relaxation signature after excitation. Traditionally, the two major relaxation rates examined are T_1 , the rate at which the longitudinal magnetization recovers post RF excitation and T_2 , the rate at which the magnetization in the transverse plane disappears [64]. A number of other relaxation mechanisms have also been described [65]. Different tissues (e.g. fat, water) have their own characteristic T_1 and T_2 values, which can alter depending on changes in temperature and structure.

Finally, this information can be combined with spatial encoding techniques to generate a MR image. Magnetic gradient fields can be introduced across a tissue sample, encoding each location with specific frequency and phase information. Knowledge of this enables decoding of the RF

relaxation information across the tissue sample in three dimensions.

Conventional MRI combine RF pulsing and gradient encoding together into a MRI *pulse sequence* to generate images. Combined with knowledge of the relaxation behavior of different tissues and structures, one can design and alter multiple parameters in pulse sequences to achieve certain image contrasts. The reader is referred to the following texts for a more detailed treatment [66, 64, 67]. Here, we discuss in particular two functional MRI techniques used in the work herein.

2.3.2.1 Diffusion MRI

Diffusion is the random movement of particles from regions of higher concentration to regions of lower concentration. Biologically, we are mostly concerned with the movement of water. Diffusion of water *in vivo* is not free; fiber tracts in the brain, intact cell membranes and structural tissues can restrict water diffusion in single or multiple directions.

MRI methods have been developed to produce *in vivo* images that are sensitive to the diffusion of (mainly) water. As discussed above, traditional anatomical MRI image contrast is determined by the relaxation characteristics of the tissue being imaged. Consistency of proton spin precession relies on the presence of a homogeneous magnetic field. If during the pulse sequence an extra gradient pulse is applied, the field is distorted and proton spins begin to disperse in phase. This dispersion can be reversed by the application of another gradient pulse opposite in magnitude to the first pulse to rephase the spins. However, this rephasing will be imperfect for spins that have diffused along the direction of the gradient pulse during the time interval and will lead to signal loss. The diffusion sequence was developed for NMR by Stejskal and Tanner [68] and adapted for MRI by Le Bihan (figure 2.2) [69]. The equation governing the signal from this sequence is:

$$S = S_0 e^{-bADC}, \quad (2.2)$$

where S_0 is the signal intensity with no diffusion weighting, S is the signal with the diffusion gradient applied, b is a scaling factor that incorporates the effect of gradients in the sequence and ADC , the apparent diffusion coefficient, is the aggregate diffusion coefficient value calculated from the imaging voxel. The ADC can be calculated by acquiring images at multiple b values and performing a curve fit.

In recent years, more complicated models of diffusion have also been applied to this to analysis the diffusion data, probing different compartments and aspects of the *in vivo* diffusion process [70, 71, 72, 73, 74].

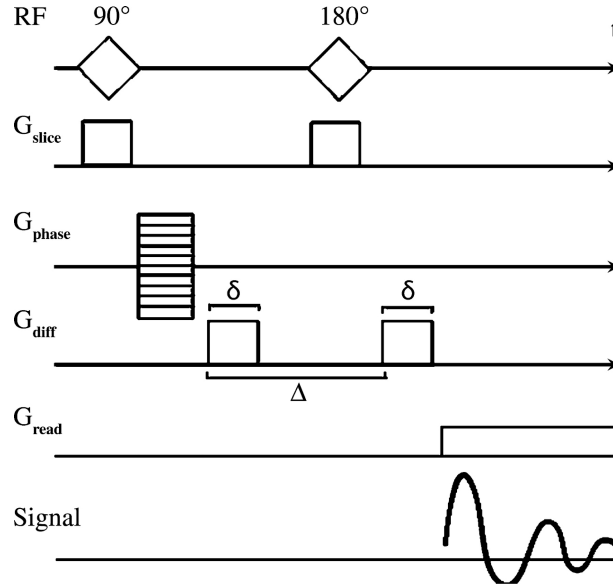


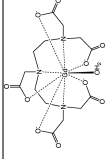
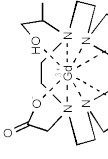
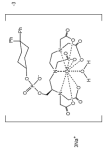
Figure 2.2: A basic pulsed gradient SE sequence for diffusion MRI imaging. Two diffusion gradients (G_{diff}) are incorporated into a standard SE sequence sensitive to different diffusion rates along the gradient direction. δ = duration of the diffusion-encoding gradient, Δ = diffusion time interval, G_{phase} = phase-encoding gradient, G_{read} = readout gradient, G_{slice} = section-selective gradient. These acquisition parameters are encapsulated into the b factor described in the text (adapted from [73]).

2.3.2.2 Dynamic-Contrast Enhanced MRI (DCE-MRI)

Conventional MRI provides high resolution images of anatomy. Paramagnetic contrast agents can alter local tissue relaxation parameters to aid image contrast enhancement and highlight specific structures. Many different MRI contrast agents have been developed (table 2.2) which can alter tissue T_1 or T_2 . DCE-MRI most commonly refers to MRI that dynamically alter the T_1 -weighting of tissues [75, 76, 77].

These contrast agents have characteristic pharmacokinetic properties, which researchers and clinicians have harnessed to study the functional properties of tissues. Most commonly, contrast agents are injected intravenously and a time series of MRI images are acquired to follow the wash-in and wash-out of the contrast agent. The vascular function of tissues such as viable tumors and

Table 2.2: Some MRI contrast agents considered in this work

Name	Formula	Structure	Molecular weight	$r_1(B_0)$ (mM/s)	$r_2(B_0)$ (mM/s)
Magnevist	$C_{28}H_{54}GdN_5O_{20}$		938 g/mol	3.4 (1T)	3.8 (1T)
Prohance	$C_{17}H_{29}GdN_4O_7$		558.68 g/mol	3.7 (1T)	4.8 (1T)
Ablavar	$C_{33}H_{40}GdN_3Na_3O_{15}P$		975.88 g/mol	19–28 (1.5T)	160 (0.47T)
Ferumoxytol	$Fe_{5874}O_{8752} - C_{111719}H_{18682}O_{9933}Na_{414}$		750 kDa	40 (0.47T)	388 (0.25T)
Albumin-(Gd-DTPA)35			107 kDa	14.8 (0.25T)	

livers can be inferred by the behavior of the contrast agent over time (figure 2.3). Other studies have also used contrast agents to study the dynamics of cellular processes like inflammation [78] and pharmacological response [79].

Several methods can be applied to analyze DCE-MRI [80, 81, 82]. Most were adopted from the field of nuclear medicine. Semiquantitative metrics such as the area under the curve (AUC), the slopes of contrast agent (CA) uptake and washout curves as well as the peak CA uptake have been applied to DCE-MRI. Alternatively, quantitative metrics based on pharmacokinetic modeling can be derived. The most widely used model is the two-compartment Kety model from which volume transfer constants (K_{trans} , k_{ep}) between compartments and volume of the tissue compartments (v_e , v_p) can be calculated.

It is important to remember that the image enhancement observed in these studies are not a direct measure of [CA], but the enhancement due to water exchange with CA. Recently, the effects of water-compartmentalization on CA-water exchange have been studied. Kinetic models which consider these trans-cytoplasmic effects have been proposed and explored for DCE-MRI analysis [83, 84, 85, 86].

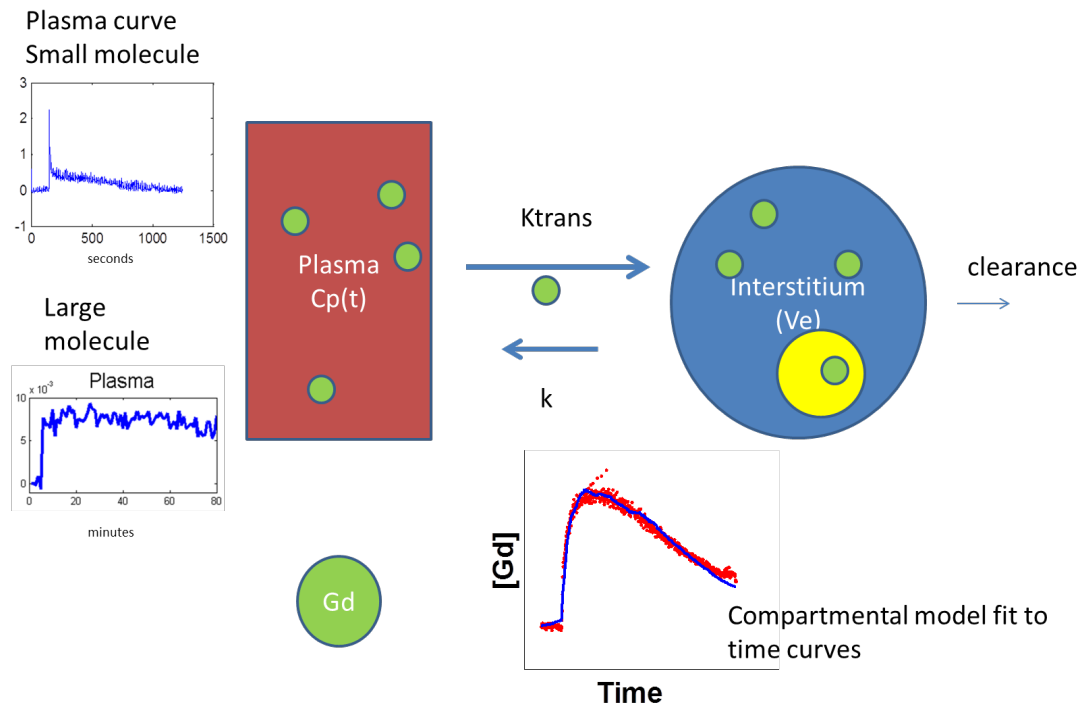


Figure 2.3: DCE-MRI can infer tissue vascular function. MRI-visible contrast agents injected intravenously can be visualized by MRI in plasma and also vascularized tissues. The pharmacokinetics of the image enhancement is related to the structure of the CA (e.g. small molecule CA have fast first-pass circulation vs. large molecule CA). Image enhancement curves can be fitted to pharmacokinetic models to infer quantitative parameters of vascular function. Shown here is the commonly used two-compartment model.

2.3.3 Combining PET and MRI

2.3.3.1 Why Hybrid PET/MRI?

While both PET and MRI are powerful imaging modalities individually, each has their own strength and weaknesses. These are summarized in table 2.3.

Table 2.3: Comparison between PET and MRI

	PET	MRI
Strength	Very sensitive (\sim nM)	high-resolution soft-tissue and anatomical information (<1 mm)
	Can monitor multiple biological processes	Metabolic (MRS) and physiological information available (e.g. diffusion, DCE-MRI)
		Multiple contrast mechanisms: flexible
Weakness		No ionizing radiation
	Poor spatial resolution ($\sim 1-2$ mm)	Not sensitive (\sim mM)
	Limited anatomic information	Multiple contrast mechanisms: complicated
	Ionizing radiation	

From the table, it is clear that PET and MRI are quite complimentary and information from the two modalities should be synergistic [14]. Yet, this alone would not justify the efforts to develop integrated systems. The key advantage of integrated systems is the ability to obtain simultaneous (or near-simultaneous) PET and MRI information. Here, we discuss why the integrated approach is worthwhile.

There are several reasons why integrated PET/MRI is useful. Although mundane, the ability to acquire two images at once can save time, which is important both in the lab and the clinic. Further, one modality can aid the image quality of the other. The most obvious application has

been the use of MRI information to improve PET quantification. MRI data can offer information for attenuation correction [87, 88] and motion correction [89]. Hybrid PET/MRI systems can also be combined with bimodal PET/MRI probes to quantify tissue CA uptake and aid interpretation of the CA imaging signal [90]. In all of these cases, robust coregistration of the PET and MRI image space enables MRI data to directly correct the PET data.

Ultimately though, it is the physiological applications possible with PET/MRI that will drive the widespread adoption of PET/MRI technology. subvoxel coregistration in space, which is difficult to achieve especially outside the head, enables us to make solid biological inferences between spatial distributions observed in PET and MRI at a fine scale. This aspect of PET/MRI integration forms the scope of our investigations in chapter 3. Synchrony of the PET and MRI signals enables us to make inferences between PET and MRI assays of time-sensitive physiological processes: this is the motivation for the investigations in chapters 4 and 5. The ability to obtain the two modalities in near real-time also enables the information obtained from one modality to drive studies performed with the alternate modality and vice versa (figure 2.4).

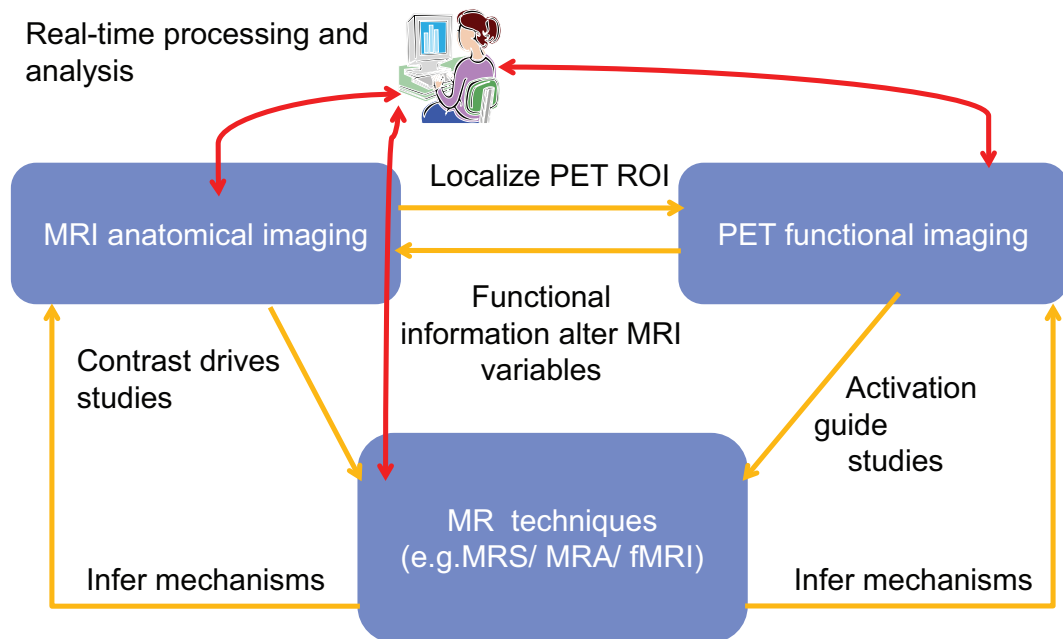


Figure 2.4: Real-time paradigm for PET/MRI studies.

2.3.3.2 Current State of Hybrid PET/MRI Systems

Current approaches for hybrid PET/MRI systems are summarized in table 2.4. Four main approaches are followed:

1. Sequential PET/MRI with PET and MRI hardware separate from each other.
2. Sequential PET/MRI with integrated PET/MRI hardware, but powered separately.
3. Simultaneous PET/MRI with radical redesign of MRI and PET hardware.
4. Simultaneous PET/MRI with novel PET hardware to fit in conventional MRI (PET insert).

The PET/MRI system developed in this work is the PSAPD-based PET insert (figure 2.5) [105]. Detailed description about the system implementation is described in [106] and chapter 3.

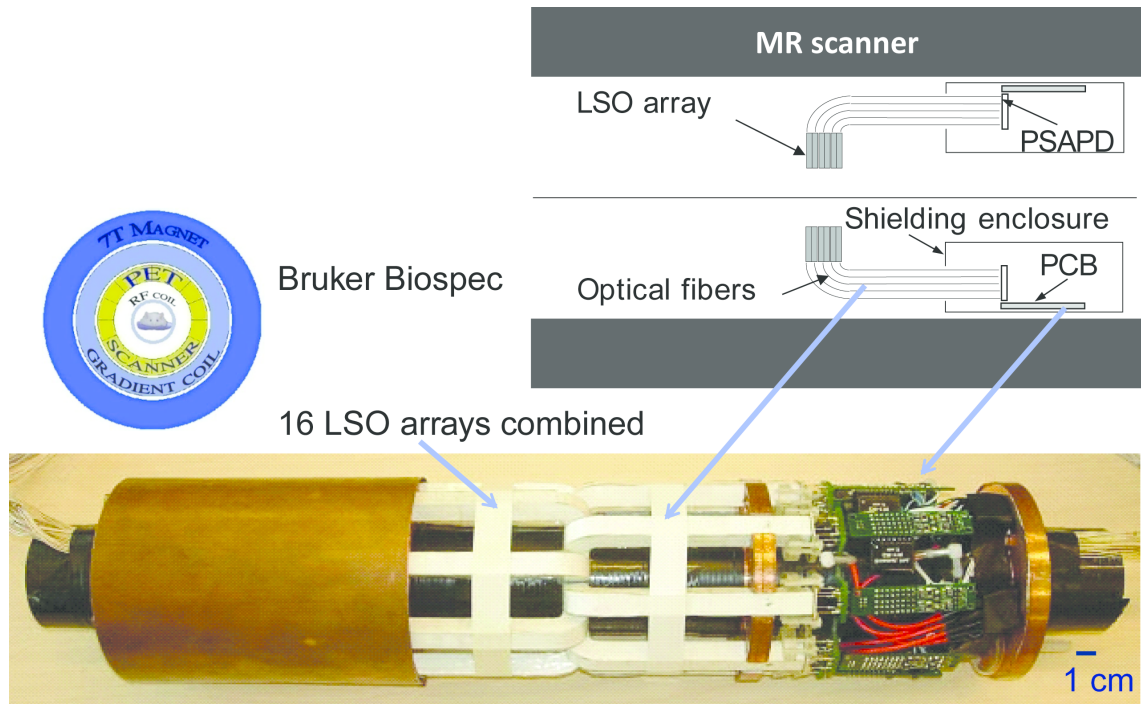


Figure 2.5: PSAPD-based MR-compatible PET insert. The insert consists of 16 LSO-PSAPD detectors arranged in a single ring. The insert is placed inside the bore of a 7 T small animal MRI. The RF coil and animal subject is placed in the PET insert.

2.3.4 Digital Whole-body Autoradiography

Digital whole-body autoradiography (DWBA) is used as an *ex vivo* assay of radioactivity distribution in tissues [107, 108, 109]. The tissue of interest is sliced and placed onto the DWBA phosphor

Table 2.4: Current state of hybrid PET/MRI systems

Approaches	Description
Sequential PET/MRI, separate hardware	Sequential clinical PET/MRI system. Mature PET and MRI technologies integrated with a moving patient table (Phillips, Netherlands) [91, 92].
Sequential PET/MRI, separate powering	Field-cycling method whereby the MRI field is turned on for MRI acquisition then turned off for PET acquisition. MRI and PET are integrated, enables conventional PET PMT detectors to be used. MRI works at low field (0.3 T) [93].
Simultaneous PET/MRI with radical redesign of MRI and PET hardware	Design of a split-magnet to house extended PMT PET detectors. MRI and PET are integrated, mature PET PMT detectors designed into the system. MRI works at low field (1 T) [94]. Integrated clinical whole-body PET/MRI system consisting of APD-based detectors housed between RF coils and MRI gradients (Siemens, Germany). MRI and PET are integrated [95]
Simultaneous PET/MRI with novel PET hardware to fit in conventional MRI	PMT-based ring inserts placed inside a open 0.2 T , 0.3 T and 3 T MRIs. Long fiber-optic cables are used to couple the scintillation elements to the PMTs and electronics [96, 97, 98, 99]. APD-based head insert for 3 T clinical MRI (Siemens, Germany). The FOV is limited to the brain [100]. APD-based PET ring system based on the RatCAP PET, can be placed in 9.4 T MRI. Insert can be removed [101]. Integrated PET insert based on APD-LSO detectors, developed for small animal 7 T MRI. Insert can be removed [102]. SiPM-based PET ring insert for small animals, tested in clinical 3 T and 0.15 T MRI. Inserts can be removed [103, 104]. Integrated PET insert based on PSAPD-LSO detectors, developed for small animal 7T MRI. Insert can be removed [105].

imaging plate. The phosphor imaging plate is designed to detect high energy radiation. Excitation of the BaFBr:Eu²⁺ crystals on the plate causes oxidation from Eu²⁺ to Eu³⁺ and the trapping of the electron in the “color-center” of the BaFBr⁻ complex. The plate can be read by shining red light (~633 nm) onto the plate and imaging the photon released during Eu³⁺ reduction back to Eu²⁺ [110].

DWBA has been used extensively in pharmaceutical research to study drug distributions and receptor binding. It has been used to verify isotope distributions observed in PET [111]. This is aided by DWBA’s relatively high spatial resolution (~100 μ m) and high sensitivity. The same tissue of interest can be imaged by DWBA several half-lives after a PET study to verify biodistribution [112], and forms an ideal “gold-standard” for PET.

2.3.5 Imaging of Targeted Nanotherapy Uptake

Knowledge of the biodistribution of targeted therapies is traditionally performed from *ex vivo* assays. Drug kinetics are determined by measuring drug content in tissues of interest (in animals) harvested at specific time points [113, 30]. However, a wide intersubject variability of drug uptake may exist and thus requires a large number of animals to make robust statistical inferences. Increasingly, these data are being complemented by *in vivo* imaging data [114, 19] that can be acquired longitudinally within single subjects. Biodistribution studies of radiolabelled antibodies and nanoparticles can be performed using PET or SPECT due to the high sensitivity of radioactivity [115, 116, 117, 118]. Although MRI is a less sensitive modality, researchers have also developed MRI approaches to monitor the targeting of nanotherapies in the tumor [119]. MR-visible agents can be linked to tumor-targeting antibodies [120] and nanoparticles [121, 48] and can utilize intrinsic properties of tumors (e.g. the presence of certain enzymes like matrix metalloproteinases) to activate the localized signal [35].

Most of these studies focus on imaging the gross uptake of targeted therapies into tumors, that is, whether the therapy will reach and stay in the tumor. However, there is recent interest in understanding how the tumor microenvironment may modulate this uptake intratumorally. *Ex vivo* studies suggest that uptake of targeted nanotherapies can be related to structural factors such as the distribution of blood vessels [113, 122]. Kobayashi *et al.* observed that MRI of breast tumor mouse models showing different vascular structures can be correlated with gross tumor antibody

uptake [123]. Thurber and colleagues have begun to investigate these factors by developing models to explain these distributions and verifying these models with fluorescent imaging [16, 20, 124]. Imaging studies that enable the dynamic visualization of the tumor microenvironment (which can be probed by MRI and PET) in concert with the distribution of the targeted therapy will contribute to the development of these models for clinical application.

2.3.6 Imaging of Targeted Nanotherapy Response

At present, clinical imaging of tumor response to targeted nanotherapies focuses on evaluating size changes of tumors as determined by the RECIST criteria [11]. Tumor size and growth are evaluated using MRI or PET/CT to monitor changes in size [125, 126]. This mirrors the standard of care for evaluating small molecule chemotherapy response. For example, the clinically approved liposomal formulation of doxorubicin (Doxil) has been monitored by PET/CT in phase I/II studies [127, 128], while albumin-bound paclitaxel (Abraxane) have been followed by PET/CT and MRI [129].

Functional imaging techniques, such as diffusion MRI [130], DCE-MRI [131] and ^{18}F -FDG-PET and ^{18}F -FLT-PET [53] and are being investigated for early treatment monitoring for small molecule anticancer drugs. These techniques have the ability to determine changes in the tumor prior to tumor size changes, and to probe changes of biological processes within the tumor. Moreover, such functional imaging data can be applied to models of tumor growth to enable prediction of tumor response [132, 133]. DCE-MRI have been used to evaluate responses to bevacizumab and its antivascular effects [134]; but fewer preclinical [126, 135, 136] or clinical studies have been pursued to investigate the utility of such techniques to monitor tumor response in other nanotherapies. The reader is referred to chapter 4 for further discussion of this topic.

Chapter 3

Development of Simultaneous PET/MRI Technology for Robust *In Vivo* Studies

3.1 Further Considerations of PET Insert Effects on *In Vivo* MRI Performance

Initial studies with the MR-compatible PET insert demonstrated good SNR and uniformity of MRI images with little distortion and narrow FWHM values of single-pulse water proton spectra in the presence of the PET [106]. Here, we address aspects of MRI image quality that are relevant for robust *in vivo* studies.

3.1.1 Materials and Methods

3.1.1.1 B_0 Effects within the MR FOV

A glass spherical phantom (diameter = 3 cm) containing water doped with Gd-DTPA (such that the solution had $T_1, T_2 = 200$ ms at 7 T) was placed in a home built birdcage RF coil (ID = 35 mm) positioned in the isocenter of the MRI for all imaging studies. B_0 maps were acquired using the *FieldMap* routine implemented in Paravision 5.1. The routine consists of a 3D double gradient echo dataset acquisition (TR = 20 ms, TE1/TE2 = 1.43/5.43 ms, FA = 20°, Matrix size = 64 × 64 × 64, FOV = 80 × 80 × 80 mm³ centered in the isocenter of the MRI, SNR threshold = 5), followed by a phase difference calculation on the reconstructed datasets, and finally a phase unwrapping and conversion to a B_0 frequency fieldmap. B_0 fieldmaps (and magnitude images) were generated by the *MAPSHIM* macro and converted to units of ppm (assuming 300 MHz at 7 T). B_0 maps were

obtained for three conditions:

1. No PET insert.
2. PET insert in the MRI, unpowered.
3. PET insert in the MRI, powered.

Magnitude images were used to identify voxels which bore real signal in the fieldmaps using a signal intensity threshold. Voxels which had viable spatial ΔB_0 values for all three conditions were compared. ΔB_0 linewidths with and without the PET were plotted against each other and the differences between the conditions calculated.

B_0 fieldmaps were also obtained with and without the presence (powered) of the PET insert for a glass cylindrical phantom (OD = 28 mm, length = 61 mm, volume = 20 mL) containing distilled water doped with $CuSO_4$ ($[CuSO_4] = 1.3$ mM, $T_1 = 440$ ms, $T_2 = 350$ ms at 7 T, *FieldMap* routine: TR = 20 ms, TE1/TE2 = 2/5.81 ms, FA = 20°, matrix size = 177 × 177 × 80, FOV = 35.35 × 35.35 × 60 mm³ centered in the isocenter of the MRI, SNR threshold = 5).

3.1.1.2 B_1 Measurements within the MR FOV

Relative B_1 maps with (powered) and without the presence of the PET insert were acquired using the $CuSO_4$ solution phantom described in section 3.1.1.1. Maps were obtained with an extended multi-flip angle method that accounts for inhomogeneous B_0 and B_1 fields [137]. A series of 21, slab selective, 3D gradient echo images were acquired (TR = 1500 ms, TE = 5 ms, matrix size = 32 × 32 × 16, FOV = 35.35 × 35.35 × 58 mm³, bandwidth = 50 kHz, second phase direction: axial). The reference pulse gain was altered across an attenuation range of 42.6 dB to 3.3 dB. This corresponded with a FA range of 10° to 400° at 20° increments. A relatively short 0.3 ms rectangular RF pulse with FWHM of 4.3 kHz was used to suppress the influence of remaining B_0 inhomogeneities during excitation besides those resulting from the slab excitation gradient. The magnitude signals from the image series were fitted to the following equation:

$$S(I) = \kappa \sqrt{(\sin(\frac{\pi}{2} - \theta(I)) \sin(\alpha(I)))^2 + (\cos(\frac{\pi}{2} - \theta(I)) \sin(\frac{\pi}{2} - \theta(I)) (1 - \cos(\alpha(I))))^2}, \quad (3.1)$$

where I is the coil current applied for each flip angle α , S is the image signal intensity, and κ is a constant term incorporating the proton spin density, coil sensitivity, and geometry. In the presence of field inhomogeneities, excitation of the sample may be off-resonance. For this scenario, the effective excitation field B_{eff} about which magnetization is being rotated is deflected out of the transverse (xy) plane towards B_0 (z plane) and is described by

$$B_{eff} = \frac{1}{\gamma}(\Delta\omega e_z + \omega_1 e_{xy}), \quad (3.2)$$

where ω_1 is the angular frequency of the rotation around the axis of the excitation field in the transverse plane, $\Delta\omega$ is the difference in angular velocity between the Larmor precession about B_0 and the rotation of the excitation field. For a given $\Delta\omega$ and B_{1u} (B_1 per unit current), the angle θ between B_{eff} and the transverse plane is given by

$$\theta(I) = \tan^{-1}\left(\frac{\Delta\omega 2\pi}{B_{1u}I\gamma}\right). \quad (3.3)$$

The actual FA in the presence of off-resonant excitations is

$$\alpha(I) = \tau \sqrt{(\Delta\omega 2\pi)^2 + (B_{1u}I\gamma)^2}. \quad (3.4)$$

τ is the duration of the RF excitation pulse.

The coil current I at different flip angles were not measured for this study. Instead, relative B_{1u} maps with and without the PET insert were compared. Coil current was derived from the nominal FA assuming a B_{1u} field strength of 1 mT/A and using the on-resonance FA equation:

$$\alpha = \gamma\tau B_{1u}I. \quad (3.5)$$

3.1.1.3 T_1 Measurements within the MR FOV

Robust quantitative MRI studies (such as DCE-MRI) require the derivations of quantitative T_1 maps. We evaluated the variations of T_1 measurements due to the presence of the PET insert. A glass cylinder (diameter = 4 mm) filled with Gd-DTPA doped water placed on the side of the animal holder during routine animal studies was used for this evaluation. T_1 maps were calculated using

a variable flip angle method. Gradient echo images (FLASH, FA = 12°, 24°, 36°, 48°, 60°, matrix size = 140 × 80, voxel size = 0.25 × 0.25 mm², slice thickness = 1 mm, 9 slices) were obtained at the center of the MRI with (TR/TE = 400/ 2 ms) the PET insert powered on in the bore and the PET insert removed (TR/TE = 200/2 ms). The TR values were different since the temperature requirements of the PET precluded the use of sequences with short TR. Voxel-by-voxel T_1 maps were derived from ROIs manually drawn at the center slice of each dataset and fitted to

$$S = S_0 \frac{\sin\theta(1 - e^{-TR/T_1})}{(1 - \cos\theta e^{-TR/T_1})}, \quad (3.6)$$

where S is the signal intensity measured from the image. T_1 maps obtained with and without the PET on five separate studies each were analyzed. A nonlinear Levenberg-Marquardt algorithm implemented in MATLAB was used for the data fitting.

3.1.1.4 Signal Drift

Feasibility of simultaneous dynamic PET/MRI was evaluated. A T_1 -weighted DCE-MRI sequence (FLASH, TR/TE = 400/2 ms, FA = 30°, matrix size = 140 × 80, voxel size = 0.25 × 0.25 mm², slice thickness = 1 mm, 11 slices, time resolution = 30 s, 90 repetitions) was run with and without the PET insert installed to image tumor-bearing mice. 0.2 mmol/kg Gd-DTPA was injected via the tail vein into each mouse 5 minutes into each scan. A dynamic R_2^* -weighted sequence (FLASH, TR/TE = 600/8.5 ms, FA = 30°, Matrix size = 128 × 128, Voxel size = 0.2 × 0.2 mm², slice thickness = 0.754 mm, 9 slices, time resolution = 60 s, 200 repetitions) was run with the PET insert installed to image the mouse brain. 20 mg/kg Fe ferumoxytol was injected into each mouse via the tail vein 20 minutes into the scan. Tumor, brain and glass cylinder (filled with olive oil, inner diameter = 1.5 mm) ROIs drawn in the appropriate datasets were used for image analysis. The following parameters [138] were measured:

1. The temporal drift of the mean signal intensity across the rod ROIs. A second-order polynomial to the time series was fitted. The difference between the minimum and maximum of the fitted curve was then determined. The result is expressed as a ratio to the signal mean.
2. Fast temporal fluctuations of the mean signal (root mean squared error, RMSE). The slow

temporal drift of the mean signal from the rod ROIs was first removed. The RMSE was determined from the ratio of the detrended signal SD to overall signal mean.

The parameters was calculated from three separate datasets for each separate condition.

3.1.2 Results

3.1.2.1 B_0 Effects within the MR FOV

ΔB_0 comparison for the spherical phantom with and without the presence of the PET is shown in figure 3.1. Fieldmaps are shown in figure 3.2. No significant difference was observed between the PET powered off and powered on conditions compared to the no PET condition. Linewidth differences (in ppm) were -0.04 ± 0.29 and -0.01 ± 0.32 respectively. Fieldmaps for the cylindrical phantom with and without the PET are shown in figure. $\Delta \Delta B_0$ comparison for this phantom is shown in figure 3.4. The linewidth difference (in ppm) between the PET powered on and no PET condition for this phantom was -0.16 ± 0.36 . For both phantoms, the linewidth remained at <1 ppm within most of the imaging volume with or without the PET insert. This is consistent with the specifications of the manufacturer which state that the main magnetic field has an inhomogeneity <1 ppm in a spherical volume with a diameter of 11 cm.

3.1.2.2 B_1 Measurements within the MR FOV

Relative B_{1u} maps for the cylindrical phantom with and without the PET insert are shown in figure 3.5. A voxel-by-voxel comparison of the B_{1u} values is plotted in figure 3.6. Mean, SD, and CoV of the relative B_{1u} values are shown in table 3.1.

Table 3.1: Relative B_{1u} values with and without the PET insert

Condition	Relative B_{1u} (mT/A)	CoV
No PET installed	0.22 ± 0.03	0.16
PET installed and powered on	0.24 ± 0.03	0.14

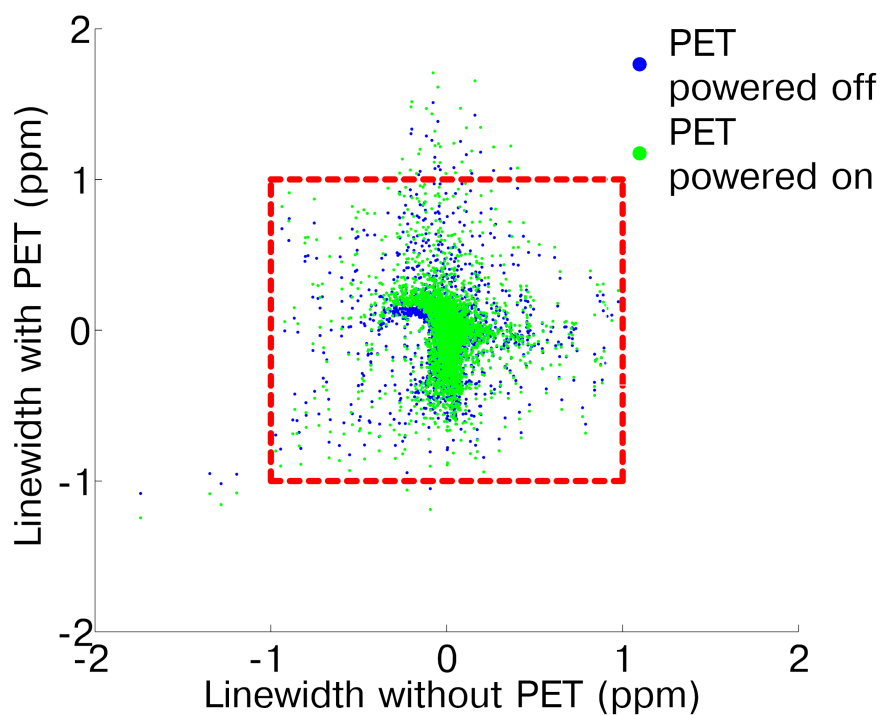
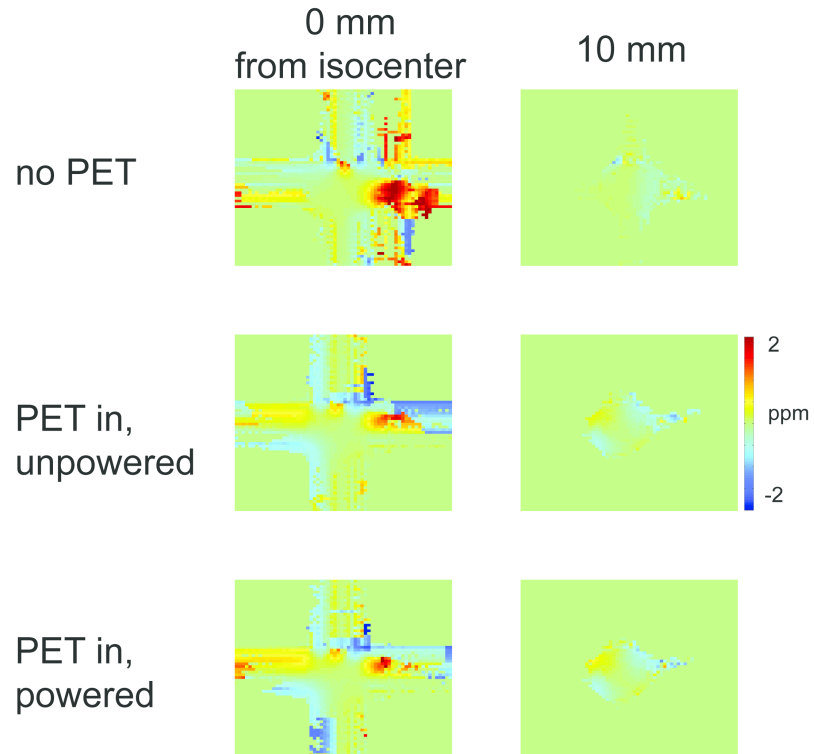
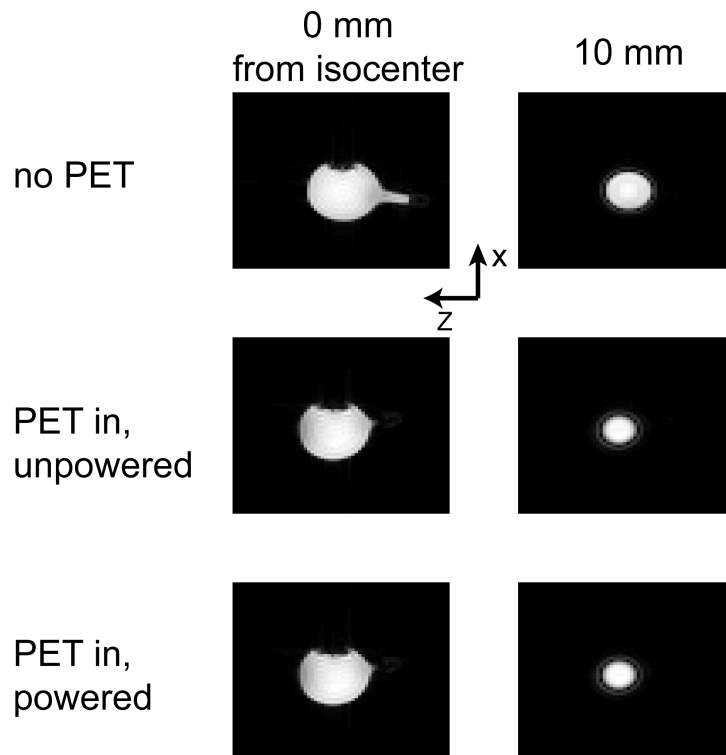


Figure 3.1: B_0 comparisons with and without the PET insert for the spherical phantom. Fieldmap voxels from matching spatial locations in the presence or absence of the PET insert (powered on and off) were compared in a scatter plot. No significant difference in ΔB_0 between the PET on and off conditions were seen. The fieldmap within the MRI imaging volume were within the B_0 inhomogeneities specified by the manufacturer (<1 ppm, defined by the red box) regardless of the presence of the PET insert inside the MRI.

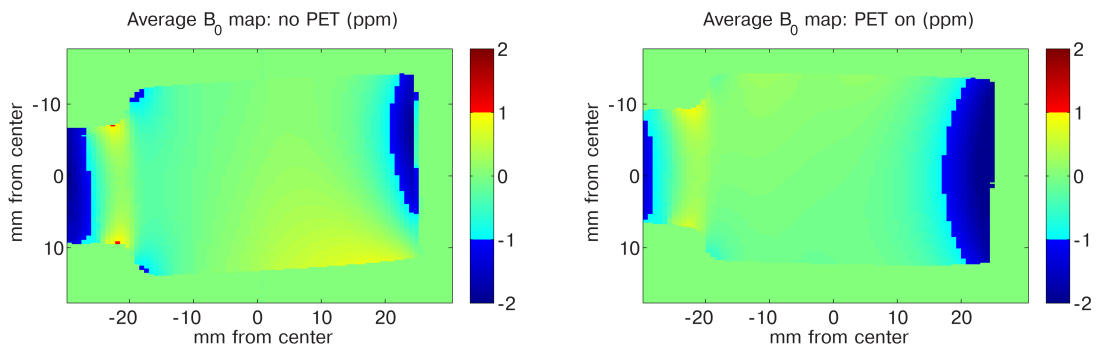


(a) Fieldmaps calculated at the MRI isocenter (left) and 10 mm lateral to the isocenter (right) for different PET insert conditions for the spherical phantom. No significant differences in the fieldmaps were seen in the presence of the PET insert.

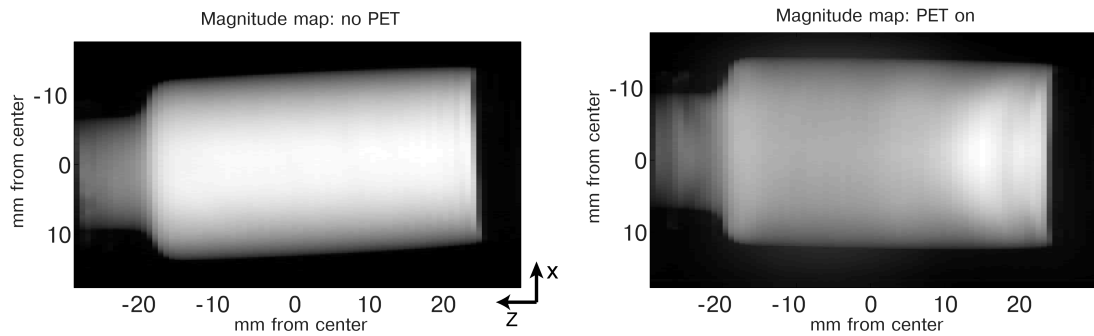


(b) Magnitude images of corresponding fieldmaps shown in (a). Slices are in sagittal orientation.

Figure 3.2: B_0 fieldmaps in the presence of the PET insert for the spherical phantom.



(a) Fieldmaps calculated for the cylindrical phantom without (left) and with (right) the PET insert. The average linewidth within the phantom were <1 ppm whether the PET was present or not. Inhomogeneities >1 ppm were observed for both conditions at outer edges of the phantom, corresponding to the cap and the bottom surface.



(b) Magnitude images of corresponding fieldmaps shown in (a). Slices are in sagittal orientation.

Figure 3.3: B_0 fieldmaps in the presence of the PET insert for the cylindrical phantom.

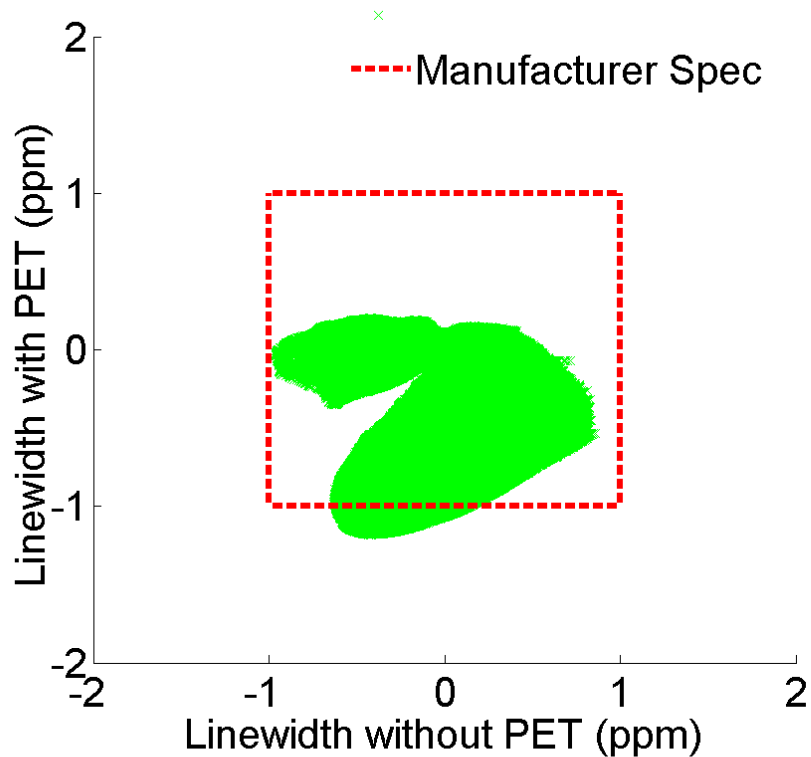


Figure 3.4: B_0 comparisons with and without the PET insert for the cylindrical phantom. Fieldmap voxels from matching spatial locations in the presence or absence of the PET insert (powered on), within the central 30 mm of the MR FOV (along the axial direction), were compared in a scatter plot. No significant difference in ΔB_0 between the PET on and off conditions were seen. The fieldmap within the MRI imaging volume were mostly within the B_0 inhomogeneities specified by the manufacturer (<1 ppm, defined by the red box) regardless of the presence of the PET insert inside the MRI. A small group of voxels lying outside the 1 ppm threshold corresponds with the bottom glass surface of the phantom (figure 3.3).

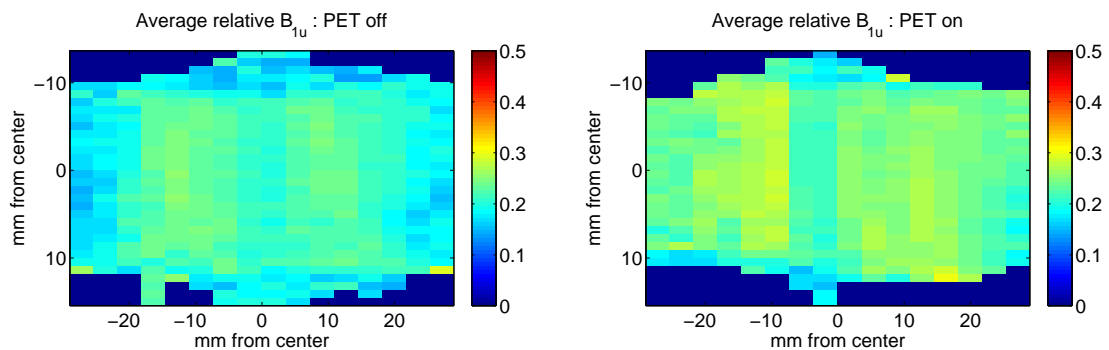


Figure 3.5: Relative B_1 maps with and without the PET insert.

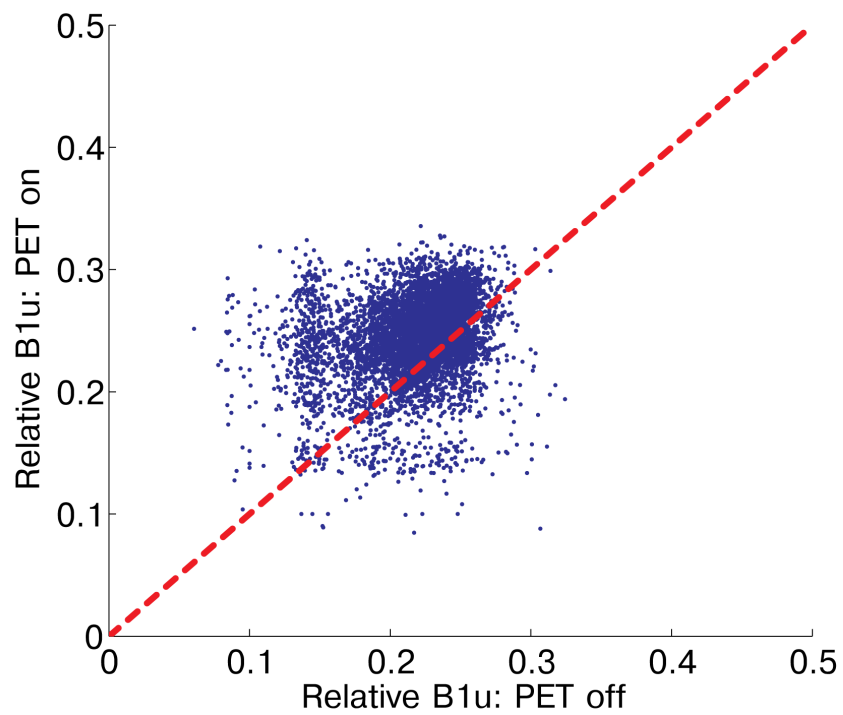


Figure 3.6: B_{1u} comparisons with and without the PET insert for the cylindrical phantom. Fieldmap voxels from matching spatial locations in the presence or absence of the PET insert (powered on) were compared in a scatter plot.

3.1.2.3 T_1 measurements within the MR FOV

T_1 rod measurements with and without the PET insert is shown in Table 3.2. The presence of the PET insert resulted in a slight increase of the mean and SD of T_1 values measured from the rod. However, this increase was not significantly different (two-sided t-test, $p = 0.2$).

Table 3.2: T_1 measurements with and without the PET insert

Condition	T_1 (ms)
No PET installed	473±27
PET installed and powered on	552±50

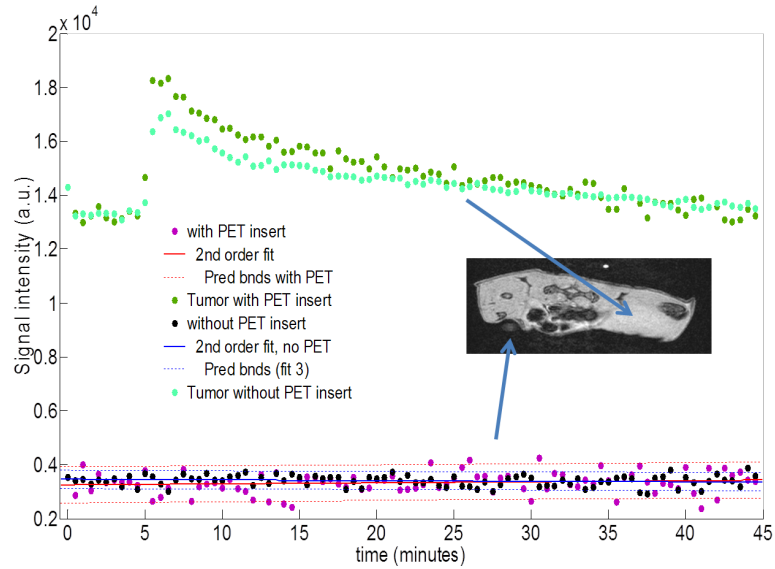
3.1.2.4 Signal Drift

Representative time traces from T_1 - and R_2^* -weighted sequences are shown in figure 3.7. No major signal drift was observed in the presence of the PET insert. Signal changes due to the injection of contrast agents were clearly seen with or without the PET insert. This observation was confirmed from the quantitative signal drift and RMSE metrics (figure 3.8). However, there were small increases in signal drift and RMSE when the PET insert installed; the latter was statistically significant.

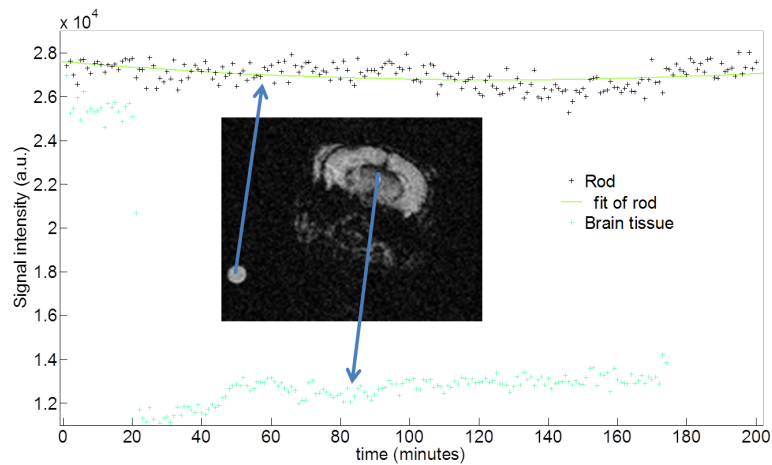
3.1.3 Discussion

Characterization of MRI performance show that ΔB_0 maps did not differ significantly in the presence of the PET insert. Small differences were observed for relative B_{1u} values obtained with and without the PET insert. B_1 inhomogeneity is a recognized issue for quantitative high field (>3 T) MRI [139, 140, 141]. However, this did not result in significant differences of the T_1 values measured during typical PET/MRI study situations. These observations are consistent with studies performed on other hybrid systems [138]. Variation between individual scans can be attributed to multiple factors. The phantoms were removed from the MRI during installation of the PET insert and thus could not be exactly repositioned. The presence of additional shielding material in the bore when the PET is installed may also introduce unwanted eddy currents and reduce SNR [142].

The slight decrease in SNR is reflected in the quantitative measurements of dynamic MR drift.



(a) T_1 -weighted DCE-MRI traces with and without the PET insert. Sudden increase of signal in the tumor corresponds to CA injection (~ 5 minutes into the scan).



(b) R_2^* -weighted time trace with the PET insert installed. Signal decrease in brain at ~ 20 minutes corresponds to injection of iron oxide contrast agent.

Figure 3.7: Dynamic MRI time traces with and without the PET insert.

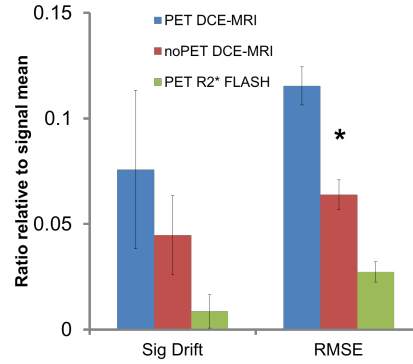


Figure 3.8: Signal drift quantification with and without the PET insert for T_1 - and R_2^* -weighted sequences. A slight increase in both signal drift and RMSE were observed when the PET was installed ($p < 0.05$ for RMSE).

Both signal drift and RMSE increased in the presence of the PET for DCE-MRI datasets. Unlike the drift observed by Wehrl *et al.* [138], these drift increases were not directional and mainly reflect the SNR attenuation in the presence of the PET. They noted that drift in both the PET and MRI signals over time on their system are influenced by temperature fluctuations. We too have observed this phenomenon, and thus utmost care is taken to maintain stable temperature during all our PET/MRI studies.

It is important to note that our drift assessments were performed on an oil-filled rod. The lower SNR of oil, compared to Gd-DTPA and $CuSO_4$ used in other studies, would contribute to the relatively lower drift and RMSE values. Gd-DTPA doped water and a rod with a larger diameter is now used for quality control of the signal drift. Importantly, qualitative assessments of signal changes due to contrast agent (both T_1 and T_2^* agents) injection showed a clear signal trace in *in vivo* tissue with and without the PET. This shows that the dynamic PET/MRI studies we wish to pursue are quite feasible since they all involve contrast agent injection. Further assessment is needed to explore the signal drift without contrast agents (e.g. BOLD studies).

In summary, we have characterized various aspects of the MRI system performance important for robust *in vivo* imaging in the presence of the PET insert. The results suggest that while the presence of the PET insert does affect the quality of MR images produced, the effects are small and should not hinder the acquisition of meaningful *in vivo* simultaneous PET/MRI data.

3.2 A Robust Coregistration Method for *In Vivo* Studies Using a First Generation Simultaneous PET/MRI Scanner

3.2.1 Abstract

3.2.1.1 Purpose

Hybrid positron emission tomography (PET)/magnetic resonance (MR) imaging systems have recently been built that allow functional and anatomical information obtained from PET and MR to be acquired simultaneously. The authors have developed a robust coregistration scheme for a first generation small animal PET/MR imaging system and illustrated the potential of this system to study intratumoral heterogeneity in a mouse model.

3.2.1.2 Methods

An alignment strategy to fuse simultaneously acquired PET and MR data, using the MR imaging gradient coordinate system as the reference basis, was developed. The fidelity of the alignment was evaluated over multiple study sessions. In order to explore its robustness *in vivo*, the alignment strategy was applied to explore the heterogeneity of glucose metabolism in a xenograft tumor model, using ^{18}F -FDG-PET to guide the acquisition of localized ^1H MR spectra within a single imaging session.

3.2.1.3 Results

The alignment method consistently fused the PET/MR datasets with subvoxel accuracy (registration error mean = 0.55 voxels, <0.28 mm); this was independent of location within the field of view. When the system was used to study intratumoral heterogeneity within xenograft tumors, a correlation of high ^{18}F -FDG-PET signal with high choline/creatine ratio was observed.

This section is published in *Medical Physics*: Thomas S. C. Ng, Daniel Procissi, Yibao Wu, and Russell E. Jacobs (2010) A robust coregistration method for *in vivo* studies using a first generation simultaneous PET/MR scanner. *Medical Physics*, 37 (5). pp. 1995–2003.

Acknowledgments: The authors thank Dr. Andrew Raubitschek for providing the mice and tumors, Dr. Scott Fraser, Dr. Simon Cherry, Dr. Jinyi Qi, Dr. Ciprian Catana, and Dr. James Bading for advice on imaging issues and support, Hargun Sohi and Marucha Sanchez for animal handling, Sonia Collazo for computer assistance and Andrey Demyanenko for making the animal RF coil. The project was funded in part by NIBIB Grant No. R01 EB000993, NCRR Grant No. U24 RR021760, Mouse BIRN, a student fellowship from the SNM Education and Research Foundation, and the Beckman Institute.

3.2.1.4 Conclusions

The authors present an implementation of an efficient and robust coregistration scheme for multimodal noninvasive imaging using PET and MR. This setup allows time-sensitive, multimodal studies of physiology to be conducted in an efficient manner.

3.2.2 Introduction

Noninvasive, multimodal imaging is increasingly being adopted for both clinical and preclinical studies, as researchers realize that information available from different image contrasts can complement each other to provide more insights into physiological processes of intact, living animals [143, 144, 58, 145, 146]. The most prominent example of this has been the widespread adoption of combined positron emission tomography (PET) and computed tomography (CT) systems. Anatomical information from the CT has been very useful in giving context to the PET image, especially in oncology research [147, 148, 149, 150]. In both clinical and small animal PET/CT systems, a combination of careful hardware alignment along with image registration via fiducial markers, phantoms, and/or matching of expected uptake patterns in the two images allows accurate spatial fusion of PET and CT images [151, 152, 153, 154].

Magnetic resonance (MR) imaging is another imaging modality widely used for noninvasive, *in vivo* imaging. It can provide high-resolution, soft tissue details, along with functional and metabolic information via techniques such as blood oxygenation level dependent (BOLD) imaging [155], diffusion [156], and spectroscopy [157]. Recognizing the complementary nature of PET and MR information, especially the utility of the information from multimodal images acquired simultaneously [158], researchers have developed hardware for hybrid PET/MR systems. Approaches range from MR-compatible PET systems using avalanche photodiode (APD) technology for simultaneous PET/MR imaging [105, 102], a split magnet that can house current state-of-the-art PET detector systems [94], to field-cycling approaches that allow PET and MR images to be obtained sequentially [159].

As the combined PET/MR technology matures, it is necessary to develop techniques and imaging strategies that maximize the capabilities of such systems to study interesting and novel biological and clinical questions. An important consideration for multimodal systems is a robust method

to merge individual datasets. For small animal PET/CT systems, significant efforts are devoted to ensure good intermodality spatial registration. Two main methods are used: A set of PET and CT visible fiducial markers are imaged with the animal to allow retrospective image registration [151, 154]. Alternatively, a registration transform is defined between the fields of view (FOVs) of the PET and CT scanners through judicious design of PET/CT phantoms that span the FOV of both systems, coupled with a reproducible method to position physically the animal holder in both FOVs [153].

Conceivably, one can adopt similar alignment approaches for PET/MR systems. Two main issues need to be considered specifically in PET/MR systems for spatial alignment purposes. First, the geometry is more constrained in PET/MR than for PET/CT setups. The typical ring diameter for a commercial small animal PET/CT is ~15 cm or greater, compared to 6 cm for the current APD-based PET/MR inserts [102, 160]. The animal subject, radiofrequency (RF) coil, and physiological maintenance and monitoring devices need to fit inside this ring. Moreover, to maximize signal-to-noise ratio (SNR) for MR images, it is often desirable to position the excite/receive RF coils close to the animal. All these factors limit the imaging of fiducial markers concurrently with an animal without specialized invasive approaches [161]. Second, the FOV of the MR is not fixed between scans. An advantage of MR imaging is the flexibility to alter the FOV geometry and resolution of the acquired data depending on the biological region of interest (ROI) within the animal. For example, fMRI BOLD imaging in monkeys and humans often use oblique brain slices to isolate specific functional brain areas; cardiovascular imaging applications may need oblique slices to image structures such as the aortic arch; while dynamic MRI scans may require a tight FOV to obtain sufficient spatial and time resolution. In such cases, we cannot determine the MR imaging FOV *a priori* to facilitate direct PET to MR image alignment. For the purposes of flexible simultaneous PET/MR imaging, we require a reliable strategy to efficiently determine the intersection of the PET and MR FOVs for all scans during the imaging session. Subsequent to the imaging, we also require a method to register the reconstructed PET/MR images to form a multimodal dataset.

In a previous study, Judenhofer *et al.* [102] showed that fusion of individual simultaneous PET and MR phantom images using a rigid body transform is possible using an APD-based PET/MR system, with the registration error on the PET/MR image sets after transformation within the spatial

resolution of the PET system. This suggests that APD-based PET systems produce images that can be aligned consistently to the MR datasets. In this paper, we extend this observation to develop and evaluate an efficient acquisition and processing setup of simultaneously acquired PET/MR data using a position sensitive APD-based, small animal MR-compatible PET insert. The setup ensures robust spatial alignment of the PET and MR images by first aligning the PET FOV and a fixed MR FOV using a PET/MR visible phantom. The registration accuracy of using a single PET to fixed MR FOV registration for the alignment of images from multiple study sessions was then evaluated. Further, we describe an algorithm to relate multiple MR FOVs to the fixed MR FOV (and hence the PET FOV), harnessing the fact that MR gradients responsible for spatial encoding of images remain fixed throughout all studies. Using the described setup, PET/MR information was acquired in real-time to follow the functional and metabolic status of the *in vivo* tumor microenvironment. Moreover, we show that the setup allows one modality to guide studies with the other within a single imaging session.

3.2.3 Materials and Methods

3.2.3.1 MR-compatible PET Insert for Simultaneous PET/MR Studies

Studies were done using a MR-compatible PET insert. The insert consists of a concentric ring of 16 lutetium oxyorthosilicate (LSO) scintillators and position sensitive avalanche photodiodes (PSAPDs) detector modules. The intact system is designed to fit within the bore of a Bruker Biospin 7 T magnet fitted with a Bruker B-GA12 gradient coil set (12 cm ID, 40 G/cm maximum, 0.2 G cm A). The FOV offered by this PET setup is $35.35 \times 35.35 \times 12 \text{ mm}^3$. Previous reports demonstrated little to no interference between the PET and MRI electronics enabling PET and MRI images to be obtained at the same time [105]. PET data were acquired using in-house developed software [162], while the MR console was run by PARAVISION (Bruker Biospin Inc., Billerica, MA) software. Since the gain of the PSAPD detectors is temperature dependent, the detectors were kept at -12.5°C for all studies using a continuous flow of chilled dried air.

3.2.3.2 PET/MR Image Alignment

We explored whether alignment using an external phantom can give accurate registration over the course of a study day, as well as over multiple days. An “alignment” phantom consisting of rods filled with $\sim 50 \mu\text{Ci}$ ^{18}F -fluoro-deoxyglucose (FDG) solution was imaged simultaneously with both PET and MR. The rods used were glass capillary tubes (OD/ID = 1.2/0.68 mm) sealed at the ends with tube sealer (Becton Dickenson, Franklin Lakes, NJ). A model of the alignment phantom is shown in figure 3.9. For all PET studies, counts were acquired over 300 s and reconstructed with a maximum *a posteriori* algorithm [61] to a matrix size of $128 \times 128 \times 15$ and a pixel size of $0.276 \times 0.276 \times 0.754 \text{ mm}^3$. MRI images were obtained with a 2D spoiled gradient echo (FLASH) sequence (TR/TE = 350/4 ms) with a matrix size of 128×128 , and 40 contiguous slices resulting in a pixel size equivalent to that of the PET images. The FOV of the MR ($35.35 \times 35.35 \times 25.6 \text{ mm}^3$) is larger than the PET ($35.35 \times 35.35 \times 12.8 \text{ mm}^3$) to ensure that the whole PET FOV is captured by the MR FOV and hence allow proper alignment between the two image bases. This MR FOV is denoted hereafter as the home FOV, FOV_{home} . Setting the FOV_{home} as the reference basis, a semiautomatic alignment procedure was adopted to match the two spaces. First, the rod phantoms along the z direction (axial) were matched manually between the PET and MR images. As the spatial resolution of the PET along the axial direction as well as the outer diameter of the rods themselves dictate that one rod in the alignment phantom will traverse multiple PET slices, the central slice of the rod in both PET and MR was used to match the two bases along the z direction. The centroid of the rod cross sections perpendicular to the z direction served as inputs for alignment in the xy plane. Voxels within five voxels of the local maximum and with intensity above 20% of the local maximal intensity were considered in a center of mass calculation of each centroid. Points were fed into a least-squares 2D affine transformation algorithm implemented in MATLAB [163]. These two steps combine to derive a 3D affine transformation matrix. This matrix obtained at the beginning of the imaging session was stored and used for all subsequent image alignment. We measured the centroid registration error between the MR images and transformed PET images of the alignment phantom using the same transformation matrix over the course of a single day of imaging as well as over several days of imaging, with the centroid of the rod cross sections on multiple image slices as the metric. The alignment phantom was unloaded and loaded between these

scans to simulate a normal *in vivo* imaging session day.

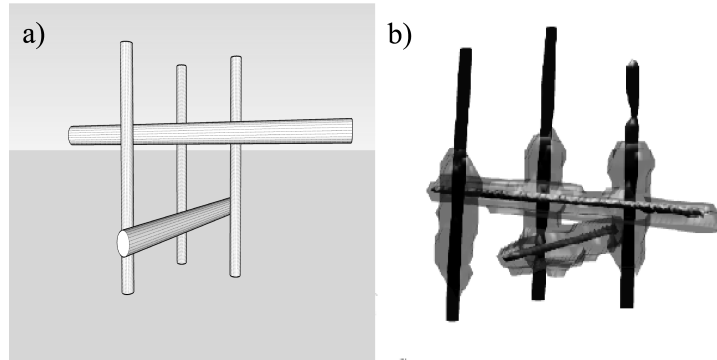


Figure 3.9: PET/MR FOV alignment phantom. (a) Rendering of PET/MR phantom. The phantom consisted of five rods, three in the z-direction for xy plane alignment and two parallel to the xy plane for z slice alignment. The latter are spaced 5 mm apart. The rods were filled with ^{18}F FDG solution. (b) PET/MR phantom image overlay. MR image rendering is given as narrow rendered objects (black); PET image rendering is wrapped around the MR rods (light grey).

To estimate the positioning accuracy of this alignment scheme as a function of location within the FOV, a phantom consisting of glass capillaries (OD/ID = 0.85/0.4 mm), filled with $\sim 50 \mu\text{Ci}$ FDG diluted in 0.05 M Prohance, and located 0, 4, 8, and 12 mm radially from the center of the FOV was imaged simultaneously with PET/MR and aligned using an independently determined transformation matrix derived as above, using the alignment phantom shown in figure 3.9. PET/MR images of this phantom are shown in figure 3.10. The centroid registration error as a function of distance from the center of the FOV was then evaluated as above. One-way ANOVA analysis was used to evaluate whether there were significant differences in registration between rods at different locations within the PET FOV. In section 3.2.7.1, we compare the alignment accuracy between images acquired with different MRI pulse sequences, with and without the PET insert, demonstrating good geometric matching between images taken with different sequences, also with and without the PET insert. In section 3.2.7.2, we compare the alignment accuracy between images registered with different transformations, showing that registration with the affine transformation is slightly better than using the rigid body transform.

The fidelity of this registration scheme was further tested with a third phantom and ^{18}F -FDG studies on mice containing small subcutaneous tumors (MC38.CEA colorectal adenocarcinoma). Experiments involving the use of animals were done in accordance with protocols approved by the Animal Care and Use Committee of the California Institute of Technology.

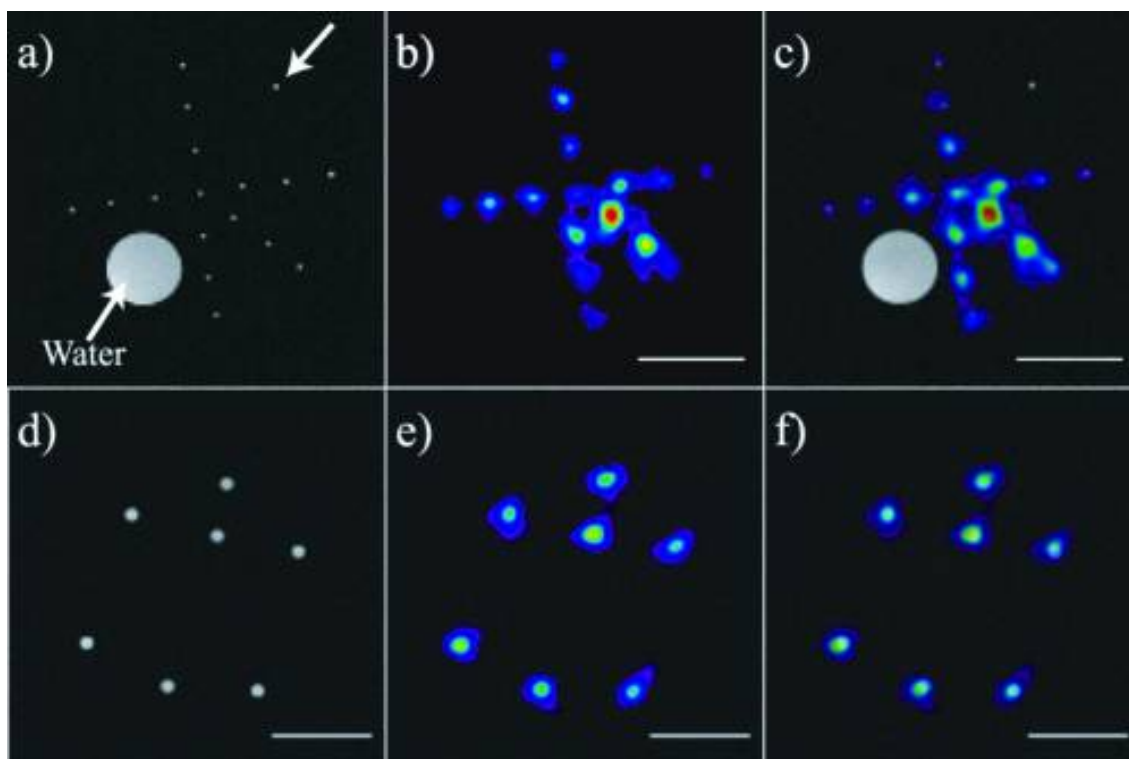


Figure 3.10: PET/MR FOV alignment strategy registers other phantom sets robustly. (a)–(c) Structured phantom used to evaluate alignment accuracy as a function of location within the FOV. Rods were located at 0, 4, 8, and 12 mm from the center of the PET/MR FOV. Alignment accuracy was evaluated after registration using a transformation derived from the alignment phantom. (a) MR image of the phantom. (b) PET image of the phantom. (c) Fused dataset. A large circular water phantom, shown as the large circle in (a) and (c), was inserted into the phantom to facilitate shim, frequency, and gain adjustments of the MR. One capillary rod was filled with water only and thus was visualized in the MR but not in PET (arrow). (d)–(f) The transform derived to form the overlay in figure 3.9 was used to fuse an image containing an alternative phantom arrangement. (f) Fused PET/MR image of a seven rod phantom shows the fidelity of the transform. (Scale bars=10 mm).

Alignment of Multiple MR FOVs

Often it is advantageous to optimize the orientation and size of the MRI FOV to accommodate a specific imaging goal. For simultaneous PET/MR imaging, care needs to be taken to ensure that the alternate MR FOV (FOV_{alt}) overlaps adequately with the PET FOV for the desired region of interest. For quick visualization of the PET and MR FOVs during an imaging session, we use the geometry defined by the MRI metadata to generate Cartesian coordinates of the centroids and vertices for each voxel of both the PET FOV and the alternate MR FOV. These values are used to visualize the “bounding box” of both FOVs in the same coordinate system, which allows a quick determination of the suitability of the FOV_{alt} for PET/MR imaging.

To generate aligned PET/MR datasets, the PET image registered to FOV_{home} , as described in section 3.2.3.2, is first resliced to an isotropic voxel size of $0.276 \times 0.276 \times 0.276 \text{ mm}^3$. It then undergoes a rigid body transformation using the transformation matrix from MRI metadata, and subsequently resliced to the voxel size of the alternate MR FOV. The whole data stream is implemented in MATLAB; a trilinear interpolation is used for all rotations and reslicing.

To demonstrate the feasibility of this method, we simulated the mapping on phantom images using different geometries that we typically encounter in our studies. An oblique slicing simulating an acquisition along an aortic vessel and a geometry that is offset and sampled at a different matrix size than the home FOV were aligned with simultaneously acquired PET data. This method was also used to remap a PET dataset to a mouse anatomical reference image.

3.2.3.3 Biological Studies with PET/MR: a Real-time Feedback Scheme

TgCEA⁺C57BL/6 mice (N = 2) were implanted with MC38.CEA colorectal adenocarcinoma cells in the groin and shoulder seven days prior to imaging. Mice were fasted 8-12 h prior to the imaging session to minimize extraneous ^{18}F -FDG signals. One hour prior to the imaging session, each mouse was injected intraperitoneally with $200 \mu\text{Ci}$ ^{18}F -FDG. The mouse was then placed in the PET/MRI system and kept at $\sim 37^\circ\text{C}$ with warm air blowing through the RF coil and anesthetized using 1.5% isoflurane mixed in air. The holder was designed in such a way that the mouse was kept comfortable while the PET insert remained stable at its operating temperature. Using the known alignment matrix, we shifted the expected region of functional interest, in this case the tumor, within

the PET FOV using the motorized stage. Once aligned, high-resolution anatomical MRI (2D RARE TR/TE = 3500/4.5 ms, matrix size = $128 \times 128 \times 34$, resolution = $0.276 \times 0.276 \times 0.754 \text{ mm}^3$) and PET (300 s duration) scans were obtained simultaneously. Both PET and MR images were respiratory gated to acquire data during the expiration phase.

Alignment time per PET dataset was 5–15 min (AMD, 4× Dual-Core Opteron 885 2.6 GHz, 32 GB memory). This relatively rapid calculation time allows processing and analysis of the PET/MR data while the animal is still in the scanner. Analysis of the processed PET/MR images of ^{18}F -FDG uptake within the MC38.CEA tumors was used to guide the next stage of the experiment. Heterogeneous PET signal within the tumor was verified using ^1H (MRS). We used the PET signal distribution to delineate ROIs for metabolic studies using ^1H MRS (PRESS with VAPOR water suppression, spectral width 8 kHz, 900 averages with 8192 sample points, TR/TE = 1685/10 ms, $3 \times 3 \times 3 \text{ mm}^3$, duration = 26 min). Three voxels were used for MRS imaging; one in the tumor at the region of high FDG uptake, one in the tumor at a region of low FDG uptake, and one in the contralateral muscle. The resultant spectra were processed and analyzed using Bruker TOPSPIN software (Bruker Biospin, Fremont, CA). A two-sided student's t-test was performed to compare the ratios between the high and low FDG regions.

3.2.4 Results

3.2.4.1 PET/MR Image Alignment

Figure 3.9 shows the overlay of PET and MR surface rendering of the alignment phantom images. Slices along the z-axis in figures 3.11 show the alignment along both the z direction and in the xy plane and demonstrate the difference in the resolution of the PET and MR images. Rods orthogonal to the z direction span multiple slices in the PET images. This is due to a combination of two factors. First, because the outer diameter of the rods is 1.2 mm and the mean positron range of the glass is $\sim 190 \mu\text{m}$, annihilation events from the ^{18}F -FDG can occur at the outer edge of the rod, which spans multiple image slices. Second, the spatial resolution of the PET along the axial direction is lower than the image slice thickness ($\sim 2 \text{ mm}$). Table 3.3 shows the mean and standard deviation of the centroid registration error in all three orthogonal directions for the alignment phantom images over the course of one and multiple days. In all directions, registration remained consistently at subvoxel

accuracy (maximum mean alignment error = 0.21 mm, voxel size = $0.276 \times 0.276 \times 0.754 \text{ mm}^3$) and well within the resolution limits of PET. This alignment procedure ably aligned alternate second rod phantom, as shown in figure 3.10 and table 3.3.

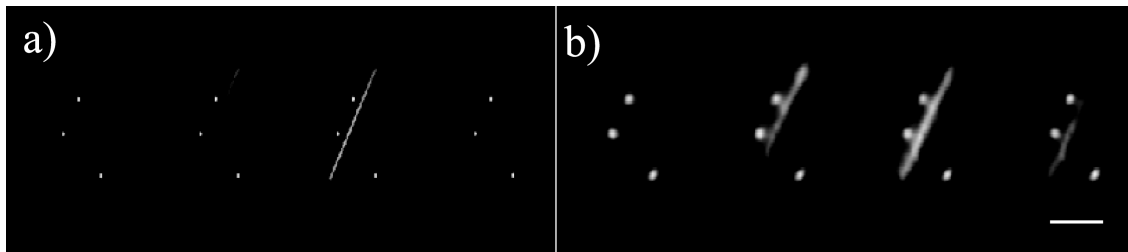


Figure 3.11: Different spatial resolution of the PET and MR images. (a) MR xy slices of aligned phantom. (b) PET slices corresponding to (a). Due to the lower spatial resolution of the PET along the axial direction and the positron range in glass matching the thickness of the capillary walls, the rod which was mostly displayed within one slice in the MR image spans almost three slices in the PET image. (Scale bar = 10 mm).

Table 3.4 shows the registration error as a function of location within the FOV. The alignment remained within <0.28 mm in accuracy throughout the whole FOV, with the mean centroid registration error ranging from about 0.18 mm in the center of the FOV to 0.28 mm at 12 mm from the center of the FOV. One-way ANOVA analysis show no significant difference between the mean registration errors at 0, 4, 8 and 12 mm from the center of the FOV in both the x ($p = 0.8$) and y ($p = 0.5$) directions.

We tested the alignment accuracy *in vivo* by imaging small xenograft tumors. Figure 3.12 shows aligned mouse PET/MR images at the level of the tumor and heart, with high ^{18}F -FDG uptake in both cases well within the expected anatomical regions.

3.2.4.2 Alignment of Multiple MR FOVs

Figure 3.13 shows the MR, PET and overlaid PET/MR datasets for common geometries used for PET/MR studies. In all cases, voxel grid alignment of the aligned PET images yielded good fit to the MR dataset.

Table 3.3: Centroid alignment error of phantoms using the PET/MR transformation scheme over multiple days. Units are in millimeters.

(mm)	PET/MR alignment phantom						Figure 3.2 (d) phantom	
	Day 1	Day 1	Day 2	Day 2	Day 3	Day 3	Mean offset	SD
X error	0.22	0.18	0.17	0.15	0.2	0.17	0.18	0.33
Y error	0.15	0.65	0.12	0.1	0.09	0.24	0.21	0.34
Z error	0.09	0.23	0.17	0.18	0.17	0.23	0.19	0.28

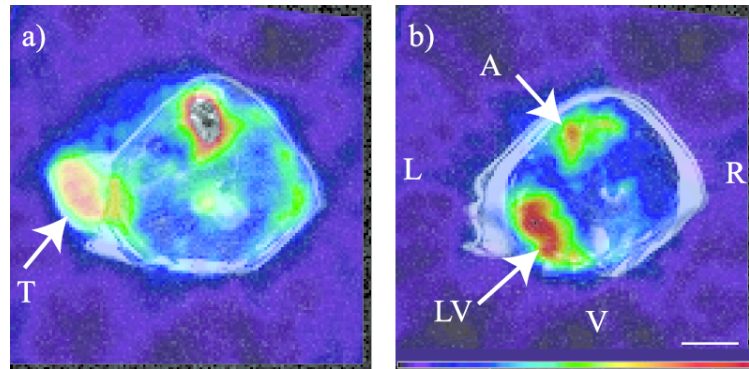


Figure 3.12: (a) PET/MR overlaid images at the level of a subcutaneous MC38.CEA flank tumor showing alignment of high ^{18}F -FDG uptake at the tumor site. (b) Image volume rostral to (a) showing corresponding high ^{18}F -FDG uptake at the left ventricle and aorta (T = tumor, LV = left ventricle, A = aorta, L = left, R = right, V = ventral, scale bar = 6 mm).

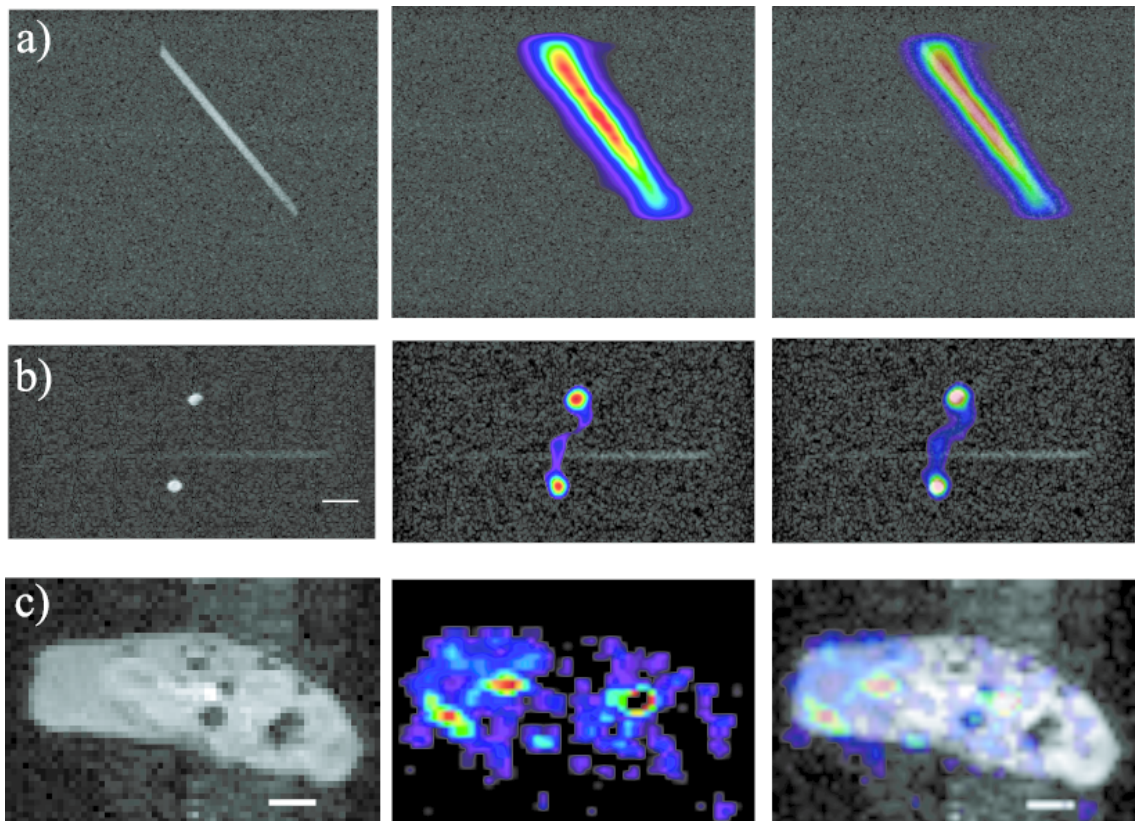


Figure 3.13: PET/MR alignment using different geometries. (a) MR slicing of a phantom along the coronal direction, at an oblique angle (40° on the left/anterior plane). (b) MR slicing along the axial direction, rotated 30° . The home coordinate system of the MR gradient set is noted to the left. (c) FDG-PET image of a mouse tumor obtained with axial slices at a FOV ($35 \times 28 \times 3 \text{ mm}^3$) smaller than FOV_{home} ($35.35 \times 35.35 \times 25.6 \text{ mm}^3$). Voxel grid alignment of PET image shows intratumoral heterogeneous uptake while accurately aligning high activity within the ureters (T = tumor, U = ureters, scale bars = 10 mm).

Table 3.4: Centroid alignment error as a function of location within the transaxial field of view, as measured by the phantom shown in figure 3.10. Units are in millimeters.

(mm)	Location from center of PET/MR FOV							
	0		4		8		12	
	mean	SD	mean	SD	mean	SD	mean	SD
X error	0.12	0.01	0.19	0.13	0.21	0.16	0.28	0.27
Y error	0.19	0.11	0.18	0.12	0.17	0.12	0.24	0.22

3.2.4.3 Real-time Feedback Studies with PET/MR Allows Multimodal Imaging of Biological Processes

Large tumors exhibit heterogeneous structures due to many factors [164]. Figure 3.14 shows that heterogeneous uptake of the glycolytic marker ^{18}F -FDG is seen within a thigh tumor. This heterogeneity was not readily apparent in the anatomical MR image. To explore this heterogeneity, MRS was obtained in ROIs guided by the variability of ^{18}F -FDG uptake shown in the PET images. ^1H MR spectra centered in regions of high ^{18}F -FDG uptake in the tumor showed a higher choline/creatinine ratio compared to ROIs in low ^{18}F -FDG areas and muscle (table 3.5).

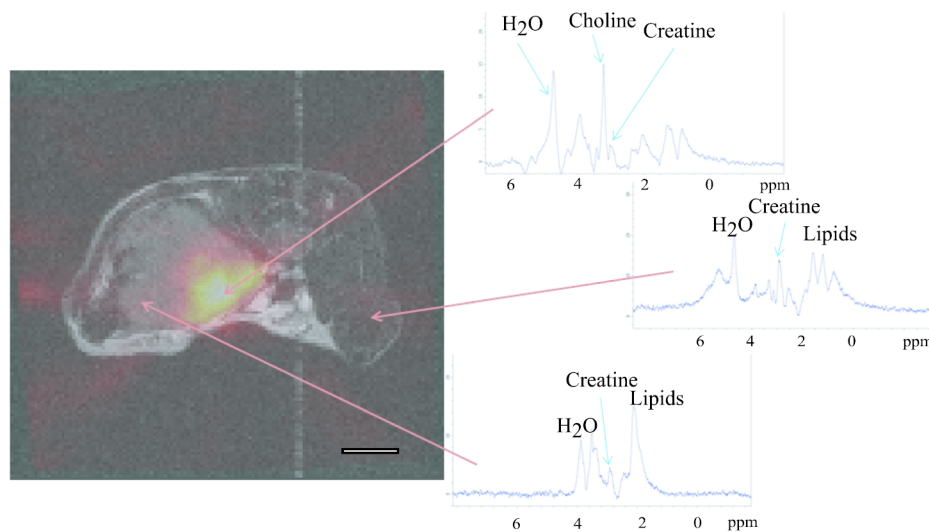


Figure 3.14: PET guided MRS assay of MC38.CEA tumor. Regions of differential ^{18}F -FDG uptake within the tumor were used to define the ROIs for ^1H MRS of the tumor. Spectra show differences between regions of high FDG uptake, low uptake, and contralateral muscle. (Scale bar = 3 mm).

Table 3.5: FDG-PET signal from xenograft tumors (N = 2) were used to guide ^1H MRS in different PET signal regions. Choline/creatine ratio were significantly different between high and low FDG regions ($p = 0.02$).

Region	Choline/creatine ratio
High FDG tumor region	3.4 ± 0.4
Low FDG tumor region	1.9 ± 0.3
Muscle	Negligible

3.2.5 Discussion

In this study, we demonstrate the feasibility of performing robust *in vivo* studies with simultaneous PET/MR imaging using a PET insert placed in a small animal MR scanner. Given the spatial constraints within the PET insert and animal holder, a method in lieu of the traditional fiducial marker system is required to ensure robust registration of the two modalities. Once the PET insert is fixed within the MR scanner, the relative orientation of the PET (as determined by the placement of the LSO crystal detectors) and MR (as determined by the placement of the imaging gradient set) coordinate systems is also fixed. Thus the transformation matrix that registers images using a single alignment phantom also brings together all subsequent PET/MR images. We confirm this by repeatedly registering the PET and MR images of the alignment phantom over a study session and over multiple days with subvoxel accuracy (table 3.3) using one transform matrix. This alignment is not dependent on the location within the FOV (table 3.4). Images of an alternate phantom and tumor bearing mice also support this alignment accuracy (figure 3.12). Straightforward registration of the PET and MR image spaces using a predetermined transformation matrix allows for an uncomplicated multimodal imaging scheme, whereby neither a specially designed PET/MR holder nor an animal mold [112, 165] is required for image alignment. This setup provides imaging flexibility; first, there are no potential intensity spillover effects due to an external radioactive marker, which may make low activity ROIs or ROIs close to the marker difficult to discern. Second, this method of alignment allows alternate MRI transmit/receive coil setups to be used without the need for a new alignment scheme, since the registration is based on the spatial encoding provided solely by MR gradient coils. This will be useful for studies that use a surface coil to achieve high SNR. Ideally, the alignment method used should be fully automatic, although previous reports have indicated that partial manual manipulation of images during processing may yield sufficient alignment

accuracy [166]. We adopt a manual alignment of the z direction because of the disparate FOV sizes between the PET and MR along that axis. As we make no prior assumption about the physical FOV alignment along this axis, a large MR FOV is taken to ensure full coverage of the PET FOV. From our observations, the removal and replacement of the PET insert within the MR scanner can cause up to 1.5 slices (~1 mm) displacement between the PET FOV and that of the MRI. Studies are in progress to design a phantom alignment setup along the lines of previous designs for PET/CT systems [153, 151, 152] that will allow fully automated alignment. Nevertheless, the general alignment strategy will remain the same as described here regardless of the phantom setup used.

One notable difference between MR and CT acquisition is the need to alter the imaging geometry in MR to maximize the SNR and to obtain images at the desirable orientation or resolution. This is especially relevant for *in vivo* applications; a compromise must be struck between a realistic scan duration time and the resolution of the acquired image. In MR-only studies, the FOV can only be determined once the animal is loaded inside the scanner. The limited PET FOV adds an extra geometry constraint for PET/MR studies. We have developed a simple software GUI visualizing the overlay of the PET and MR FOVs to allow a quick check to ensure that our anatomical regions of interest lie completely in the useful PET FOV prior to image acquisition.

The constrained geometry of the PET/MR system (which limits the use of external fiducial markers) and the imaging flexibility of the MR require a robust method to coregister PET and MR images with multiple FOV geometries. In previous studies, this has been addressed by making assumptions about the anatomical distribution of the functional PET signal [167, 168, 169] using a transmission source or implanting fiducial markers [165]. The first two strategies may not yield an optimal solution if the distribution of the PET signal is unknown or heterogeneous, while the latter is invasive. Given the fact that the PET is fixed physically within the MR during a single imaging session, a simple algorithm was developed that aligns the voxel grids of the “home” PET/MR FOV to any alternate MR FOVs. We make the assumption here that the MR gradients behave consistently between different scans such that the images acquired at a set geometry in software is the same in the hardware. Common Fourier imaging, as described by the k-space formalism [170], relies on spatial encoding determined by spatially and temporally varying magnetic fields created by the MR gradients. Advances in hardware design of gradient coils [171] and post-acquisition

processing [172, 173, 174] means that most commercial scanners have robust gradient performance, especially for the pulse sequences using Cartesian k-space trajectories (see [64, 175] for discussion of gradient coil design, specifications, and performance). From a simultaneous PET/MR viewpoint, the pertinent concern is that the presence of the PET insert inside the gradient set may distort the generated gradient fields. Previous characterization of APD-based PET inserts has demonstrated that MR images acquired in the presence of the PET insert show negligible geometric distortions compared to those acquired without the PET [105, 102] (see also section 3.2.7.1).

In our implementation, we transform the PET image to match that of the MR images. We chose this approach because the resolution of the PET is lower than the MR, so there would be less potential loss of information from image interpolation. Also, the PET FOV is fixed and typically smaller than the MR FOV, so this approach also simplifies the formation of the fused dataset. Other interpolation methods, apart from trilinear interpolation, can be adapted to improve the quantitative value of the transformed images [176, 177]. However, the interpolation method we adopted should suffice for PET images. Simulation of some common geometries that require this schema show that the registered PET images align well with the corresponding MR image (figure 3.13). The algorithm described is time efficient; all datasets generated took 20 min or less.

Simultaneous PET/MR imaging allows examination of the different signals in both spatial and temporal registration. In figure 3.14, we see heterogeneity within a tumor microenvironment highlighted with both ^{18}F -FDG-PET imaging and high-resolution anatomical MRI. ^1H MRS, guided by the ^{18}F -FDG signal, confirms the heterogeneous profile of the tumor. Rapid reconstruction, processing, and visualization of the aligned initial PET/MR images provide the information necessary to perform the later MRS study within the same imaging session. Thus, obtaining feedback between the two modalities during a single imaging session is eminently doable with this system. This will have multiple uses. Phantom alignment information allows us to position the mouse to maximize PET signal in the FOV. While new versions of the PET insert will aim to have whole body coverage, this is typically not feasible in clinical systems or in situations where one may want to sacrifice coverage for higher sensitivity and resolution. The feedback schema can also be performed during the experiment to guide study directions. The ability to process and align the PET/MR images quickly within an imaging session allows basic analysis of the combined dataset. In our study, this

allowed us to determine regions of tumor functional heterogeneity via ^{18}F -FDG accumulations and subsequently, ^1H MRS studies, to assess corresponding heterogeneity in metabolite concentration. Again, the external means of image registration proved useful in this situation; no assumption of the expected distribution of the image intensities in either image was used for alignment, allowing us to delineate the heterogeneity within the tumor. Although there is a correlation between the regions of high ^{18}F -FDG uptake and high choline/creatine ratio (table 3.5), more studies are required to determine the significance of this observation as the relationships between phospholipid metabolism and glycolysis remain unclear [178, 179, 54, 180, 181]. Further studies along these lines will involve correlating the tumor characteristics such as perfusion [182] and hypoxia [183] with these functional markers.

Simultaneous PET/MR technology has the potential to impact both preclinical and clinical realms. The time savings that can be obtained by doing two scans at once will facilitate the efficiency of longitudinal studies. Cross-modal image corrections methods such as MR-guided PET motion and attenuation correction, which rely on robust PET/MR coregistration, will improve image quality and aid image interpretation [89, 88]. Perhaps more importantly, like the development of multicolor fluorescent proteins and dyes that allow multiple processes to be studied concurrently [184, 12], simultaneous PET/MR will enable similar interactive studies to be done within intact mammalian systems. Molecular imaging agents are being developed with both PET and MR contrast that can look at biological processes such as gene expression [58], receptor binding [120, 57], cell tracking [185], and vascular inflammation [186]. Combining these agents within one study will allow multiple physiological processes to be probed simultaneously.

3.2.6 Conclusions

We describe a coregistration design for performing time-sensitive *in vivo* studies using a simultaneous PET/MR scanner. Robust image registration between PET and MR is shown, based on the fixed relative orientation of the PET detectors and MR imaging gradient set. Using this setup, we demonstrate heterogeneous metabolic activity within a tumor using ^{18}F -FDG-PET, which was found to correlate with choline/creatine ratios determined using MRS guided by the ^{18}F -FDG signal levels.

3.2.7 Supplemental Data

3.2.7.1 Comparison of Alignment Accuracy Between Images Acquired with Different MRI Pulse Sequences

Methods. A hot rod phantom filled with water was imaged with three different MR pulse sequences at the same FOV and matrix size ($35.35 \times 35.35 \times 0.754 \text{ mm}^3$ and $128 \times 128 \times 1$ respectively):

1. A 2D spoiled gradient echo FLASH sequence (TR/TE = 500/4.4 ms)
2. A 2D spin echo RARE sequence (TR/TE = 2000/11 ms)
3. A 2D EPI sequence (TR/TE = 1000/20.4 ms), acquired in 4 shots. The Bruker native gradient adjustment macro *EPI_ADJUST*, which compensates for the time lags of the gradients and filters and the first order eddy currents, as executed prior to image acquisition. No other correction was applied.

The acquired images were then coregistered to determine the registration error between them. A rigid body registration algorithm was used [163]. We calculated the translational and rotational mismatches from the resultant transformation matrices.

This was repeated with and without the PET insert being powered on. Five images were acquired for all pulse sequences for both conditions. Registration differences were compared for all images in a combinatorial manner.

Results. Figure 3.15 shows sample images acquired with the three sequences. Both translation and rotation differences between images acquired by the three pulse sequences are shown in table 3.6. Alignment between the RARE and FLASH images show lower translational and rotational registration difference compared to EPI. This is expected, as the EPI sequence is inherently more prone to geometric distortions compared to the other two pulse sequences. A two-way ANOVA examining the translational differences of the three different image comparisons with and without the PET powered on showed no significant differences between the comparison groups ($p = 0.06$) and whether the PET is on or off ($p = 0.69$). In contrast, analysis of the rotational differences showed a significant difference between groups ($p = 0.01$), PET power status ($p < 0.01$) and their interaction

($p = 0.05$). Although this is the case, it must be noted that the absolute values of the rotational differences are $<0.01^\circ$. Coupled with the <0.2 mm translational offset for all the comparison groups, this alignment difference remains well within the spatial resolution of PET and supports the claim that our methodology is robust enough to coregister PET/MR images accurately. Of course, this is under the proviso that the MR images are properly corrected, as one would do for any MR-only experiment.

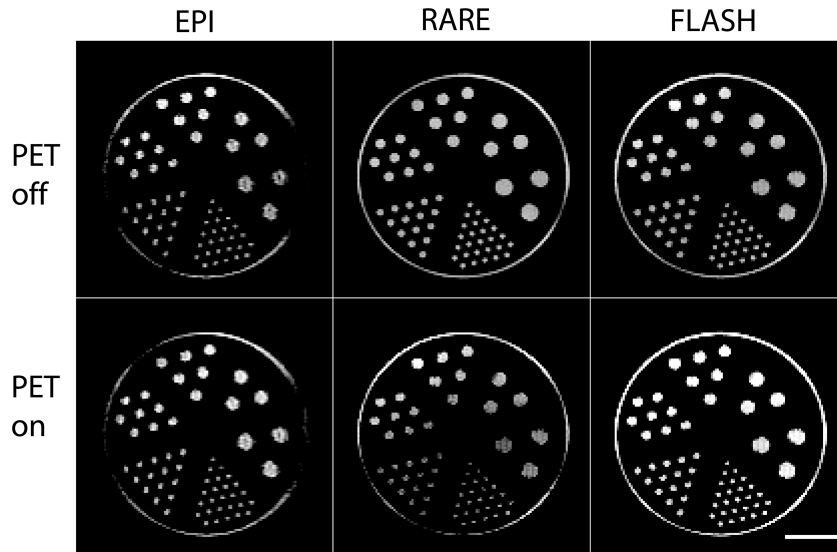


Figure 3.15: Images acquired with different pulse sequences and with PET on and off show no noticeable geometric distortions, enabling robust PET/MR coregistration; see table 3.6 (Scale bar = 10 mm).

Table 3.6: Alignment displacements between images acquired by different pulse sequences. Images were aligned by a 2D rigid body algorithm; the translational and rotational terms were used to determine the displacement and rotational offset between images.

Sequence A	Sequence B	PET powered status	Translation offset (mm)		Rotation offset (degrees)	
			mean	SD	mean	SD
EPI	RARE	On	0.05	0.09	0.001	0.01
EPI	RARE	Off	0.04	0.05	0.009	0.01
EPI	FLASH	On	0.07	0.1	0.002	0.01
EPI	FLASH	Off	0.07	0.11	0.008	0.01
RARE	FLASH	On	0.03	0.03	0.001	0.001
RARE	FLASH	Off	0.06	0.01	0.001	0.001

3.2.7.2 Comparison of Alignment Accuracy Between Images Registered with Different Transformations

Methods. The same dataset used in section 3.2.3.2 was coregistered by two additional methods:

1. Same as section 3.2.3.2, except a rigid body transformation algorithm was used.
2. A 3D rigid body algorithm, as implemented in 3D-Slicer version 3.4 (www.slicer.org), was used.

For method 2 above to work, PET images had to be pre-processed manually to approximately align the PET and MR space before being fed into the 3D algorithm. Without the pre-processing step, the algorithm tends to over-rotate the PET image, pushing one of the rod sources out of the FOV

Results. Table 3.7 and table 3.8 show the registration alignment error by both the 2D and 3D rigid body algorithm respectively. Both algorithms yielded good registration, which was not significantly different from the affine ($p = 0.76$). The affine transformation was slightly better than the rigid body algorithms (the Euclidean distance of the mean alignment errors for the affine, 2D rigid body and 3D rigid body transformations were 0.34, 0.38, 0.36 mm respectively). It must also be noted that a manual preprocessing step is required to approximately align the PET/MR dataset for the 3D algorithm to work.

Table 3.7: Centroid alignment error of phantoms using the PET/MR transformation scheme over multiple days, using a 2D rigid body transformation. Two-way ANOVA analysis comparing between x, y, z errors showed no significant differences between groups ($p = 0.66$), nor between rigid and affine transformations ($p = 0.51$). Both rigid and affine transforms yielded alignment errors well within the PET spatial resolution.

PET/MR positioning phantom									
(mm)	Day 1	Day 1	Day 2	Day 2	Day 2	Day 3	Day 3	mean	SD
X error	0.2	0.2	0.22	0.18	0.2	0.27	0.22	0.21	0.03
Y error	0.16	0.74	0.17	0.18	0.2	0.18	0.15	0.25	0.22
Z error	0.09	0.23	0.18	0.25	0.29	0.14	0.16	0.19	0.07

Table 3.8: Centroid alignment error of phantoms using the PET/MR transformation scheme over multiple days, using a 3D rigid body transformation. Two-way ANOVA analysis comparing between x, y, z errors showed no significant differences between groups ($p = 0.64$), nor between rigid, affine and 3D rigid transformations ($p = 0.76$). All transforms yielded alignment errors well within the PET spatial resolution.

PET/MR positioning phantom									
(mm)	Day 1	Day 1	Day 2	Day 2	Day 2	Day 3	Day 3	mean	SD
X error	0.25	0.2	0.19	0.38	0.21	0.24	0.3	0.25	0.07
Y error	0.2	0.19	0.25	0.19	0.17	0.14	0.25	0.2	0.04
Z error	0.13	0.03	0.43	0.51	0.46	0.05	0.32	0.17	0.2

3.3 Phantom Designs for Robust *In Vivo* Coregistration of Hybrid Imaging Systems: Comparison of Semiautomatic and Automatic Approaches

3.3.1 Introduction

Increasing efforts are being devoted to develop and validate hybrid techniques for multimodality imaging of biological processes *in vivo*. Several dual modality platforms have been successfully developed and tested. For example, positron emission tomography (PET) has been combined with computed tomography (CT), magnetic resonance imaging (MRI) [105] and optical tomography [187]. The major advantage of these methods lies in the possibility of imaging the same living subject in a single session, in some cases simultaneously. A vital component for multimodal imaging is the requirement of accurate spatial coregistration of the separate image spaces. Significant efforts have been devoted to cross-modal registration in small animal imaging, based upon optimizing animal holders and utilizing manually segmented phantom designs. Hybrid imaging systems adds an extra complexity; the geometry constraints of integrated systems along with the disparate field of view between the individual modalities require a modification to previous approaches. A registration phantom design that can be adapted for different hybrid systems and can perform image registration automatically is highly desirable.

Here, we evaluate a phantom design adapted for use in a MR-compatible PET insert for simultaneous PET/MRI imaging. The phantom design allows simple image acquisition, fully automatic segmentation of the phantom components and subsequent image coregistration. We compare the registration error of this fully automated strategy with our previous semiautomatic alignment strategy outlined in section 3.2. Both strategies aligned the PET and MR image spaces to within single voxel accuracy throughout the whole field of view of the combined scanner with no significant difference of registration errors (two-sample t-test: $p = 0.2$). In addition to providing equivalent coregistration results the automatic alignment strategy guarantees a non-biased, fast and versatile tool which could be adapted easily for other types of combined imaging systems.

3.3.2 Materials and Methods

3.3.2.1 Semiautomatic Alignment Phantom

The semiautomatic alignment phantom was constructed as described in section 3.2.3.2.

3.3.2.2 Fully Automatic Alignment Phantom

The fully automatic alignment phantom consists of rods placed within a truncated 50 mL Falcon tube (BD). A Falcon tube was truncated to a length of 60 mm. Holes were drilled in the end caps (the native lid of the tube or a thick plastic cylinder) according to the pattern outlined in the schematic shown in figure 3.16. Holes were drilled to fit glass capillary rods (OD/ID = 0.7/0.5 mm, Wales Apparatus) snugly. The central rod was fitted diagonally across the diameter of the tube. Rods were filled with ~50 mCi of ^{18}F -FDG prior to placement in the tube. A tube filled with water (ID = 6.5 mm, Micronic) was placed along the inner edge of the tube in line with the central rod to facilitate MRI imaging.

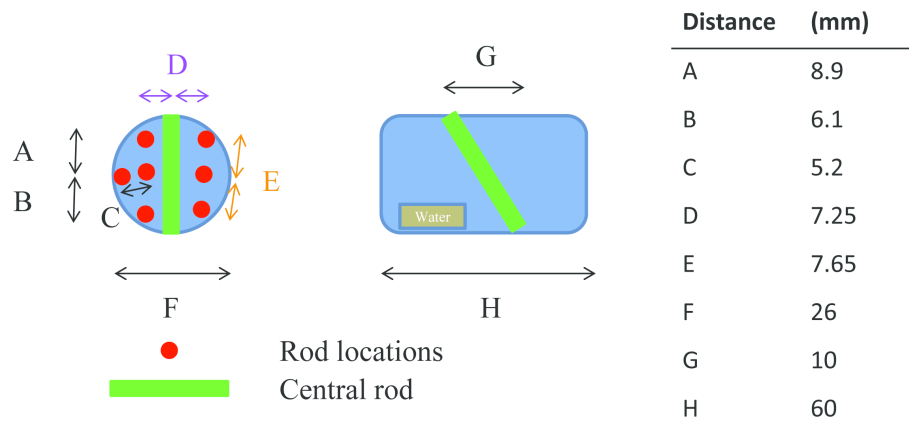


Figure 3.16: Schematic of automatic phantom. End cap view (left) and side view (right) of the phantom, with associated distance measurements are shown. The current phantom is implemented with a 50 mL Falcon tube. The asymmetric distributions of rods on either side of the central rod facilitates their segmentation. The presence of the water tube facilitates MRI.

3D renderings of both the semiautomatic and automatic alignment phantoms from PET/MRI datasets are shown in figure 3.17.

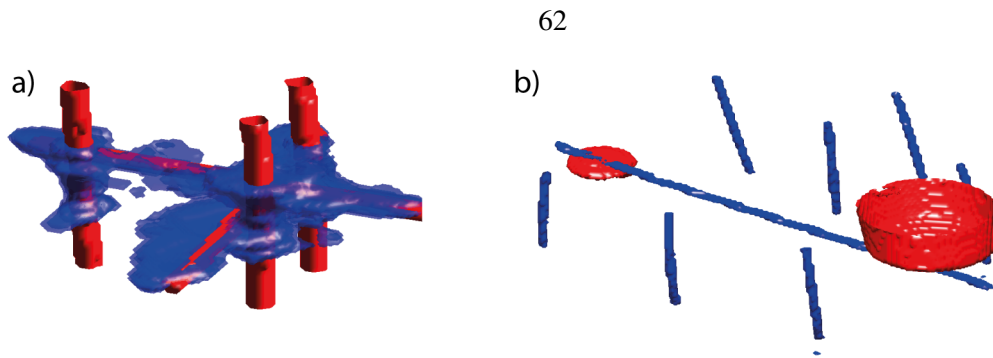


Figure 3.17: Semiautomatic (a) and automatic (b) alignment phantom models. Red denotes MR-visible portion of the phantom. Blue denotes PET/MR visible portion of the phantom. Glass capillary tubes filled with ^{18}F -FDG and saline enable multimodal visualization. In (b), large red portions are present to allow robust MRI shimming and adjustments.

3.3.2.3 Simultaneous PET/MRI Imaging

Phantoms were imaged using the MR-compatible PET insert combined with a 7 T Biospec small animal MRI. PET images were acquired with durations ranging between 300 and 600 s and reconstructed as described in section 3.2.3.2. MRI were obtained using a gradient echo FLASH (TR/TE = 350/4 ms, FOV = $35.35 \times 35.35 \text{ mm}^2$, slice thickness = 0.754 mm, 34 slices).

3.3.2.4 Semiautomated Alignment Strategy

PET and MRI datasets of the semiautomatic alignment phantom were aligned as described in section 3.2.3.2.

3.3.2.5 Fully Automated Alignment Strategy

PET and MRI datasets of the fully automatic alignment phantom were aligned using the following steps:

1. Each individual rod in the alignment phantom seen in both the MRI and PET images was segmented using an intensity-based algorithm. A predefined threshold of 25% of the maximum intensity of the image and a radius of $\sim 4 \text{ mm}$ was used to segment voxels belonging to each rod. The central rod was identified by the fact that it showed the greatest x/y displacement across the image slices. The other rods were identified using the fact that they were situated in a known orientation about the central rod. The result of a sample segmentation is shown in figure 3.18.

2. The axial FOVs of the MRI and PET datasets are different (25.6 and 12.8 mm respectively). We first aligned MRI and PET images along the axial directions using a procedure outlined in [151]. Briefly, the ratio of the distances between the central rod and two other rods in the phantom, as shown in figure 3.18, are calculated across all the imaging slices. These values were plotted as a function of slice number. A quadratic curve was fitted to the plots to reduce the effect of image noise or segmentation errors. At equivalent locations in the phantom, these ratios should be similar. Thus, the displacement between the minima of the PET and MRI plots corresponds to the axial displacement between the two datasets. Sample plots outlining this process is shown in figure 3.19.
3. Once axially aligned, the PET and MRI phantoms were aligned using a 3D affine transformation [188]. Rod coordinates from every slice were treated as individual points as an input to this algorithm. All alignment software was implemented in MATLAB.

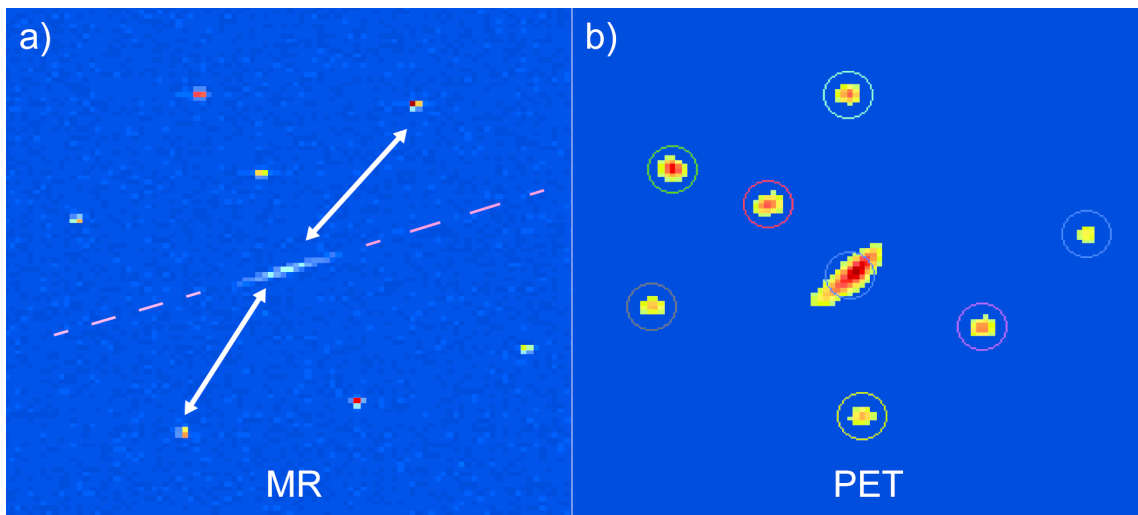


Figure 3.18: Automatic phantom rod delineation. a) MR image of phantom. Pink dashed line shows trajectory of central rod. White arrows show the two distances from which a ratio is derived. This changes according to axial position. b) PET image of phantom with circles showing automatic rod segmentation.

3.3.2.6 Evaluation of Alignment Accuracy

A separate PET/MRI image scan (acquired with the same parameters described in section 3.3.2.3) of the automatic phantom was used to evaluate the alignment accuracy of both methods. PET and MRI

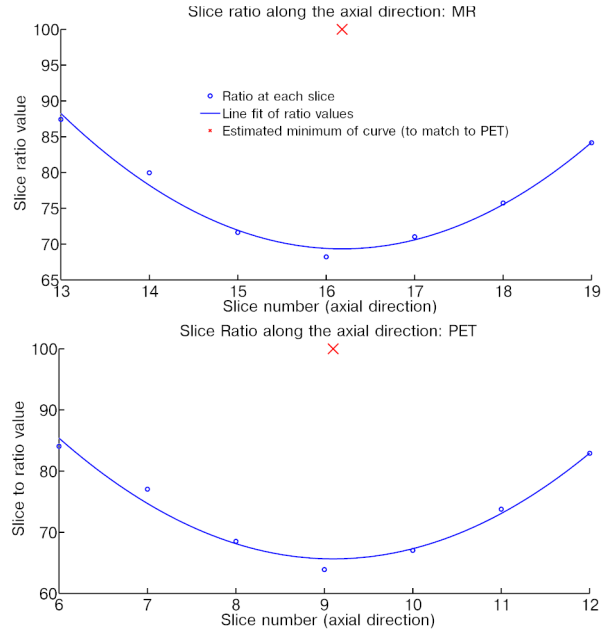


Figure 3.19: Automatic axial alignment of images. Due to the disparate field of views between modalities, we first approximately align in the axial direction. Ratios between a central, moving, rod and other rods were used to landmark slice positions. A quadratic fit reduced noise errors. The red X marks the minima of the PET and MR curves for axial matching.

images from this dataset were aligned with transformations derived from either the semiautomatic or automatic phantom alignment. The centroid alignment error of individual rods within aligned images were then calculated as per section 3.2.3.2.

3.3.3 Results

PET/MRI images of the semiautomatic and automatic phantoms are shown in figure 3.20. Figure 3.20 e shows an overlay of an automatic phantom image using a automatic alignment transform.

The centroid alignment error over x/y/z directions are shown in table 3.9. Both strategies aligned PET and MRI images within the image resolution of both systems (<0.3 mm). Although the mis-registration error for the semiautomatic alignment approach was slightly higher than the automatic approach, this was not significant ($p = 0.2$).

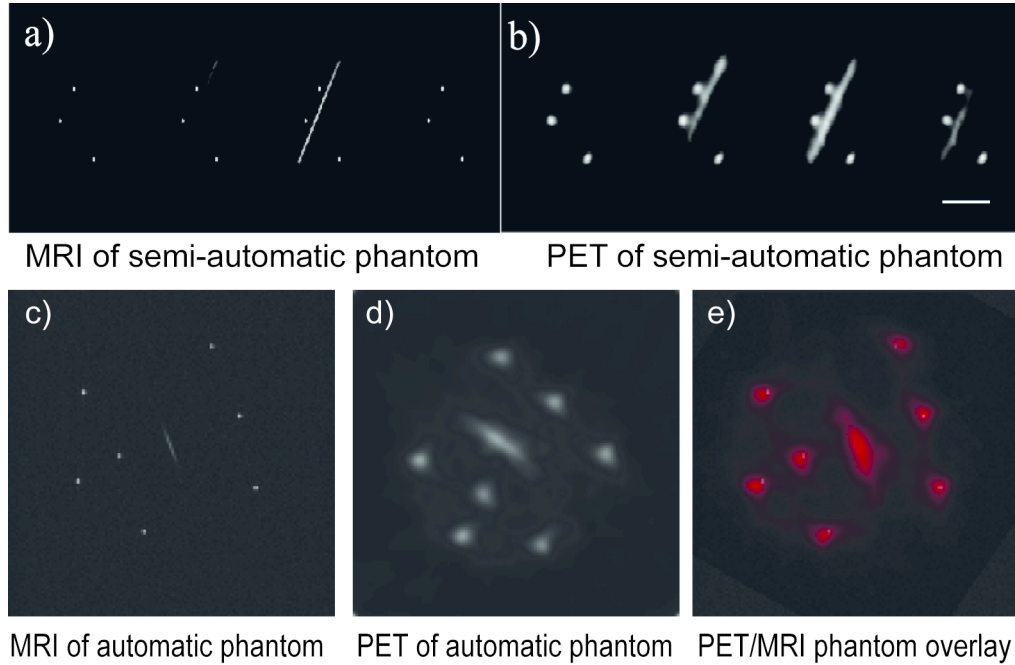


Figure 3.20: PET/MRI images of semiautomatic (a)-(b) and automatic (c)-(e) phantoms. Note in (b), the axial rods traverse multiple slices, which may lead to alignment errors. The configuration in (c)-(e) may reduce alignment errors and simplify registration. (Scale bar = 10 mm).

Table 3.9: Alignment error comparison between automatic and semiautomatic alignment methods.

Method	Alignment error (mm)	
	mean	SD
Semiautomatic alignment	0.26	0.16
Fully automatic alignment	0.11	0.1

3.3.4 Discussion

In this study, we developed a phantom that enabled automatic alignment of PET and MRI image spaces. Prudent design of rod locations within the phantom allowed facile automatic rod segmentation in both PET and MRI image sets. The presence of a sloping rod across the axial direction enabled automatic identification of axial location and subsequent alignment. This was necessary in our case because the FOVs of the PET and MRI were quite different, such that direct application of standard 3D alignment transform found in common image processing programs did not work.

Once the phantoms were axially aligned, we applied a closed-form algorithm for full 3D-

alignment. We chose this method over more common alignment algorithms again because of the different FOV sizes. Commonly found 3D alignment transforms [189] are iterative in nature. In phantom images with sparse signal, such as those encountered here, these algorithms can often result in a failure to converge to a reasonable solution. A closed-form solution based on matching points returns an exact result that can be easily implemented into an automatic pipeline.

Both semiautomatic and automatic alignment strategies were able to align the PET and MRI image spaces well within the spatial resolution limits of PET (~1–2 mm, whereas the alignment error was <0.3 mm) and were not significantly different. The automatic strategy returned slightly lower errors overall. This may be due to the fact that the automatic phantom contained more rods covering a larger portion of the FOV, thus improving the accuracy of the overall FOV alignment. Accuracy of the FOV alignment can be further improved by increasing the number of rods in the FOV, at the expense of increased computing time to segment the rods.

On a day-to-day basis, the semiautomatic phantom is an easier phantom to make and use since it requires fewer rods (5) than the automatic phantom (8). However, incorporation of a long half-life agent (such as ^{68}Ge) in the rods would enable a more permanent implementation of the automatic phantom. In this scenario, the automatic alignment phantom would be a simple and accurate method to ensure robust coregistration of the PET and MRI image spaces. Such a phantom is being explored for use in the second generation PET/MRI system.

In summary, we have developed a phantom that can align multimodal image spaces automatically. The phantom is straightforward to make and can fit in the tight geometries found in novel hybrid imaging systems. Alignment accuracy with this phantom was comparable with a previously developed semiautomatic approach. These phantom designs, when coupled with appropriate contrast agents (e.g. PET/MRI/CT/SPECT/optical dyes), can be used to align images acquired from multiple modalities with high accuracy.

3.4 Quantitative, Simultaneous PET/MRI for Intratumoral Imaging with a MR-compatible PET Scanner

3.4.1 Abstract

Noninvasive methods are needed to explore the heterogeneous tumor microenvironment and its modulation by therapy. Hybrid PET/MRI systems are being developed for small animal and clinical use. The advantage of these integrated systems depends on their ability to provide MR images that are spatially coincident with simultaneously acquired PET images, allowing combined functional MRI and PET studies of intratissue heterogeneity. Although much effort has been devoted to developing this new technology, the issue of quantitative and spatial fidelity of PET images from hybrid PET/MRI systems to the tissues imaged has received little attention. Here, we evaluated the ability of a first-generation, small animal MR-compatible PET scanner to accurately depict heterogeneous patterns of radiotracer uptake in tumors.

3.4.1.1 Methods

Quantitative imaging characteristics of the MR-compatible PET (“PET/MRI”) scanner were evaluated with phantoms using calibration coefficients derived from a mouse-sized linearity phantom. PET imaging performance was compared to a commercial small animal PET system (microPET R4) and autoradiography in tumor-bearing mice. Pixel and structure-based similarity metrics were used to evaluate image concordance among modalities. Feasibility of simultaneous PET/MRI functional imaging of tumors was explored by following ^{64}Cu -labeled antibody uptake in relation to diffusion MRI using cooccurrence matrix analysis.

This section is published in the *Journal of Nuclear Medicine*: Thomas S.C. Ng, James R. Bading, Ryan Park, Hargun Sohi, Daniel Procissi, David Colcher, Peter S. Conti, Simon R. Cherry, Andrew. A. Raubitschek, Russell E. Jacobs (2012) Quantitative, simultaneous PET/MRI for intratumoral imaging with a MR-compatible PET scanner. *Journal of Nuclear Medicine*, 53 (7).

Acknowledgments: We thank Dr. Kofi Poku for preparing the ^{64}Cu -DOTA-NHS-M5A antibody and Dr. Andrey Demyanenko, Desiree Crow, Alex Poznak, Sonia Collazo and Bitu Alaghebandan for their technical assistance. Drs. Yibao Wu and Scott Fraser gave helpful advice. The project was funded by NIBIB R01 EB000993, NCCR S10 RR015703, S10 RR019253, Beckman Institute, USC Molecular Imaging Center and the Caltech/City of Hope Biomedical Initiative.

3.4.1.2 Results

The PET/MRI scanner showed stable and linear response. Activity concentration recovery values (measured/true activity concentration) calculated for 4 mm diameter rods within linearity and uniform activity rod phantoms were near unity ((0.97 ± 0.06) and (1.03 ± 0.03) respectively). Intratumoral uptake patterns for both ^{18}F -FDG and a ^{64}Cu -antibody acquired using the PET/MRI scanner and microPET were highly correlated with autoradiography ($r > 0.99$) and with each other ($r = 0.97\pm 0.01$). Based on this, we performed a preliminary study comparing diffusion MRI and radiolabeled antibody uptake patterns over time and visualized movement of antibodies from the vascular space into the tumor mass.

3.4.1.3 Conclusions

The MR-compatible PET scanner provided tumor images that were quantitatively accurate and spatially concordant with autoradiography and the microPET R4. Cooccurrence matrix approaches enabled effective analysis of multimodal image sets. These observations confirm the ability of the current simultaneous PET/MRI system to provide accurate observations of intratumoral function and serve as a benchmark for future evaluations of hybrid instrumentation.

3.4.2 Introduction

The tumor microenvironment greatly impacts the efficacy of cancer treatment [1]. Factors such as heterogeneous perfusion and subpopulations of cells within tumors affect tumor progression and response to therapy. Investigations of these factors usually involve measurements at a whole tumor level (e.g. size) and tissue sampling for histological or biochemical assays. noninvasive imaging complements these studies by providing intact tissue information at multiple timepoints in the same individual [12].

The utility of multimodal imaging is well demonstrated in cancer research [14]. Advances in hybrid positron emission tomography/magnetic resonance imaging (PET/MRI) systems [190] show particular promise for understanding the heterogeneous nature of the tumor microenvironment. When spatially and temporally matched, high-resolution anatomical and functional information such as the perfusion status [191], cellular density [192] and metabolic status of specific tissue

regions acquired with MRI can enhance the interpretation of functional data provided by PET (e.g., oxygenation [183], cellular proliferation [53] and receptor expression [193]) and vice versa.

Conventional PET image analysis focuses on regions of interest (ROIs) encompassing whole tumors, with some studies omitting obvious “necrotic” regions during analysis [192]. Efforts to improve the spatial resolution of reconstructed PET images [194] and availability of coregistered PET and MRI have engendered interest in understanding the heterogeneity of radionuclide uptake observed with PET. For example, a recent clinical study by Metz, *et al.*, examined heterogeneity of tumor perfusion using MRI and correlated it with PET studies of integrin expression and tumor metabolism [195]. Similarly, Cho, *et al.*, compared MRI measures of tumor perfusion with uptake of the PET hypoxia tracer ^{18}F -MISO within rat tumor xenografts [183].

Correct interpretation of PET images, especially within regions of heterogeneous tracer uptake, requires that fidelity be verified between these images and actual tissue activity concentration patterns. Characterization of PET instrumentation usually entails measuring a standard set of metrics in a variety of phantoms [196], followed by gross *in vivo* verification. While this approach examines the general performance of the scanner, simple geometric patterns of phantoms may be insufficient to predict *in vivo* performance. To validate the heterogeneous spatial patterns seen in PET images, one needs to compare these images with a “gold standard” such as (QAR) [197].

We have evaluated the image quality of a first-generation, MR-compatible PET scanner (“PET/MRI scanner”) [160]. Previous reports used standard metrics to assess the performance characteristics of the scanner [198] and its ability to function within the integrated PET/MRI environment [105]. Here, we examined the image fidelity of the PET/MRI scanner and its ability to quantify heterogeneous uptake patterns in mice compared with QAR and a commercial small animal PET system. Phantoms were used to evaluate the quantitative capability of the PET/MRI scanner. Next, the three systems were used to image patterns of ^{18}F -fluoro-deoxyglucose and ^{64}Cu -antibody uptake within mice tumor xenografts. Finally, a preliminary, simultaneous *in vivo* diffusion MRI/radiolabeled antibody PET study was performed and a cooccurrence matrix method was applied to analyze the bimodal dataset.

3.4.3 Materials and Methods

3.4.3.1 MR-compatible PET Scanner

The PET/MRI scanner being evaluated has been described in detail [160]. The system fits in a Bruker–Biospin 7 T MRI system run using PARAVISION4 (Bruker-Biospin). PET data were acquired using custom software. PET/MRI data were collected with an energy window of 350–650 keV. No attenuation, random coincidence, scatter or dead-time corrections were applied to PET/MRI datasets (All data were collected at count rates low enough to avoid significant effects from dead-time). Images were reconstructed with a 3D maximum *a posteriori* (MAP) algorithm (30 iterations, $\beta = 1 \times 10^{-5}$) [60]. Detector sensitivity normalization was incorporated into the forward model in MAP reconstruction. The FOV of reconstructed PET/MRI scanner images is $35.4 \times 35.4 \times 12.8 \text{ mm}^3$. Image matrix dimensions were $128 \times 128 \times 17$ and voxel size was $0.28 \times 0.28 \times 0.75 \text{ mm}^3$. The average spatial resolution of the scanner (mean of values measured at off-axis distances of 0, 5, 10 mm using filtered back-projection reconstructed images) is 1.5 mm [198].

3.4.3.2 Phantom Studies

We measured the linearity and uniformity of reconstructed image intensities from the PET/MRI scanner. A linearity phantom was constructed by evenly spacing four 1 mL syringes (Becton Dickinson, BD, inner diameter = 4 mm) on the inner surface of a 50 mL Falcon tube (diameter = 30 mm, BD, figure 3.21). Syringes were filled with ^{18}F -FDG at concentrations of 2.5, 1.3, 0.63, and 0.31 MBq/mL, as measured by a well counter (CRC-15R, Capintec). The phantom was centered in the PET FOV and imaged simultaneously with PET/MRI 9 times over 2 hours (PET: duration = 720 s; MRI: FLASH TR/TE = 500/4 ms, FOV: $35.4 \times 35.4 \text{ mm}^2$, slice thickness = 0.75 mm, matrix size = 128×128 , 40 slices).

The phantom was rotated 90° clockwise about the long axis of the system between each scan to test for activity-dependent differences in response among different regions of the reconstructed images. Response homogeneity within PET images was measured with a “hot rod” phantom configured with the same geometry as the linearity phantom, except that all syringes contained 1.5 MBq/mL of ^{18}F -FDG. The hot rod phantom was imaged 10 times over 2 hours (PET: 600 s) with a 90° clockwise rotation between consecutive scans. The first linearity phantom scan of the study ses-

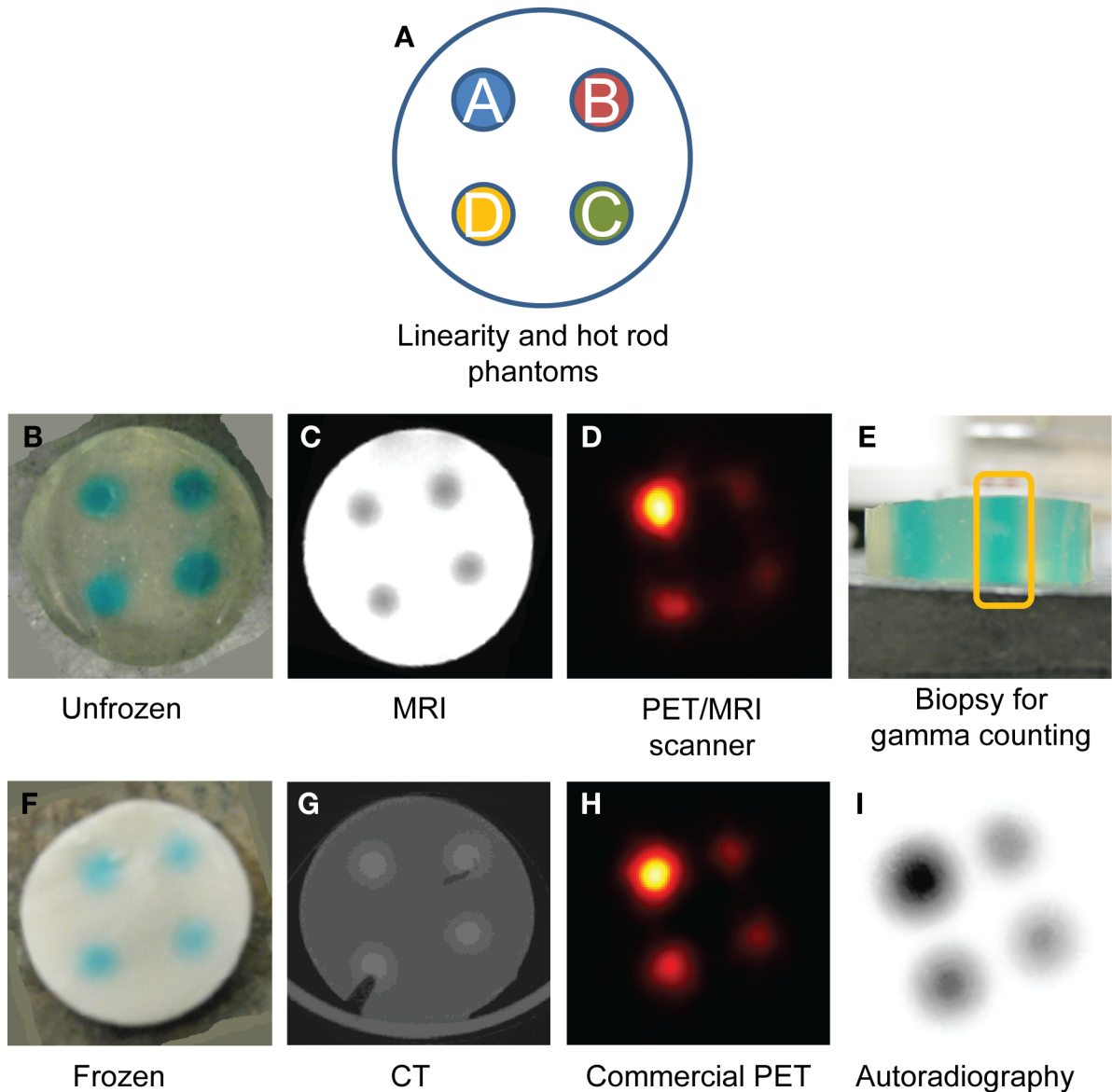


Figure 3.21: Phantoms used in this study. (A) Schematic of the linearity and hot rod phantoms (syringe and gelatin) used in the study. (B)–(I) Images of gelatin linearity phantoms acquired across modalities. Blue food dye was used to visualize rods (B,F), while MR (Prohance) and CT (Isovue 300) visible contrast agents were mixed with radioactivity to enable visualization in MRI and CT respectively (C,G). A small crack is evident in a frozen test phantom prepared for CT imaging (G); this phantom was not used in the studies. The physical properties of the gelatin phantom (E) enabled sampling for gamma counting as well as thin, frozen sectioning for autoradiography (I). The orange box in (E) outlines a rod that was sampled with a biopsy punch and transferred for weighing and gamma counting.

sion was used to derive regression coefficients with which other scans were calibrated; this method incorporated phantom-specific compensation for attenuation, scatter and partial volume effects. Detailed description of the calibration procedure is given in section 3.4.7.1.

We also validated stability of the PET/MRI scanner over multiple imaging sessions. Linearity phantoms were prepared and imaged as described above for 3 separate imaging sessions over 10 days. The coefficient of variation (CoV) of calibration coefficients across sessions were calculated.

3.4.3.3 Animal Studies

Animal studies were approved by the Animal Care and Use Committee at Caltech. Ten days prior to imaging, TgCEA⁺C57BL/6 mice were implanted in the right flank with 8×10^5 MC38.CEA colorectal adenocarcinoma cells [199].

¹⁸F-FDG. A tumor-bearing mouse was fasted for 4 hours, injected intravenously (i.v.) with 37 MBq of ¹⁸F-FDG, then warmed and sedated with a 1.5% isoflurane/air mixture. The injected activity was sufficient to allow imaging of the same mouse by PET/MRI, microPET and QAR in the same study session. After 60 min, the mouse was euthanized and secured to a cardboard platform; mouse and platform were placed on a custom-designed plastic holder. The mouse was positioned with its long axis orthogonal to the transaxial imaging planes of the PET/MRI scanner and imaged unfrozen with simultaneous PET/MRI (PET: 600 s; MRI: RARE TR/TE = 3500/4.5 ms, matrix size = 128 × 128, resolution = 0.28 × 0.28 mm², slice thickness = 0.75 mm, 34 slices). Following the initial PET/MRI scan, the mouse was frozen in a dry ice and isopropyl alcohol bath, repositioned into the holder and reimaged (PET: 1200 s; MRI: same as above). Using recorded prompts count rate and previous work relating prompts rate to true coincidence count rate for the PET/MRI scanner [198], we estimated the true-to-prompt coincidence event ratio for our scans to be ~50–75%.

To facilitate a) shielded transport between the laboratories where PET/MRI and microPET/autoradiography experiments were done; and b) cryosectioning for autoradiography, the frozen mouse was cut to obtain a 3.5 cm long section axially-centered on the tumor. A laser guide ensured that the cut face was orthogonal to the long axis of the mouse. The section was positioned in an imaging holder parallel to the holder's axis to ensure that the cut-face was orthogonal to the long axis of the microPET R4 scanner (Concorde Microsystems) [200]. The mouse section was

then serially imaged with microPET and microCT (Siemens InveonCT) (PET: 1200 s, 350–650 keV energy window, 6 ns timing window, corrections made for detector normalization, dead-time and random coincidence events, CT: 80kVp, 500 μ A, 200 ms/step, 361 steps covering 360°, 2 axial bed positions with a 20% overlap, voxels binned \times 4). Measured true-to-prompt event ratio in all microPET scans were >99%. MicroCT images were reconstructed with the COBRA-3D reconstruction algorithm (Exxim) to produce datasets with isotropic voxels (210 μ m per side). Prior to reconstruction, microPET list-mode data were truncated to contain the same number of prompt coincidence events as in the PET/MRI frozen-state scan. This was done in order to make true count densities at least roughly comparable in the PET/MRI and microPET scans. Images were then reconstructed using 3D OSEM-MAP (3D OSEM: 4 iterations, 12 subsets, followed by MAP: 30 iterations, $\beta = 0.33$, optimized for uniform resolution).

After microPET imaging, the mouse section was embedded in a 4% carboxy-methyl-cellulose (Sigma-Aldrich) water mixture within a custom-steel mold. The mold was placed in a dry ice and isopropyl alcohol bath for 10 minutes and then into a -20°C freezer for 1 hour before mounting onto a cryomicrotome (Bright 5030/WD/MR, Hacker Instruments). Slices were removed until tumor tissue was apparent. After that, 50 μ m thick transaxial frozen sections, spaced 250 μ m apart, were acquired for autoradiography until all tumor tissue had been sectioned, ensuring at least 3 autoradiography slices per PET/MRI image slice. During sectioning, the block face was photographed (Nikon D70, Tamron 90 mm 1:2.8 Macro ϕ 55 lens). Sections were placed onto storage phosphor screens (Super Resolution Screen, PerkinElmer). A ^{14}C standard strip (Amersham) was placed on each screen for calibration of screen sensitivity. Screens were exposed to collected sections for 3.5 days at -20°C and then read with a laser scanner (Packard Cyclone).

^{64}Cu -labeled Antibody. Distribution of a radiolabeled antibody against CEA, ^{64}Cu -DOTA-NHS-M5A (9), was imaged in a tumor-bearing mouse. The antibody (5.6 MBq, specific activity = 0.37 MBq/ μ g) was injected i.v., and *in vivo* simultaneous PET/MRI imaging was performed at 4 and 20 hours post injection. The animal was kept at 35°C – 37°C with a warm air flow. At each timepoint, PET (3600 s); anatomical MRI (RARE, same parameters as above) and diffusion MRI images (TR/TE=3000/25ms, matrix size = 128×128 , resolution = $0.28 \times 0.28 \text{ mm}^3$, slice thickness = 0.75 mm, 10 slices, $\delta/\Delta = 7/14\text{ms}$, b-values = 0, 300, 1000 s/mm^3 , 1 direction) were acquired. The mouse

was sacrificed 24 hours post injection. Images were then acquired with the PET/MRI scanner, microPET and autoradiography and processed as per the ^{18}F -FDG experiment.

3.4.3.4 Image Analysis

Image Coregistration. PET/MRI scanner images were aligned with MRI as previously described [201]. Images from non-frozen and frozen specimens were aligned using a rigid-body transformation obtained via landmarks along the anatomic contour. MicroPET and microCT images were coregistered with a rigid-body transformation (Amira) using landmarks present on both images. Autoradiography images acquired from different phosphor screens during the same study session were cross-calibrated using ^{14}C standard strips. For animal studies, slices within each autoradiography and photography image z-stacks were first aligned across the stack using the Fiji StackReg function (<http://pacific.mpi-cbg.de/wiki/index.php/Fiji>). The two stacks were then coregistered using a rigid-body transformation derived from 12 landmarks per slice clearly seen on both stacks. Three adjacent slices falling within a given PET slice were averaged to match the slice thickness of the PET/MRI scanner. Prior to cross-modal registration, PET/MRI and autoradiography/photography datasets were resliced to 1.2 mm thickness to match the slice thickness of reconstructed microPET images. Finally, PET/MRI and microPET/microCT image stacks were aligned to the autoradiography/photography stack using a landmark-based rigid-body algorithm implemented in MATLAB, resulting in a coregistered combined dataset with voxel dimensions of $0.28 \times 0.28 \times 1.2 \text{ mm}^3$.

Regions of Interest. For phantom images acquired in PET/MRI studies, cylindrical volumes of interest (VOIs) were axially centered within images of rods (diameter = 40% of the rod, length = 8.3 mm). Tumor and whole-animal VOIs were drawn on photographic stacks using MRICro (<http://www.MRIcro.com>) and applied to PET and autoradiography images.

PET/autoradiography Comparisons. Similarity metrics used to compare animal images are summarized in table 3.10. Image intensities within VOIs were scaled to fall between 0 and 1 for similarity analysis. We used scaled images because it was not feasible to perform autoradiography of a linear calibration phantom during day-long animal imaging experiments. Scaling was valid since phantom studies showed that the PET/MRI scanner, microPET and autoradiography response

were linear (see section 3.4.7, figures 3.23 and 3.30).

Table 3.10: Image similarity metrics used to compare PET image quality with autoradiography

Metric Name	Equation	Description
Correlation coefficient	$\frac{E[(x-\mu_x)(y-\mu_y)]}{\sigma_x\sigma_y}$	Voxel by voxel correlation between two regions of interest. x, y refer to the voxel value for the first and second image respectively, μ and σ refer to the mean and standard deviation of the voxel values in images X and Y. E denotes expectation value.
Peak signal-to-noise ratio (PSNR)	$10\log_{10}\frac{Max-voxel-value_i \times Max-voxel-value_j}{Mean-voxel-difference_{ij}}$	Voxel by voxel measure of SNR within a ROI between images i and j [202].
Structural similarity index (SSIM)	$SSIM(x, y) = l(x, y)^\alpha c(x, y)^\beta s(x, y)^\gamma,$	Similarity index comparing local image structure. l, c, s refer to the luminance, contrast and structure of the image, respectively. α, β, γ are adjustable parameters. (Default settings from [202] were used.) See reference for a detailed description.
Complex wavelet structural similarity index (CWSSIM)		Same as SSIM, but with wavelet analysis incorporated [203].

***In vivo* PET/diffusion MRI.** Aligned and calibrated (using a linearity phantom as described in section 3.4.7) PET/MRI scanner images were converted to units of percent injected dose per gram (% ID/g). (ADC) tumor maps were generated from diffusion MRI data [192]. Cooccurrence matrix analysis was used to compare ADC and PET images while taking into account the resolution differences between imaging modalities. The cooccurrence matrix C was calculated using the following equation:

$$C_{\Delta x \Delta y \Delta z}(i, j) \sum_{p=1}^n \sum_{q=1}^m \sum_{r=1}^l = \begin{cases} 1, & \text{if } ADC_r(p, q, r) = i \text{ and } PET_r(p + \frac{\Delta x}{a}, q + \frac{\Delta y}{b}, r + \frac{\Delta z}{c}) = j, \\ 0, & \text{otherwise.} \end{cases}$$

ADC_r and PET_r are ADC and PET images whose voxel values have been binned to one of 15 evenly spaced values lying within the intervals $i \in [0, 1.5 \times 10^{-3} \text{ mm}^2/\text{s}]$ and $j \in [0.25d, 0.75d]$ (d is

the maximum % ID/g value in the VOI), respectively. p , q and r are voxel coordinates along x, y and z directions of the $n \times m \times l$ image volume (defined by the VOI). a , b and c are the PET voxel dimensions ($0.28 \times 0.28 \times 0.75 \text{ mm}^3$). The parameters $|\Delta x|$, $|\Delta y|$ ($\leq 1.5 \text{ mm}$) and $|\Delta z|$ ($\leq 2.1 \text{ mm}$) were equated to the image resolution (average FWHM values) of the PET/MRI scanner [198].

Statistical Analysis Two-way ANOVA was used to compare image homogeneity and linearity of PET/MRI scanner phantom data. Differences between rod intensities measured from different quadrants of the image and individual rod intensities measured from separate images during the study session were tested. Differences were considered significant when p -values were < 0.05 .

3.4.4 Results

3.4.4.1 PET/MRI Scanner Response

Activity Concentration Recovery. Activity concentration recovery (ACR = measured value/true value, measured value obtained from images using calibration coefficients derived as described in section 3.4.7.1) from PET/MRI scanner phantom images are shown in figure 3.22. Linearity phantom images had ACRs close to unity (0.97 ± 0.06) for all rods (diameter = 4 mm) across a 10-fold range of activity concentrations. No significant difference in activity concentration recovery among spatial locations ($p = 0.3$) or among different rod activity concentrations ($p = 0.3$) were observed. However, reproducibility of the scanner-derived ACR was inversely related to rod activity concentration (ACR standard deviation = 23% for the lowest activity concentration rod compared to 9% for the highest activity concentration rod). This is likely due to increased noise in reconstructed images at lower activity concentrations. Hot rod phantom images also had ACRs (1.03 ± 0.03) close to unity for a range of activities. Again, no significant dependence of ACRs on spatial location ($p = 0.5$) or rod identity ($p = 0.5$) was seen.

Stability Across Imaging Sessions. Calibration curves and regression coefficients obtained with linearity phantoms from 3 separate imaging sessions over 10 days are shown in figure 3.23. The data show that the PET/MRI scanner has a temporally stable and linear response across a wide range of activity concentrations when system parameters are kept constant.

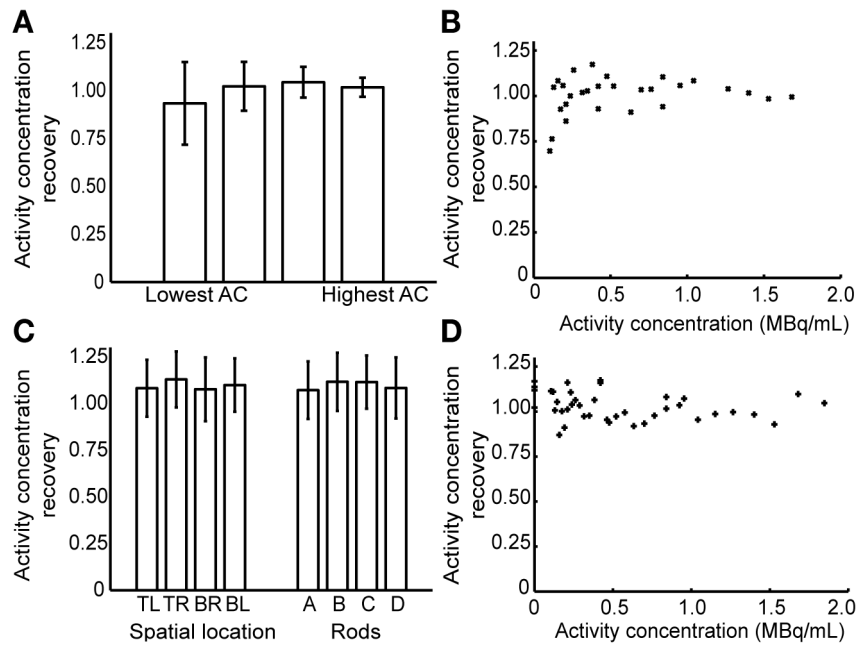


Figure 3.22: PET/MRI scanner accuracy and stability within an imaging session. Measurements were made on syringe “rod” phantoms described in 3.4.3.2. (A) Activity concentration recovery (ACR) for ^{18}F -FDG linearity phantom images acquired over 2 hours, with ROIs drawn over rods with varying activity concentrations. No significant dependence on spatial location ($p = 0.3$) or activity concentration ($p = 0.3$) was observed. (B) Rod ACRs compared with actual rod activity concentrations. (C) ACRs of ^{18}F -FDG hot rod phantom images acquired over 2 hours, compared with respect to spatial location (TL = top left of image FOV, TR = top right of image FOV, BR = bottom right of image FOV, BL = bottom left of image FOV) and rod identity. No dependence on spatial location ($p = 0.5$) or rod identity ($p = 0.5$) was observed. (D) Rod ACRs compared to actual rod activities at the time of imaging. All hot rod syringes contained the same activity concentration. Error bars denote SD.

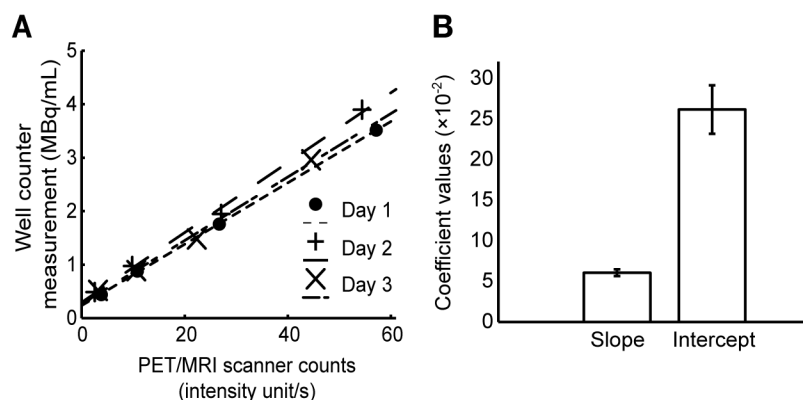


Figure 3.23: Linearity and stability of the PET/MRI scanner across multiple imaging sessions. Measurements were made on syringe “rod” phantoms described in 3.4.3.2. (A) Linearity phantom rod image intensities from 3 separate imaging sessions over the course of 10 days are plotted against actual activity concentrations. Fitted linear regression lines used to determine the calibration coefficients are also shown. (B) Slope and intercept calibration coefficients (mean and SD) across the 3 sessions. CoVs for the slope and intercept were 6.8% and 11% respectively.

3.4.4.2 Comparison of Image Intensity Patterns Across Modalities

Qualitative Assessments. Figure 3.24A shows coregistered images of a mouse injected with ^{18}F -FDG and imaged using PET/MRI, microPET/CT and autoradiography/photography. As expected, FDG uptake in the tumor was elevated compared to surrounding tissues. The image intensity pattern was heterogeneous within the tumor and approximately congruent among all 3 imaging systems. Regions of high activity were present in lateral and medial lobes of the tumor, with a region of lower activity in between. The central region had somewhat higher relative intensity in autoradiography compared to PET images. Images acquired 24 hours after injection of ^{64}Cu -DOTA-NHS-M5A are shown in figure 3.24B. Expected tumor localization of the antibody is observed, along with intratumoral heterogeneity. The multilobed intratumoral uptake pattern is similar across PET/MRI, microPET and autoradiography.

Quantitative Evaluation. Image similarity between different pairs of radioactivity image sets was quantified using several metrics. Comparisons of PET/MRI scanner and microPET R4 with autoradiography are shown in figures 3.25 and 3.26. Pixel-based correlation coefficients for all PET to autoradiography comparisons were moderate to high (>0.7) for both whole-mouse cross sections and tumor ROIs (figure 3.25A–B). Not surprisingly, correlation increased when autoradiography was blurred to match resolution to the PET/MRI scanner and microPET, and dropped nearly to zero

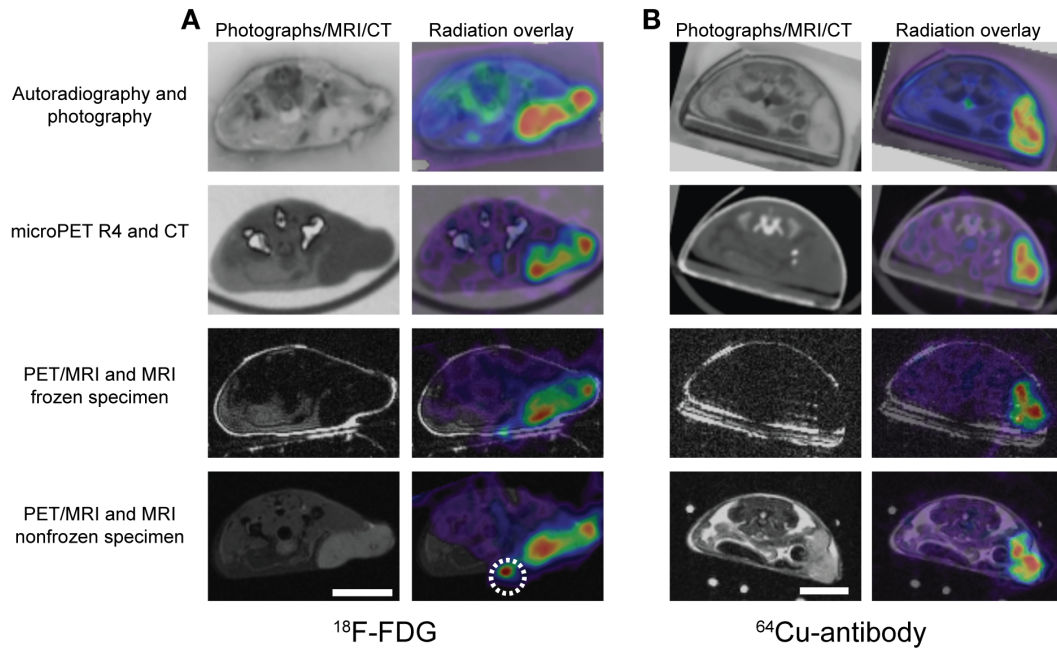


Figure 3.24: Multimodal imaging of radiotracer uptake in tumors. Mice bearing MC38.CEA tumors were injected either with (A) ^{18}F -FDG or (B) anti-CEA ^{64}Cu -DOTA-NHS-M5A antibody and sacrificed after an uptake period. Tumor regions were then imaged with the PET/MRI scanner, frozen, reimaged with PET/MRI, imaged in the frozen state with microPET and microCT, cryosectioned and imaged with autoradiography. Matched tumor slices show qualitatively similar uptake patterns. PET/MRI scanner images of ^{18}F -FDG show a hot spot (circle) not observed with other modalities. Comparison with MRI showed the hot spot to be on the animal's surface, indicating that it was caused by urine residue that was removed prior to subsequent imaging (Scale bar = 10mm).

when the autoradiography dataset was scrambled. An alternative pixel-based metric, peak signal-to-noise ratio (PSNR), gave similar results except that values were higher for whole-body than tumor ROIs and the drop in metric value was less pronounced for a randomly scrambled image (figure 3.25C–D).

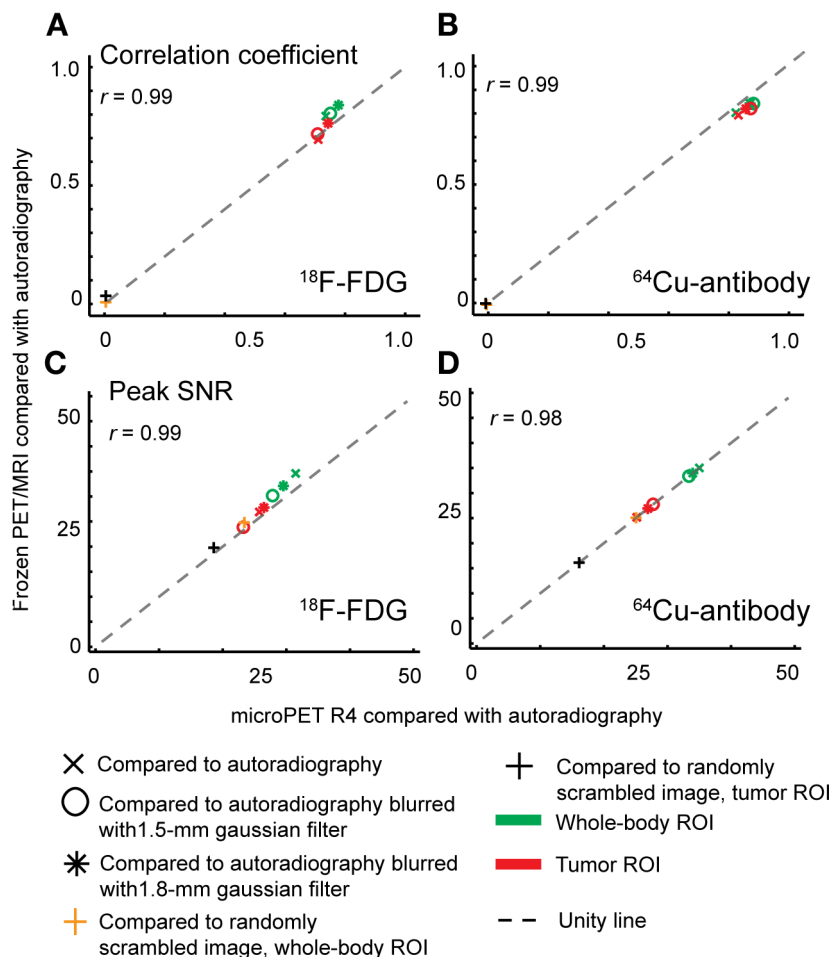


Figure 3.25: Pixel-based similarity across PET/MRI scanner (frozen specimens), microPET and autoradiography images. $^{18}\text{F-FDG}$ and $^{64}\text{Cu-antibody}$ coregistered datasets are compared at whole-body and tumor ROI levels using correlation coefficients (A–B) and PSNR (C–D). Similarity between each PET dataset and autoradiography (with and without a Gaussian filter applied to autoradiography) were calculated and plotted against each other. A control comparison between PET datasets and a scrambled autoradiography volume showed large decreases for correlation coefficient but not PSNR. Pearson correlation coefficients comparing PET/MRI vs. autoradiography and microPET vs. autoradiography metrics are shown. Similarity metrics are described in table 3.10.

Images were also analyzed with structure-based metrics (figure 3.26). Mean structural similarity index (SSIM) and Complex wavelet structural similarity index (CWSSIM) analyses showed no clear difference between PET/MRI and microPET R4 scanners. With both measures, comparison

of PET images for tumor ROIs generally showed higher intermodal similarity than did whole-body ROIs. When autoradiography dataset was scrambled, structure-based comparisons decreased to nearly zero, confirming that the metrics do reflect image similarity. Similarity metrics obtained by comparing PET/MRI and microPET images to autoradiography were highly correlated ($r \geq 0.9$).

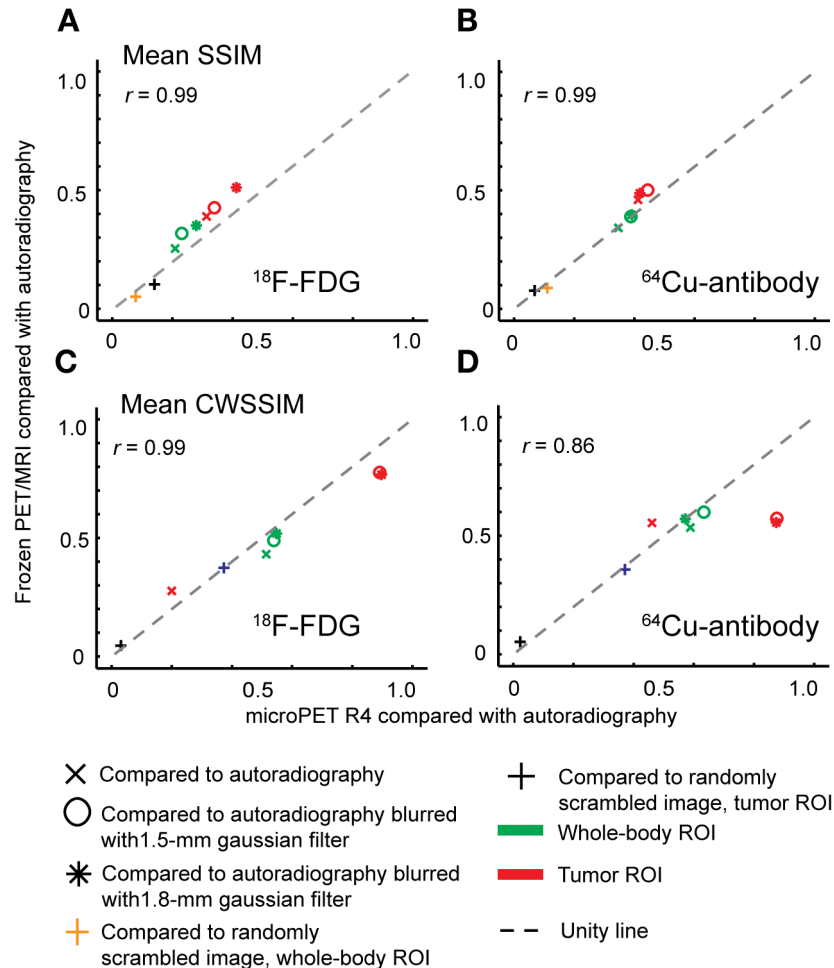


Figure 3.26: Structure-based similarity among PET/MRI scanner (frozen specimen), microPET and autoradiography images. $^{18}\text{F-FDG}$ and $^{64}\text{Cu-antibody}$ coregistered datasets were compared as in figure 3.25, except using SSIM (A–B) and CWSSIM (C–D). Pearson correlation coefficients comparing PET/MRI vs. autoradiography and microPET vs. autoradiography metrics are shown.

Small differences shown by the metrics can be related to images. For example, comparison of FDG data slightly favored the PET/MRI scanner over microPET. A possible explanation for this can be seen in figure 3.24A, where PET/MRI of the frozen specimen and QAR images show a more pronounced low activity region between the two main high activity lobes and relatively flat dorsal tumor contours compared to the microPET image. Differences among modalities are

less pronounced in the antibody images; this is seen in figures 3.25B, D and 3.26B, D, where on average data points lie closer to the identity line than for FDG images. CWSSIM, a metric less sensitive to geometric distortions compared to other metrics [203], attenuates these differences but also indicates better structural agreement between microPET and blurred autoradiography images of ^{64}Cu in tumor compared with PET/MRI.

Simultaneous *In Vivo* PET/MRI. Tumor uptake of ^{64}Cu -DOTA-NHS-M5A at 4 and 20 hours post injection is compared to simultaneously acquired MR-ADC images in figure 3.27. At 4 hours post injection, much of the antibody was still in blood, as shown by the high signal in the inferior vena cava (figure 3.27A) and low uptake within the ventral portion of the tumor. At 20 hours, the antibody signal was spread throughout the tumor parenchyma (figure 3.27B). Cooccurrence matrix analyses of the uptake pattern reflect these observations (figure 3.28). At 4 hours, regions of relatively high antibody concentration within the tumor tended to be in regions with high ADC values, suggesting that the antibodies were in the tumor's intravascular and/or interstitial spaces (figure 3.28A). By 20 hours, this high uptake/high ADC cooccurrence disappeared, suggesting uniform antibody distribution within the tumor (figure 3.28B).

3.4.5 Discussion

Feasibility of *in vivo* PET/MRI has been well demonstrated [190]. However, it remains to be shown that PET images from such a scanner accurately depict activity distribution within the imaged tissue. Here, we demonstrated the ability of a MR-compatible PET scanner [105] to produce quantifiable intratumoral images that are stable, linear and concordant with images from a commercial small animal PET scanner and autoradiography.

PET systems require a uniform and linear image intensity response. PET/MRI scanner-derived images of linearity and hot rod phantoms showed the system to be stable and linear during a single imaging session and across multiple sessions. The linearity phantom allowed us to demonstrate the stability of the PET/MRI system for measuring multiple activity concentrations in the same image across multiple time points within an imaging session. These characteristics are crucial for successful dynamic simultaneous PET/MRI studies. Activity concentration recovery in this study compares well with previous reports for small animal PET [204, 205].

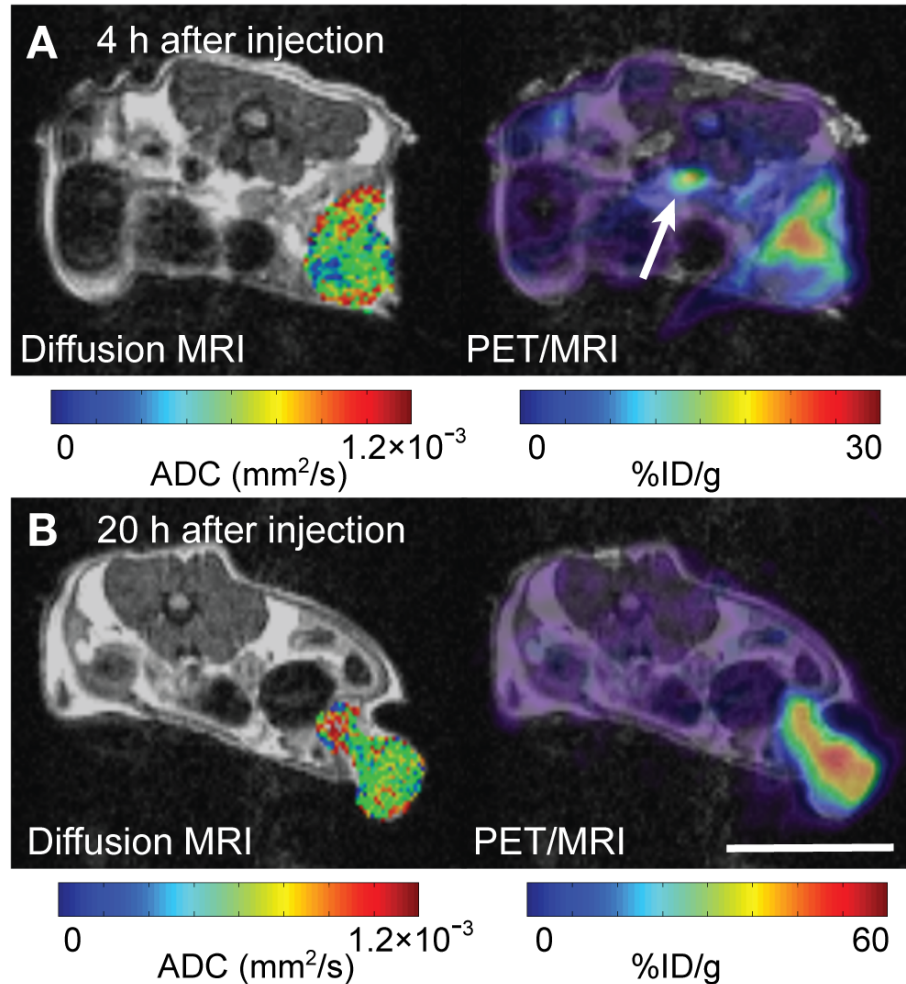


Figure 3.27: *In vivo* simultaneous diffusion MRI/radiolabeled antibody PET reveals phases of antibody uptake. PET/MRI of a mouse was obtained at 4 (A) and 20 (B) hours post injection. Slices from the two time points were matched as closely as possible. Both PET and diffusion MRI show intratumoral heterogeneity of uptake and ADC values respectively. A general accumulation of antibody was observed between 4 to 20 hours. Focal distribution of antibody was observed in the more dorsal portion of the tumor at 4 hours post injection; by 20 hours, the distribution encompassed most of the tumor mass. Spatial patterning of the ADC (shown only for the tumor) was similar at both time points. PET images were calibrated using a linearity phantom as described in section 3.4.7. Arrow points to the inferior vena cava (Scale bar = 10mm).

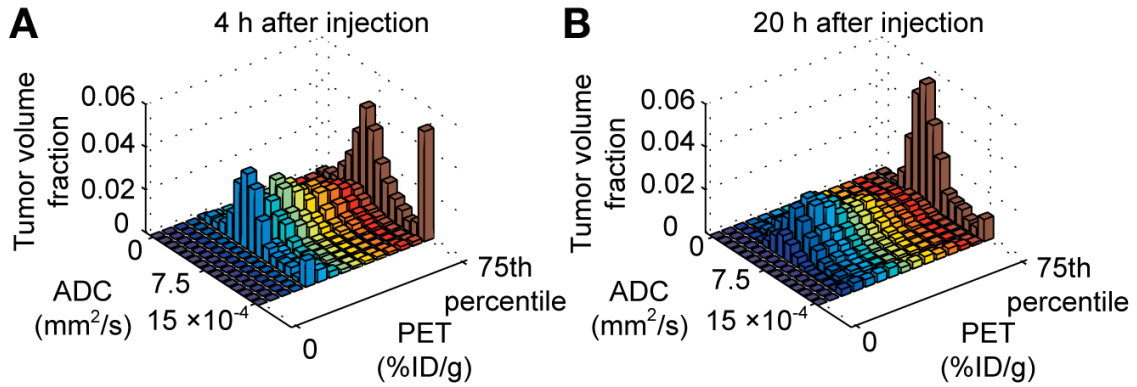


Figure 3.28: Cooccurrence matrix analysis of functional PET and MRI data offers insight into tumor antibody uptake. (A) cooccurrence matrix comparing antibody uptake and ADC values at 4 hours post injection. The uptake comparison window was adjusted to account for the lower spatial resolution of PET (1.5 mm FWHM) compared to MRI. At 4 hours, a large fraction of the antibody signal colocalized with regions of high ADC, ($>0.0015 \text{ mm}^2/\text{s}$) suggesting much of the antibody was in vascular and/or interstitial spaces. (B) By 20 hours, that component had disappeared; the antibody was spread more evenly across the tumor mass. This was not apparent with pixel-by-pixel matching (figure 3.31).

To quantitatively interpret and compare PET and QAR images, image intensities for both modalities need to be linearly related to object activity concentration. To demonstrate that PET and QAR imaging systems used in this study are linear and to confirm that our intended strategy for animal studies is valid, we developed a gelatin phantom that could be visualized by optical imaging, MRI, CT, PET, QAR, and assayed for radioactivity concentration by gamma counting (figure 3.23). Figure 3.30 shows that image intensities derived from phantoms were linearly related to sample activity concentration for all 3 imaging systems, enabling us to compare images from different systems with confidence.

The ability to return images with intensity patterns reflecting actual *in vivo* activity distributions was compared among the PET/MRI scanner, microPET and QAR. intratumoral activity distributions for a metabolic marker (^{18}F -FDG) and a targeted antibody were in good overall spatial concordance among modalities. However, detailed examination of the images revealed some differences. Resolution differences between autoradiography and PET can be seen by the presence of finer structures in autoradiographs compared to their PET counterparts. For example, the antibody distribution in figure 3.24B showed a small rim of relatively high activity in the ventral portion of the tumor autoradiographs not visible with PET. Christian *et al.*, reported similar observations, attributing them

to differences in resolution between PET and autoradiography [206]. Application of a Gaussian filter to autoradiography images acquired in this study support this assertion (figure 3.29). Lack of attenuation and scatter correction in PET/MRI scanner images may also contribute to disparities. Attenuation of 511 keV photons can be as high as 15% with small animal-sized objects [207]. However, since tumors imaged in our experiments were superficial, we expect attenuation-related differences between PET and autoradiography to be minimal. Regardless of the limitations of the imaging techniques used in this study, the intratumoral patterns are qualitatively similar among the PET/MRI scanner, microPET and QAR for both ^{18}F -FDG and the ^{64}Cu -antibody. Furthermore, similarity metrics showed good overall correlation between both PET systems and QAR. Image differences between the two PET systems may be due to resolution differences between the systems and, in case of the ^{18}F -FDG study, high count rates during the PET/MRI scan compared to the microPET.

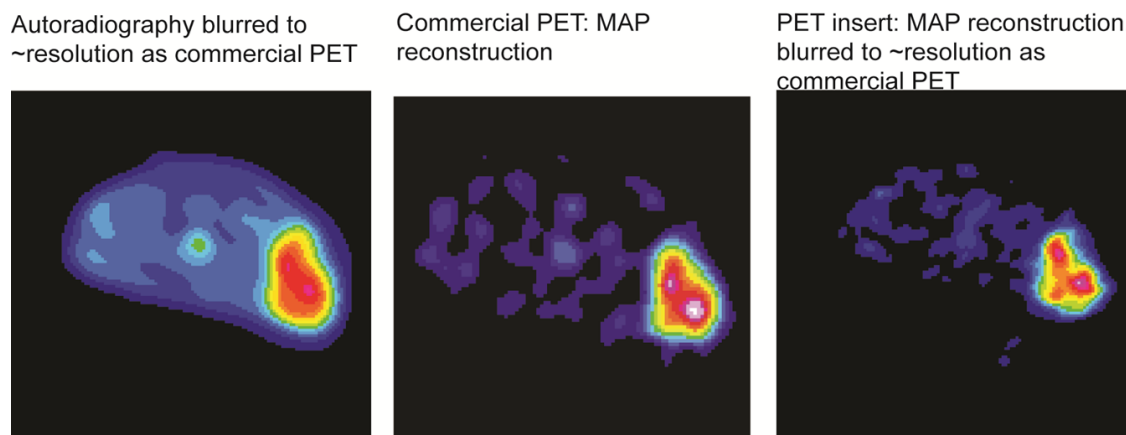


Figure 3.29: Resolution differences between autoradiography and PET. Images from the antibody study used for analysis. 2D Gaussian filters were applied to the autoradiography and PET insert images to simulate the spatial resolution of the commercial microPET R4 (~1.8 mm). Image filtering of the autoradiography and PET insert images improved correspondence to the microPET image. This highlights the resolution differences between the three imaging systems.

The necessity and utility of detailed quantitative analyses are illustrated in figure 3.27. Having demonstrated good spatial fidelity of PET/MRI scanner images, we hypothesized that biological inferences can be made by comparing simultaneously acquired PET and MR images. Fidelity of the PET images allowed us to conclude that there was a time dependent heterogeneous tumor accumulation of antibody during a preliminary study (figures 3.27, 3.28).

Previously, two methods have been employed to compare multimodal intratumoral datasets. Cho *et al.* performed a pixel-wise comparison of PET and DCE-MRI maps [183], while Metz *et al.* used arbitrary thresholds to segment tumor subregions for comparison [195]. The former approach neglects differences in resolution between the imaging modalities, while the latter requires multiple PET datasets and is observer dependent. We accounted for differences in resolution between PET and MRI by analyzing image sets with a cooccurrence matrix bin-offset equal to the mean FWHM of the scanner. This analysis demonstrated spreading of antibody from a highly intravascular/extracellular region throughout the tumor. There is recent interest in modeling tumor growth kinetics using multimodal imaging datasets on a pixel-by-pixel basis [208]. The cooccurrence matrix method can be incorporated into these analyses to account for resolution differences between the different modalities. Further improvements can be made to this method. For instance, one can vary the FWHM window to account for varying spatial resolution within the PET FOV. Further considerations of the method is explored in appendix C.

To date, few studies have been published that evaluate PET image fidelity to actual *in vivo* activity distributions. Christian *et al.* developed a Styrofoam holder surrounding a mouse to allow coregistered PET and autoradiography [112]. Cho *et al.* developed a foam mold/plastic holder for rat imaging [183]. The current PET/MRI scanner is not large enough to accommodate these solutions. Instead, landmarks visible on all anatomical images (MRI, CT, photography) along with laser-guided positioning of the mice allowed effective coregistration between PET and QAR.

It is remarkable that, despite limitations inherent in a first-generation prototype (e.g. low sensitivity and lack of random coincidence or dead-time corrections), the current PET/MRI scanner, operated simultaneously with MRI, provided PET images with essentially equivalent spatial patterns as the well-established microPET R4. This demonstrates the ability of the MR-compatible PET scanner to deliver useful *in vivo* information acquired simultaneously with MRI. Next generation systems will likely improve on the quantitative ability and image quality observed in the current system. Methods developed here can be utilized as a benchmark to assess image quality of future systems. Further, availability of good fidelity, coregistered PET/MRI datasets and their QAR/photography counterparts offers the opportunity to explore the biological implications of complementary imaging information, and provide a test bed to develop and evaluate *in vivo*-relevant

PET partial-volume, motion-correction and attenuation-correction algorithms.

3.4.6 Conclusions

We evaluated the ability of a MR-compatible PET scanner to generate spatially and quantitatively accurate images. Images acquired from tumor-bearing mice using different radioisotopes showed good correspondence among the PET/MRI scanner, microPET R4 and autoradiography. A co-occurrence matrix method enabling effective comparison of complementary PET and MR images was presented. This work provides a basis for pursuing biologically relevant simultaneous PET/MRI studies. Progress in hybrid PET/MRI technology will provide improvements in image quality. Methods from this study can be applied to evaluate such improvements.

3.4.7 Supplemental Data

3.4.7.1 Materials and Methods

Calibration of PET/MRI Scanner Images. PET/MRI scanner images of syringe phantoms were decay corrected and normalized for scan duration prior to analysis. The first linearity phantom image acquired during a given study session was used to convert image intensities to units of absolute activity concentration (kBq/mL). Rod image intensities from the PET/MRI image, obtained from cylindrical volumes of interest axially centered on each rod (diameter = 40% of the rod diameter, length = 8.3 mm), were plotted against activity concentrations measured by well counting of samples taken from the phantom. Plots were fitted by linear regression, taking into account the random variability of both the measured independent and dependent variables [209]. The resulting regression coefficients were used to calculate activity concentrations for all images acquired during the corresponding study session. This calibration procedure incorporates phantom-specific compensation for attenuation, scatter and partial volume effects into the calibration coefficients.

Cross-comparison of PET/MRI Scanner and microPET Linearity with Autoradiography and Direct Assay. To enable quantitative comparison of images across PET and QAR systems, it was necessary to ensure that all three systems had a linear response. Two phantoms were used for this purpose. A linearity phantom was made by solidifying a 10% gelatin solution (solid state density =

1.01 g/mL) in a cylindrical mold made from a 50 mL Falcon tube (BD). While the gel was liquid, 4 rods, each 4 mm in diameter, were evenly spaced in the mold. Once the gel had set, the rods were removed, and the holes were filled with gelatin mixed with $^{64}\text{CuCl}_2$ solution (Washington University School of Medicine) containing Prohance (Bracco; 0.1 mM) and Isovue 300 (Bracco; 1mM). Initial mixture activity concentrations were 3.7, 1.9, 0.93, and 0.56 MBq/mL. The 12.7 h half-life of ^{64}Cu enabled the phantom to be imaged on the same day with the PET/MRI scanner, commercial small animal PET and QAR. A second “hot rod” gelatin phantom was made in the same manner as the linearity phantom, except that the 4 rods each contained an initial activity concentration of 1.9 MBq/mL. The rods were surrounded with gelatin containing 0.19 MBq/mL of ^{64}Cu .

Phantoms were cut to 15 mm length to remove gelatin spillover at the ends. The removed sections of the phantom were sampled with a biopsy punch (inner diameter = 2 mm, Miltex), and the samples were placed in pretared Eppendorf tubes for gamma counting. Each region of interest (background and rod regions) was sampled twice. The phantoms were imaged simultaneously with PET/MRI (PET: 2700 s; MRI: FLASH TR/TE = 500/4ms, FOV: $35.4 \times 35.4 \text{ mm}^3$, slice thickness = 0.75 mm^2 matrix size = 128×128 , 40 slices). Immediately after imaging, the phantoms were placed in a dry ice and isopropyl alcohol bath for 5 minutes. The phantoms were subsequently imaged on a microPET R4 (Concorde Microsystems) for 20 minutes (350–650 keV energy window, 6 ns timing window).

After microPET imaging, the phantoms were cut in half. One half was sampled for gamma counting, while the other half was mounted onto a cryomicrotome (Bright 5030/WD/MR, Hacker Instruments). Five $50 \mu\text{m}$ thick frozen transaxial sections, spaced $250 \mu\text{m}$ apart, were obtained and transferred onto a chilled autoradiography cassette containing a storage phosphor screen (Super Resolution Screen, PerkinElmer). The loaded cassette was stored for 1 day at -20°C . Screens were read with a laser scanner (Packard Cyclone). Tubes containing phantom samples were assayed for radioactivity using a calibrated gamma counter (Model 1480 Wizard 3°, Wallac Oy). Sampling of the phantom was done at each stage of the imaging procedure (PET/MRI imaging, microPET R4 imaging and autoradiography) to account for diffusion of the radioactivity and contrast agent as evident in figure 3.21.

PET images were reconstructed and analyzed as described in section 3.4.3.4. Circular ROIs (diameter = 80% of rod diameter) were used for rod analyses on autoradiography images. Background activity was analyzed with ROIs (diameter = 5.3 mm) placed at five different locations per slice. Although variable slice thickness is a potential source of error in QAR, it was found to be negligible in our study. The CoVs of activity concentrations measured across several slices of the gelatin hot rod phantom (background = 0.19 MBq/mL, rods = 1.9 MBq/mL) were 3.0% and 3.2% for background and hot rod regions respectively. These values are lower than observed by Christian *et al.* (3.5%) after adjustment for differences in slice thickness [210].

Rod and background intensity values from gelatin phantom images were plotted against activity concentrations measured by direct weighing and gamma counting of relevant samples. Plots were fitted by linear regression. Pearson correlation coefficients compared to gamma counting were also calculated.

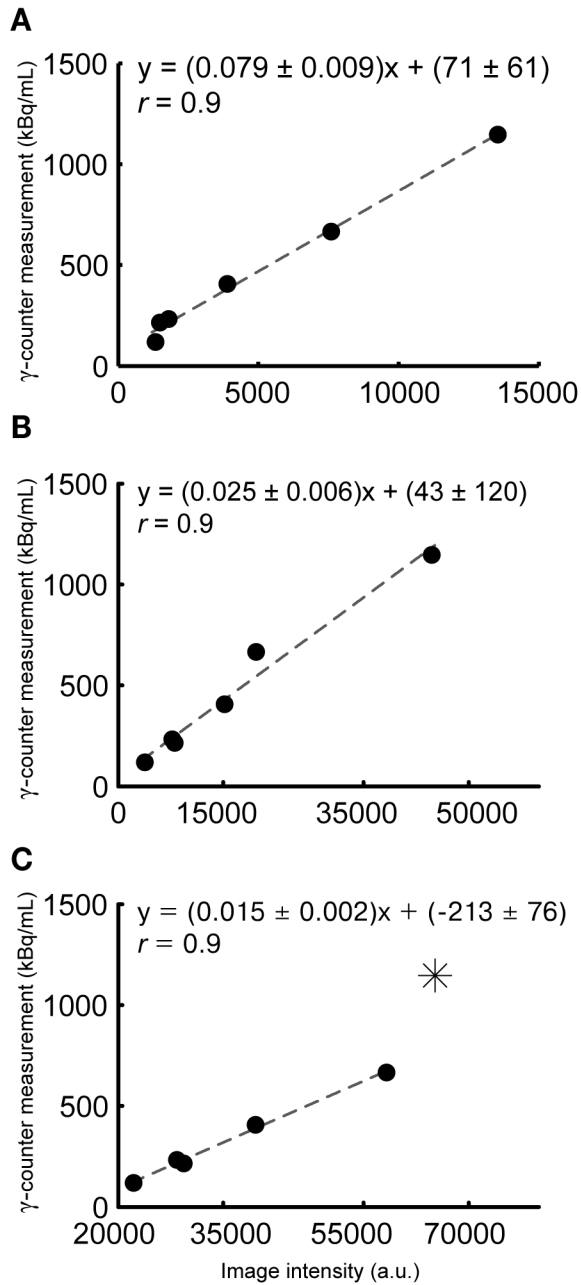


Figure 3.30: Linearity of PET/MR scanner, microPET R4 and autoradiography. Image intensities acquired from the same gelatin-based linearity and hot rod phantoms were plotted against direct assay measurements for (A) PET/MR scanner, (B) microPET R4 and (C) autoradiography. Linear regression was performed for each dataset. Pearson correlation coefficients are shown for each dataset. Software processing revealed that the linearity phantom rod with the highest activity was overexposed on the autoradiography phosphor imaging plate (the * data point in C). That data point was excluded from further analysis. (a.u. = arbitrary units)

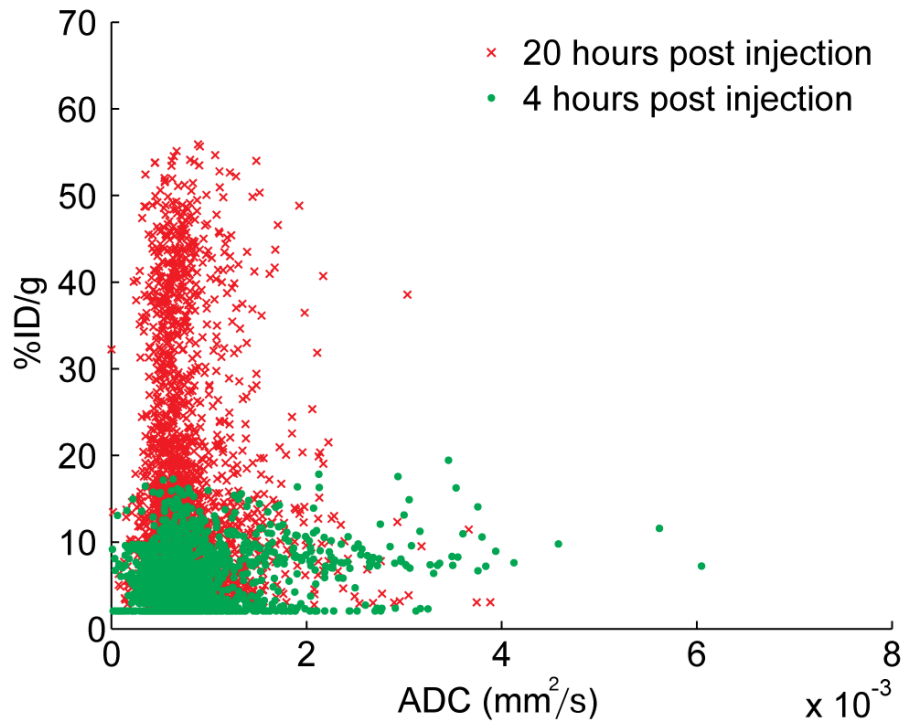


Figure 3.31: Scatter plot of simultaneous diffusion MRI and PET antibody measurements at two different times after injection of ⁶⁴Cu-labeled antibody. Quantitative pixel values from the tumor ROIs shown in figure 3.27 show low correlation between antibody uptake and ADC values ($r = 0.21$ and -0.02 at 4 and 20 hours, respectively).

3.5 Synchronization of PET/MRI Hardware

Simultaneous PET/MRI instrumentation enables PET and MRI images to be acquired in spatial and temporal coregistration. The issue of spatial coregistration of PET and MRI information was addressed in sections 3.2 and 3.3. Here, we address the issue of accurate temporal synchronization of the PET insert and MRI. We describe a system to allow synchronous PET/MRI data acquisition.

A schematic showing how the workflow for synchronous PET/MRI acquisition is shown in figure 3.32. Software modules were inserted into the PET acquisition program and MRI pulse sequence to allow cross-communication of the two systems. The modules can either trigger the process of synchronization or wait for a signal from the other signal. The user can begin acquisition via a PET or MRI trigger.

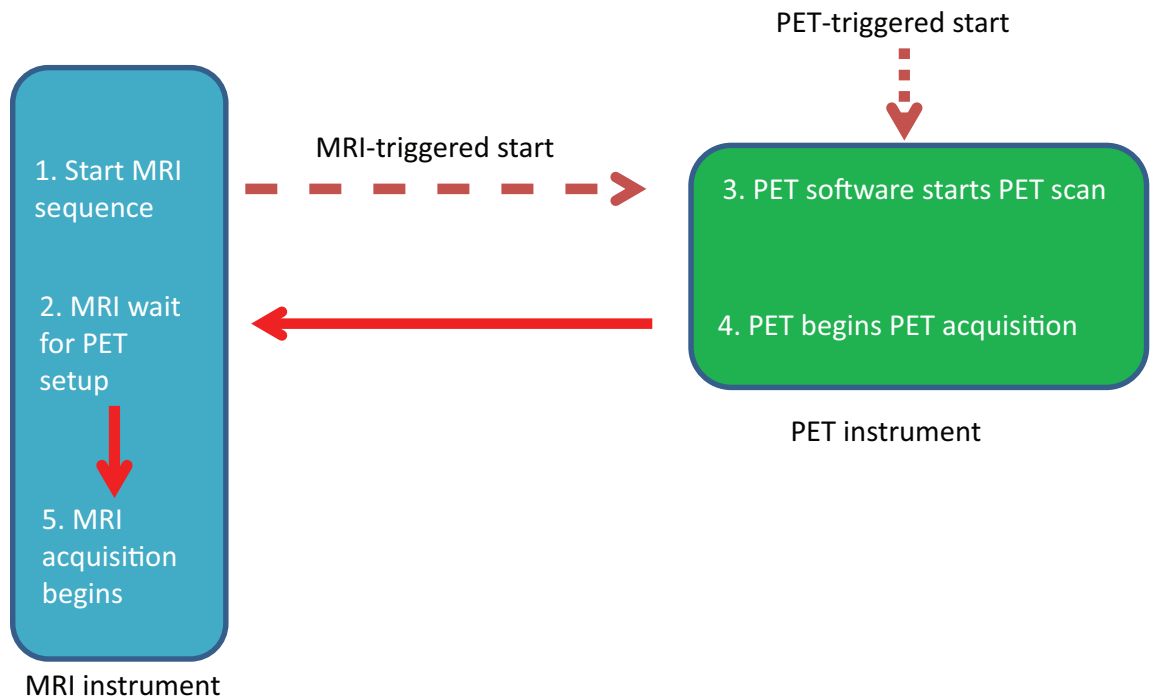


Figure 3.32: Synchronous PET/MRI acquisition may be dictated by either PET or MRI acquisition. Software modules embedded in the MRI and PET programs are written to allow cross-communication between the two systems. PET acquisition can be started by a MRI trigger embedded in an MRI pulse sequence or manually. The PET software then sends a sync signal back to the MRI, allowing the pulse sequence to begin acquisition at a fixed time. Each arrow (except between step 2 and 5) represents a synchronization signal.

Acknowledgment: Thanks to Martin Judenhofer for help with PET software coding. An updated version of the PET software including the module can be obtained on request.

3.5.1 Materials and Methods

3.5.1.1 PET setup

The current PET hardware utilizes the NIM standard, while the input/output of both the MRI system and the PET computer system are based on TTL. A logic level translator (Phillips Scientific, NIM model 726) was used to allow cross-communication between the NIM and TTL standards. The current PET software [162] was modified to enable system cross-communication using TTL via pins available on a standard parallel port.

3.5.1.2 MRI setup

Paravision 5.1 (Bruker, MA) software is used for MRI control. Communication with other systems can be achieved via TTL ports on the MRI hardware console. A software module that can be inserted at the beginning of any Bruker MRI pulse sequence was written to enable cross-communication with the PET system.

The code for the pulse sequence modules, implemented here for a standard FLASH sequence, is shown in appendix D.

3.5.2 Discussion

Temporal synchrony of PET and MRI data is an integral advantage of simultaneous PET/MRI systems. For many PET/MRI applications, the synchrony required are on the scale of the study session (e.g. ~minutes/hours). In these cases, temporally registered PET/MRI datasets can simply be acquired separately in the same study session.

A need for a higher degree of synchrony (~seconds) arises when the physiological processes being studied are transient (e.g. BOLD responses can change within seconds) and when the contrast agents being imaged have fast kinetic properties (e.g. Gd-DTPA or ^{18}F -FDG, section 3.33). Perfect (within milliseconds) synchronization of PET and MRI in these cases facilitates the posthoc analysis of the dual-dynamic datasets.

Further, the availability of temporally aligned data is also beneficial for improving the quantification of PET images. Posthoc MR-guided correction of PET datasets, such with the use of

MR-navigator echoes to reduce motion blurring in reconstructed PET images [100] require that the MRI and PET data be synchronized.

In summary, a system was implemented to enable perfect synchrony of PET and MRI data acquisition for the integrated small animal PET/MRI scanner. All or parts of the system can be easily ported to future versions of the scanner.

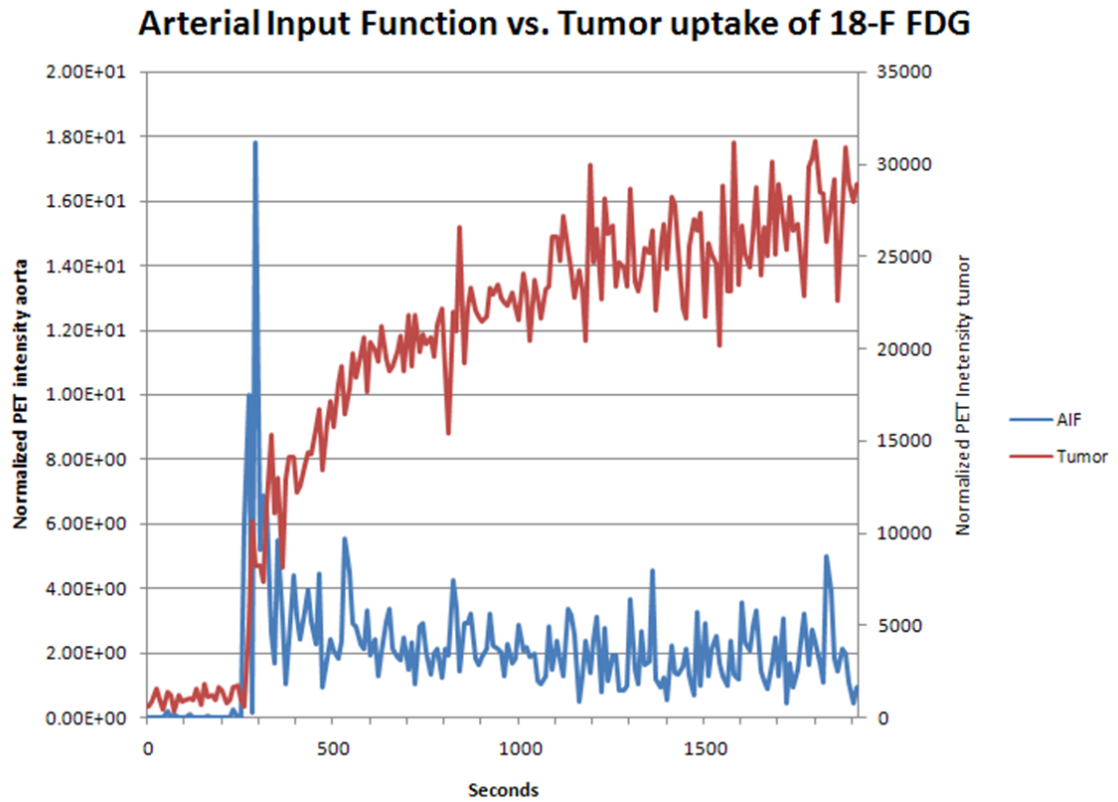


Figure 3.33: Fast kinetics of small molecular agents necessitate synchronous PET/MRI. Time curves of ^{18}F -FDG uptake in the abdominal aorta (AIF) and tumor in a tumor-bearing mouse. The ROI for the obtained time curves were defined by spatially coregistered MRI. Perfect temporal synchrony of such datasets with DCE-MRI will facilitate kinetic modeling and comparisons of multimodal datasets.

3.6 MR Gradient Effects on the PET Insert

In section 3.4, we demonstrated that the PSAPD-based MR-compatible PET system show good quantitative fidelity when used simultaneously with the MRI. However, initial studies with the current PET insert did show a slight decrease (7%–10%) of count rates in the presence of MRI pulse sequences [105]. It is important to understand the effect of such observations as next generation hybrid PET/MRI systems are being developed. Peng [142] explored the effect of MR-gradient switching using a single PET module. They found that count rate attenuation using a single PET detector was related to the location of the detector in relation to the gradient being operated, the magnitude of the gradient waveform and the ramp-time of the gradient. Here, we present results further examining this effect using an intact PET system.

3.6.1 Materials and Methods

Studies were performed using the MR-compatible PET insert. A ^{68}Ge cylindrical source (PET 2.5 C6/0.5, Sanders Medical) was placed in the center of the PET FOV inside a standard RF coil at the center of the MRI FOV. The PET insert was powered as per the conditions described in 3.4. PET data were acquired using in-house software [162]. Each dataset was acquired with a buffer size of 5 K and a duration of 300 s.

To examine the effects of individual MRI pulse sequence components on count rates, data acquisition was performed during trapezoidal/sawtooth waveforms set along the Y gradient direction (TR = 500 ms, no RF pulse was applied). By using electronic TTL gating signals programmed into the pulse sequence, count rates during specific portions of the pulse sequence were examined (figure 3.34):

1. Gradient off
2. Data acquired during the whole sequence (“Combined”)
3. Gradient on (Set at 20% of the maximum magnitude)
4. During ramping (50 ms risetime)
5. During ramping (10 ms risetime)

6. During ramping (1 ms risetime)

Decay and duration normalized counts were compared between portions. Three datasets were acquired for each portion. The global coincidence counts as well as the coincidence counts per detector were recorded. ANOVA with Bonferroni correction was used to analyze the counts data. The peaks and FWHM for energy spectra of each detector were analysed with Kruskal-Wallis test. No thresholds were applied to the spectra.

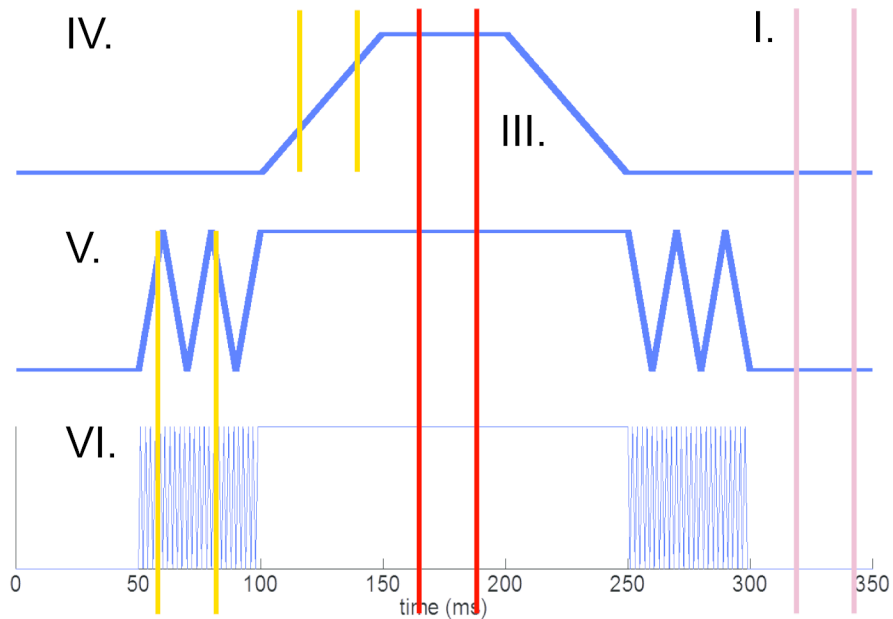


Figure 3.34: MRI gradient effects on count rates. A schematic of different pulse sequences used to probe gradient effects on PET insert count rates. PET data were acquired at different portions of the gradient waveform. I. When the gradient was off, II. during the whole pulse sequence, III. when the gradient is on (here set at 20% of maximum magnitude), during the gradient ramping with a risetimes of IV. 50 ms, V. 10 ms and VI. 1 ms. Pulse sequences were set with a TR = 500 ms. Acquisition windows were done within 50 ms (i.e. vertical bars were truncated to clarify the regions, rather than reflecting the exact timing).

3.6.2 Results

Count rates across all portions are shown in figure 3.35. Consistent with previous results, count rates were highest when the gradient was off. In the presence of gradient power, global coincident counts were attenuated ($p = 0.06$) by 2%–8%. The greatest attenuation occurred during rapid oscillation of the gradient (1 ms risetime, ~8% decrease). Steady-state gradient powering and slower risetimes showed similar attenuation (~2%–4%). Gradient effects on individual detector counts are shown in

figure 3.36. Different count rates across detectors were observed due to the different amplification gains for individual PSAPDs. Count attenuation due to different portions of the gradient waveform on each detector reflects global observations, with the 1 ms risetime showing the greatest decrease. In general, no statistically significant interaction between gradient portions and detector locations was observed ($p = 1$). However, examination of the individual detectors counts versus gradient portions data by one-way ANOVA revealed the detectors that showed significant or close to significant decreases during gradient oscillations were those aligned along the Y gradient direction (quadrant II and IV in figure 3.37, table 3.11). This is consistent with previous results obtained with a single detector.

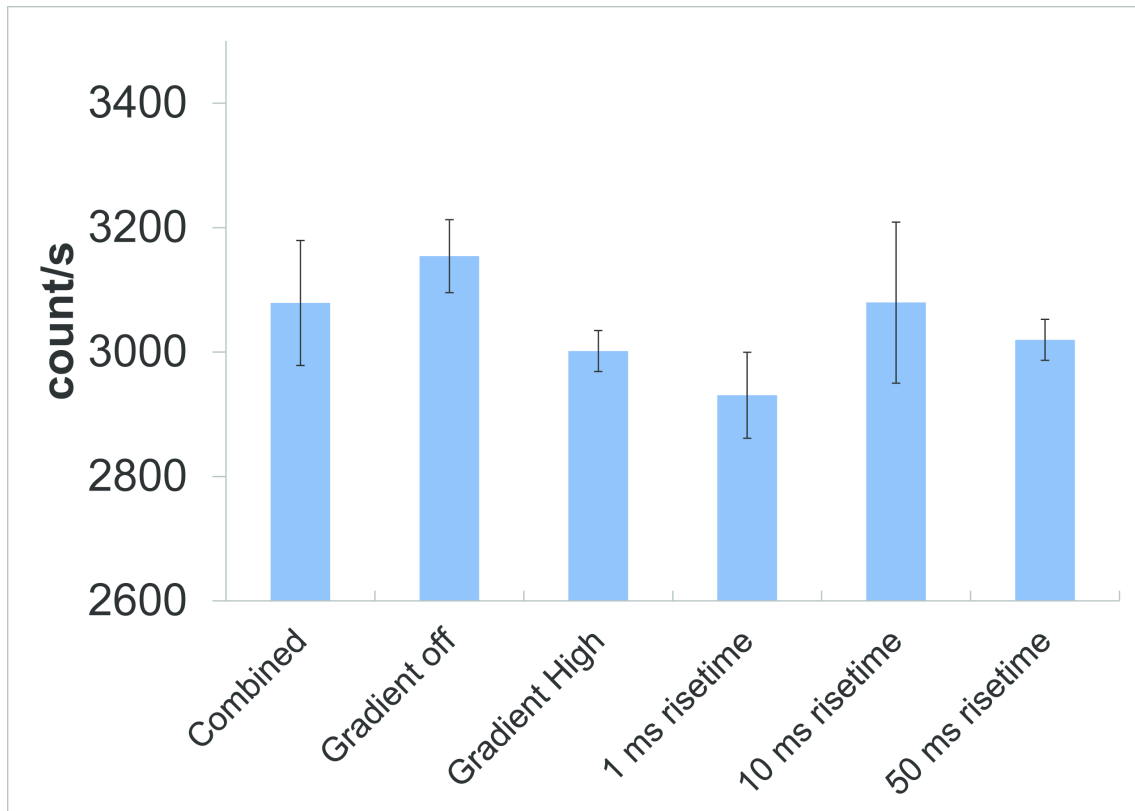


Figure 3.35: MRI gradient effects on count rates for the PET insert. Global coincident count rates for the PET insert under different gradient conditions are shown. No significant differences were observed. However, the presence of the gradient appears to attenuate the count rate slightly. Error bars are SD.

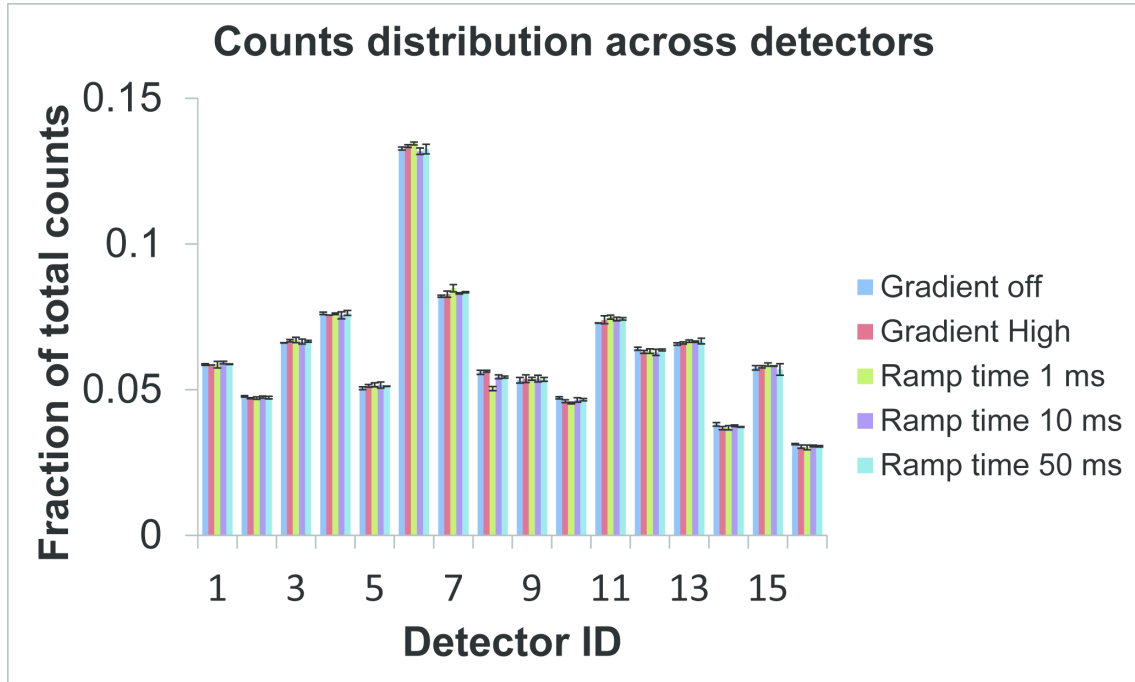


Figure 3.36: MRI gradient effects on count rates for individual detectors. Coincident counts measured from the PET insert were sorted to relevant detector pair (each count was thus counted twice) for each gradient pulsing condition. The count variation across multiple detectors is due to the different amplification gains of individual PSAPDs. The differences between different gradient conditions were generally small (<10%). The greatest count attenuation were observed during rapid risetimes (~1ms). This was most pronounced for detector 8. Error bars are SD.

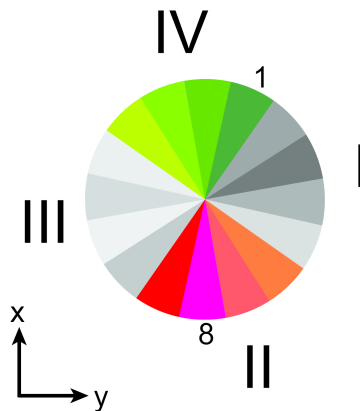


Figure 3.37: Orientation of PET detector modules in MRI. The PET insert was orientated within the MRI as shown for the gradient effect experiments. The axis shows the orientation of the x-y MRI gradients. The location of each detector (numbered clockwise in Arabic numerals and shown by slice wedges) is approximated by the wedges. The locations were split into for quadrants (numbered in Roman numerals and colored) for analysis.

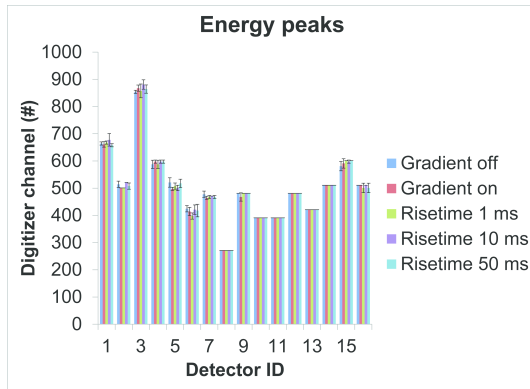
Table 3.11: Count rate differences across different gradient conditions for individual detectors. P-values from one-way ANOVA analysis across different gradient conditions are listed, with significantly different conditions (when applicable) from subsequent multiple comparison analyses.

Detector ID	<i>p-value</i> from ANOVA analysis	Descriptions of significantly different conditions
1	0.4	–
2	0.2	–
3	0.4	–
4	0.52	–
5	0.29	–
6	0.05	–
7	0.02	1 ms risetime was different to all others
8	<0.01	1 ms risetime was different to all others
9	0.9	–
10	0.01	1 ms risetime was different to all others
11	0.09	–
12	0.23	–
13	0.18	–
14	0.07	–
15	0.4	–
16	0.15	–

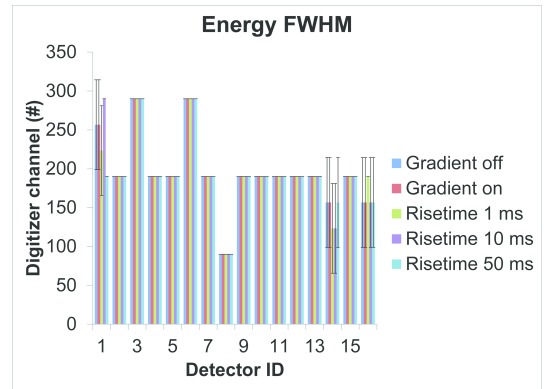
Energy spectra information at different gradient conditions for each detector are shown in figure 3.38. No significant differences for both the peak position and FWHM were observed between all conditions.

3.6.3 Discussion

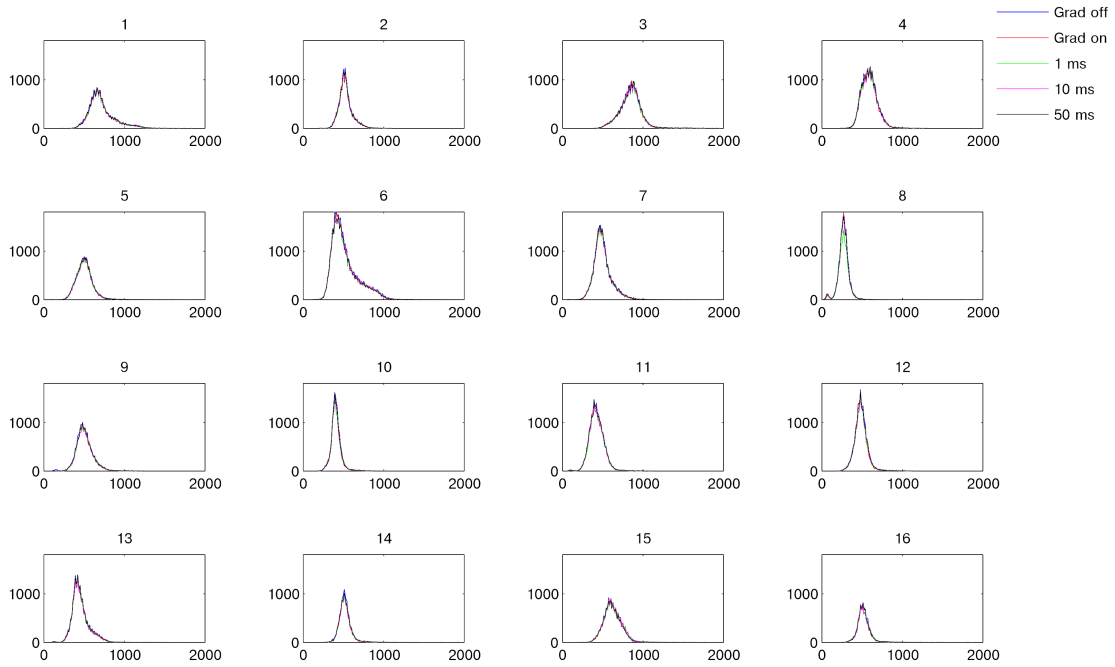
An important consideration in the design of hybrid imaging systems is the presence of interference effects that may hinder each individual imaging modality's performance. Previous studies showed a decrease in count event rates from the PET insert in the presence of running MR-pulse sequences (including gradient switching and RF pulsing) [106]. Further studies using a single PET detector



(a) Energy spectra, peaks, for different gradient conditions



(b) Energy spectra, FWHM, for different gradient conditions.



(c) Energy spectra, for different gradient conditions.

Figure 3.38: Energy spectra for different gradient conditions. Error bars are SD.

module inside the MRI highlighted the effects of gradient strength, switching rates and the location of the detector in relation to the MR gradients toward this decrease [142]. Here, we extended those observations by recording counts from different portions of the gradient waveform. This confirmed that the presence of the MR gradient, whether in a switching or on state, does cause a small but noticeable count attenuation of PET data. Further, increased gradient oscillations showed greater attenuation. These observations are consistent with the fact that greater count attenuation was seen for RARE compared to SE [106] and the fact that sequences with longer TR (lower gradient duty cycle) show less count attenuation.

The interference due to the gradient did not distort the energy spectra, suggesting that the mode of interference is not pure electrical noise. A possible cause for the interference is the presence of eddy currents [142, 211]. However, the exact mechanism of this effect remains unknown and requires further investigation.

Similar investigations with the X and Z gradients, as well as higher (>20%) and longer gradient on states were not pursued because of difficulties with the temperature control of the PET system in these situations. Amplification gains of PSAPDs are temperature dependent [212]. While the MRI and PET temperature controllers can maintain the system's temperature for regular pulse sequences, it is unable to maintain temperature stability for prolonged switching of the gradient. Future PET systems should be more stable [213] and allow further investigations of gradient effects. A corollary of this finding is that the gradient duty cycle for regular pulse sequences are usually low and thus results in a small loss of events.

The findings from this and other studies [211] suggest that strategies can be developed to correct for gradient interference effects. PET data acquired simultaneously with MRI can be gated to different portions of the pulse sequence corresponding to different gradient shapes. Data acquired in the presence of the gradient pulse can either be removed or corrected for count attenuation post acquisition.

RF effects on the PET system were not systematically studied. We observed that RF pulses can cause low energy noise, saturate PET electronics but not affect count rates (consistent with [211]). Prudent shielding and grounding of the cables connecting to the RF coil and leading out of the PET insert, along with proper energy thresholding of PET data eliminated virtually all RF interference

effects. These precautions were adopted for all studies described herein.

In summary, we found that PET count attenuation during pulse sequences is directly related to the presence of the MR gradient. Energy spectra are not degraded during gradient on states, suggesting that counts acquired during these periods do provide useful data provided they are corrected for attenuation effects.

3.7 PET/MRI Informatics Considerations

Multimodal imaging datasets are usually acquired sequentially and integrated posthoc manually. We describe the database and image file generation system that was used in all studies described herein. The system enables almost-automatic integration and processing of multimodal datasets. The setup allows facile analysis of multimodal imaging data individually or together.

3.7.1 Image Generation

MRI and PET images were reconstructed and processed using their native software. To facilitate storage and analysis, images were subsequently converted to the open source NIFTI-1 image format (<http://nifti.nimh.nih.gov/nifti-1>). Subject, timing and imaging parameter information are stored in either the filename or the header file.

3.7.2 Storage

Images are stored on a linux server. The following directory heirarchy is defined:

- Subject
 - Study day
 - * Study number
 - Type of study (PET/ DCE-MRI/ DWI/ MRI anatomical scans etc...)
 - Image files

A screenshot of this heirarchy is shown in figure 3.39.

3.7.3 Integration

The database heirarchy inherently allows different image files acquired from the same study to be linked. However, this information will be lost if images are transferred to another location separately. To account for this, we define a unique identifier that is stored in the NIFTI-1 extension header which permanently links multimodal files from the same study.

The unique identifier is defined by 3 aspects:

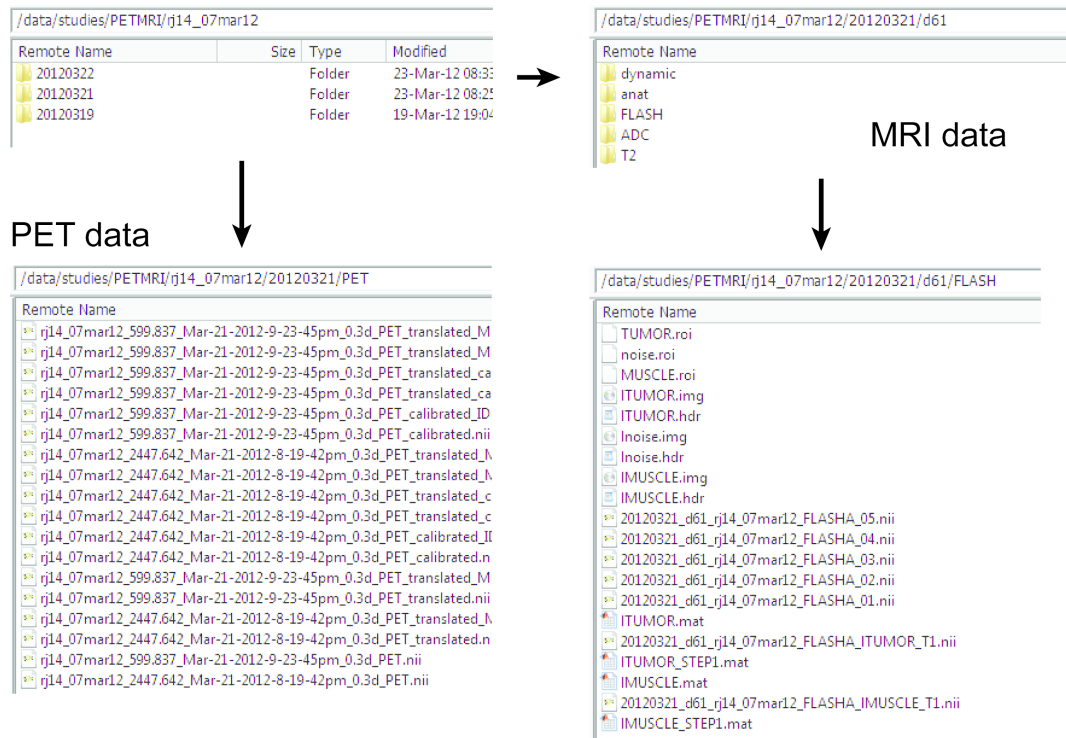


Figure 3.39: PET/MRI database setup. Individual image files (stored as NIFTI-1) are stored according to the subject, date and type of data. An example hierarchy for a typical PET/MRI study subject is shown here. The database is setup on a linux server and implemented using MATLAB.

1. The native modality, which heads the start of the identifier.
2. Associated modalities, which are listed following the native modality information.
3. The time of image acquisition. The timestamp is defined at image acquisition and encoded for all linked modalities during NIFTI-1 file generation.

Code to generate this unique identifier using MATLAB is shown in appendix E.

3.7.4 Discussion

Automatic databasing and integration of multimodal datasets provide several advantages. Firstly, human error during data processing is minimized. Secondly, the introduction of multimodal imaging in recent years is now reaching a stage where complete datasets are now beginning to be sufficiently complex, such that manual analyses are not feasible. Automatic databasing and integration is a step toward approaches that are now commonplace in bioinformatics. The current database setup enables the user to analyse simultaneous PET/MRI data easily in real-time, thus harnessing the advantages offered by the instrumentation. Alternatively, the database also allows the user to analyse large multimodal datasets easily post-acquisition, since the linkage information is already encoded in the hierarchical setup.

Although each imaging modality may have their own proprietary data format, we chose to adopt the open source NIFTI-1 format. The format can be read by a number of free image viewers. The image and header information are also stored as a single file, which is useful for storage and transfer.

A unique identifier to link multimodal images is a compromise between a fully external approach, whereby a spreadsheet is kept of all the data and an fully internal approach, where this spreadsheet is kept inside the image header. The identifier is space efficient and contains all the information that one needs to determine linkage between any two image datasets (type of modalities involved and timing information). The identifier can be stored within the headers of existing data formats and hence will not impede manipulation with current software. A simple plugin can be developed on any software platform to read this identifier and link image datasets together during post-hoc analysis.

In summary, we developed a database system to enable facile processing and integration of

multimodal datasets. This facilitates the analysis of multi-subject, longitudinal imaging studies that are being pursued with the PET/MRI system.

Chapter 4

Serial Diffusion MRI to Monitor and Model Early Treatment Response to the Targeted Nanotherapy CRLX101

4.1 Abstract

4.1.1 Purpose

Targeted cancer nanotherapies are being developed to enhance local tumor therapeutic response. The nanotherapy CRLX101 (formerly IT-101), has been shown to be effective in preclinical models and is currently in clinical trials. We evaluated the efficacy of diffusion-weighted magnetic resonance imaging (diffusion MRI) to monitor early response of CRLX101 and to evaluate its potential as a therapeutic response predictor using a mechanistic model of tumor cell proliferation.

4.1.2 Experimental design

Diffusion MRI was serially performed following CRLX101 administration in a murine lymphoma model. Apparent diffusion coefficients (ADC) were extracted from the data and used as a treatment response biomarker. Animals treated with irinotecan (CPT-11) and saline were imaged for comparison. ADC data were input into a mathematical model of tumor growth to evaluate its ability

This section is being prepared for publication: Thomas S.C. Ng, David Wert, Hargun Sohi, Daniel Procissi, David Colcher, Andrew A. Raubitschek, Russell E. Jacobs. (2012) Serial diffusion MRI to monitor and model early treatment response to the targeted nanotherapy CRLX101.

Acknowledgments: We thank Dr. Thomas Schlupe of Calando Pharmaceuticals for providing the CRLX101 (formerly IT-101), Dr. Andrey Demyanenko, Desiree Crow, Bita Alaghebandan, and Sonia Collazo for their technical assistance. Drs. Mark Davis, Yun Yen and Scott Fraser gave helpful advice and support. The project was funded by NIBIB R01 EB000993, NIH R01 EB00194, NRSA T32GM07616, City of Hope Lymphoma SPORE Grant (P50 CA107399), the Beckman Institute and the Caltech/City of Hope Biomedical Initiative.

to predict therapeutic response. Histological analysis using cleaved-caspase 3, TUNEL, Ki-67 and H&E were conducted on tumor samples for correlation with imaging results.

4.1.3 Results

Mean ADC changes for CRLX101 treated tumors at day 2, 4 and 7 post-treatment were $16 \pm 9\%$, $24 \pm 10\%$ and $49 \pm 17\%$ respectively, which were statistically greater than the controls ($p \leq 0.02$) and noticeably greater than CPT-11 treated tumors ($5 \pm 5\%$, $14 \pm 7\%$ and $18 \pm 6\%$). Model-derived parameters for cell proliferation obtained using ADC data distinguished CRLX101 treated tumors from controls.

4.1.4 Conclusions

Temporal changes in the functional imaging biomarker, ADC, specified early CRLX101 treatment response and could be used to model image-derived cell proliferation rates following treatment. Comparisons of different treatments (targeted and non-targeted) highlight the utility of noninvasive imaging and modeling to evaluate, monitor and predict responses to targeted nanotherapeutics.

4.2 Translational Relevance

Targeted nanotherapies are being developed for cancer treatment. The advantage of these therapies over conventional treatments lies in their ability to increase drug uptake in tumors while reducing treatment-related toxicity. The availability of clinically applicable biomarkers will facilitate the clinical translation of nanotherapies. We evaluated the applicability of diffusion MRI to monitor CRLX101 (a cyclodextrin-based polymer particle containing the DNA topoisomerase I inhibitor camptothecin) efficacy in a preclinical model of malignant lymphoma. Diffusion MRI distinguished animals treated with CRLX101 from controls as early as day 2 after treatment. Diffusion MRI also demonstrated the reduced efficacy of irinotecan compared to CRLX101. Incorporating diffusion MRI data into a mathematical model of tumor growth allowed prediction of the enhanced antiproliferative effect of CRLX101 as compared to the non-targeted agent. These results demonstrate that serial imaging using diffusion MRI, combined with judicious modeling of imaging data, provides useful biomarkers to evaluate, monitor and predict the efficacy of targeted nanotherapies in

the clinic.

4.3 Introduction

Targeted cancer nanotherapies are increasingly being explored as alternatives to conventional therapeutics. They have the potential to increase treatment efficacy and reduce treatment-related toxicity (TRT) through improved tumor drug delivery [22]. Compared to conventional therapies, nanoscale therapeutics show increased plasma half-life and can localize to the tumor mass via targeting mechanisms such as enhanced permeability and retention (EPR) [21, 214]. Recently, the EPR effect has been coupled with surface functionalization of particles [31] to improve retention in the tumor and target specific tumor cell subsets. Moreover, evidence exists that nanotherapies can also escape multidrug resistance pathways since their mode of cellular uptake can bypass P-glycoprotein efflux pumps that cause resistance to conventional drugs [214].

Nanotherapies may prove to be useful for the treatment of malignant lymphoma. Despite great advances in lymphoma management, over half of the patient population diagnosed with aggressive non-Hodgkin lymphoma, 30%–40% with advanced Hodgkin's lymphoma, and many with indolent lymphoma still develop resistance or relapse of the disease [215, 216, 217]. Several strategies, including the single or combined application of multi-drug chemotherapy, immunotherapy and radiation-based therapies, are currently being explored as salvage regimens [216, 217]. Important considerations during the treatment selection process include the need to minimize TRT to the patient as well as the need to avoid cross-resistance from first-line regimens [218, 217]. Thus, the use of targeted nanotherapies offers an interesting therapeutic alternative.

The nanoparticle CRLX101 (formerly IT-101, Cerulean Pharma Inc.) is a conjugate of a β -cyclodextrin-based polymer and 20(S)-camptothecin (CPT). CPT is a topoisomerase I inhibitor with a broad activity spectrum. CRLX101 increases the solubility of CPT, keeps CPT in its active lactone form, improves CPT tumor localization and minimizes CPT-associated TRT [24, 19]. Preclinical *in vivo* studies of CRLX101 demonstrated its efficacy in a broad range of solid tumors [217, 17], including subcutaneous and disseminated xenograft lymphoma models [217]. CRLX101 is currently in phase I and phase II trials for a variety of solid tumors [219].

A major challenge for clinical translation of cancer nanotherapies is the effective evaluation of

treatment response. Imaging technologies have been used to monitor responses to conventional therapy [220]. Typical methods rely on changes in tumor size [11, 221]. Morphological imaging using computerized tomography (CT), ultrasound and anatomical magnetic resonance imaging (MRI) can assess changes in the appearance or growth of tumor masses. However, such changes often occur at least several weeks after treatment, which may delay useful modifications of the treatment course. A functional imaging technique, diffusion MRI [222], is being investigated to evaluate therapeutic responses in animal models [223, 224] and human clinical studies [156, 225]. A quantitative metric derived from these studies, the apparent diffusion coefficient (ADC), has been shown to be sensitive to tumor therapy response. Although the diffusion of water within tumors is mediated by many complex processes, ADC has been demonstrated to be related to tumor cellularity and extracellular volume [226]. Increased ADC values over the course of a treatment time course are correlated with tumor treatment response to small molecule chemotherapy [223, 224], adoptive immunotherapy [227] and photodynamic therapy [33].

Mathematical models of cancer growth have been shown to predict tumor treatment response on an individual basis. Modeling adds an extra dimension to clinical management by enabling prospective, patient-specific adjustments of treatment regimens [228, 229]. noninvasive imaging data have been applied successfully to models of tumor growth and treatment response in brain [230, 132, 231, 232] and kidney [233] tumors. These studies demonstrate that incorporation of imaging data into mathematical models of tumor growth can provide insights at the cellular scale that may elude conventional measures of tumor progression, such as the RECIST criteria [234]. Furthermore, since the efficacy of nanotherapies is a complex function of the drug payload and the carrier's interaction with the tumor microenvironment [124], image-based modeling of treatment response may also provide mechanistic insights into the functioning of nanotherapies *in vivo*.

The purpose of this study is to determine the feasibility of diffusion MRI to evaluate and predict early treatment efficacy of the nanotherapy CRLX101. Using a preclinical model of Burkitt's lymphoma, we compared the diffusion MRI response of low dose CRLX101 to a high dose administration of a water-soluble CPT analog, irinotecan (CPT-11), and to controls. Further, serial diffusion MRI data were incorporated into a mathematical model of tumor cell proliferation to evaluate its ability to highlight and predict the antiproliferative activity of CRLX101 *in vivo*.

4.4 Materials and Methods

4.4.1 Cell Culture, Animal Model, and Human Lymphoma Xenograft Models

Daudi cells (human Burkitt's lymphoma line) were obtained from the American Type Culture Collection. Cells were maintained in sterile culture media as previously described [235]. Six to eight week old female athymic nu/nu mice (Charles River) were injected with 0.2 mL of 1:1: mixture of tumor cell suspension in 1% human serum albumin in HBSS (Mediatech) and Matrigel (BD Biosciences) subcutaneously into their right groin region. Approximately 3×10^6 cells were injected for each mouse. Mouse care and experimental procedures were carried out in accordance with protocols approved by the Research Animal Care Committee at the City of Hope and the Animal Care and Use Committee at Caltech.

4.4.2 *In Vivo* MRI Studies

A Biospec (Bruker-Biospin Inc. Billerica, MA) 7 T MRI scanner and a home-built birdcage coil with an 8 cm axial field of view (FOV) were used for mouse MRI image acquisition. For all imaging sessions, animals were anesthetized using 1.3%–1.75% isoflurane and body temperature was maintained at 36°C–37°C with warmed air flowing through the bore. For anatomical imaging, a rapid acquisition with relaxation enhancement (RARE) MRI sequence (TR/TE = 4000/23 ms; RARE factor, 4; number of averages, 2; FOV, 35.4×35.4 mm²; image matrix, 128×128 ; slice thickness, 0.754 mm) was used to collect 40 contiguous images across the mouse torso, allowing tumor visualization.

For diffusion MRI, treatment and therapy monitoring began approximately 21 days post xenograft inoculation, when tumors reached the size of 300–800 mm³. Tumor sizes were determined from region of interests (ROI) drawn from anatomical MRI images. On the day of treatment, mice were either injected with: a) 0.9% saline intravenously (i.v.), b) 100mg/kg CPT-11 intraperitoneally (i.p.) or c) 5mg/kg CRLX101 (i.v.). Anatomical and diffusion MRI scans were acquired immediately before treatment (day 0, baseline), 2, 4 and 7 days posttreatment. A total of 19 mice were imaged for this study. Both CRLX101 and control groups contained 7 mice. Within those treatment groups, N = 3 were imaged on days 0, 2 and 4 and N = 4 were imaged on days 0, 2, 4 and 7. All mice in the

CPT-11 group (N = 5) were imaged on days 0, 2, 4 and 7.

Diffusion MRI was acquired with a spin-echo diffusion MRI sequence [69] (TR/TE = 3000/25 ms ; $\Delta = 15$ ms, $\delta = 3$ ms, with three b values = 0, 800, and 1,200 s/mm² acquired in 3 orthogonal directions; FOV, 35 × 25 mm²; image matrix, 175 × 125 (zero filled to 256 × 125 ; slice thickness, 0.754 mm). The number of slices acquired in each study was determined by the tumor size to ensure full coverage of the tumor mass.

ADC tumor maps were generated using these trace diffusion images by fitting to the Stejskal-Tanner equation [68] using MATLAB. The S_0 images derived from this analysis were used as templates to segment the tumor region. Segmentation was done manually using MRIcro (<http://www.mricro.com>).

4.4.3 Modeling Tumor Growth Using Diffusion MRI

A simplified logistic model of tumor growth, developed by Atuegwu *et al.* [230], was applied to the dynamic diffusion MRI data in order to estimate tumor cell proliferation rates and tumor cell numbers. Since it was not possible to spatially coregister tumor images from multiple time points on a voxel-by-voxel basis, we only considered ROIs based on the whole tumor. Briefly, the model is defined by

$$N(t) = \frac{\vartheta N(t_1)}{N(t_1) + (\vartheta - N(t_1))e^{-kt}}, \quad (4.1)$$

where $N(t)$ is the number of cells per tumor voxel at time t , $N(t_1)$ is the number of cells present at $t = t_1$, the first time point in the calculation. k is the cell proliferative rate and ϑ the cell carrying capacity in the population, here assumed to be the maximum number of cells in the imaging voxel. If a linear relationship between ADC and cellularity is assumed, ADC can be related to cell number by

$$\frac{ADC(t) - ADC_w}{ADC_{min} - ADC_w} = \left(\frac{N(t_1)}{\vartheta} \right), \quad (4.2)$$

and derive k and $N(t)$ by combining (4.1) and (4.2) [229]:

$$\frac{ADC(t) - ADC_w}{ADC_{min} - ADC_w} = \left(\frac{ADC(t_1) - ADC_{min}}{ADC(t_1) - ADC_w} \right) e^{-kt}. \quad (4.3)$$

ADC_w is the ADC of free water ($\sim 3 \times 10^{-3} \text{ mm}^2/\text{s}$) [236] and ADC_{min} is the minimum voxel ADC value in a given tumor.

The ability of the model to calculate tumor growth was tested by calculating $N_{calculated}(4)$ and $N_{calculated}(7)$, which were calculated with k values derived from day 0/2 and day 2/4 ADC data respectively using equation 6. These were compared to $N_{estimated}(4)$ and $N_{estimated}(7)$, which were measured from actual ADC data taken on day 4 and 7 and calculated using equation 5.

The cellular proliferation rate k using a combination of ADC data from different time points (day 0/2, 0/4, 2/4, 4/7) were also calculated for each individual.

4.4.4 Histological Assessment

A separate group of animals with Daudi lymphoma tumors were prepared for histological comparison with noninvasive imaging (N = 24). Animals were divided into control, CPT-11 and CRLX101 groups. The animals were treated identically as those in the imaging studies. At days 0, 2, 4 and 7, animals (N = 2 per time point) from each treatment group were sacrificed by transcardiac perfusion and tumors were excised. Tumors were placed in 4% paraformaldehyde overnight, dehydrated in 70% ethanol and subsequently embedded in paraffin. Paraffin blocks were sectioned at a slice thickness of 4 μm .

Paraffin sections were deparaffinized in xylene and rehydrated through a descending gradient of alcohol (100%, 95%, 80%, 2 minutes at each concentration) and then water.

Antigen retrieval was achieved with 10mM Tris, 1mM EDTA, 0.05% Tween 20 pH9.0 for 20 minutes in a steamer and then cooled for 20 minutes. Individual sections from each treatment cohort and time point were then incubated with primary antibodies to the cellular proliferation marker Ki-67 (1:200, Neomarkers, RM-9106-SO) or the apoptotic marker cleaved caspase-3 (1:500, Invitrogen, 700182). Immunohistochemistry was performed on a DAKO Autostainer utilizing a peroxidase DAB method (Leica, Novalink RE7150-K) followed by counterstaining with hematoxylin.

Staining for apoptosis was performed using a terminal nucleotidyl transferase-mediated nick end labeling (TUNEL) assay (Roche, In situ Cell Death Detection Kit) and visualized with a peroxidase DAB method (Leica, Novalink), followed by counterstaining with hematoxylin. Corresponding sections were also stained with H&E for overall tumor and cellular morphology.

All slides were scanned on a Ventana Coreo slide scanner for visualization.

4.4.5 Statistical Analysis

Comparison of ADC, tumor size and cell proliferation data among the three treatment groups was accomplished at each time point using a non-parametric Kruskal-Wallis test. Multiple comparison tests were performed with Bonferroni correction after a Mann-Whitney test. $N(t)$ data were compared using Pearson's (PCC) and concordance (CCC) correlation coefficients. A p -value of 0.05 or smaller was considered to be statistically significant.

4.5 Results

4.5.1 Diffusion MRI is Sensitive to Early CRLX101 Treatment Response

Diffusion MRI was used to quantify the temporal response of the lymphoma microenvironment to CRLX101, CPT-11, and control treatments in animals implanted with Daudi tumors. ADC maps of representative tumor response to the various treatment groups are shown in figure 4.1. According to figure 4.1, ADC values remain relatively constant for the control animal (top row) over the course of 7 days, with most of the tumor volume having relatively low ADC values (green) at each time point. A small pocket of high ADC can be seen by day 7, possibly due to spontaneous necrosis as a result of increasing tumor size. The CPT-11 treated animal (bottom row) showed a similar ADC map pattern throughout most of the tumor, with low ADC values over a substantial part of the tumor volume across all time points. On day 2 after CPT-11 administration, clusters of high ADC values (as indicated by red to orange pixels) can be seen around the edges of the tumor, suggesting CPT-11 response. By day 4 and day 7, small high ADC clusters still existed, but appeared to approximately the same as were seen on day 2. The ADC map patterning remained similar between day 4 and day 7. Compared to the two other treatment cohorts, the CRLX101 treated tumor (middle row) showed a steady increase in the ADC value throughout the whole tumor bulk. By day 2 posttreatment, the whole tumor volume showed an increase in ADC. This trend continued onto day 4 and day 7. These findings were also observed when visualized with one-dimensional histograms of ADC tumor voxel distributions (figure 4.2).

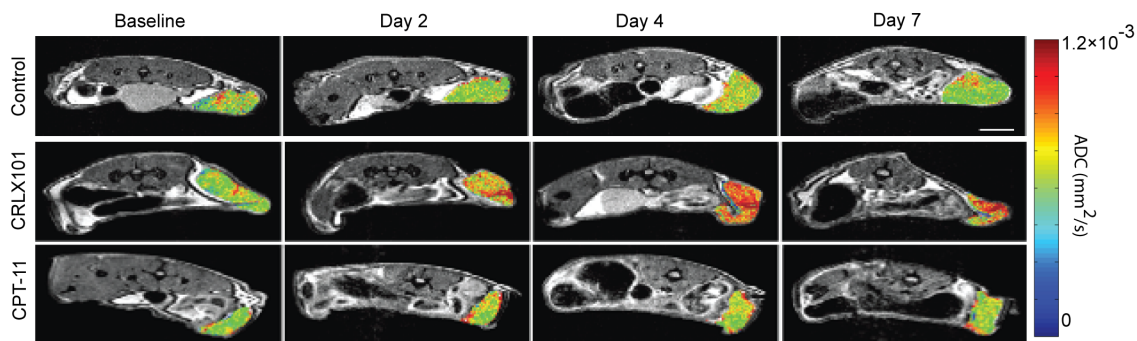


Figure 4.1: Diffusion MRI is sensitive to early CRLX101 response. Representative ADC map of Daudi tumors are shown as color overlays on T_2 -weighted anatomic MRI images. Diffusion MRI images were acquired on day 0 (pretreatment), day 2, day 4 and day 7 for control (top row), CRLX101 treated (middle row) and CPT-11 treated (bottom row). Diffusion MRI clearly shows an increased ADC response to CRLX101 throughout the whole tumor mass as early as day 2 posttreatment, compared to CPT-11 treated and control animals (scale bar = 10 mm).

To compare the diffusion MRI response between treatment groups, the mean percentage change of ADC values from baseline were calculated and graphed in figure 4.3. CRLX101 treated tumors clearly exhibited increasing tumor ADC values over the course of 7 days compared to baseline ($16 \pm 9\%$, $24 \pm 10\%$ and $49 \pm 17\%$ change from baseline on day 2, 4 and 7, respectively). CPT-11 treated tumors also showed a mean increase in ADC values over the week ($5 \pm 5\%$, $14 \pm 7\%$ and $18 \pm 6\%$), while control tumors showed a slight decrease in ADC value compared to baseline ($-4 \pm 3\%$, $-7 \pm 3\%$ and $-9 \pm 3\%$). Compared to the control group, the increases observed in the CRLX101 group were significant on all days (day 2: $p = 0.02$, day 4: $p < 0.01$, day 7: $p < 0.01$). This was not the case for the CPT-11 group (day 2: $p = 0.4$, day 4: $p = 0.05$, day 7: $p = 0.05$).

4.5.2 Diffusion MRI Response Correlates with Traditional Measurements of Tumor Growth

Drug efficacy is typically measured by analyzing tumor volumetric changes over time. Tumor volume information was obtained from MRI scans concurrent with diffusion MRI studies. Volume changes as sorted by treatment cohort are shown in figure 4.4. Control tumors steadily increased in size during the week time course ($25 \pm 17\%$, $49 \pm 15\%$ and $130 \pm 44\%$ change from baseline on day 2, 4 and 7, respectively), while CRLX101 treated tumors steadily decreased in size ($-5 \pm 3\%$, $-30 \pm 4\%$ and $-45 \pm 13\%$). As with the ADC values, size decrease in the CPT-11 treated group was less

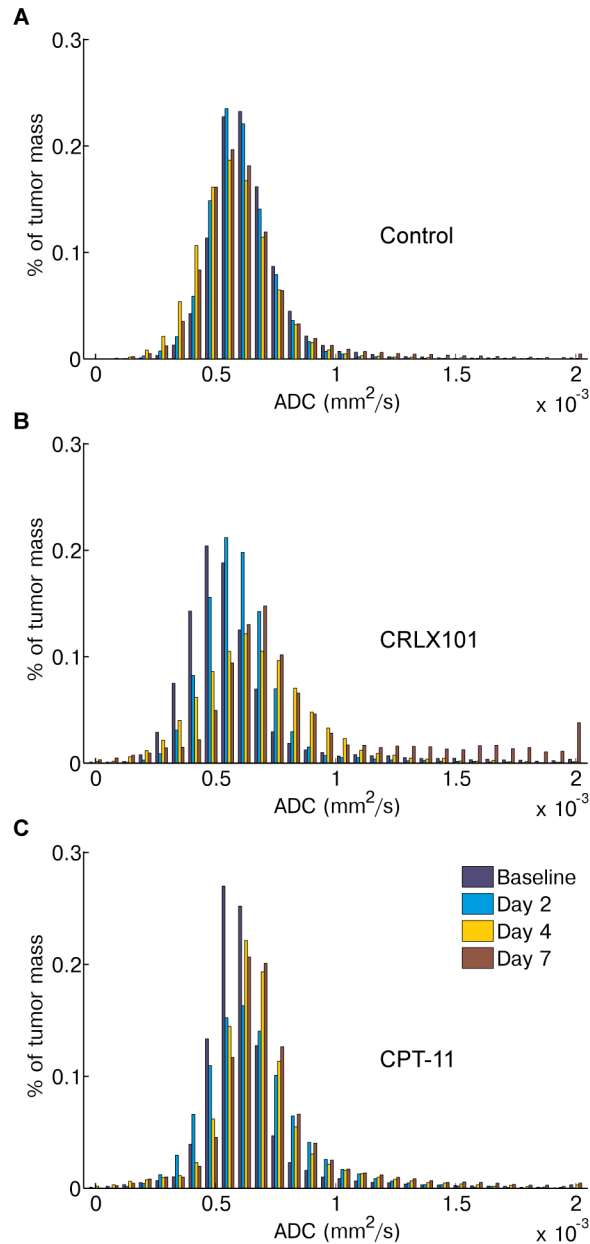


Figure 4.2: Histogram analysis of diffusion MRI. One dimensional histogram of ADC values from animals treated with (A) saline, (B) CRLX101 and (C) CPT-11 over the course of 1 week are shown. In a control animal (A), the distribution of ADC values within the tumor remained relatively stable over the course of the week. In a CRLX101 treated animal (B), a gradual right shift of the ADC value distribution toward higher values can be observed as early as day 2 and continuing onto day 4 and 7. In the CPT-11 treated animal, the ADC distribution showed a slight right shift toward higher values by day 4. However, the magnitude of this shift was less than that of observed in (B). The day 7 distribution remained similar to the day 4 histogram. These observations are consistent with the MR images (figure 4.1), and highlight the efficacy of CRLX101.

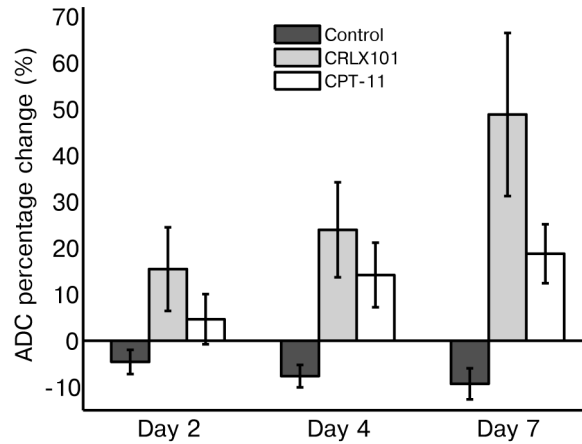


Figure 4.3: ADC changes over treatment week show efficacy of CRLX101. Percentage change of mean ADC values compared to baseline is graphed for the three different treatment groups over one week posttreatment. Plots show a significant increase in ADC for CRLX101 treated animals compared to CPT-11 and control ($p < 0.001$). CPT-11 animals showed a slight increase ($p \geq 0.05$) in the ADC values over the week compared to baseline, while control animals showed a slight decrease. CRLX101 treated animals showed an increase in ADC values at all time points, which was significant on day 2 ($p = 0.02$), day 4 ($p < 0.01$) and day 7 ($p < 0.01$). Error bars denote standard error.

drastic ($-15 \pm 5\%$, $-22 \pm 13\%$ and $-26 \pm 8\%$) compared to the nanoparticle-treated group. The tumor size decreases in the CRLX101 treated group were not significantly different to control on day 2 ($p = 0.08$), but were significant by days 4 and 7 (both $p < 0.01$). In comparison, CPT-11 group tumor size changes were only significantly different to the control group on day 4 ($p < 0.01$).

4.5.3 Logistic Model of Tumor Growth can be Applied to Diffusion MRI of Malignant Lymphoma

Tumor cell number determined by incorporating diffusion MRI data into a model of tumor growth is shown in figure 4.5. $N_{calculated}$ compared to $N_{estimated}$ for days 4 and 7 are shown in figures 4.5A and 4.5B respectively. The PCC between $N_{calculated}(4)$ and $N_{estimated}(4)$ is 0.92 ($p < 0.0001$). The CCC is 0.83. PCC and CCC between $N_{calculated}(7)$ and $N_{estimated}(7)$ are 0.91 ($p < 0.0001$) and 0.9. These values demonstrate a strong relationship between the simulated and estimated data, demonstrating that the logistic model is applicable to this lymphoma model.

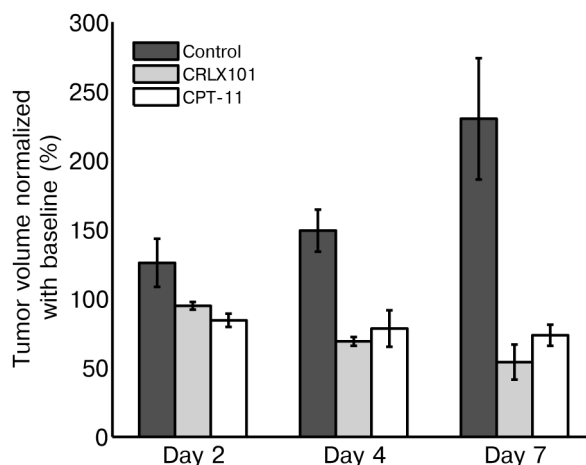


Figure 4.4: Tumor volume size changes over treatment week. Mean tumor sizes, as measured from anatomical MRI images, are graphed for the three different treatment groups over one week posttreatment. CRLX101 treated tumors decreased significantly compared to control tumors over 7 days ($p < 0.001$) and significantly different to CPT-11 tumors on day 7 ($p = 0.01$). Compared to baseline, CRLX101 tumor sizes significantly decreased on both day 4 and 7 ($p < 0.01$). Error bars denote standard error.

4.5.4 Modeling of Tumor Proliferation using Diffusion MRI show Antiproliferative Activity of CRLX101

Model-derived mean cell proliferation rates (in units of 1/day) measured from different time points across treatment groups are shown in figure 4.6. Corresponding boxplots are shown in figure 4.7. CRLX101 treated animals showed negative tumor proliferation rates across all time points (-0.09 ± 0.05 , -0.05 ± 0.03 , -0.05 ± 0.01 and -0.11 ± 0.05 for day 0/2, 0/4, 2/4 and 4/7 respectively) and were significantly different ($p = 0.02$) to control tumors (0.03 ± 0.02 , 0.02 ± 0.01 , 0.02 ± 0.02 and 0.04 ± 0.04). CPT-11 animals (-0.04 ± 0.04 , -0.02 ± 0.02 , -0.06 ± 0.02 and 0.01 ± 0.01) showed negative proliferation rates between day 0 and day 4. These were significantly different to controls for rates calculated between day 2/4 ($p = 0.03$). Interestingly, proliferative rates in CPT-11 tumors calculated between day 4 and 7 became positive.

4.5.5 Histological Assessment of CRLX101 Response

Treatment-induced changes observed by diffusion MRI were correlated with histological observations of tumor response. Tumor sections were stained for activated (cleaved) caspase-3 to moni-

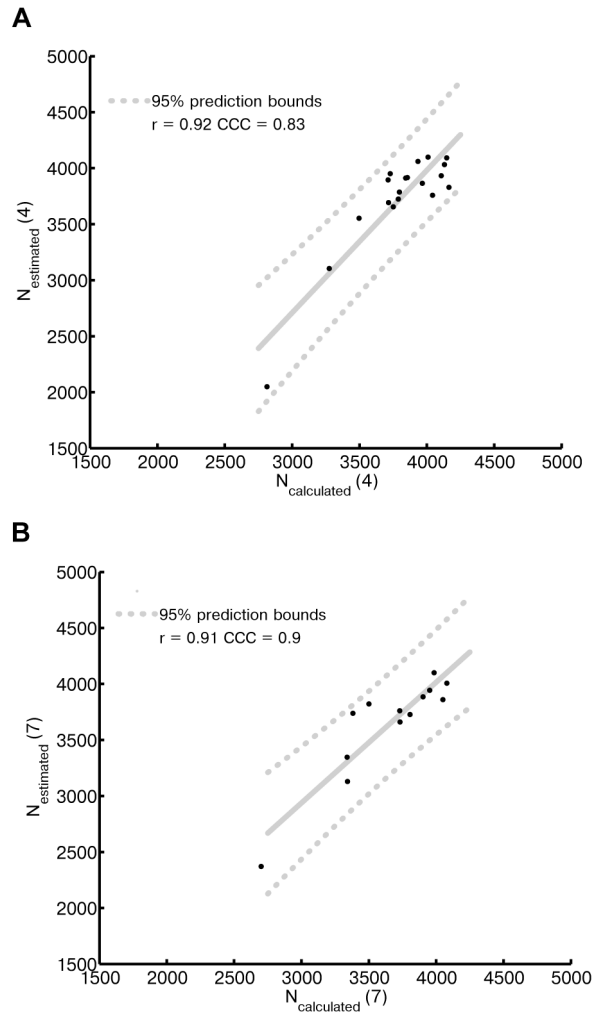


Figure 4.5: A logistic model of tumor growth can be applied to ADC data. (A) $N_{calculated}(4)$ (using ADC data from day 0 and day 2) is compared to $N_{estimated}(4)$. The linear fit (with 95% prediction intervals) is also plotted. The Pearson's correlation coefficient, r , is 0.92 ($p = 0.0001$) and the concordance correlation coefficient, CCC, is 0.83. (B) $N_{calculated}(7)$ (using ADC data from day 2 and day 4) is compared to $N_{estimated}(7)$. $r = 0.91$ ($p = 0.0001$) and CCC = 0.9.

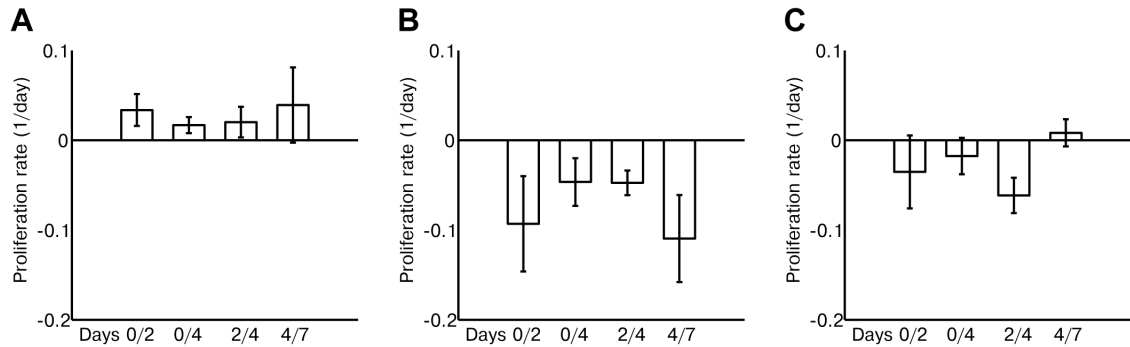


Figure 4.6: Cellular proliferation rates for different treatment groups were calculated by applying ADC data to a logistic model of tumor growth. Rates were calculated for (A) control, (B) CRLX101 and (C) CPT-11 animals between day 0/2, day 0/4, day 2/4, and day 4/7. Rates from CRLX101 animals were negative for all time periods and were significantly different to controls ($p = 0.02$). Rates for CPT-11 animals were negative between day 0 to day 4, being significantly different to controls between day 2/4 ($p = 0.03$). By day 4/7, CPT-11 proliferation rates became positive and similar to controls. Error bars denote standard error.

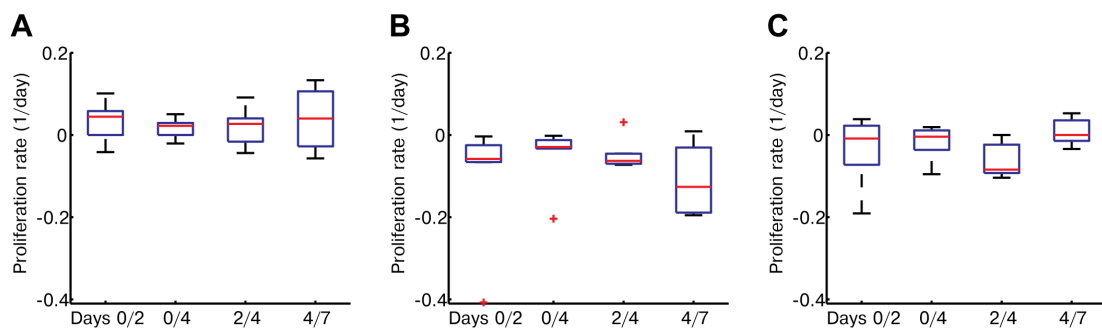


Figure 4.7: Boxplots of cellular proliferation rates for different treatment groups calculated by applying ADC data to a logistic model of tumor growth. Boxplots for (A) control, (B) CRLX101 and (C) CPT-11 animals between day 0/2, day 0/4, day 2/4, and day 4/7 are shown.

tor apoptotic activity (figure 4.8A). Control tumors showed minimal staining for active caspase-3 throughout the week. In comparison, CRLX101 treated tumors showed a dramatic increase in caspase-3 activation on day 2. Levels remained increased compared to time-matched control tumors on day 4 and day 7, albeit lower than day 2 cleaved caspase-3 levels. CPT-11 treated animals also showed a noticeable increase in active caspase-3 levels compared to control tumors on day 2. CPT-11 active caspase-3 levels were indistinguishable to time matched controls by day 4 and day 7. Analysis using a TUNEL assay (figure 4.8B) to stain for apoptotic cells by detecting 3' DNA strand breaks (a biochemical hallmark of apoptosis) showed similar results. CRLX101 treated tumors showed an increase in apoptotic cells by day 2 of treatment, which persisted on day 4 and day 7. CPT-11 treated tumors did not show a noticeable increase in apoptotic cells on day 2 post-treatment, but a number of apoptotic cells were observed on day 4 and day 7. By comparison, control tumors did not show an increase in apoptotic cell staining throughout the week.

Since the active ingredient of CRLX101 and CPT-11, camptothecin, inhibits cellular proliferation, we also stained tumors using the cellular proliferation marker Ki-67 (figure 4.8C). Control tumors maintained high Ki-67 expression throughout the week. By comparison, both CRLX101 and CPT-11 treated tumors showed decreased Ki-67 staining by day 2 of treatment. Ki-67 expression in CRLX101 tumors decreased steadily throughout the week, while Ki-67 expression in CPT-11 treated tumors on day 4 remained similar to day 2 and were comparable to baseline by day 7.

H&E-stained sections from the control group showed a dense cellular pattern that remained consistent from baseline to day 7 (figure 4.8D). By comparison, CRLX101 tumors showed a gradual decrease in cellular density over 7 days. An increase in the number of amorphous cells can be observed in day 4 and day 7 tumors. CPT-11 tumor sections show a slight decrease in cellular density on day 2. By day 4 and day 7, the cellular patterns have reverted to baseline patterning. These cell density pattern differences between treatment groups were also seen on the other hematoxylin-stained sections (figure 4.8A–C).

4.6 Discussion

In the current study, diffusion MRI was used to follow the response of a preclinical model of malignant lymphoma to a targeted nanotherapy (CRLX101) and its small molecule chemotherapy coun-

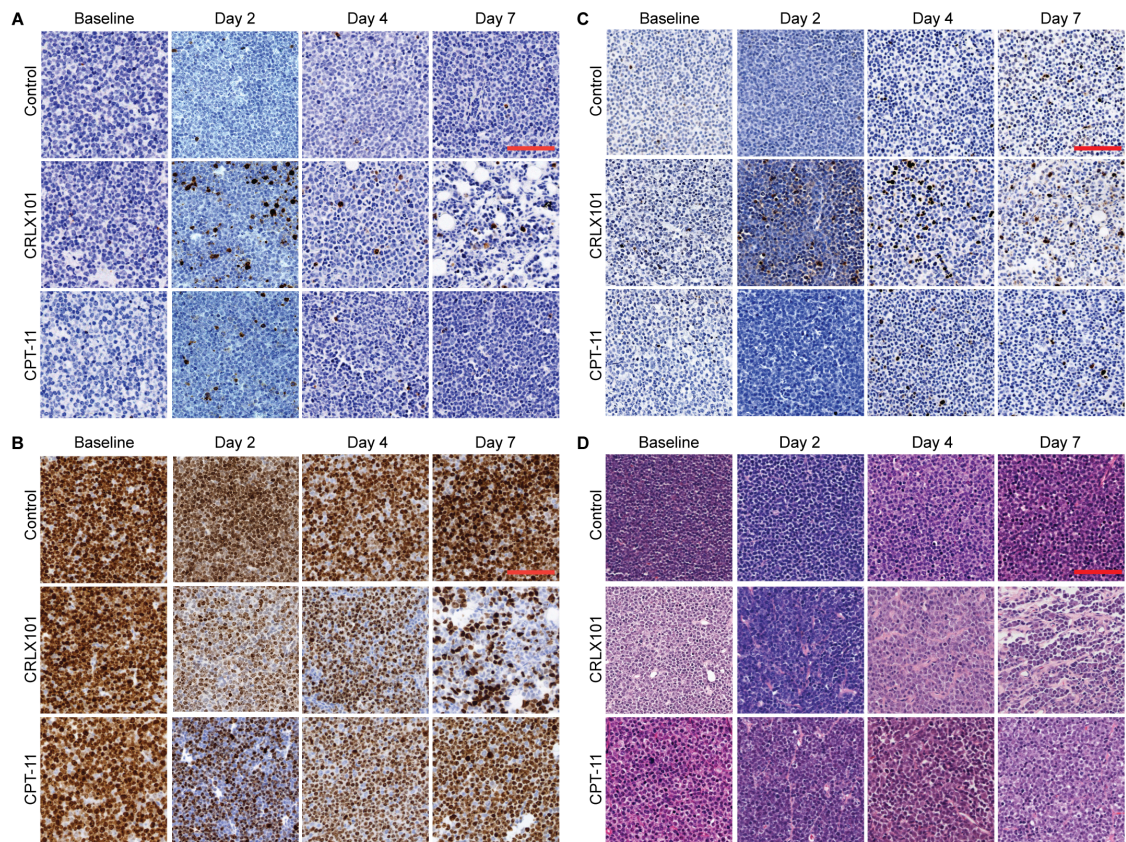


Figure 4.8: Histological assessment of CRLX101 and CPT-11 response. Tumors treated with CRLX101 (5 mg/kg), CPT-11 (100 mg/kg) or saline were harvested for histology on days 0, 2, 4, and 7. Tumor samples were subsequently sectioned and stained with (A) Cleaved caspase-3 (costained with hematoxylin), (B) TUNEL (costained with hematoxylin), (C) Ki-67 (costained with hematoxylin) and (D) H&E (scale bar = 500 μ m).

terpart (CPT-11). As shown in figures 4.1 and 4.3, CRLX101 treatment led to quantifiable changes in ADC as early as day 2. By comparison, CPT-11 treatment also resulted in detectable changes in ADC, but was attenuated compared to the CRLX101 treatment. This correlated with tumor growth kinetics, which indicated that CRLX101 treatment resulted in marked tumor regression while only mild regression was seen with CPT-11 treatment (figure 4.4). Moreover, diffusion MRI results correlated with histology. CRLX101 and CPT-11 treated tumors showed increased apoptotic events by day 2. Decreased cellularity was observed in both treatment cohorts compared to controls across the week. A decrease in the proliferation marker Ki-67 was also observed in both treatment cohorts. This reflects the fact that CPT inhibits cell proliferation and is concordant with previous studies showing high topoisomerase I inhibition by CRLX101 and CPT-11 within 48 hours of administration [217]. Taken together, these results confirm the improved efficacy of CRLX101 compared to small molecule chemotherapy. Furthermore, diffusion MRI was able to demonstrate this improved efficacy at an early time point.

Other functional imaging techniques are being investigated to monitor early responses in lymphoma [221]. Many of these studies involve nuclear imaging, specifically PET. In particular, ^{18}F -fluoro-2-deoxy-d-glucose (FDG-PET) [13, 237, 238] and $3'$ - ^{18}F -fluoro- $3'$ -deoxy-L-thymidine [239, 240, 107] are promising imaging biomarkers of lymphoma response. Interpretation of nuclear imaging studies can be complex, as many different physiological processes can result in a positive signal during treatment. For example, local inflammation following therapy can increase the FDG-PET signal, masking treatment response [241]. Diffusion MRI readouts are less sensitive to such inflammatory effects [192]. Concerns of ionizing radiation overexposure, especially in lymphoma patients who may be exposed to serial imaging scans and/or radiation therapy [242] also necessarily limits the number of nuclear imaging scans that can be obtained from a patient, especially at early treatment time points.

Although ADC by itself is already a promising imaging biomarker to indicate tumor response to CRLX101, the availability of ADC datasets from multiple time points enables mathematical modeling of tumor growth. This potentially allows the prediction of future treatment response in an individual patient. We applied a simple logistic model of tumor growth [229] to ADC data. The model makes the simplifying assumption that each imaging voxel consist only of tumor cells and

that ADC changes are entirely due to the reduction in cellularity; yet it still provides instructive predictions using diffusion MRI datasets. This was shown by the strong correlation between simulated (using data from previous time points) and estimated (data from the time point of interest) tumor cell number at both day 4 and day 7 (figure 4.5). Proliferation rates generated from this model separated CRLX101-treated and control groups (figure 4.6) and highlighted the enhanced antiproliferative effect of CRLX101 [217]. Analysis of proliferative rates across time points may add insights to a treatment's mode of action. For example, consideration of the CPT-11 ADC and tumor growth data alone through day 7 would indicate that the tumor may still be responding to treatment, albeit less than with the nanotherapy. However, analysis of the proliferation data indicated that between day 4 and 7 CPT-11 tumors showed a trend toward positive proliferation rates, suggesting treatment failure. The latter analysis is consistent with histology; by day 7 the Ki-67 staining in CPT-11 tumors were similar to baseline and control. In contrast, CRLX101 proliferation rates were negative between day 0 and day 2, increased slightly between days 2 and 4 before decreasing again from day 4 to 7. This observation is consistent with CRLX101 Ki-67 staining, but is not immediately apparent from looking at ADC changes alone. The reason for this fluctuation of proliferation rate is unclear; tumor uptake and biochemical activity of CRLX101 have only been followed for up to 48 hours [217]. It has been suggested that CRLX101 may have antiangiogenic effects and enable prolonged drug release via hydrolytic and enzymatic cleavage of the cyclodextrin-polymer [19]. Such effects may be synergistic and lead to the increased efficacy observed at later time points. Techniques that can probe CRLX101's dynamic antiangiogenic effects within the tumor, such as dynamic contrast-enhanced MRI [131], may be able to elucidate this process.

Since it was difficult to spatially coregister individual tumor images across time points, imaging data were only analyzed at a whole-tumor ROI level. Thus, the heterogeneity of the tumor mass, which may also be an important determinant to treatment response, was neglected. This may be addressed in future studies by prudent spatial coregistration across time points. Furthermore, the current model can be integrated into more sophisticated models [208] of tumor growth by incorporating data acquired concurrently with other modalities (e.g.PET) [201].

In conclusion, we have demonstrated that diffusion MRI can monitor the early response to CRLX101 treatment in a preclinical model of malignant lymphoma. Modeling of the ADC data

emphasized the enhanced antiproliferative effect of CRLX101 compared to controls and CPT-11. This demonstrates the utility of diffusion MRI for preclinical and clinical evaluation of targeted nanotherapies such as CRLX101 and suggests that an image-driven modeling approach can provide insights to their mechanism(s) of action *in vivo*.

Chapter 5

Imaging the Tumor Response to the Tumor-penetrating Peptide iRGD

Improvement of drug uptake into the tumor mass is highly desirable. Recently, a tumor-penetrating peptide, iRGD, has been shown to improve the uptake of a number of different classes of drugs into the tumor mass without seeming to alter the pharmacokinetics of the drugs in other tissues. Translation of iRGD to the clinic would be facilitated by a noninvasive assay that can identify patients sensitive to iRGD. Furthermore, a noninvasive assay may provide further insights into the *in vivo* mechanism of iRGD. We hypothesize that iRGD can modulate the uptake of MRI and PET-visible contrast agents by altering the perfusion characteristics of the tumor. We hypothesize that this modulation would be visible by DCE-MRI, diffusion MRI and PET.

In this chapter, we present preliminary results of MRI and PET experiments probing the tumor response to iRGD. The results show that DCE-MRI may be a potentially useful tool to visualize iRGD response in the clinic. However, further investigations into the effects of iRGD in animal models of cancer needs to be pursued to build on these results.

Acknowledgments: We thank Drs. Kazuki Sugahara, Tabet Tessalu and Erkki Ruoslahti for interesting discussions and for providing the mice for these studies, Dr. Andrey Demyanenko, Dr. Sharon Lin, Dr. Xiaowei Zhang, Dr. Kofi Poku, Naomi Santa Maria, Desiree Crow, and Junie Chea for their technical assistance. Drs. Andrew Raubitschek, David Colcher provided the Herceptin and provided welcome feedback. Drs. Shengxiu Li, David Koos and Scott Fraser provided useful advice. The project is funded by a NCI STRAP grant (P01 CA043904), City of Hope Lymphoma SPORE Grant (P50 CA107399), the Beckman Institute and the Caltech/City of Hope Biomedical Initiative.

5.1 Introduction

5.1.1 CendR Rule

Teesalu *et al.* identified a peptide motif (via phage display) which mediated uptake of labelled phage into a variety of tumor cells [50]. The motif consists of RXXR. They found that this motif needs to be at the C-terminus of the peptide chain (either endogenously or exposed by enzymatic cleavage) to be active (thus the CendR rule). Furthermore, they discovered that the motif interacts with the neuropilin-1 receptor, a mediator in the VEGF pathway [243, 244]. VEGF165A, a potent mediator of vascular permeability, contains the CendR motif. Incorporation of multimeric CendR peptides increased vascular permeability and uptake of CendR-labelled phage into lung and subcutaneous tissue. Interestingly, several viruses express the CendR sequence on their membrane and envelope proteins.

5.1.2 iRGD

CendR peptides have no specific tissue homing ability. Sugahara *et al.* identified a class of CendR peptides that contain the RGD motif [48]. The RGD motif has been well characterized to bind to α_v integrins receptors, which are often overexpressed in tumor blood vessels and have been used to target agents to tumor blood vessels [245, 136]. CendR-containing, internalizing-RGD (iRGD) peptides, when linked to nanoparticles, phage and micelles increased their tumor penetration significantly. In a BT474 xenograft mouse model, iRGD-Abraxane concentration in tumors were increased 10-fold over Abraxane alone.

In a subsequent study, Sugahara *et al.* further demonstrated that iRGD effects can be mediated without linkage of the peptide to the agent of interest [49]. Coadministration of iRGD was shown to increase tumor penetration of a small-molecule doxorubicin, doxorubicin-containing liposomes, and the antibody trastuzumab. iRGD's *in vivo* mechanism of action remains unclear. It is postulated that the RGD motif allows tumor homing. An as yet unknown protease is responsible for the peptide cleavage, exposing the CendR motif. Interaction of the CendR motif with the neuropilin-1 receptor results in both increased vascular permeability and increased tumor cell uptake of agents. The contribution of both mechanisms to effective drug uptake remains unknown. Indeed, the ac-

tion of neuropilin-1 expression in tumors is complex and remains unclear [246, 247]. The exact timing of uptake efficacy is also unknown, although significant uptake increases of coadministered agents have been shown within a 30 minute to 3 hour time window post iRGD injection (private communication, K.S.).

5.1.3 Noninvasive Measures of Vascular Permeability with MRI

DCE-MRI is a commonly used method to evaluate vascular permeability in tumors (see section 2.3.2.2). The majority of DCE-MRI studies focus on either differentiating tumor grades or studying the vascular modulation as a result of antiangiogenic therapies. Angiogenic factors within tumors are often dysregulated, favoring neovascularization rather than vessel maturation [248, 249]. As a result, tumor blood vessels are often tortuous and leaky. The basis behind this is incompletely understood. However, many studies have shown that increased tumor leakiness, measured by DCE-MRI, correlates with tumor grade and malignant potential [250, 251, 252]. Permeability has also been correlated with other tumor microenvironmental factors, such as hypoxia [253].

Folkman hypothesized that cutting off the tumor blood supply is a viable anti-tumor strategy [254]. This has led to the development of several antiangiogenic and vascular disruptive therapies for cancer. DCE-MRI has shown potential to monitor the effects of these therapies [255, 221]. Decreases in permeability parameters (e.g. K_{trans}) has been demonstrated as a positive biomarker of antiangiogenic treatment efficacy [256, 131, 257].

For both tumor phenotyping and treatment response scenarios, tumor vascular changes usually occur over days to months. We hypothesize that iRGD increases the uptake of MRI-visible contrast agents via an increase in vascular permeability and that this occurs within a short timescale (<30 minutes). Few studies have explored the use of DCE-MRI to measure drug-modulated increases in vascular permeability, especially at such a short timescale. Su *et al.* observed pharmacokinetic changes of Gd-DTPA uptake immediately after the intravenous application of angiotensin II, hydralazine and histamine [258]. Tumor enhancement was decreased in the presence of all three modulators. Only the vasodilator histamine delayed Gd-DTPA washout. Wang *et al.* investigated the hydralazine response using Gd-DTPA-Albumin, observing a decrease in the tumor blood volume fraction occupied by the contrast agent [259].

The effect of localized angiogenic stimuli has also been monitored by DCE-MRI. Dafni *et al.* observed increased dermal permeability to Gd-DTPA-Albumin in response to intradermal injection of VEGF165 within 30 minutes of administration [260]. In a separate study, they also showed that VEGF165 attenuation in tumors decrease Gd-DTPA-Albumin within 48 hours in a C6 cell line with tetracycline-inducible VEGF expression [261]. Recently, Cartwright *et al.* also showed increased permeability and vascular changes of urinary bladder tissue in the presence of a VEGF121-containing graft-matrix over a 3-week period using Gd-DTPA [262]. These results suggest that tumor permeability increases mediated by iRGD may be probed by DCE-MRI.

5.2 Materials and Methods

5.2.1 Preparation of compounds

iRGD's structure is described elsewhere [48]. iRGD was synthesized commercially (Bachem) and lyophilized for long term storage. Aliquots of iRGD for individual studies were made up in $1 \times$ PBS and stored at -80°C until use. Tests on this material demonstrated that iRGD was stable at 4°C for at least 2 weeks (private communication, A.R.).

Platelet-activating factor (PAF, Sigma-Aldrich, P4904) was diluted with $1 \times$ PBS, aliquoted and stored at -20°C until use.

5.2.2 Cells and Tumor Models

The HER2-expressing BT474 human breast cancer cell line was cultured in SFM4MAB medium with 10% fetal bovine serum and penicillin/streptomycin. 17β -estradiol pellets (Innovative Research of America) were implanted subcutaneously into the back of the athymic BALB/c nude mice one day prior to orthotopic inoculation (6th and 9th mammary fat pad) of 5×10^6 cells in matrigel (BD Biosciences). Tumors were $\sim 2\text{--}300 \text{ mm}^3$ at the time of imaging. Mouse care and experimental procedures were carried out in accordance with protocols approved by the Research Animal Care Committees at the Sanford Burham Institute, City of Hope and Caltech.

5.2.3 MRI-only Studies

A timeline for MRI-only studies is shown in figure 5.1. Before each imaging session, each mouse is catheterized with a 30G needle attached to PE10 tubing in the tail vein for contrast agent and peptide administration inside the MRI. Baseline and treatment imaging sessions were separated by ~3 hours to allow adequate washout of CA from the first scan (Gd-DTPA, Magnevist, Bayer, plasma half-life = 12 minutes in mice).

5.2.3.1 Anatomical MRI

A Biospec (Bruker-Biospin Inc., Billerica, MA) 7 T MRI scanner and a home-built birdcage coil with an 8 cm axial field of view (FOV) were used for mouse MRI image acquisition. For all imaging sessions, animals were anesthetized using a 1.3%–1.5% isoflurane/air mixture and body temperature was maintained at 36°C–37°C with warmed air flowing through the bore. For anatomical imaging, a RARE sequence (TR/TE = 4000/23 ms; RARE factor = 4; number of averages = 2; FOV = 35.4 × 35.4 mm²; image matrix = 128 × 128; slice thickness = 0.754 mm) was used to collect 40 contiguous images across the mouse torso, allowing tumor visualization.

5.2.3.2 T₁ mapping

A variable flip angle method outlined in section 3.1.1.3 was used to generate T₁ maps. Gradient echo images (FLASH, FA = 12°, 24°, 36°, 48°, 60°, matrix size = 140 × 80, voxel size = 0.25 × 0.25 mm², slice thickness = 1 mm, TR/TE = 200/2 ms) centered on the tumor (3 slices) and the left ventricle (1 slice) were acquired.

5.2.3.3 DCE-MRI

After T₁ maps were acquired, 0.9% saline, 10 nmol/kg PAF or 0.2 mg/mouse iRGD in a volume of 0.1 mL was injected into the mouse, followed by a 0.1 mL saline chase to clear the catheter. 12 minutes was allowed to elapse prior to starting the DCE-MRI scan. The DCE-MRI time series were acquired using a gradient echo sequence (FLASH, FA = 35°, TR/TE = 25/2 ms, geometry the same as the T₁ maps, time resolution = 2 s, duration = 22 minutes). After a baseline of 2.5 minutes, Gd-DTPA (0.1 mmol/kg per DCE-MRI scan) was injected intravenously via the catheter using a

powered-injector (New Era Inc., Farmingdale N.Y.) at 0.5 mL/min.

To retain good spatial coregistration between baseline and treatment scans, mice were secured in the animal holder between the two imaging sessions obtained on the same day. The holder was placed on a warm electric blanket outside the MRI to keep the mice warm during this period (~3.5 hours, to allow for CA washout). A motorized stage enabled exact repositioning of the holder in the MRI. Mice were kept lightly anesthetized using ~0.5%–0.7% isoflurane. Lactate Ringer’s solution (0.15 mL per mouse) was injected subcutaneously halfway through the intersession period to reduce metabolic acidosis. Mice were kept in their home cage at all other times. All the MRI scans described above were performed for both baseline and treatment scan sessions. A total of 10 mice were used in this study. Half ($N = 5$) were treated on the first day with PAF, while the other half ($N = 5$) were treated with iRGD on the first day. Treatments were reversed on day 3.

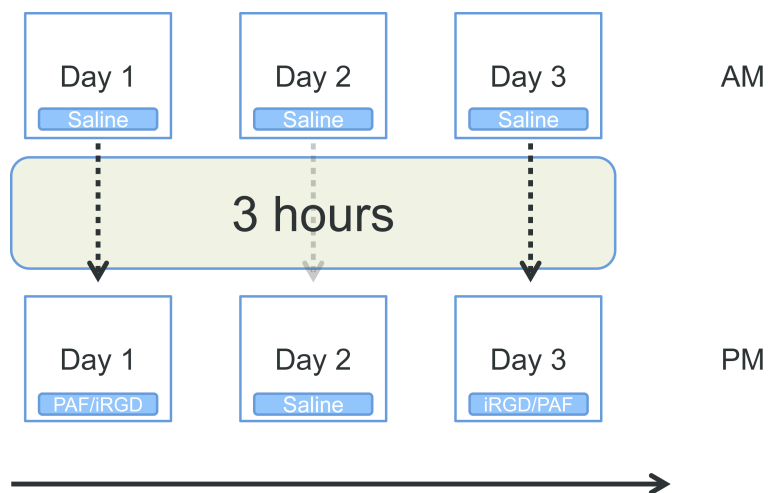


Figure 5.1: Study design for iRGD MRI. Each BT474-bearing mouse was imaged on three consecutive days. Each day consisted of two DCE-MRI scan sessions. PAF or iRGD was injected intravenously 15 minutes before the second DCE-MRI scan on day 1. The alternative treatment was administered on day 3. Saline was administered on day 2. 3 hours were allowed to elapse between baseline and treatment scans to allow adequate CA washout.

5.2.3.4 Image Analysis

DCE-MRI data were analyzed with the extended Kety model [82]. The model incorporates the exchange of CA between the extracellular vascular space (plasma) and the tissue extracellular space (figure 2.3). The influx rate of CA moving from the plasma to tissue space is denoted K_{trans} . The efflux rate from the tissue back to the plasma is related to the extracellular volume fraction v_e by

$\frac{K_{trans}}{v_e}$. Assuming instantaneous homogeneous distribution of CA in both compartments, the model can be described by

$$\frac{d}{dt}C_t(t) = K_{trans}C_p(t) - \left(\frac{K_{trans}}{v_e}\right)C_t(t). \quad (5.1)$$

$C_t(t)$ and $C_p(t)$ are the concentrations of CA in tissue and plasma respectively. The solution to this equation is

$$C_t(t) = K_{trans} \int_0^t C_p(u) e^{-\left(\frac{K_{trans}}{v_e}\right)(t-u)} du. \quad (5.2)$$

This equation neglects the vascular volume in the tissue, which may be invalid in pathological tissues. The model can be extended to include a vascular fraction component v_p :

$$C_t(t) = K_{trans} \int_0^t C_p(u) e^{-\left(\frac{K_{trans}}{v_e}\right)(t-u)} du + v_p C_p(t). \quad (5.3)$$

$C_t(t)$ and $C_p(t)$ are obtained from the dynamic time series. ROIs drawn over the tumor and left ventricle (LV) were used for $C_t(t)$ and $C_p(t)$ respectively. Signal intensity for each voxel in the ROIs was first converted to $R_1 = 1/T_1$:

$$R_1(t) = \frac{1}{TR} \ln \left(\frac{(S_0 \sin \alpha e^{-TE/T_2^*}) - S(t) \cos \alpha}{(S_0 \sin \alpha e^{-TE/T_2^*}) - S(t)} \right). \quad (5.4)$$

R_1 , TR, TE described previously, α is the flip angle, $T_2^* \gg TE$, $S(t)$ is the signal intensity time course and:

$$S_0 = S_{SS} \frac{(1 - e^{-TR/T_1} \cos \alpha)}{(1 - e^{-TR/T_1}) \sin \alpha e^{-TE/T_2^*}}. \quad (5.5)$$

S_{SS} is the steady state average signal intensity before CA administration. $R_1(t)$ is converted to $C(t)$ using the fast exchange limit assumption:

$$R_1 = r_1(1 - h)C + R_{10}. \quad (5.6)$$

r_1 is the relaxivity of Gd-DTPA at 7 T ($4.71 \text{ s}^{-1} \text{ mM}^{-1}$), h is the hematocrit of a mouse ($h = 0.45$ based on literature values) and R_{10} is derived from the T_1 map.

Calculation of $C_p(t)$, the arterial input function (AIF) is a subject of intense investigation. For this study, we adopted an image-based method similar to Loveless *et al.* [263]. For our studies, voxels with SNR <5 at all time points in the LV ROI on each individual dataset were first removed. Next, each voxel in the ROI was visualized individually. Voxels that do not show a time curve reflecting plasma uptake (i.e. fast uptake, rapid washout) were further excluded. The remaining voxels were averaged together to represent the individual AIF for the particular study (AIF_{ind}). Each AIF_{ind} was fitted to a model derived by MacGrath *et al.* [264], described as a mixture of a Gaussian and an exponential modulated by a sigmoid:

$$C_p(t) = \begin{cases} 0 & , t \leq t_0, \\ \sum_{n=1}^N \frac{A_n}{\sigma_n \sqrt{2\pi}} e^{\left(\frac{-(t-T_n-t_0)^2}{2\sigma_n^2}\right)} + \frac{\alpha e^{-\beta(t-t_0)}}{(1+e^{(-s(t-\tau-t_0))})} & , t \geq t_0, \end{cases} \quad (5.7)$$

where $N = 1$, A_n , T_n and σ_n are the scaling constants, centers and widths of the n th Gaussian; α and β are the amplitude and decay constant of the exponential; s and τ are the width and center of the sigmoid respectively. t_0 marks the start time of CA injection. The Gaussian constants are related to the speed of injection and the shape and concentration of the bolus, while the other constants are related to the decay of the CA in the plasma. We chose this model as opposed to other models described in the literature because it gave the best visual fit among all the AIFs considered in this study. Most AIFs showed a maximum peak concentration of approximately 2.5–3 mM, peaking at approximately 15 seconds post CA injection. The AIFs measured for one mouse on a single imaging day had peaks at ~1 mM. This resulted in vascular parameters which were, on average, twice as high as parameters from other datasets. Thus, for consistency, we replaced these AIFs with an AIF generated from the same animal on the preceding day. Parameters generated from either AIF did not significantly affect subsequent cohort analysis.

The fitted AIF was applied to equation (5.3) to derive K_{trans} , v_e and v_p . Values were fitted for the averaged whole ROI time curve (global ROI) and voxel-by-voxel using a Levenberg-Marquardt nonlinear algorithm implemented in MATLAB. For voxel fitting, voxels that did not converge to a realistic fit ($r^2 < 0$, $K_{trans} \geq 5$, $0 < v_e < 1$ and $0 < v_p < 1$), were removed from further analysis.

The second DCE-MRI dataset on each day was compared to the baseline dataset acquired earlier in the same day.

A sample AIF and tumor curves from a single dataset (with associated model fits) are shown in Figure 5.2.

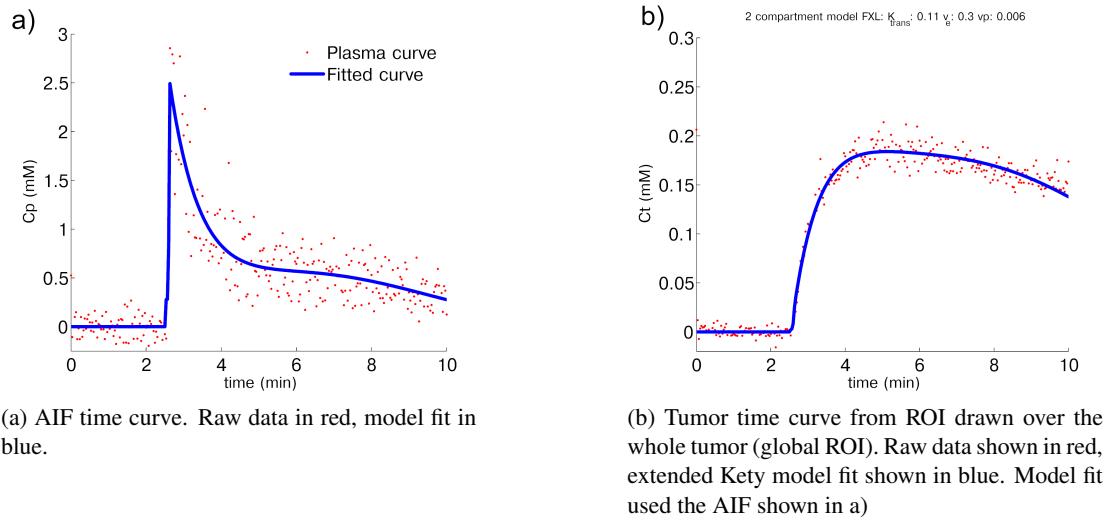


Figure 5.2: AIF, tumor time curves and model fits from Magnevist injection.

A semiquantitative metric, the area under the curve (AUC), was also calculated for each global

ROI and voxel concentration vs. time curve. AUC was calculated using the trapezoidal rule over the course of 8 minutes post CA injection.

5.2.4 PET/MRI studies

A timeline for the PET/MRI studies is shown in figure 5.3. Mice were setup as per the MRI-only studies.

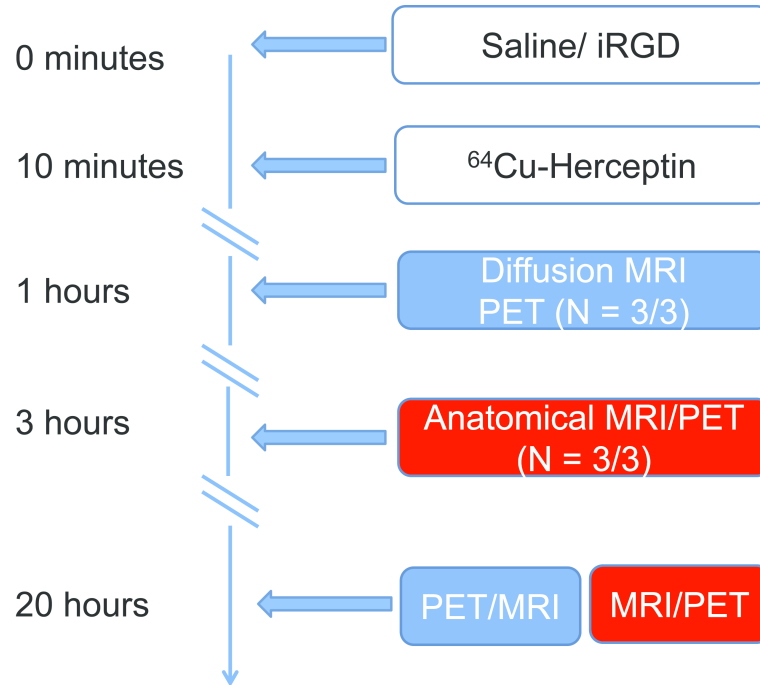


Figure 5.3: Study design for Diffusion MRI/PET. Each BT474-bearing mouse was imaged over the course of 20 hours. Saline or iRGD was injected intravenously 10 minutes before the injection of ⁶⁴Cu-DOTA-NHS-Herceptin. Simultaneous PET/ diffusion MRI was performed 3 and 20 hours after antibody injection.

5.2.4.1 Anatomical MRI

Anatomical MRI was obtained as per section 5.2.3.1.

5.2.4.2 *In Vivo* PET/MRI

Simultaneous diffusion MRI/ PET was performed with and without iRGD administration. Saline (N = 3) or iRGD (0.5 mg/mouse, N = 3) at a volume of 0.1 mL was injected i.v. , followed by ⁶⁴Cu-DOTA-NHS-Herceptin (3–4 MBq/mouse, i.v.) 10 minutes later. ⁶⁴Cu-DOTA-NHS-Herceptin was

synthesized as per previous studies [115].

Combined diffusion MRI and PET was obtained 3 and 20 hours post radiolabelled antibody injection. Anatomical MRI was first done to position the tumor in the center of the PET FOV. Diffusion MRI was obtained with a spin-echo sequence (TR/TE=3000/23ms, matrix size = 140 × 80, resolution = 0.25 × 0.25 mm³, slice thickness = 1 mm, 10 slices, $\delta/\Delta = 3/15$ ms, b-values = 0, 300, 1000 s/mm³, 1 direction) and processed as described in section 3.4.3.4. PET was obtained with a duration of 1200s at the 3 hour time point and 1800s at the 20 hour time point.

An additional 6 mice (N = 3 per cohort) were also imaged with anatomical MRI/PET. Images were acquired at 1 and 20 hours after antibody injection. PET was obtained with a duration of 600 and 1800 s at the 1- and 20-hour time points respectively.

5.2.4.3 Image Analysis

PET images were processed and calibrated as described in section 3.4.3. PET and anatomical MRI images were aligned to ADC datasets using the method described in Section 3.2.3.2. Tumor ROIs were drawn on the anatomical MRI images in order to extract tumor ADC and PET uptake values (in units of % ID/g). Due to a hardware malfunction during one of the study days, 20-hour time points PET images were not obtained for 2 saline and 1 iRGD-treated mice. Diffusion MRI were obtained for those animals.

5.2.5 Histological Assessment

iRGD effects on the uptake of Herceptin were assessed by histology. Mice bearing BT474 tumors were injected with saline or iRGD (0.5 mg/ mouse) intravenously. This was immediately followed by an injection of Alexa 633-conjugated Herceptin (0.1 mg, i.v.). Tumor samples were obtained at 1, 3 and 20 hours post Herceptin injection (N = 2 per time point, per treatment). 20 minutes prior to tumor extraction, FITC-labelled Lycopersicon esculentum lectin (0.15 mg per mouse i.v., Vector Laboratories) were injected to visualize perfused vessels. Mice were sacrificed by transcardiac perfusion and tumors were excised. Tumors were placed in 4% paraformaldehyde overnight and then cryoprotected in a sucrose gradient (10%–30%) over three days. Tumors were then embedded in OCT (Sakura) and 20 μ m cryosections were obtained.

All tumor slices were stained with DAPI and then visualized using either a 5x/0.15 Ph1 (Plan-Neofluar) objective on a Zeiss LSM 5 Exciter confocal microscope. Five random FOVs were imaged from slides containing slices from each tumor to evaluate antibody uptake.

5.2.6 Statistical Analysis

Two-sided paired t-tests were used to compare iRGD or PAF cohorts to the control cohort. A p -value of 0.05 or smaller was considered to be statistically significant.

5.3 Results

5.3.1 MRI-only Studies

Uptake curves in the tumor were highly heterogeneous (figure 5.4). Thus, we analyzed the tumor both using global ROI-generated parameter values and on a voxel-by-voxel basis. Voxel-by-voxel parametric maps for a mouse treated with saline, iRGD and PAF are shown in figure 5.5.

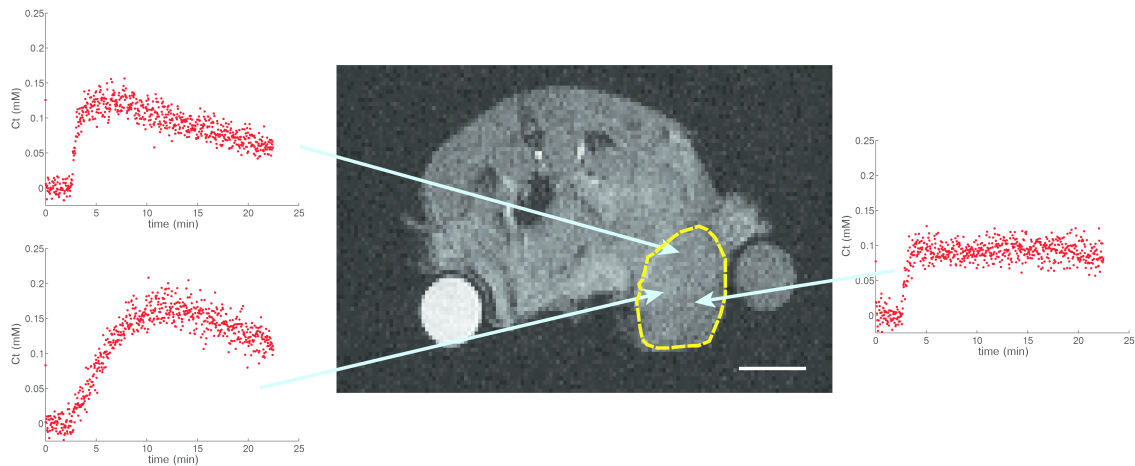
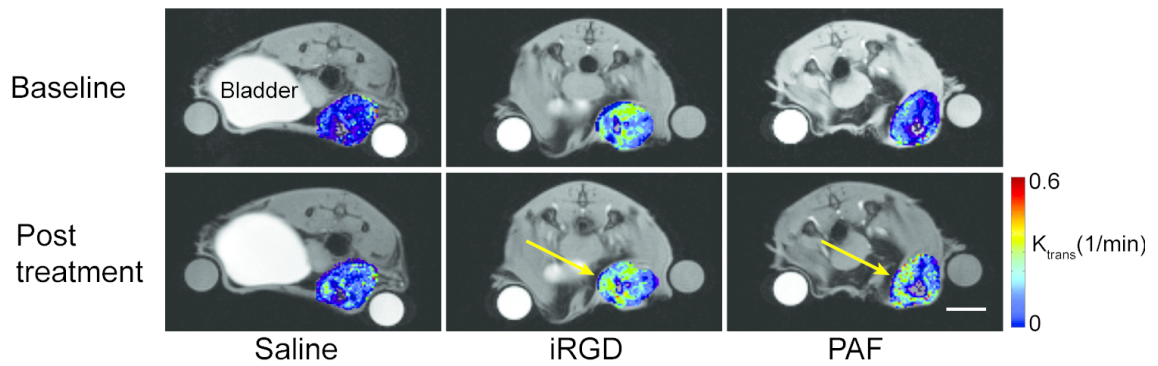
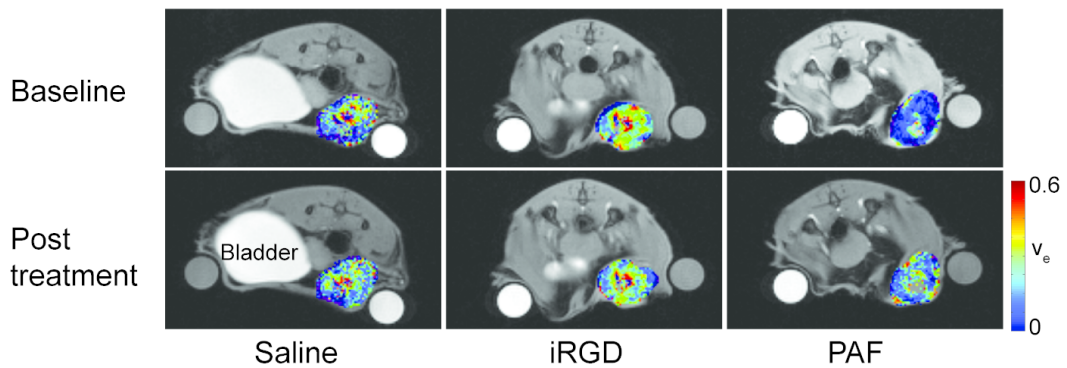


Figure 5.4: Heterogeneity of tumor CA uptake. Curves taken from 3 different ROIs within the tumor shown in figure 5.2 show that different regions of the tumor (outlined in yellow) show different uptake kinetics (scale bar = 5 mm).

Mean K_{trans} , v_e and v_p values derived from global and whole (mean from voxels fits obtained for the whole tumor) ROIs are shown in table 5.1. No significant differences were observed between baseline values for all treatment cohorts across Days 1–3, suggesting that administration of PAF or iRGD on Day 1 of the study did not have dramatic long term (>12 hours) effects on tumor vascular



(a) K_{trans} maps for an individual mouse due to different treatments. An increase in K_{trans} was observed after both iRGD and PAF treatment, mostly around the medial side of the tumor (yellow arrows). In contrast, no dramatic increase was seen after saline treatment (scale bar = 5 mm).



(b) v_e maps for an individual mouse due to different treatments. An increase in v_e was observed after PAF treatment throughout the tumor slice. In contrast, no dramatic increase was seen after saline or iRGD treatment (scale bar = 5 mm).

Figure 5.5: Vascular parametric maps for a single mouse over multiple days.

parameters and justified the study design.

Table 5.1: Mean vascular parameters for different treatment cohorts for global ROI and whole ROI (voxels). Standard errors of the mean are shown. All global fits had a r^2 value greater than 0.98. Although in both ROIs increases in K_{trans} and v_e were observed, these were not statistically significant ($p > 0.05$).

	K_{trans} (1/min)	v_e	v_p	K_{trans} (1/min)	v_e	v_p
saline	0.1±0.02	0.19±0.03	0.01±0.002	0.1±0.02	0.18±0.02	0.01±0.003
iRGD	0.08±0.01	0.16±0.02	0.01±0.002	0.17±0.06	0.24±0.08	0.01±0.002
PAF	0.08±0.01	0.18±0.03	0.01±0.004	0.17±0.06	0.38±0.17	0.02±0.007
	Baseline (AM)			12 minutes posttreatment (PM)		
	Global ROI					
saline	0.13±0.02	0.23±0.02	0.01±0.002	0.12±0.01	0.21±0.01	0.01±0.003
iRGD	0.1±0.01	0.2±0.02	0.01±0.001	0.17±0.04	0.21±0.03	0.01±0.001
PAF	0.11±0.02	0.22±0.03	0.01±0.003	0.2±0.05	0.26±0.03	0.02±0.003
	Baseline (AM)			12 minutes posttreatment (PM)		
	Whole ROI, from voxels					

Table 5.1 shows that both iRGD and PAF caused an increase in both K_{trans} and v_e calculated from a global ROI and also voxels from the whole tumor (whole ROI). However, neither cohort was statistically significantly different from the saline cohort. To account for the intersubject variability of tumor vascular parameters, we calculated the percentage change from baseline of each parameter for each subject and compared these values. These are tabulated in table 5.2. Again, both iRGD and PAF cohorts showed increased percentage changes from baseline values for both K_{trans} and v_e compared to the saline treated cohort. The PAF cohort showed statistically significant increases in K_{trans} (for both global, $p \leq 0.01$ and whole ROI, $p \leq 0.01$) and v_e (whole ROI, $p = 0.02$) compared to the control cohort.

Table 5.2: Mean percentage change from baseline of vascular parameters for both global ROI and whole ROI (voxels). SEMs are shown. * and ** denote significant differences with the saline cohort ($p \leq 0.01$ and $p = 0.02$ respectively).

% change from baseline	K_{trans}	v_e	v_p	K_{trans}	v_e	v_p
saline	14±20	3.7±8.9	78±40	10±16	-1.9±7.4	36±21
iRGD	94±63	32±33	45±20	56±28	4.5±9.4	6.7±9.4
PAF	105±32 *	77±38	137±78	80±25 *	23±10 **	73±32
	Global ROI			Whole ROI, from voxels		

Heterogeneity of treatment response was probed further by segmenting the tumor. Two segmentation criteria were examined. First, voxels from each tumor were sorted into percentile bins

according to K_{trans} values (e.g. top 10% K_{trans} values, top 10%–20% K_{trans} values etc.). Percentage changes from baseline of both K_{trans} and v_e for each percentile bin were compared between treatment cohorts. These comparisons are shown in figure 5.6. K_{trans} values after PAF treatment generally increased across all K_{trans} percentile bins. In contrast, K_{trans} increases after iRGD treatment were greater for highly enhancing voxels (higher K_{trans} bins) compared to the lower enhancing voxels (low K_{trans} bins). v_e increases due to PAF were greater for highly enhancing voxels compared to lower enhancing voxels, while v_e did not change from the baseline for the iRGD cohort.

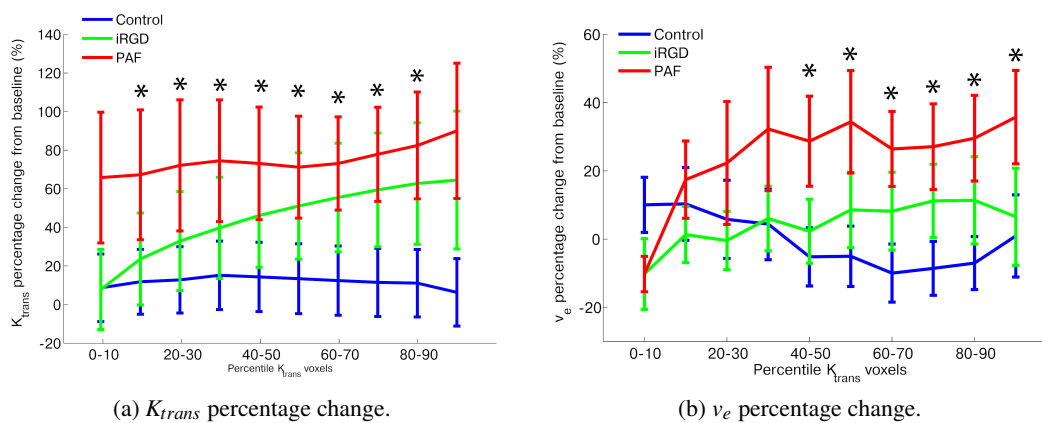


Figure 5.6: Mean percentage change from baseline, sorted by tumor K_{trans} value. Stars (*) denote that PAF treatment was significantly different to the saline control ($p < 0.04$). Error bars denote SEM.

Next, voxels from each tumor were sorted based on their distance from the tumor edge, which was determined based on the ROI mask. Percentage changes from baseline of both K_{trans} and v_e as a function of distance from the tumor edge were compared between treatment cohorts. These comparisons are shown in Figure 5.7. K_{trans} increases from the baseline were consistent regardless of the distance from the edge of the tumor for both PAF and iRGD cohorts. This was also the case for v_e increases observed in the PAF treated cohort.

AUC parameters calculated for the global ROI and the whole ROI are shown in table 5.3 and table 5.4. While not statistically significant, AUC results showed similar trends to compartmental modeling results, showing an increase in CA uptake post iRGD and PAF treatment compared to the saline controls.

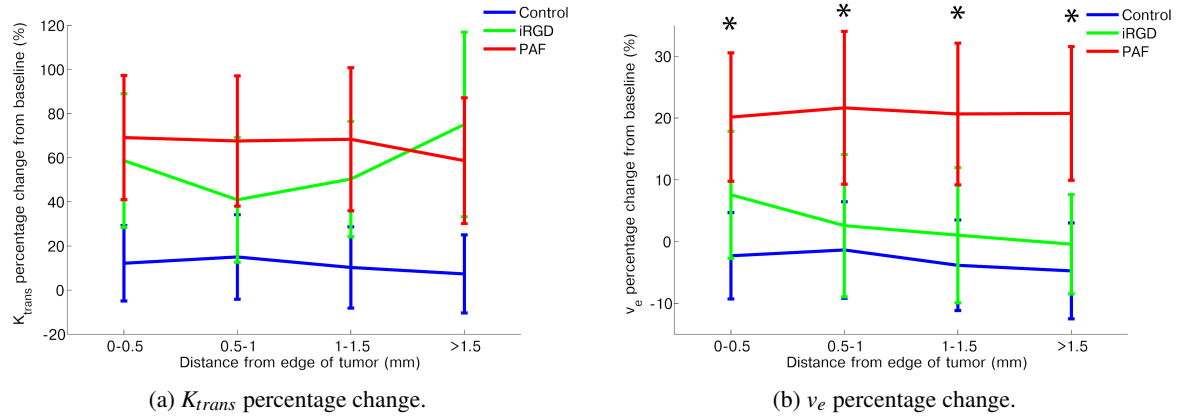


Figure 5.7: Mean percentage change from baseline, sorted by distance from the tumor edge. Stars (*) denote that PAF treatment was significantly different to the saline control ($p < 0.04$). Error bars denote SEM.

Table 5.3: Mean AUC calculated over 8 minutes post CA injection for different treatment cohorts for global ROI and whole ROI (voxels). Standard errors of the mean are shown. Although both iRGD and PAF cohorts showed increases in AUC, these were not statistically significant ($p > 0.05$). AUC had units of mM min.

	AUC_{pre}	AUC_{post}	AUC_{pre}	AUC_{pre}
saline	0.16 ± 0.02	0.16 ± 0.02	0.17 ± 0.02	0.16 ± 0.02
iRGD	0.14 ± 0.02	0.21 ± 0.07	0.14 ± 0.02	0.22 ± 0.07
PAF	0.15 ± 0.03	0.32 ± 0.13	0.16 ± 0.03	0.33 ± 0.13
	Global ROI		Whole ROI, from voxels	

Table 5.4: Mean percentage change from baseline of AUCs for both global ROI and whole ROI (voxels). SEMs are shown. AUC had units of mM min.

% change from baseline	$AUC_{Global ROI}$	$AUC_{whole ROI}$
saline	6 ± 10	5 ± 10
iRGD	40 ± 37	42 ± 37
PAF	78 ± 32	77 ± 31

5.3.2 PET/MRI Studies

PET/MRI images acquired at different time points for saline-treated and iRGD mice are shown in figures 5.8 and 5.9. A general trend from low to high antibody uptake over time was observed regardless of treatment. For the particular mice shown, higher antibody uptake in the tumor was observed at all time points when treated with iRGD. Interestingly, the spatially matched diffusion MRI images showed that high ADC values were present in the iRGD-treated tumor. Lower ADC values were present in the time matched saline-treated control.

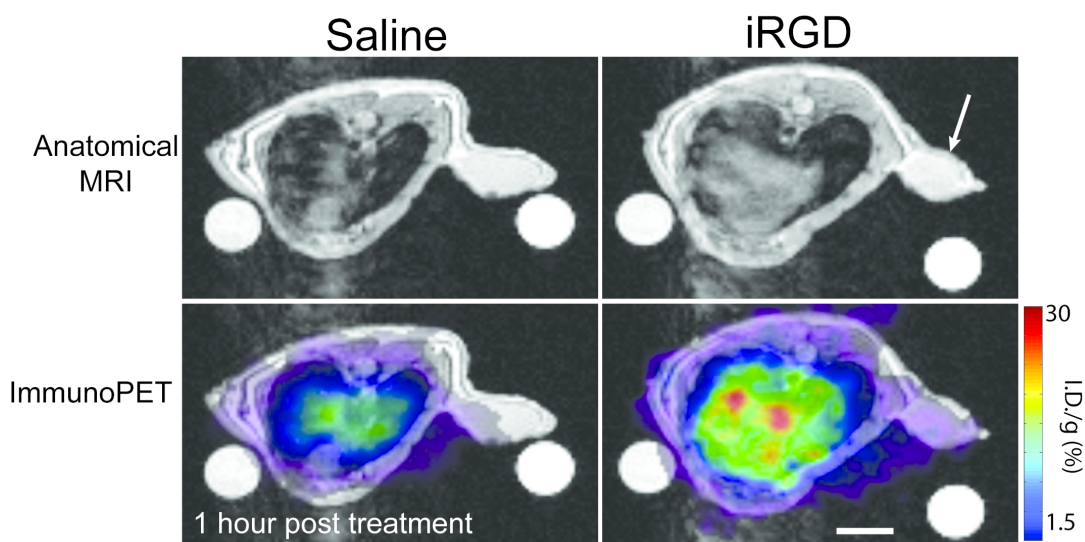
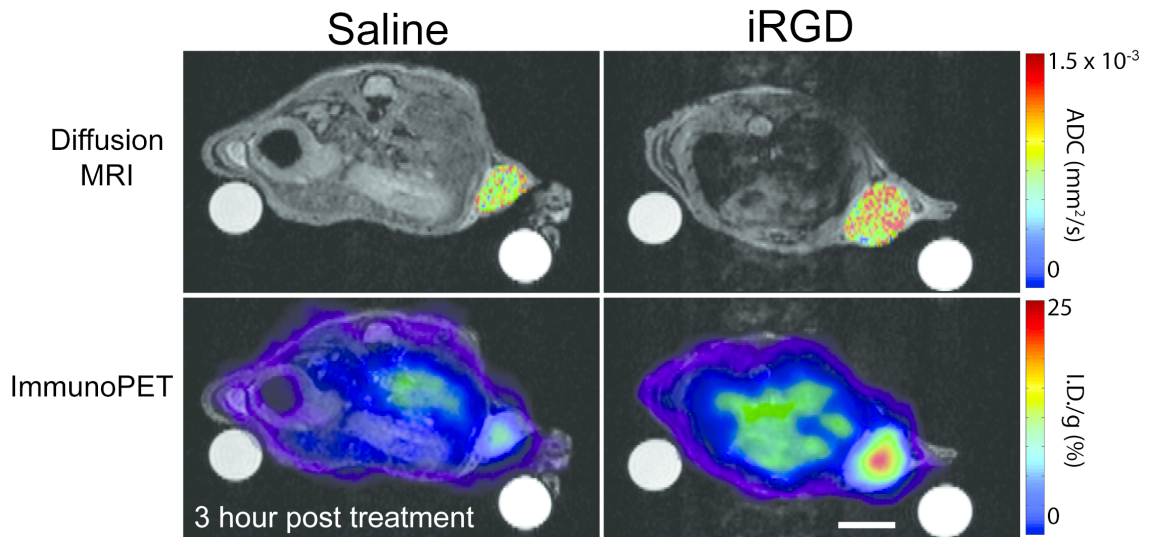
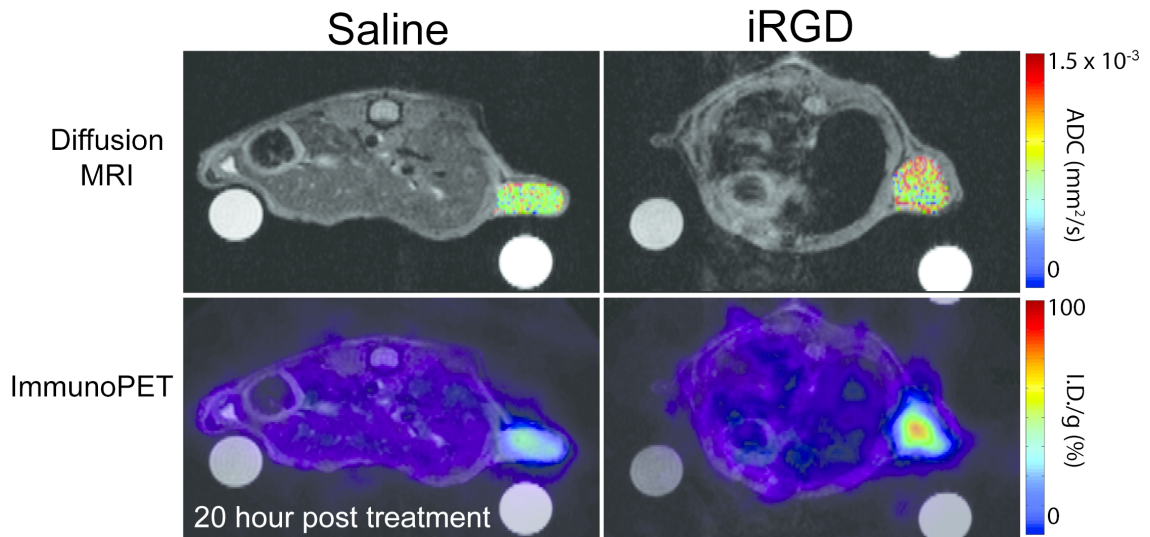


Figure 5.8: PET/MRI of radiolabelled-Herceptin uptake 1 hour post saline/iRGD treatment and antibody injection. At 1 hour, most of the antibody was still in the systemic circulation, as demonstrated by the high activity in the torso. A small but significant increase in antibody uptake within the iRGD-treated (most of the tumor contained activity at the image threshold level) tumor compared to saline-treated control (half the tumor does not show any activity at the image threshold level) was observed. Arrow points at the tumor (scale bar = 5 mm).

Mean ADC and antibody uptake values across both treatment cohorts are shown in tables 5.5 and 5.6. Maximum antibody uptake values are shown in table 5.7. No significant difference in mean ADC values were observed between treatment cohorts at all time points. A 50% increase in mean antibody uptake in iRGD-treated animals compared to the control animals 1 hour after treatment and antibody injection ($p < 0.02$) was observed. However, by 3 and 20 hours, no difference was seen between the two cohorts. No significant difference in the maximum tumor PET uptake value was observed between the two cohorts at all time points.



(a) 3 hours posttreatment/ antibody injection in a saline control and iRGD-treated mouse. This particular iRGD-treated mouse showed high antibody uptake in the tumor compared to the saline control. Correspondingly, the tumor ADC values were also higher in this mouse compared to the saline control (scale bar = 5 mm).



(b) 20 hours posttreatment/ antibody injection in a saline control and iRGD-treated mouse. This particular iRGD-treated mouse showed high antibody uptake in the tumor compared to the saline control. Correspondingly, the tumor ADC values were remained higher in this mouse compared to the saline control.

Figure 5.9: PET/ Diffusion MRI of radiolabelled-Herceptin uptake 3 and 20 hours post saline/iRGD treatment and antibody injection. This particular iRGD-treated mouse showed high antibody uptake. However, no significant differences of ADC or PET uptake were observed between the iRGD and saline cohorts.

Table 5.5: Mean tumor ADC values at 3 and 20 hours post iRGD treatment. No significant differences between cohorts were observed. Errors denote SEM.

$\times 10^{-3} \text{mm}^2/\text{s}$	3 hours	20 hours
saline	1.27 \pm 0.1	1.18 \pm 0.1
iRGD	1.22 \pm 0.2	1.23 \pm 0.2

Table 5.6: Mean tumor PET uptake values at 3 and 20 hours post iRGD treatment. Mean antibody uptake in iRGD treated animals was significantly higher than controls at the 1 hour time point (*, $p < 0.02$). Errors denote SEM.

% ID/g	1 hour	3 hours	20 hours
saline	1.62 \pm 0.1	6.76 \pm 0.1	20.9 \pm 2.5
iRGD	2.55 \pm 0.2*	7 \pm 1.8	18.8 \pm 5.7

Table 5.7: Maximum tumor PET uptake values at 3 and 20 hours post iRGD treatment. Errors denote SEM.

% ID/g	1 hour	3 hours	20 hours
saline	4.25 \pm 0.3	8.50 \pm 1.5	53.5 \pm 8.8
iRGD	6.90 \pm 1.1	15.1 \pm 7.7	56.6 \pm 20.5

5.3.3 Histological Assessment

Sample immunofluorescence images of optically labelled Herceptin antibody are shown in figures 5.10 and 5.11. Qualitatively, iRGD-treated tumors showed higher antibody uptake compared to the saline cohorts across all time points. However, high antibody uptake was also observed in certain saline-treated tumors. intratumoral antibody distribution patterns can be also be variable (figure 5.12).

5.4 Discussion

The ability to identify iRGD-responsive patients prior to treatment will facilitate iRGD's path to translation and maximize its patient impact. Several approaches can be used for this process. A tumor biopsy can identify the presence of the putative targets of iRGD, α_v integrin and neuropilin-1 receptors. However, information about the heterogeneous spatial expression of these markers, an important determinant for efficacy [265, 266], may not be available with this technique. Moreover, biopsies cannot be obtained with sufficient time resolution to gauge the efficacy of the iRGD response (~hours).

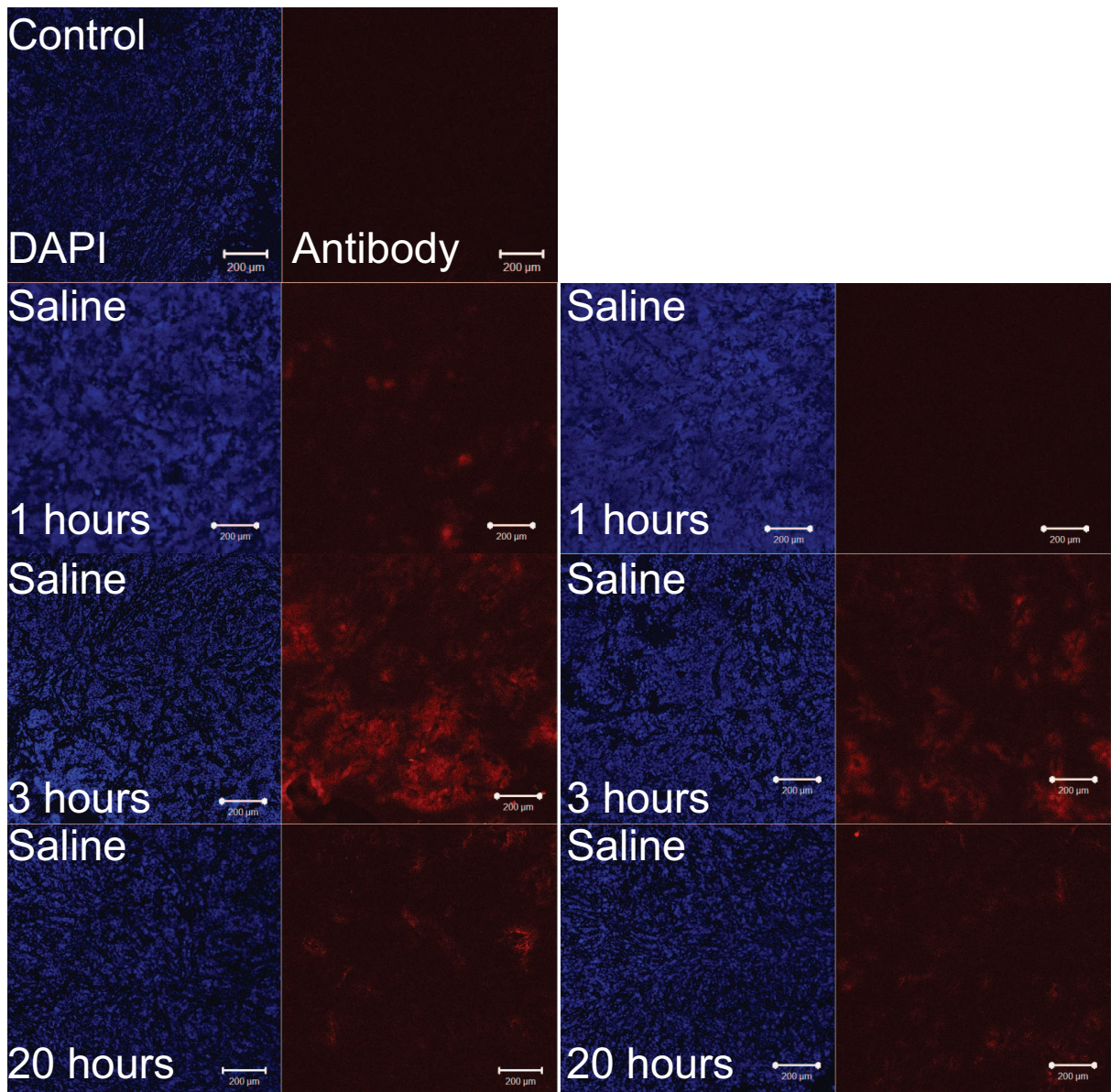


Figure 5.10: Immunofluorescence of antibody uptake with saline. Alexa-633 Herceptin antibody injected into saline-treated BT474 mice over the course of 20 hours. Tumors were harvested at various time points post injection. Images were all acquired using the same laser and aperture settings. Images with the highest antibody signal from each slide are shown on the left. Regions with lower uptake from the same slide are shown on the right. Some saline-treated tumors did show high antibody uptake (seen here especially at the 3 hour time point). A control tumor with no antibody injected is presented. Lycopersicon esculentum lectin signal was variable across all tumors and thus is not presented (scale bars = 0.2 mm).

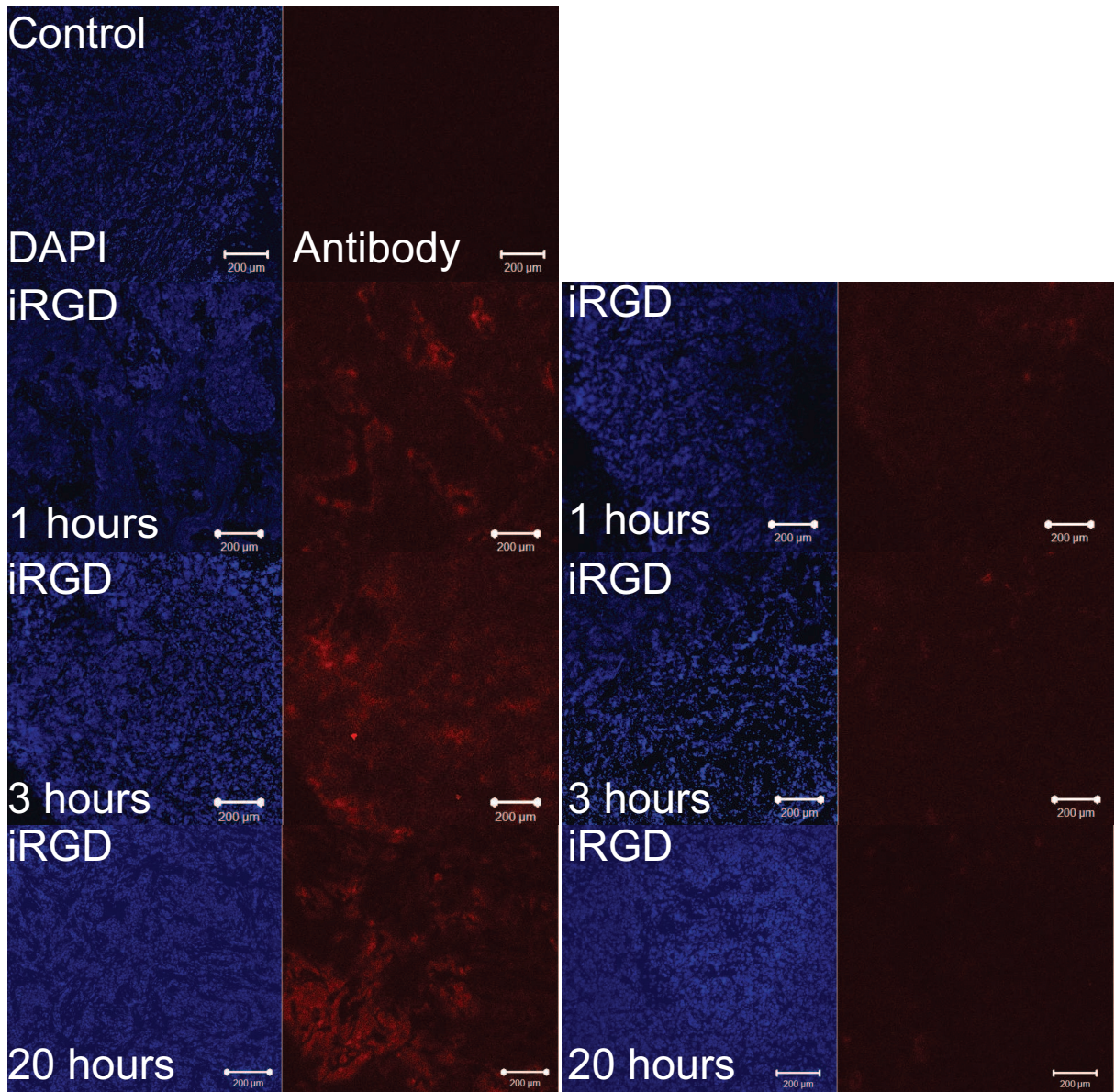


Figure 5.11: Immunofluorescence of antibody uptake with iRGD. Alexa-633 labeled Herceptin antibody was injected into BT474 mice with iRGD over the course of 20 hours. Tumors were harvested at various time points post injection. Images were all acquired using the same laser and aperture settings. Images with the highest antibody signal from each slide are shown on the left. In general, an increased uptake of antibody was observed over the course of 20 hours, with more uptake visible in iRGD-treated animals compared to saline controls. A control tumor with no antibody injected is presented. Lycopersicon esculentum lectin signal was variable across all tumors and thus is not presented (scale bars = 0.2 mm).

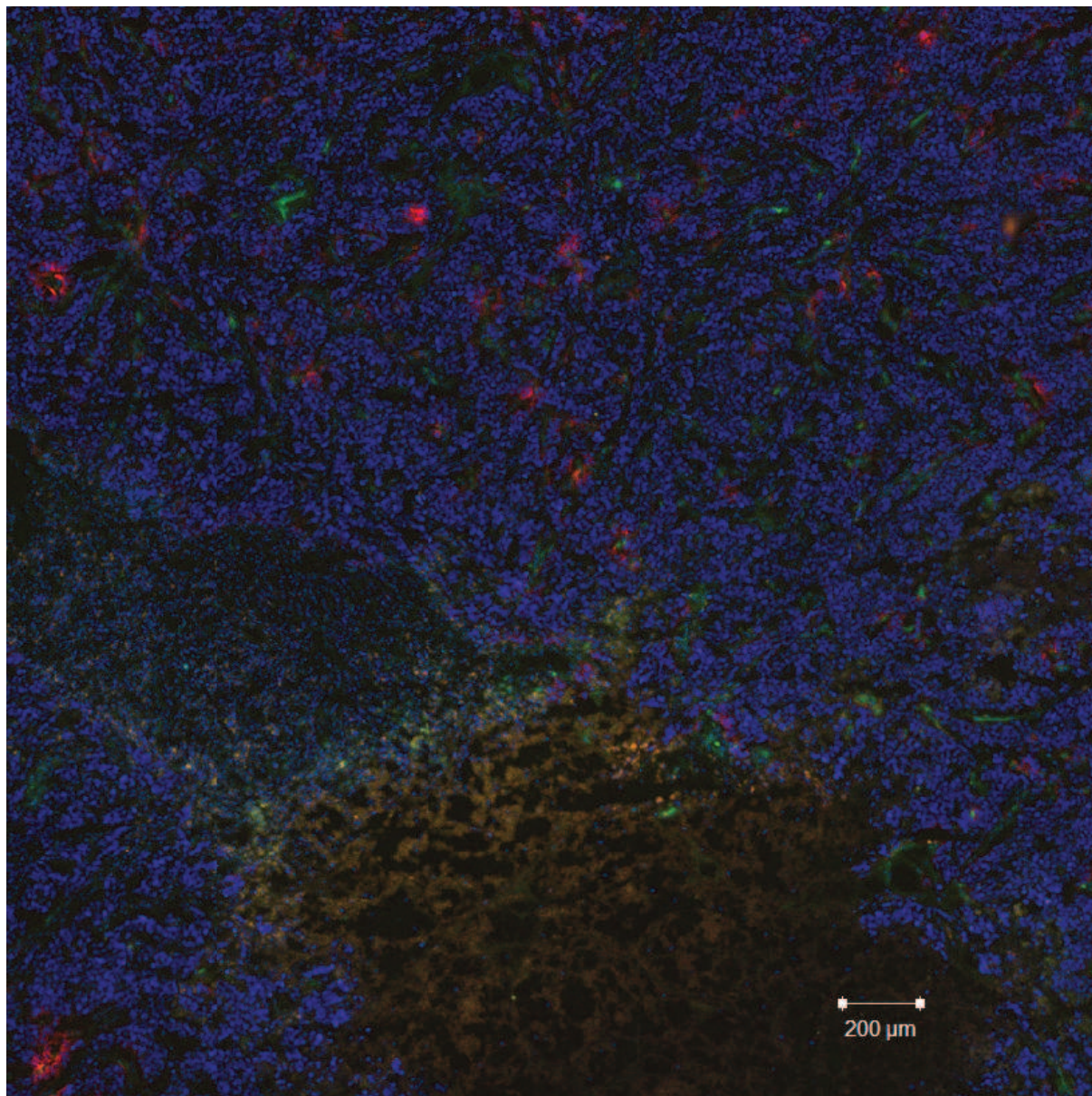


Figure 5.12: Tiled images of a BT474 tumor treated with iRGD and Alexa-633 labelled Herceptin antibody and harvested 3 hours post injection. Distribution of antibodies (red) vary greatly across the tumor, with several concentrated regions of antibody uptake (blue: DAPI, green: lycopersicon esculentum lectin, orange: matrigel plug, scale bar = 0.2 mm).

Noninvasive imaging represents an interesting alternative approach to monitor iRGD efficacy. In particular, MRI can provide high-resolution images of tumor tissue with no ionizing radiation. Further, dynamic MRI can monitor physiological changes in the tumor in real time.

5.4.1 DCE-MRI

We designed the DCE-MRI protocol used in this study with consideration for its direct clinical applicability. Gd-DTPA is a clinically approved CA which is widely used to quantitatively evaluate tumor vascular permeability preclinically and clinically and has a short plasma half-life (<12 minutes in murine models). Since iRGD was shown to improve the uptake of small molecule doxorubicin [49], we hypothesized that it would also increase the uptake of Gd-DTPA. Pre- and posttreatment DCE-MRI scans were obtained in the same animal to account for the tumor response variability between subjects; a critical factor for patient studies. This variability also motivated the need to treat the same tumor with all three different conditions. A key assumption made here is that PAF and iRGD have short acting time windows (<12 hours). We believe that this was reasonable based on previous reports showing that both PAF and iRGD have high activity within 3 hours of administration [267, 49]. Other classes of small molecule vasoactive agents also have short time windows of action (<3 hours) [258]. Furthermore, the plasma half-life of iRGD in mice is less than 10 minutes (private communication, A.R.), suggesting that very little, if any, peptide will be in circulation more than 12 hours post administration. The fact that baseline DCE-MRI parameters for different treatments, which were obtained on separate days, did not differ significantly from each other also supported this assumption. Baseline scans were also obtained to account for intrasubject variability of DCE-MRI parameters over time, since this may change relatively quickly (~days) during the natural progression of preclinical tumor models [268].

Preliminary DCE-MRI results presented here suggest that DCE-MRI can monitor systemic administration of a potent vascular permeability modulating agent. Significant increases in vascular permeability (K_{trans}) and tumor extracellular volume (v_e) compared to saline control were observed in PAF-treated mice (table 5.2). PAF was chosen as the positive control in this study based on previous reports describing the ability of localized [269, 270] and systemically administered PAF [271, 267] to increase vascular permeability in a variety of tissues [272, 273]. Moreover, VEGF

pathway activation has been implicated as a factor for this increase [272, 273]. The neuropilin-1 receptor, which interacts with the cleaved-iRGD product, is also involved in the VEGF pathway [274, 243, 275, 244], specifically by increasing tissue vascular permeability [276, 277, 246]. We chose to deliver PAF systemically to mimic the administration of iRGD; the dose was chosen based on previous reports [271, 267] and preliminary toxicity studies. Increases in both K_{trans} and v_e are consistent with PAF's ability to increase tissue vessel permeability and to cause localized inflammation which would lead to delayed CA washout.

On average, iRGD-treated tumors showed a slight increase in K_{trans} above baseline compared to saline treatment, but this increase was not significantly different. This suggested that a vascular permeability effect is present, but is lower than that effected by PAF. No observable v_e deviations from baseline was seen. The latter observation suggests that the extracellular space in the tumor does not expand due to iRGD, suggesting that the CA may be taken up by cells.

Since vascular permeability parameters (and changes compared to baseline) were heterogeneous throughout the tumor (figure 5.5), we stratified tumor voxels according to the presence of viable vessels (defined by K_{trans}) and distance from the tumor edge. PAF caused a significant increase in all K_{trans} values across the whole tumor, highlighting its potency. In contrast, K_{trans} increases were greater in iRGD-treated tumors as a function of voxel K_{trans} status. Tumor voxels with higher K_{trans} values most likely contain higher density of viable vessels. Thus, increases in vascular permeability should be most visible in these regions. v_e did not change at the lowest K_{trans} voxels, corresponding to poorly enhancing regions. v_e increases observed for PAF-treated tumors are consistent across other K_{trans} values. We did not observe any trends in K_{trans} or v_e values as a function of distance from the tumor edge. Voxels were analyzed only if a reasonable parameters were able to be fitted. Thus, the matrigel plug and obvious central necrotic regions that are visible in certain tumors were excluded from analysis.

A semiquantitative metric, AUC, showed similar trends between cohorts as the pharmacokinetic model parameters. Along with the good model curve fits (figure 5.2), this suggests that pharmacokinetic modeling can be applied to the current dataset.

Quantitative DCE-MRI, especially in small animals, is challenging. Several factors can affect the output parameter values. To keep relatively good spatial coregistration between pre and

posttreatment DCE-MRI data, mice were kept lightly anesthetized in the animal holder between imaging sessions. Isoflurane is a vasodilator and increases vascular permeability via caveolae transport [278]. Studies with Gd-DTPA-Albumin showed that anesthesia induction with isoflurane can cause increased CA extravasation from vessels [279]. A study with a similar protocol as our study (maintainance of anesthesia using 2% isoflurane for 4–5 hours) did not show a demonstratable K_{trans} increases between the two imaging sessions [280]. Caveolae are not necessary for the hyperpermeable tumor vascular phenotype [281], but their role in iRGD activity remains unknown. Another confound is the acquisition of the AIF. Image-derived AIF can be corrupted by flow and motion artifacts. AIFs used in this study were comparable to literature [264, 263]. A population-based AIF or the use of a reference region based DCE-MRI analysis method [84] can be used to verify the consistency of these results. The small size and contrast generating mechanism of Gd-DTPA may also have confounded results. Since tumor vasculature is hyperpermeable, Gd-DTPA may leak through the tumor vessels regardless of the presence of iRGD. Although not clinically approved, larger-sized CA such as Gd-DTPA-Albumin may be more sensitive to permeability changes [282]. Further, the long half-life of such agents may enable the pharmacodynamics of iRGD to be visualized. Previous results suggest that iRGD may mediate uptake of agents by tumor cells [48]. The lack of observable v_e increase supports this. Signal intensity changes caused by intracellular Gd-agents are significantly attenuated compared to their extracellular counterparts, since the water compartment within organelles and the cytoplasm are small and water exchange with external compartments can be slow [283]. An alternative method of MRI visualization that is less affected by these issues is the use of R_2^* -agents such as iron oxide particles [284, 78]. Studies using these different types of agents are being pursued in the lab.

5.4.2 PET/MRI

Sugahara *et al.* showed that iRGD increased Herceptin uptake in BT474 tumors [49]. Thus, we hypothesized that this uptake could be observed with PET, coregistered with diffusion MRI. The DCE-MRI protocol in the MRI-only study was not used here because its MRI gradient requirements made temperature control of the PET difficult. Diffusion MRI can be sensitive to sudden changes in vascular permeability [285]. We hypothesized that this technique may also be sensitive to iRGD

effects.

While certain animals treated with iRGD did show increases in both ADC values and radio-labelled antibody uptake (figures 5.8 and 5.9), no significant differences were observed for either biomarker between saline and iRGD-treated cohorts overall. An increase in antibody uptake for iRGD-treated animals compared to control was present 1 hour post injection, but the difference was not prolonged into later time points. Unfortunately, no ADC images were acquired with the 1 hour PET images; so no intratumoral structural information was available to guide our PET image interpretation.

Histological results were variable. Visual inspection of random tumor regions suggested that slightly higher antibody uptake was present overall in iRGD-treated tumors. Yet there were some saline-treated tumors that also exhibited high antibody uptake. Antibody distribution showed high intratumoral variability. A method that allows histological visualization of large tumor volumes, such as the VIBRA-SSIM technology (D. Koos, S. Fraser, Caltech), would complement current imaging studies by providing a complete picture of tumor microstructure and intratumoral antibody uptake.

5.4.3 Conclusions

Preliminary results outlined in this chapter did not show dramatic changes in vascular permeability (using DCE-MRI) nor antibody uptake (using PET and optical imaging) due to iRGD. Concurrent studies using the same mouse tumor model, using luciferase, different radiolabelled agents (e.g. minibodies) and treatment response as alternative readouts of iRGD reported similar variable results (private communication, A.R.). Several issues need to be considered when evaluating these results apart from those discussed above. Firstly, PET and MRI may be too insensitive to the changes caused by iRGD. If the changes occur in concentrated regions within the tumor, then partial volume effects may average out the iRGD effects. The heterogeneity of tumor iRGD response, as observed in the DCE-MRI results presented here, is an important factor that needs to be considered and may explain the variability of the histology and the results from the communicated treatment response studies. Secondly, the current iRGD is monovalent. This may not efficiently activate the neuropilin-1 receptor, since its signalling requires dimerization or multimerization [50]. A mul-

imeric form of iRGD may interact with neuropilin-1 better than monomeric iRGD and result in enhanced downstream effects. Another consideration is the applicability of the mouse tumor model for these studies. Tumor growth in mice are much faster than in humans. Thus, one would expect the angiogenic process to be quite different to human tumors too. BT474 was chosen as the model system based on previous reports showing the good neuropilin-1 receptor expression in this cell line [48] and good iRGD response [49]. However, other investigators reported that BT474 actually show low neuropilin-1 expression in their hands [286]. Others have also reported that $\alpha_v\beta_3$ integrin expression are low in BT474 tumors [287]. This suggests that the development of suitable cancer mouse models for certain applications remains very challenging. Human tumor pathology and treatment response may be significantly different to their animal counterparts. Of course, our discussion assumes that the proposed mechanism of action of iRGD is accurate. In light of these results, it will be important to elucidate and verify iRGD's mode of action in more basic studies.

Ultimately, the clinical efficacy of iRGD and the applicability of noninvasive imaging to monitor iRGD effects may only be determined by pursuing human studies. Imaging and analysis techniques developed in this chapter will be directly applicable to these pursuits.

Chapter 6

Summary and Future Work

6.1 Summary

Three major contributions were made in this work:

- A small animal simultaneous PET/MRI system was developed to enable robust intratumoral imaging *in vivo*.
 - We developed image coregistration techniques that align simultaneously acquired PET and MRI images to subvoxel accuracy.
 - We characterized the interference effects between the PET and MRI instrumentation in the hybrid system. We showed that quantitative, dynamic PET/MRI studies can be performed with the hybrid PET/MRI system with minimal distortions to either the PET or MRI images.
 - A method was developed to enable the precise spatial coregistration of PET/MRI and DWBA images obtained from the same animal subject. This method was used to demonstrate that the hybrid PET/MRI system returns tumor images that are commensurate with intratumoral activity distributions in the underlying tissue.
- The diffusion MRI technique was adapted to monitor the response of the cancer nanotherapy CRLX101
 - We showed that diffusion MRI is sensitive to CRLX101 response within 2 days of treatment and before significant tumor size changes were observed.

- Model-based analysis of the diffusion MRI data was able to predict the antiproliferative effects of CRLX101 and the reduced antiproliferative effect of CPT-11 by comparison.
- PET and MRI techniques were developed to monitor the effects of the tumor-penetrating peptide iRGD
 - DCE-MRI was able to visualize increased vascular permeability and extracellular volume due to PAF-administration.
 - DCE-MRI did not show significant differences in vascular permeability and extracellular volume due to iRGD-administration.
 - PET/MRI studies showed that iRGD responses can be variable and may be tumor growth-dependent.

6.2 Future Work

6.2.1 Next Steps for Hybrid PET/MRI

Catana and Peng outlined a road map for the potential of hybrid PET/MRI [106, 142]. Since their discussions, the field of hybrid PET/MRI has grown substantially. In light of the current work, we elaborate on some of the points they raised and add to the PET/MRI roadmap .

6.2.1.1 Hardware

The major motivation for our work in sections 3.2 and 3.4 is the belief that the availability of high-resolution PET information to synergize with high-resolution information provided by anatomical and functional MRI will be an important motivator for the adoption of PET/MRI technology. Hardware for next-generation systems will be driven partly by this motivation. Increasing the number of detectors in the system and incorporating DOI capability to each PET detector will improve the sensitivity of the system, reduce parallax errors and enlarge the axial FOV. DOI can be implemented by placing PSAPD detectors on both ends of the scintillation crystal array. Decreasing the scintillation crystal size from $1.5 \times 1.5 \text{ mm}^2$ to $1 \times 1 \text{ mm}^2$ can improve the spatial resolution to close to 1 mm at the center of the FOV. The number of detector rings can be increased from 1 to 4. These

modifications can extend the axial FOV up to 6 cm (sufficient for whole body mouse scans) and improve the sensitivity of the system to 20%–30% [213]. The enlarged FOV will improve the time efficiency of small animal PET/MRI studies, as the animal can remain static during the whole study. Increased sensitivity of the PET system will be very important for combined dynamic PET/MRI studies since each time bin for these studies will contain low activity counts.

A major challenge towards this goal is to design PET detectors, and a system that house these detectors, that will fit within the confined space imposed by the MRI system. An obvious solution is to miniaturize all the parts that are found in the current system. However, the presence of more electronics in the same volume may amplify the shielding and temperature challenges (e.g. section 3.6) that underlie the current technology. These challenges can only be explored and met as the next system is being built. Methods developed in this and previous works will aid in evaluating new systems at each stage of development.

6.2.1.2 Software

Concurrent PET and MRI datasets can be used to improve the data quality of each separate dataset. Some active avenues of research in this area were outlined in section 2.3.3. One important line of research is the development of partial volume correction techniques for reconstructed PET images using MRI information. Current studies are restricted to phantom explorations and/or lack gold standard verification [288, 289]. The availability of datasets such as those in section 3.4) will be useful to verify these techniques in *in vivo* situations.

6.2.1.3 Applications

Widespread adoption of PET/MRI technology will be dependent on the utility of its applications. There is no doubt that PET and MRI information are synergistic, but as mentioned in section 2.3.3, it will be the necessity of near-simultaneous PET/MRI data acquisition that will drive hybrid system development.

Verification of Image-based Models. We used a diffusion MRI-based model of tumor growth to understand treatment response of a cancer nanotherapy. The model can be improved by introducing more measurable parameters, which PET/MRI can provide. For example, tumor glycolytic and pro-

liferation information from ^{18}F -FDG and ^{18}F -FLT images can be fed as the proliferative parameter in the logistic model [208]. Conversely, the robustness of parameters derived from a unimodal model (e.g. diffusion MRI only) can be verified with information obtained from the alternative modality (figure 6.1).

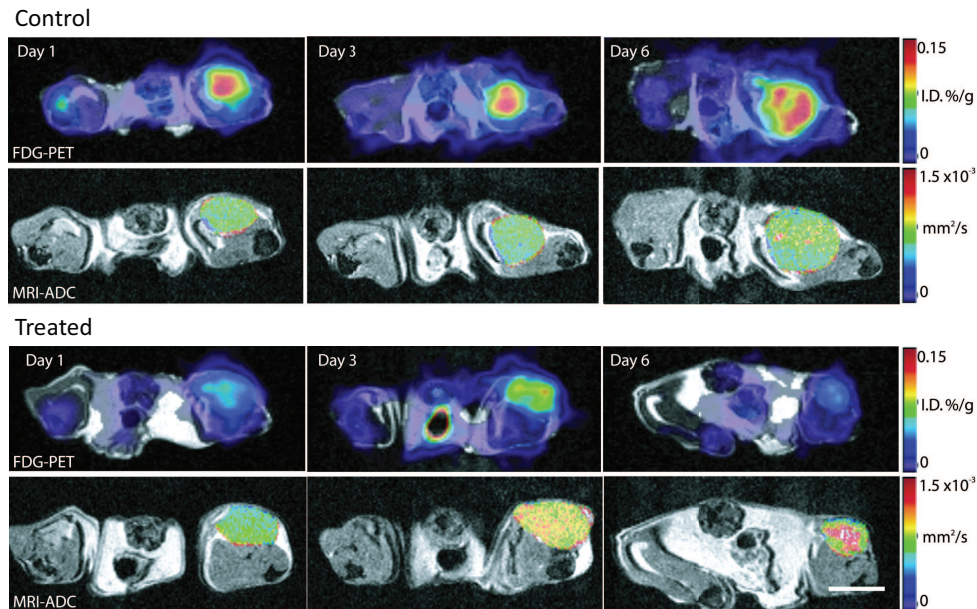


Figure 6.1: Simultaneous PET/MRI data can analyzed with image-based models. Availability of simultaneous PET/MRI data, such as the FDG-PET/diffusion MRI data shown here, can be integrated into multimodal models of tumor growth or be used to verify unimodal models. FDG-PET/diffusion MRI images were acquired in mice treated with cyclophosphamide or saline and followed over the course of a week. (Scale bar = 10 mm).

Improved PET and MRI quantification. Quantification of PET is challenging and is the subject of numerous investigations. In section 3.4 we showed that PET images from a small animal PET/MRI scanner return good quantitative images. This was aided by the fact that attenuation effects of tissue and bone in small animals on 511 keV photons are minimal. Robust quantitation of PET images in larger animals and patients requires good attenuation correction. Availability of temporally and spatially coregistered PET/MRI images will provide accurate anatomical maps (from MRI) that can be used to correct PET datasets. However, since MRI does not provide direct measures of photon attenuation, it will be important to determine optimal ways to convert the MRI data into attenuation maps.

Similarly, quantification of MRI signals can be complex. MRI image intensities can be mod-

ulated by several mechanisms, ranging from the intrinsic relaxation properties of the underlying tissue, the type of pulse sequence being used, to the presence of CA. In particular, quantification of “smart” MRI CAs that are sensitive to physiological changes *in vivo* would benefit from the availability of concurrent PET data. The PET data aids the interpretation of the MRI signal changes. An example of this concept has been shown by Frullano *et al.*, who developed a bimodal PET/MRI probe that is sensitive to pH [90]. PET imaging of this probe provided its concentration. This concentration information was then used to normalize the MRI relaxation information to determine pH.

In chapter 5, we demonstrated the utility of quantitative pharmacokinetic modeling to study physiological processes. Most kinetic models require an AIF to derive quantitative parameters. Spatially coregistered MRI images can guide ROI delineation for imaged-derived AIFs for PET (figure 5.2, [290]). Alternatively, bimodal CAs can be used in conjunction with the hybrid instrumentation to allow the AIF to be obtained using one modality (optimized to collect AIF data) while tissue information can be obtained with the other modality (optimized to collect information from the tissue).

Real time PET/MRI-guided imaging. The availability of near-perfect spatially coregistered PET/MRI images will allow one modality to guide image acquisition by the other modality in real-time. For example, rapid location of tumor metastases by PET can inform the choice of the specialized functional or anatomical MRI imaging sequence, which can vary depending of the location being imaged, to pursue in the same study session. Another area of study where real-time analysis of simultaneous PET/MRI can have a big impact is in the area of cardiology and peripheral vascular disease. PET or PET/MRI visible probes targeted to vascular inflammation or early atherosclerotic plaque formation can be located by PET, followed by high-resolution MRI of the anatomy around the highlighted region [186]. These types of studies are not only time efficient, but the combined imaging technique can be potentially more sensitive and specific than the single modality tests currently available.

Multimodal studies of uptake and response. The current work developed a PET/MRI strategy to follow the uptake and response of cancer nanotherapy where simultaneity of image acquisition

is important. Future studies can build upon the initial results presented here. In particular, PET insert-compatible DCE-MRI in combination of radiolabelled nanotherapies will allow us to further understand the interactions between tumor structure and drug uptake. Another realm of inquiry where multimodal PET/MRI will be useful is the monitoring of immunotherapy. Multimodal immunotherapy, such as the combination of *in vivo* cell and cytokine therapies, act synergistically in short time scales. Near-simultaneous PET/MRI will be useful here to monitor real-time biodistribution and interactions between these therapies at an organ-level scale.

6.2.2 Translational Considerations

In this work, we developed noninvasive imaging techniques to understand cancer nanotherapy uptake and response in the preclinical setting. Unimodal or multimodal preclinical imaging provide important links between basic biological studies and their clinical application. Ultimately, the success of these preclinical studies will be gauged by whether they can positively impact patient care. Simultaneous PET/MRI systems are being introduced in the clinic; the methods and imaging approaches developed here are directly applicable for use in these systems. The diffusion and DCE-MRI protocols described herein are currently being adopted for clinical trials. It will be very important in future studies to verify the applicability of these protocols in human patients. Concurrently, methods developed in this thesis can be used to match imaging information to volumetric microscale data (DWBA/histology) and to infer mechanistic insights (via image-based modeling), both of which can inform the basic development of next-generation therapies.

It is hoped that the techniques and advances described herein will contribute in some way towards the collective effort against cancer.

Appendix A

A Study of the Timing Properties of Position-sensitive Avalanche Photodiodes

This paper describes work done in collaboration with Simon Cherry's group at the University of California, Davis. The timing of scintillation signals emanating from different areas of the PSAPD surface were found to be related to the distance from readout pins. An algorithm was developed to normalize for this effect for PSAPD detector-based PET systems. I was involved in the setup of the experimental apparatus to characterize the PSAPD timing properties and contributed software towards the implementation of the algorithm.

This section is published in *Physics in Medicine and Biology*: Yibao Wu, Thomas S. C. Ng, Yongfeng Yang, Kanai Shah, Richard Farrell, and Simon R. Cherry (2009) A study of the timing properties of position-sensitive avalanche photodiodes. *Physics in Medicine and Biology*, 54 (17). pp. 5155-5172.

Published in final edited form as:

Phys Med Biol. 2009 September 7; 54(17): 5155–5172. doi:10.1088/0031-9155/54/17/006.

A study of the timing properties of position-sensitive avalanche photodiodes

Yibao Wu¹, Thomas SC Ng², Yongfeng Yang¹, Kanai Shah³, Richard Farrell³, and Simon R Cherry¹

¹Department of Biomedical Engineering, University of California, Davis, CA 95616, USA

²Beckman Institute, Department of Biology, California Institute of Technology, Pasadena, CA 91125, USA

³Radiation Monitoring Devices, Inc. Watertown, MA, USA

Abstract

In this paper we study position-dependent timing shifts and timing resolution in position sensitive avalanche photodiodes (PSAPDs) and their effect on the coincidence window used in positron emission tomography (PET) systems using these devices. There is a delay in PSAPD signals that increases as the excitation position moves from the corner to the center of the device and the timing resolution concurrently worsens. The difference in timing between the center and corner can be up to 30.7 ns for a 14×14 mm² area PSAPD. This means that a PSAPD-based PET system could require a very wide coincidence timing window (>60 ns) if this effect is not corrected, although the individual crystal pairs still have full-width half-maximum (FWHM) timing resolutions better than 7.4 ns. In addition to characterizing the timing properties of PSAPDs, two correction methods were developed and applied to data from a pair of PSAPD detectors. These two timing offset corrections reduced the timing shift of a crystal pair from 52.4 ns to 9.7 ns or 1.3 ns, improved FWHM timing resolution of the detector pair from 24.6 ns to 9.5 ns or 6.0 ns and reduced the timing window (sufficient to cover at least twice the FWHM for all crystal pairs) from 65.1 ns to 22.0 ns or 15.2 ns respectively. A two-step timing alignment method is proposed for a PET system consisting of multiple PSAPDs. Lastly, the effect of PSAPD size on the timing performance was also evaluated.

Keywords

photodiodes; photodetectors; instrumentation; PET

1 Introduction

The use of position sensitive avalanche photodiodes (PSAPDs) is emerging as an interesting alternative to traditional photodetector technology such as photomultiplier tubes (PMT) for positron emission tomography (PET) detector development (Shah *et al.*, 2004; Catana *et al.*, 2006; Zhang *et al.*, 2007; Yang *et al.*, 2008). The small size of PSAPD-based detectors compared to more bulky PMT-based types may be advantageous for use in confined geometries. Compact detector designs possible with PSAPDs allow for scanner configurations with increased sensitivity and high and uniform spatial resolution. PSAPDs also have high

Yibao Wu, PhD, Department of Biomedical Engineering, University of California, Davis, Genome and Biomedical Sciences Bldg., 451 East Health Sciences Dr., Davis, CA 95616. Tel: 530-752-2809, fax: 530-754-5739, ybwu@ucdavis.edu.

PACS: 85.60.Dw, 85.60.Gz, 87.57.uk

quantum efficiency, a wide spectral response and are insensitive to magnetic fields (Pichler *et al.*, 2006). Thus, PSAPD-based PET detectors have been adapted for applications such as depth-of-interaction (DOI)-encoding (Yang *et al.*, 2008) and MR-compatible PET systems (Catana *et al.*, 2008). Although one of the main advantages of using PSAPDs compared to conventional avalanche photodiodes (APDs) is the significant reduction in the number of electronic readout channels, this technology also presents challenges compared to APD- and PMT-based detectors. The most obvious, though most easily addressed, challenge is the pin-cushion distortion of spatial positional readout information due to the non-linear fashion in which charge is shared among the four corner anodes (Shah *et al.*, 2004). Several groups have proposed both software (Despres *et al.*, 2007; Zhang *et al.*, 2007; Chaudhari *et al.*, 2008) and hardware (Grazioso *et al.*, 2002; Shah *et al.*, 2002) solutions to correct or account for this distortion for flood map histogram discrimination. One other notable effect that our group has observed is the apparent time shift between signals originating from the center of the PSAPD versus those from the edges or corners. Previous studies have noted a timing shift of up to 25 ns (Catana *et al.*, 2006). This has been attributed to the resistive readout present on PSAPDs. In order to maintain the high spatial resolution offered by a crystal array setup while capturing all coincidence events, a wide timing coincidence window of 80 ns is currently used in our PSAPD-based detectors. Here, we further characterize the time difference of signals originating from different positions on the PSAPD and explore their dependence on the size of the PSAPD. Using this information, we propose an approach to correct the timing signal after signal read out from the detector to the data processing portion of the system. The ability to correct for this timing shift will improve the timing resolution of a crystal array/PSAPD-based detector and reduce sensitivity to random events via much tighter coincidence windowing.

2 Materials & Methods

2.1 Timing shift and timing resolution at various locations on PSAPD surface

To determine the timing shift and timing resolution at different locations on the surface of a PSAPD, an experimental setup was built as shown in Figure 1. A 14×14 mm² PSAPD was coupled to three individual LSO crystals each of size $1.43 \times 1.43 \times 6$ mm³. The crystals were polished on all sides and wrapped with teflon tape on five sides except the one coupled to the PSAPD. The three crystals were placed at three representative locations, corner, edge and center, using a positioning guide made of teflon. Optical coupling between the LSO crystals and PSAPD was accomplished using optical grease (BC-630, Saint-Gobain Ceramics & Plastics, Inc., Newbury, OH). A PMT (R580, Hamamatsu, Hamamatsu City, Japan) coupled to a single LSO crystal with size of $1.5 \times 1.5 \times 20$ mm³ was used as the timing reference. The separation between the front surfaces of the two detectors was 60 mm. A ²²Na point-like source with activity 23 μ Ci was placed at the center of the setup.

The signal from the PMT was buffered with a fan-out unit (740, Philips Scientific, Mahwah, NJ); one output was fed to an ORTEC 584 constant fraction discriminator (CFD) (Advanced Measurement Technology, Inc., Oak Ridge, TN) and the generated trigger was used for PMT timing. The delay for the CFD was ~ 3 ns. Another fan-out output was shaped with a shaping amplifier (N568B, CAEN Technologies, Staten Island, NY) and fed to a data acquisition (DAQ) board (PD2-MFS-2M/14, United Electronic Industries, Inc., Walpole, MA). The shaping time was 1 μ s.

Signals from the PSAPD were first amplified with 5 CR-110 charge sensitive pre-amplifiers (Cremat, Watertown, MA). The cathode signal from the PSAPD was then shaped using a fast filter amplifier (ORTEC 579) with a differentiation and integration time of 10 ns and fed to a CFD to generate the timing signal for the PSAPD. The shaped signal from the corner was observed to have a rise time of 55 ns and fall time of 110 ns and the signal from the center had a rise time of 80 ns and fall time of 160 ns. The delay for the CFD was ~ 45 ns. The 4 anode

signals from the PSAPD were shaped using the N568B shaping amplifier with a shaping time of 1 μ s and recorded by the data acquisition system.

A coincidence trigger was made from the timing signals obtained from the PMT and PSAPD using a coincidence unit (Philips Scientific 756). The trigger was then delayed and width-extended using a delay and gate generator (ORTEC 416A) before being sent to the DAQ system as the trigger. The coincidence timing window 2τ was set to 88 ns where τ was the width of the trigger signals from the PMT and PSAPD. To ensure correct timing for coincidence processing, a delay of 72 ns was introduced to the PMT timing signal before being passed to the coincidence unit to account for the intrinsic timing delay between PMT and PSAPD signals. The position-dependent timing difference between the PMT and PSAPD was measured with a time-to-analog convertor (TAC) unit (ORTEC 566). The PMT timing signal was used as the start signal and the PSAPD timing signal was used as the stop signal. The output was recorded by the DAQ system. In-house developed DAQ software was used to store the raw data (Judenhofer *et al.*, 2005).

The timing spectrum for each crystal was generated and analyzed. The centroid of the timing spectra (with respect to an arbitrary reference time) and the full-width at half-maximum (FWHM) of the timing spectra (corresponding to the timing resolution) were calculated for each crystal. The timing shift is defined as the difference in the centroid locations for events occurring in two different crystals. The CFD thresholds were set just above the noise (~ 60 keV) and no software energy windows were applied, either for the PMT or PSAPD signals.

2.2 Timing shift and timing resolution of a crystal array on a PSAPD

A setup similar to Figure 1 was used to measure the timing shift and timing resolution of a complete LSO crystal array on a PSAPD. The individual crystals on the PSAPD were replaced with an array consisting of 8×8 crystal elements, where the size of each element was $1.43 \times 1.43 \times 6$ mm³. The dimension of the whole array was $12 \times 12 \times 6$ mm³ thus it covered 73% of the area of the PSAPD. The array was centered on the PSAPD with a positioning guide made of teflon. The single crystal on the PMT was replaced with an LSO crystal array. The crystal array was composed of 12×12 individual crystals with size of $1.51 \times 1.51 \times 10$ mm³ and the size of array was $19.2 \times 19.2 \times 10$ mm³. An LSO array was used on the PMT because it is impractical to perform the experiment using the movable stage with a point source. The ²²Na source was replaced with a cylindrical ⁶⁸Ge source and placed at the center of setup. The cylindrical source had a diameter of 25 mm and a length of 50 mm, and its activity was 71 μ Ci. A cylindrical source was chosen to avoid constrained solid angles that might bias the results. The separation between the front surfaces of the two detectors was 120 mm and the source was placed at the center of the setup.

The digitized timing and energy data were acquired, and the flood histogram was generated with the energy data and segmented with a method modified from (Chaudhari *et al.*, 2008). The timing data were assigned to each crystal based on the crystal lookup table (LUT). Timing spectra were generated and the shift of the centroid of the timing spectrum and the timing resolution of each crystal measured. The spectra of the three selected locations closest to the ones described in Section 2.1 were compared to the results obtained with the individual crystals.

2.3 Timing shift and resolution between a pair of crystal array-PSAPD detectors

The experimental setup shown in Figure 2 was used to measure the timing shift and timing resolution between two PSAPD detectors. The same 8×8 LSO arrays described in Section 2.2 were centered on the PSAPDs with positioning guides made of teflon. Coincidences were determined directly from the two detector triggers. The timing window 2τ was 88 ns. A delay of 64 ns was added to the timing signal of one PSAPD, which was then used as the stop signal

for TAC. This PSAPD detector is denoted ¹⁶³PSAPD1. The other PSAPD detector is used as the start signal for the TAC and is denoted PSAPD2. The separation between the front surfaces of the two detectors was 120 mm and the same ⁶⁸Ge source was placed at the center of setup.

To collect sufficient information for timing alignment, a cylindrical source was chosen which was large enough to cover coincidence events between all individual crystal pairs. This measurement does not require that all pairs have exactly the same number of events. If a point source had been used, the overall timing spectrum might be artificially narrow because only a few LORs are intersecting the source.

Flood histograms and crystal LUTs were generated from the data acquired. Each event was assigned to a pair of crystals based on crystal LUTs. The timing spectrum for each pair of crystals was created and the shift of the timing centroid and the FWHM timing resolution of each pair calculated. In addition, a corner crystal on PSAPD2 was chosen as a reference crystal and the shift in the timing centroid and the FWHM timing resolution of all the crystals in the PSAPD1 detector with respect to this crystal were calculated.

2.4 Timing alignment using PMT-based detector as a reference (Method 1)

To improve the timing resolution of the pair of detectors and therefore reduce the coincidence timing window required, the timing shift differences between individual crystal pairs need to be corrected by applying a calibration offset to each pair. All PET systems generate coincidence events from single events in a coincidence unit, either in hardware or software, either centralized or distributed. A direct time alignment approach can be implemented in the coincidence processing unit, during coincidence processing, where the timing shifts of all crystal pairs are aligned by applying an offset to each crystal pair. However, this approach is not practical for two reasons. Firstly, the offset lookup table required is large, on the order of N^2 , where N is the total number of crystals in the whole system. Secondly, it requires complex coincidence logic; a wide coincidence window is still needed initially to find all possible coincidence events. The offset would then need to be applied from the offset LUT. Only at this point can coincidence events within a narrower coincidence window be selected. In contrast, a component-based approach can be implemented in either the coincidence or single event processing units. The difference here from the direct method is that the offset is applied to each single event using the offset value for the corresponding crystal before forming a coincidence event.

For the component-based approach, there are two ways to generate the offset LUT. One is to use a PMT-based detector as a reference, i.e. use the timing offset table derived from the timing data from a crystal array/PSAPD detector with a PMT-based detector. This would use the data generated in Section 2.2, and will be called Method 1. Method 2 uses offset tables derived from timing data obtained from a pair of PSAPD detectors, and is discussed in the next section.

For Method 1, each PSAPD can use either the same timing offset LUT (assumes timing shifts are invariant across different PSAPDs of the same size) or LUTs can be obtained for each detector separately (not studied here) in reference to a PMT-based detector. Although each individual offset LUT includes a fixed value which incorporates the intrinsic timing delay between the PMT and PSAPD signals, this cancels out if the same offset LUT is used for the two PSAPDs. A difference between the two fixed values will be included if different offset LUTs are used. However, this is not an issue for alignment correction because these timing differences only change the mean value of final timing spectra. This mean value can be subtracted. Implementation of this is further discussed in Section 4.2.

In a PET system, individual time alignment LUTs can be acquired if the detectors can be removed for individual measurement or the system has spare readout channels to insert a timing

164
 probe (Moses and Thompson, 2006) to determine multiple LUTs simultaneously. Here, we compare the use of a single, common offset LUT applied to both PSAPD detectors (Method 1) versus the use of a unique LUT for each detector (Method 2). The hypothesis is that if the timing differences are dominated by effects intrinsic to the PSAPD design, then a single common offset LUT may be sufficient for accurate time alignment. In this case, the two methods should give similar improvements in timing resolution. All offset tables were applied with a step-size of 0.3125 ns to mimic the resolution of typical commercial PET electronic systems (Musrock *et al.*, 2003).

The timing spectra after offset correction were calculated and compared with the results obtained before correction. A coincidence timing window was calculated that would be sufficient to cover at least twice the FWHM for all crystal pairs. To calculate the overall timing window, the left ($TW_{left,i,j}$) and right ($TW_{right,i,j}$) boundaries of the individual timing window were first calculated for each crystal pair using Equations 1 and 2, where $TS_{i,j}$ is the timing shift between crystal i from PSAPD1 and crystal j from PSAPD2 forming this pair and $FWHM_{i,j}$ is the timing resolution. The overall timing window width $TWW_{overall}$ was then calculated with Equation 3. For calculating the overall timing window after correction with Method 1, the timing shift $TS_{i,j}$ was replaced by the timing shift after correction $TS_{i,j} - (TS_{i,PMT} - TS_{j,PMT})$.

$$TW_{left,i,j} = TS_{i,j} - FWHM_{i,j} \quad (1)$$

$$TW_{right,i,j} = TS_{i,j} + FWHM_{i,j} \quad (2)$$

$$TWW_{overall} = \max_{i,j}(TW_{right,i,j}) - \min_{i,j}(TW_{left,i,j}) \quad (3)$$

2.5 Timing alignment using a pair of PSAPD-detectors (Method 2)

Method 2 generates two different LUTs, one for each PSAPD-detector in a pair. This may help improve the resultant timing spectra because the relative location of the crystal array coupled to the PSAPD can be slightly different for every detector and the arrays may also have slightly different characteristics, not to mention the potential timing delay differences between each PSAPD in the system. Moreover, Method 2 can be implemented without the need to remove the detectors from a system and without the use of additional electronics channels to attach external probes.

Two timing offset LUTs were generated from the data obtained with a pair of LSO array-PSAPD detectors. M_{TS} , the mean value of the timing shifts was first calculated using Equation 4 where $TS_{i,j}$ is the timing shift between crystal i from PSAPD1 and crystal j from PSAPD2 and N is the total number of crystal elements in one detector (here it was 64). The timing offset values for each crystal i from PSAPD1 ($TO_{1,i}$) and crystal j from PSAPD2 ($TO_{2,j}$) were calculated with Equations 5 and 6. To compare with the results obtained with Method 1, the offset LUTs were manually shifted to have the same mean value $M_{TS,PMT}$ as Method 1 calculated using Equation 7. As per Method 1, these timing offset LUTs include an arbitrary fixed mean value $M_{TS,PMT}$, but this can be subtracted. For each pair, the offset $TOP_{i,j}$ was calculated using Equation 8 and applied to the timing data.

165

$$M_{TS} = \sum_{i,j} TS_{i,j} / N^2 \quad (4)$$

$$TO_{1,i} = M_{TS,PMT} + \sum_j (TS_{i,j} - M_{TS}) / N \quad (5)$$

$$TO_{2,j} = M_{TS,PMT} - \sum_i (TS_{i,j} - M_{TS}) / N \quad (6)$$

$$M_{TS,PMT} = \sum_i TS_{i,PMT} / N \quad (7)$$

$$TOP_{i,j} = TO_{1,i} - TO_{2,j} \quad (8)$$

The timing shifts and coincidence timing window (same definition as in Section 2.4) after timing alignment correction were calculated and compared with those obtained with no timing alignment in Section 2.3. For calculating the overall timing window after correction with Method 2, the timing shift $TS_{i,j}$ was replaced by the timing shift after correction $TS_{i,j} - TOP_{i,j}$.

2.6 PSAPD size effect on timing

With larger area PSAPDs, more detector elements can be decoded with one photodetector and less electronics channels are needed per unit detector area. Due to the finite deadspace of the packaging around PSAPDs, this also increases the packing fraction, potentially increasing the sensitivity that is of significance for PET applications. However, the timing shift is mainly caused by the capacitance of the PSAPD and the resistive readout on the anode side that provides spatial location information. Increasing the size of the PSAPD should increase the capacitance and cause greater timing shifts between different regions of the PSAPD. To explore this, we compared the timing shifts measured from a $20 \times 20 \text{ mm}^2$ PSAPD to those from a $14 \times 14 \text{ mm}^2$ PSAPD, using the methods described in Section 2.1. The signal from a corner crystal had similar rise time and fall time to those observed with the $14 \times 14 \text{ mm}^2$ PSAPD. As the signal from the center of a $20 \times 20 \text{ mm}^2$ PSAPD was very slow (rise time of $\sim 150 \text{ ns}$ and fall time of $\sim 300 \text{ ns}$), the timing shift was studied at two different CFD delays of 45 and 125 ns.

3 Results

3.1 Timing shift and timing resolution at various locations on PSAPD surface

Figure 3 shows the timing spectra at three representative locations on a PSAPD. The timing is measured relative to the PMT signal, so each centroid includes a fixed value corresponding to the timing delay between the PMT and PSAPD. The corner position had the fastest signal and the best timing resolution of 2.3 ns while the center position had the slowest signal and worst timing resolution of 3.9 ns. The timing shift between the corner and the center crystals was 30.7 ns. Because of this shift, current PET systems using PSAPD technology need a wide timing window to accept coincident events from all locations across the surface of the PSAPDs.

This necessarily increases the random events detected as well, decreasing the noise equivalent count rate (NECR), especially at high count rates.

3.2 Timing shift and timing resolution of a crystal array on a PSAPD

The timing characteristics for each crystal of an LSO array/PSAPD detector in coincidence with a PMT-based detector are plotted as a spatial distribution map in Figures 4a and 4b. The timing centroids had a standard deviation of 6.8 ns and the maximum timing shift was 26.9 ns. For timing resolutions, mean values of 3.4 ns with a standard deviation of 0.3 ns were observed with a maximum value of 3.9 ns and a minimum of 2.5 ns. The timing spectra for three crystal locations, corner, edge and close to the center are shown in Figure 4c. In agreement with the single crystal data, the results showed that corner locations had the fastest signal and best timing resolution of 2.8 ns and the central locations had slower signals and a worse timing resolution of 3.5 ns. The timing shift from the corner to center was 23.6 ns. The reduction in timing shift compared with the single crystal data of Section 3.1 is presumably due to some light sharing between crystals, which results in a greater spread of the scintillation light once it reaches the PSAPD surface.

3.3 Timing shift and resolution between a pair of crystal array-PSAPD detectors

The map of the centroids of the timing spectra is shown for each pair of crystals in Figure 5a and the histogram of these centroid locations is shown in Figure 5b. The 64 crystals in the array in Figure 5a are numbered horizontally with 1 corresponding to the top left corner, 8 to the top right corner and 64 to the bottom right corner of the array. The timing centroids had a standard deviation of 9.5 ns and the maximum timing shift was 52.4 ns. The timing resolution map and the corresponding timing resolution histogram for each pair of crystals are shown in Figures 5c and 5d respectively. A mean FWHM timing resolution of 5.2 ns with a standard deviation of 0.6 ns was measured, with a maximum value of 7.4 ns and a minimum value of 3.0 ns.

The centroid of the timing spectra and the timing resolutions for the crystals in PSAPD1 in coincidence with one corner crystal of PSAPD2 (opposing to the corner crystal on PSAPD1) are plotted in Figures 6a and 6b. Three representative locations were chosen and the timing spectra are plotted in Figure 6c. The results showed that the corner crystal had the fastest signal and timing resolution of 4.0 ns while the center had the slowest signal and worst timing resolution of 5.3 ns. The timing shift difference from the corner to the center was 23.8 ns.

3.4 Timing alignment using PMT-based detector as a reference (Method 1)

The timing offset LUT derived from Section 3.2 was applied to both PSAPDs. A map of the timing centroid for all crystal pairs after offset correction is plotted in Figure 7a (same scale as Figure 5a) and in Figure 7b (expanded scale). The histogram of the timing centroids is plotted in Figure 7c. The timing centroids had a standard deviation of 2.3 ns and the maximum timing shift was 9.7 ns. The measured averaged timing spectra of the pair of arrays before correction (red line) and after correction using Method 1 (green line) are plotted in Figure 10. The FWHM timing resolutions of the pair of arrays were 24.6 and 9.5 ns before and after correction respectively. The required timing window improved from 65.1 ns to 22.0 ns after correction.

From Figures 7a and 7b, it is apparent that using the same offset LUT to correct both PSAPDs does not align all crystal pairs evenly. The maximum residual timing shift of 9.7 ns is still greater than the worst FWHM timing resolution of 7.4 ns measured between crystal pairs, thus these residual timing shifts still are the primary determinant of the timing window. This suggests that using one LUT is not likely the optimal method for time alignment.

3.5 Timing alignment using a pair of PSAPD-detectors (Method 2)

The timing offset LUTs generated from the two individual PSAPDs are shown in Figure 8. PSAPD1 which was used in the LSO array-PSAPD versus PMT measurements had almost the same offset table as measured previously (Figure 4a) while PSAPD2 had slightly different behavior (difference up to 4.5 ns), although overall metrics were similar. The timing offset table of PSAPD1 had a mean value of 89.7 ns, standard deviation of 6.8 ns, a maximum value of 100.6 ns and a minimum value of 73.8 ns. The timing offset table of PSAPD2 had a mean value of 89.7 ns, standard deviation of 6.7 ns, maximum of 100.3 ns and minimum of 74.8 ns.

A map of the timing centroids for all crystal pairs after correction is shown in Figure 9a (same scale as Figure 5a) and in Figure 9b with expanded scale. The histogram of these centroids is plotted in Figure 9c. The timing centroids had a standard deviation of 0.2 ns and the maximum timing shift was reduced to just 1.3 ns. Compared to the results in Figure 7, no obvious correction bias to any particular crystal pair was observed in the map. A narrower timing centroid distribution was also seen. The measured averaged timing spectrum of the pair of arrays after this timing correction was applied is plotted in Figure 10 (blue line) and the FWHM timing resolution was measured to be 6.0 ns. The timing window necessary to cover twice the FWHM timing resolution for all crystal pairs was 15.2 ns.

The results without correction and with the two time alignment correction methods are summarized in Table 1. The timing resolutions of individual crystal pairs were the same with and without correction. The difference between the maximum and minimum of the timing centroids after correction was significantly reduced from 52.4 ns to 9.7 ns or 1.3 ns respectively, and the FWHM timing resolution was improved from 24.6 ns to 9.5 ns or 6.0 ns respectively. The timing windows that could be applied were reduced from 65.1 ns to 22.0 ns or 15.2 ns respectively. The correction with one offset table for each PSAPD (Method 2) gave better results than one offset table for all PSAPDs (Method 1).

3.6 PSAPD size effect on timing

Using a 45 ns CFD delay, the results from a larger 20×20 mm² PSAPD are plotted in Figure 11a. The center and edge crystals had very broad and asymmetric timing spectra with a FWHM of up to 13.9 ns. The left bump observed in the timing spectra of the center crystal in Figure 11a is probably caused by triggering on noise and the right bump is likely due to energy-dependent walk when the CFD operates as a leading-edge discriminator for low energy events. With a 125 ns CFD delay (Figure 11b), all three crystals had narrow timing spectral peaks and had timing centroids of 145.4, 196.5 and 224.7 ns and FWHM of 3.3, 9.0 and 10.7 ns respectively. Compared to the 14×14 mm² PSAPD, the 20×20 mm² PSAPD had a similar timing shift effect but the magnitude of both the offset of the centroids and the FWHM were greater. These results suggest that a 45 ns CFD delay was not enough to resolve signals arising from the crystal at the center of the 20×20 mm² PSAPD. This signal required a longer CFD delay for proper peak resolution.

4 Discussion

4.1 Comparison of timing shift and timing resolution in different experimental setups

Moving from individual crystals (Figure 3) to crystal arrays (Figure 4c), the timing shift was reduced, from 30.7 ns to 23.6 ns, and the timing resolution degraded slightly for a crystal located at the corner (from 2.3 ns to 2.8 ns), while there was a small improvement in timing resolution for crystals located on the edge or at the center (from 3.7 ns to 3.5 ns and 3.9 ns to 3.5 ns respectively). This is presumably due to effects of light sharing within the crystal array that results in a greater spread of the scintillation light once it reaches the PSAPD surface. The exact positioning of the crystal with respect to the PSAPD surface may also contribute to the

168
small differences in timing resolution. Comparing the timing resolution obtained using a PMT reference (Figure 4c) to that obtained using one corner crystal on PSAPD2 as a reference (Figure 6c), the timing resolution became worse due to the lower timing resolution of the reference crystal (2~3 ns) and possible scattering (causing event mispositioning) in the crystal array on PSAPD1. The timing shift however remained almost the same, 23.6 ns and 23.8 ns respectively.

4.2 Implementation of timing alignment in an intact detector system

Timing alignment methods have been reported by several groups to improve timing resolution in detectors (Lenox *et al.*, 2007) or systems (Lenox *et al.*, 2006; Moses and Thompson, 2006). Because of the large timing shift in the PSAPD and potential integration with a MR system, these methods cannot be directly implemented in a PSAPD-based system. The timing correction/alignment described in Method 2 can however be implemented in a system with multiple PSAPDs in two steps: the first step is to determine the offset LUT for each PSAPD detector; this is followed by an alignment between the LUTs for all the detectors in the ring. The first step is shown in Figure 12a and can be performed in sequential pairs. In the single-ring configuration shown, there are 16 PSAPDs that are divided into 8 directly opposing pairs. The method described in Section 2.5 can be applied to each pair of PSAPDs. The mean value of each LUT can be subtracted to generate individual offset tables.

The second step is to time align the offset LUTs between all the detectors in the ring. As shown in Figure 12b, this can be achieved by choosing one PSAPD detector as the reference. In the figure, PSAPD #1 is selected as the reference and the residual offset of PSAPD #2 compared to PSAPD #1 can be calculated by acquiring coincidences between detectors 1 and 2 after applying their individual offset tables. The offset of PSAPD #3 can be obtained by using #2 as reference, and so on. The source should be placed at the center as precisely as possible to minimize measurement error. After all 16 offsets are obtained, the mean value of these 16 offsets can be subtracted to generate a unique residual offset value for each PSAPD in the ring. By adding this residual offset value of PSAPD to the offset table of each PSAPD, the final offset table for the system calibration can be achieved. The second step can be easily extended to apply to multiple-ring systems.

4.3 PSAPD size effect

Using a long CFD delay (125 ns) gave reasonable timing resolution across the surface of 20×20 mm² PSAPD, but it also caused energy thresholding problems, as shown in Figure 13a and 13b. For a CFD delay of 45 ns, the effective energy threshold for the corner was slightly higher than the edge and center, albeit still sufficient for adequate thresholding for a PET system. For a delay of 125 ns however, the effective threshold for the corner is much higher than the center despite having similar photopeak energies. The reason is that the constant fraction (CF) signal comes later than the duration of the thresholded signal for low energy events and therefore it is not triggered. This non-uniform response across the surface of PSAPD may cause normalization and/or random subtraction problems. The higher effective threshold associated with the longer CFD delay forces the PSAPD to work at very low threshold level, increasing the count rate and false triggers which have effects on dead time. Thus using larger PSAPDs, there is a challenge in simultaneously obtaining good energy and timing resolution because it is hard to find a CFD delay that is good for both measures. The proper functioning of a CFD relies on pulses varying only in amplitude, not in shape. But this is not the case in PSAPDs. A short delay did not provide good timing resolution because of the high noise associated with the signal. We are therefore exploring other techniques, including non-cable delay CFD (Binkley *et al.*, 2002) and other signal processing techniques, for these large-area PSAPDs.

Another effect that can be seen from Figure 13¹⁶⁹ is the shift of photopeak and this is due to the sampling in the DAQ. The DAQ digitizes only one peak value for each signal per event and the sampling position is determined by the DAQ trigger which is a delayed version of the coincidence trigger. A shift in the trigger location caused the shift in energy photopeak, however this is not an issue as each individual crystal is calibrated using its own photopeak. In Figure 13a, the relatively small fraction of events that exhibit energy-dependent walk and the relatively small magnitude (up to 30 ns) of that walk does not have a significant effect on energy spectra in our studies because of the long shaping time used (1 μ s).

5 Conclusions & Future Work

The position-dependent timing shift and timing resolution of PSAPDs were studied and two methods to correct these phenomena were described. Moving from the corner to the center of a PSAPD, the rise time of the signal becomes slower and the timing resolution worsened. Larger area PSAPDs magnified this effect. Correction of this effect using one offset lookup table derived from events acquired between an LSO array/PSAPD detector and a PMT reduced the timing shift and improved the timing resolution, thus allowing the coincidence timing window to be tightened. Using individual offset tables derived for each individual PSAPD the shift was further reduced. This additional improvement was probably because of the other contributions to the timing shift in addition to the intrinsic effect of PSAPD design, such as positioning of crystal array or unique characteristics of each crystal array. The timing correction methods described in this study can be applied to whole detector systems with multiple PSAPDs using a two-step algorithm. Future studies will involve applying these correction methods in novel PSAPDs detector systems. Further work is needed to determine the optimal detection electronics for larger area PSAPDs where the changes in signal shape across the face of the PSAPD make it hard to simultaneously achieve good timing and energy resolution.

Acknowledgments

The authors thank Dr Ciprian Catana from Athinoula A. Martinos Center for Biomedical Imaging, Department of Radiology, Massachusetts General Hospital for useful discussions; Dr Guobao Wang from the Department of Biomedical Engineering, University of California, Davis for useful discussions; and RMD Inc. for providing the PSAPDs. This work was supported by NIH under grants R01 EB000993, R01 EB006109 and R44 NS055377.

References

- Binkley DM, Puckett BS, Swann BK, Rochelle JM, Musrock MS, Casey ME. A 10-Mc/s, 0.5- μ m CMOS constant-fraction discriminator having built-in pulse tail cancellation. *IEEE Transactions on Nuclear Science* 2002;49:1130–1140.
- Catana C, Proccisi D, Wu Y, Judenhofer MS, Qi J, Pichler BJ, Jacobs RE, Cherry SR. Simultaneous in vivo positron emission tomography and magnetic resonance imaging. *Proc Natl Acad Sci U S A* 2008;105:3705–3710. [PubMed: 18319342]
- Catana C, Wu YB, Judenhofer MS, Qi JY, Pichler BJ, Cherry SR. Simultaneous acquisition of multislice PET and MR images: Initial results with a MR-compatible PET scanner. *Journal of Nuclear Medicine* 2006;47:1968–1976. [PubMed: 17138739]
- Chaudhari AJ, Joshi AA, Bowen SL, Leahy RM, Cherry SR, Badawi RD. Crystal identification in positron emission tomography using nonrigid registration to a Fourier-based template. *Physics in Medicine and Biology* 2008;53:5011–5027. [PubMed: 18723924]
- Despres P, Barber WC, Funk T, McClish M, Shah KS, Hasegawa BH. Modeling and correction of spatial distortion in position-sensitive avalanche photodiodes. *IEEE Transactions on Nuclear Science* 2007;54:23–29.
- Grazioso, R.; Farrell, R.; Shah, KS.; Glodo, J.; Olschner, F. A novel, distortion-free position sensitive APD for nuclear imaging; *Nuclear Science Symposium Conference Record, 2002 IEEE*; 2002. p. 464-467.

- Judenhofer MS, Pichler BJ, Cherry SR. Evaluation of high performance data acquisition boards for simultaneous sampling of fast signals from PET detectors. *Physics in Medicine and Biology* 2005;50:29–44. [PubMed: 15715420]
- Lenox, M.; McFarland, A.; Burbar, Z.; Hayden, C. Coincidence timing analysis of APD based PET detectors; Nuclear Science Symposium Conference Record, 2007. NSS '07. IEEE; 2007; p. 3766-3769.
- Lenox, MW.; Atkins, BE.; Pressley, DR.; McFarland, A.; Newport, DF.; Siegel, SB. Digital Time Alignment of High Resolution PET Inveon Block Detectors; Nuclear Science Symposium Conference Record, 2006. IEEE; 2006. p. 2450-2453.
- Moses WW, Thompson CJ. Timing Calibration in PET Using a Time Alignment Probe. *IEEE Transactions on Nuclear Science* 2006;53:2660–2665.
- Musrock MS, Young JW, Moyers JC, Breeding JE, Casey ME, Rochelle JA, Binkley DM, Swann BK. Performance characteristics of a new generation of processing circuits for PET applications. *IEEE Transactions on Nuclear Science* 2003;50:974–978.
- Pichler BJ, Judenhofer MS, Catana C, Walton JH, Kneilling M, Nutt RE, Siegel SB, Claussen CD, Cherry SR. Performance test of an LSO-APD detector in a 7-T MRI scanner for simultaneous PET/MRI. *Journal of Nuclear Medicine* 2006;47:639–647. [PubMed: 16595498]
- Shah KS, Farrell R, Grazioso R, Harmon ES, Karplus E. Position-sensitive avalanche photodiodes for gamma-ray imaging. *IEEE Transactions on Nuclear Science* 2002;49:1687–1692.
- Shah KS, Grazioso R, Farrell R, Glodo J, McClish M, Entine G, Dokhale P, Cherry SR. Position sensitive APDs for small animal PET imaging. *IEEE Transactions on Nuclear Science* 2004;51:91–95.
- Yang YF, Wu YB, Qi JY, James SS, Du HN, Dokhale PA, Shah KS, Farrell R, Cherry SR. A prototype PET scanner with DOI-encoding detectors. *Journal of Nuclear Medicine* 2008;49:1132–1140. [PubMed: 18552140]
- Zhang J, Foudray AMK, Cott PD, Farrell R, Shah K, Levin CS. Performance characterization of a novel thin position-sensitive avalanche photodiode for 1 mm resolution positron emission tomography. *IEEE Transactions on Nuclear Science* 2007;54:415–421.

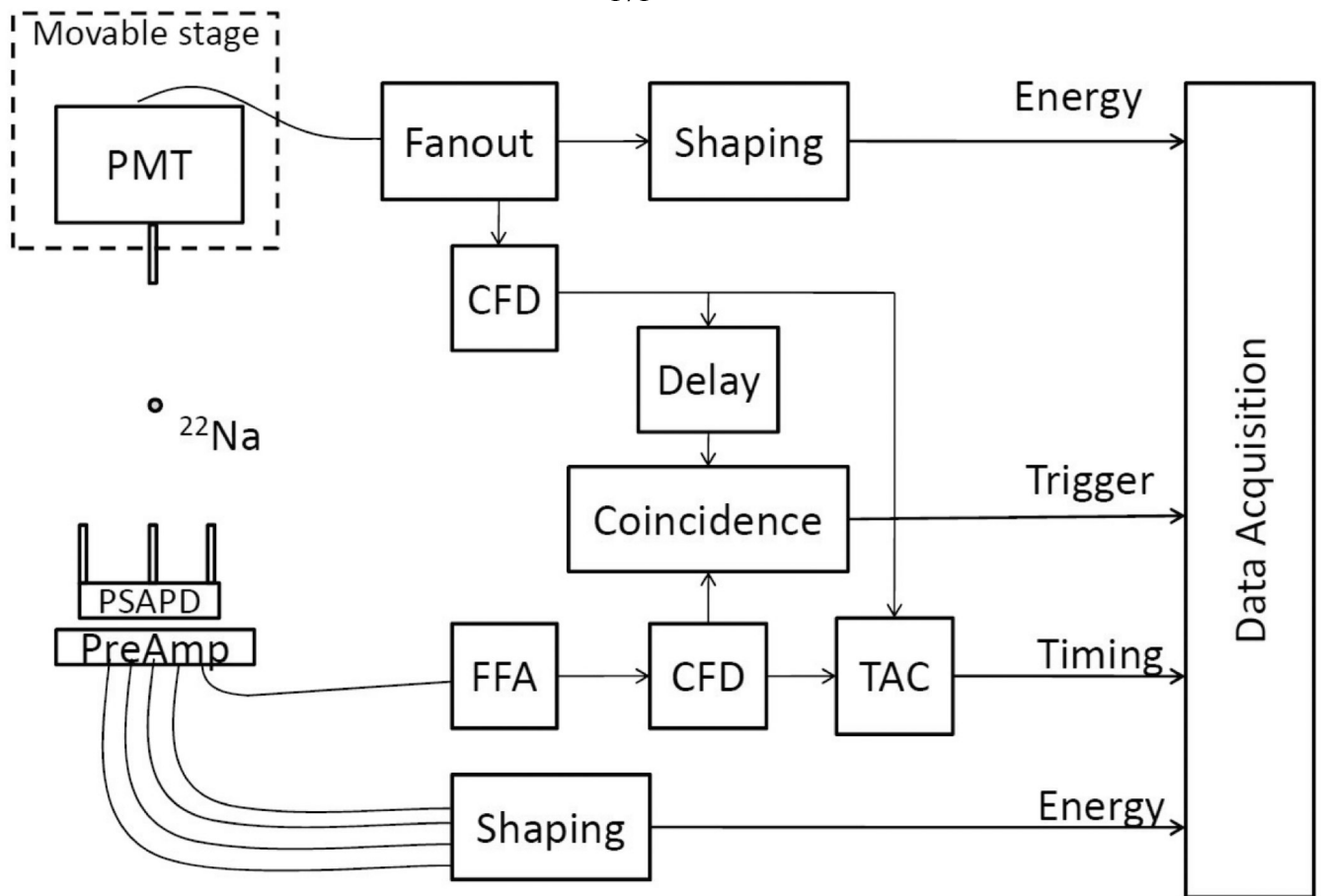


Figure 1. Experimental setup for timing measurements of a PSAPD-based LSO detector in coincidence with a PMT-based LSO detector.

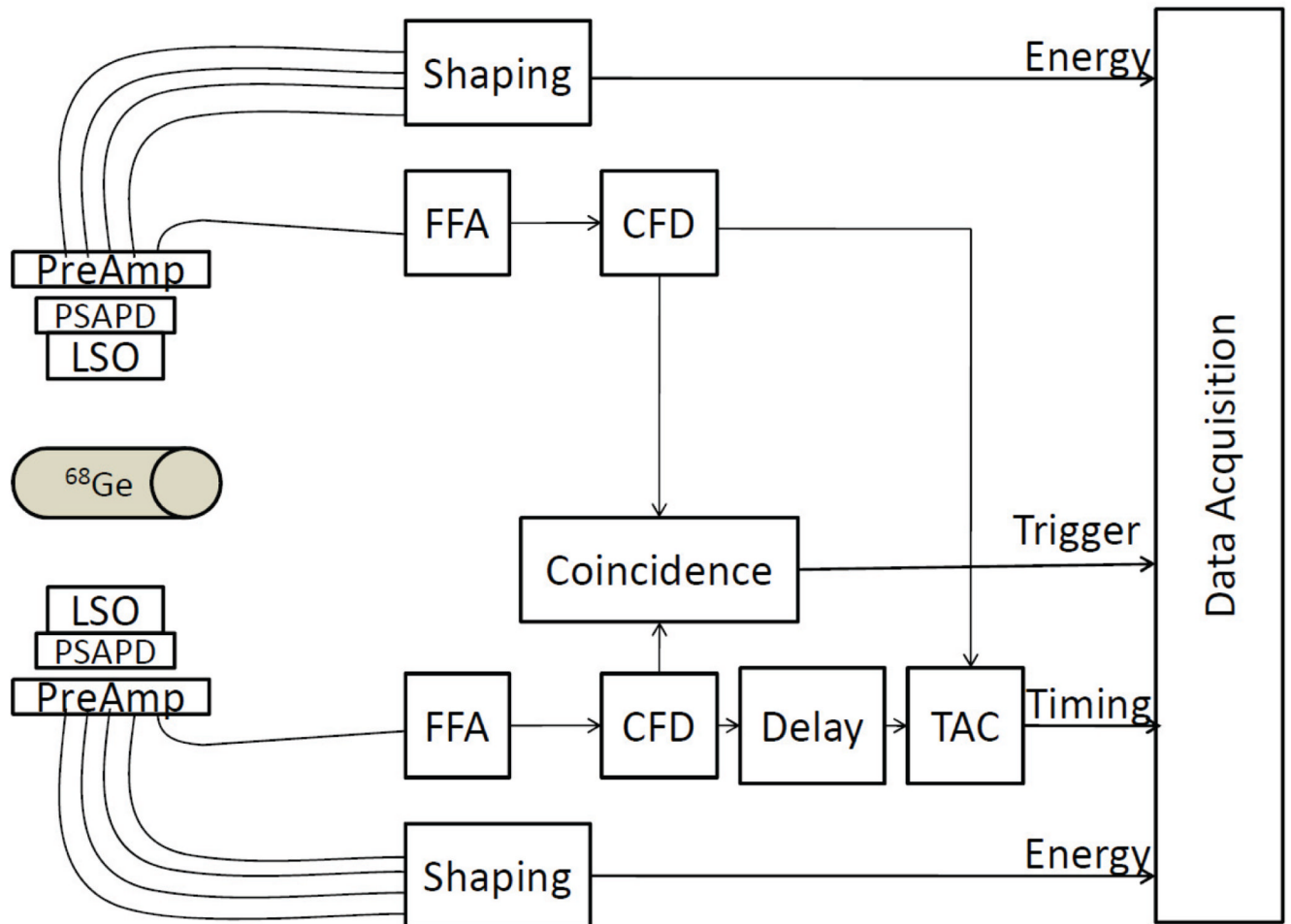


Figure 2. Experimental setup for timing measurements of two PSAPD-based LSO detectors in coincidence.

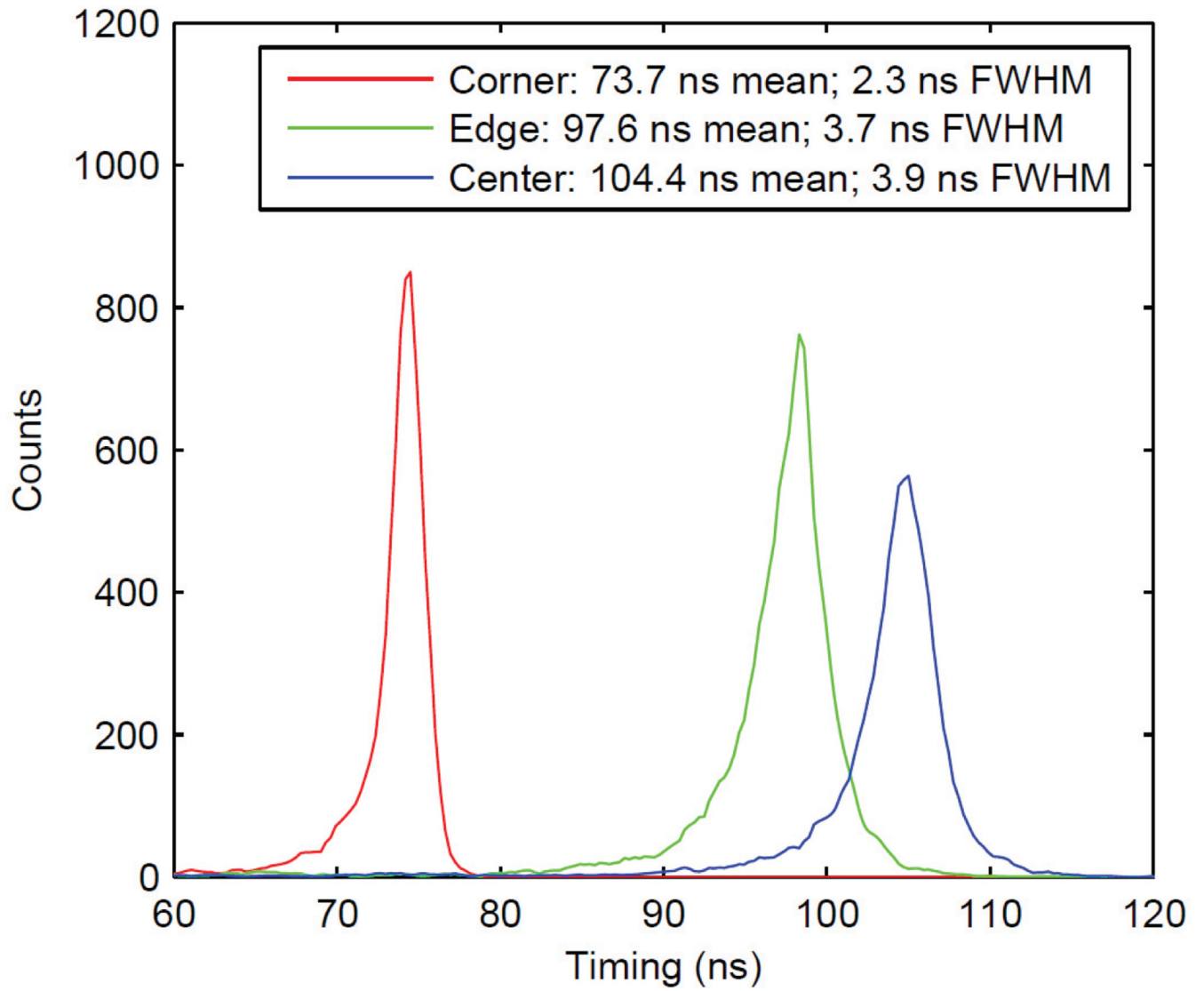


Figure 3.
Timing shift and resolution at three locations on the surface of a PSAPD.

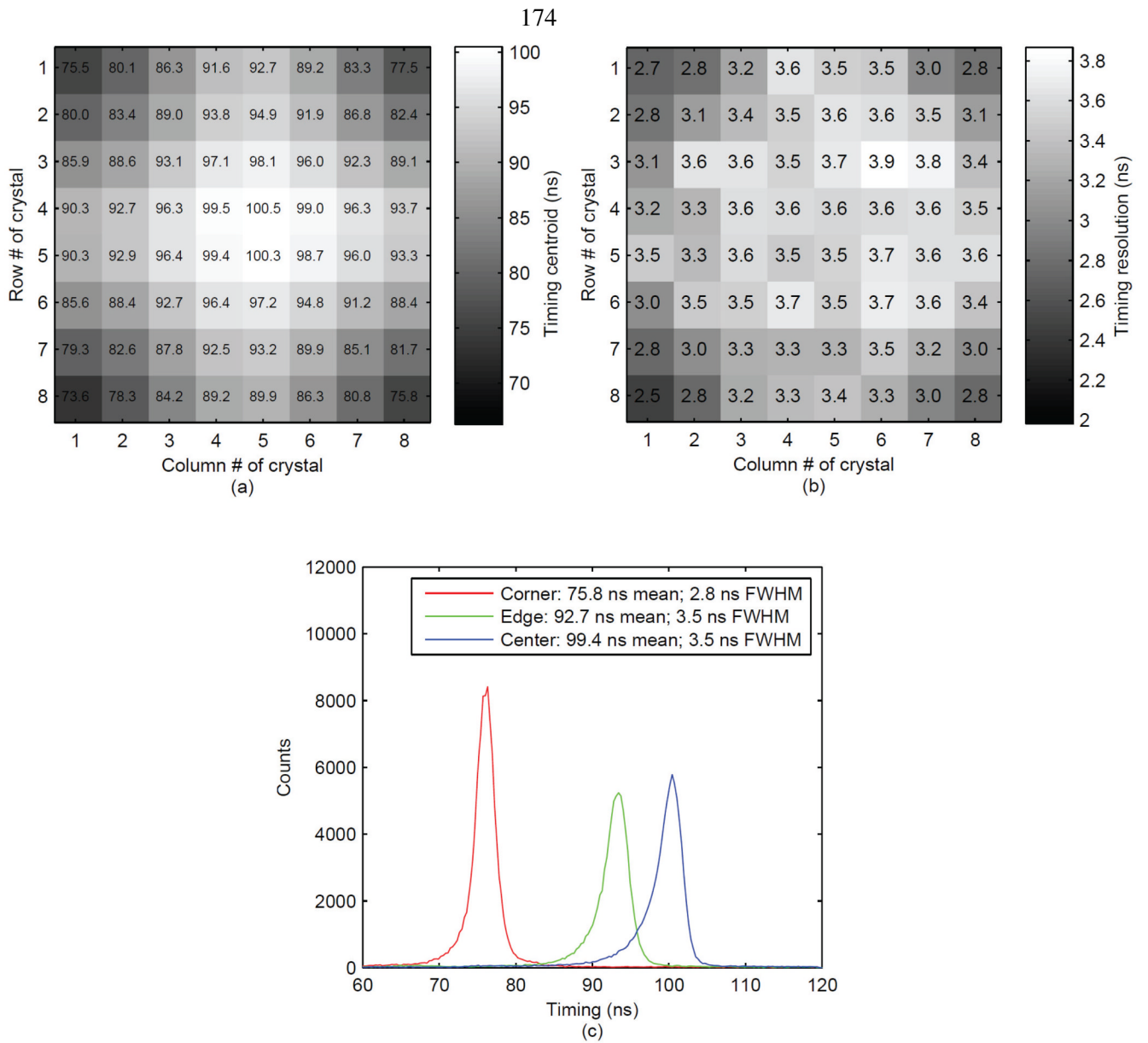


Figure 4. Spatial map of (a) the centroids of timing spectra (ns) and (b) the timing resolution (ns) for the whole array and timing spectra (c) for crystals at three representative locations on the PSAPD (comparable to the locations in Figure 3).

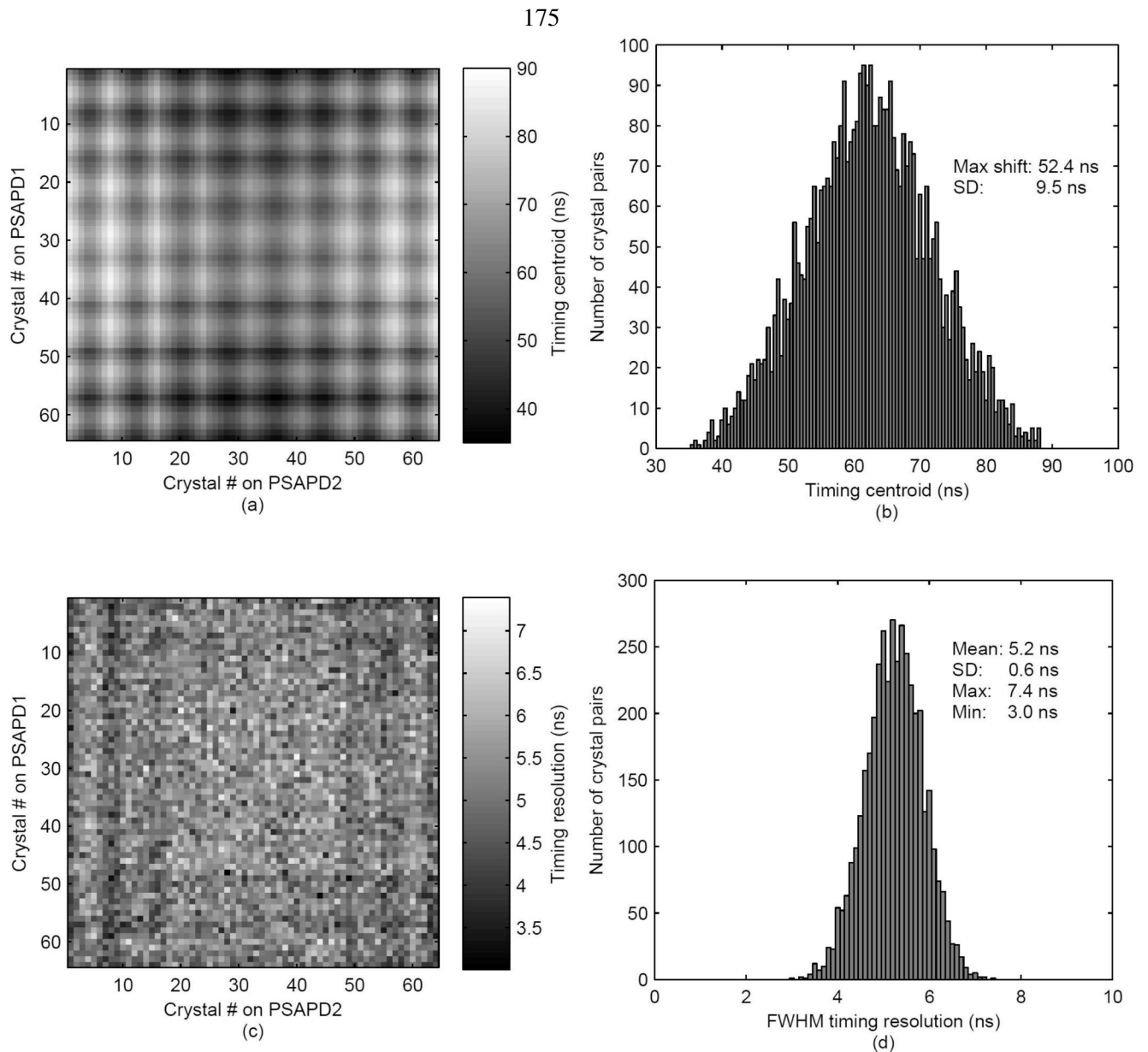


Figure 5. Crystal-crystal map of (a) centroids of timing spectra, (b) histogram of centroids, (c) map of timing resolution and (d) histogram of timing resolution for all crystal pairs.

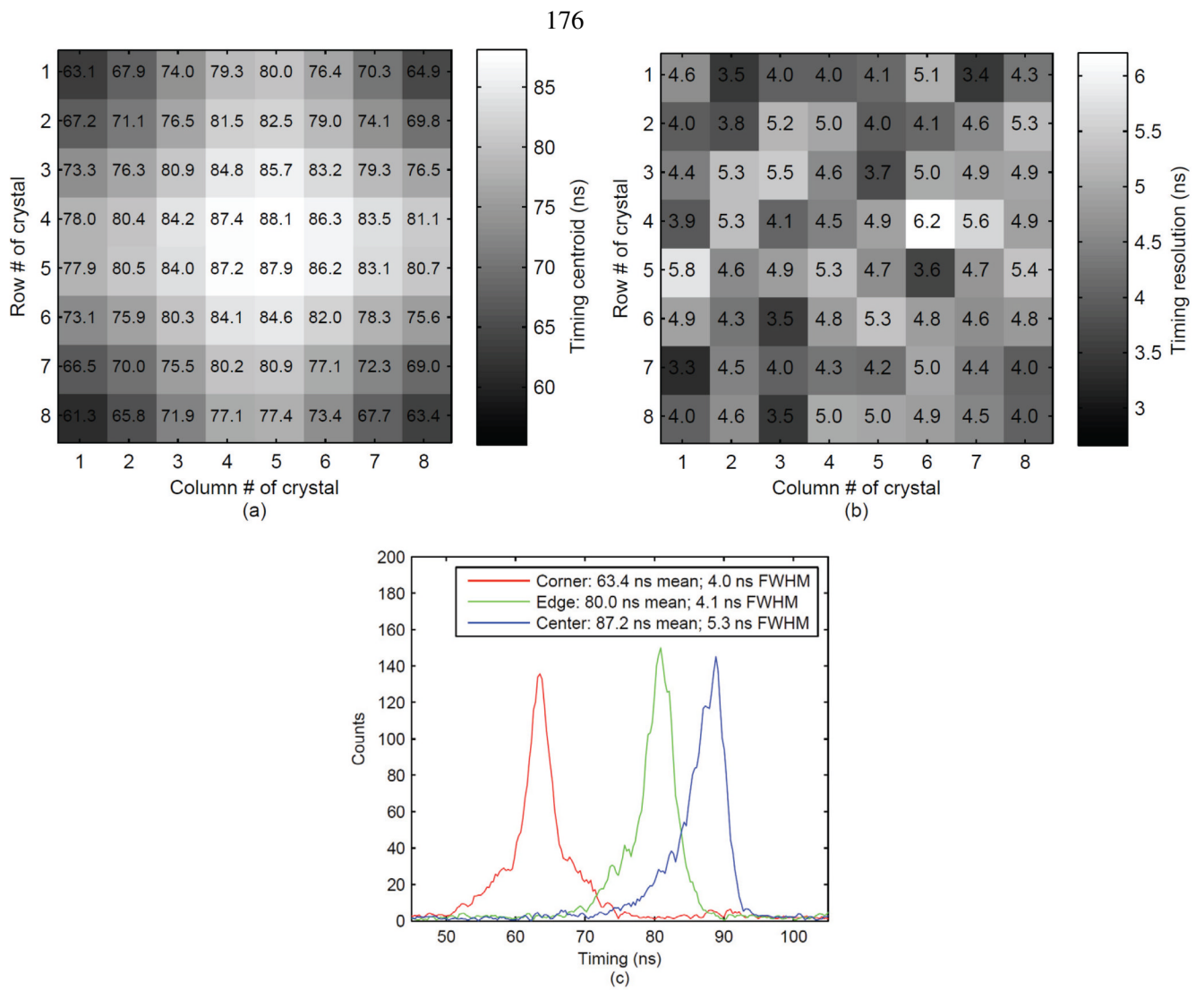


Figure 6. Spatial map of (a) centroids of timing spectra (ns), (b) timing resolution (ns) of crystals in PSAPD1 with respect to corner crystal in PSAPD2 and (c) timing spectra for three representative locations.

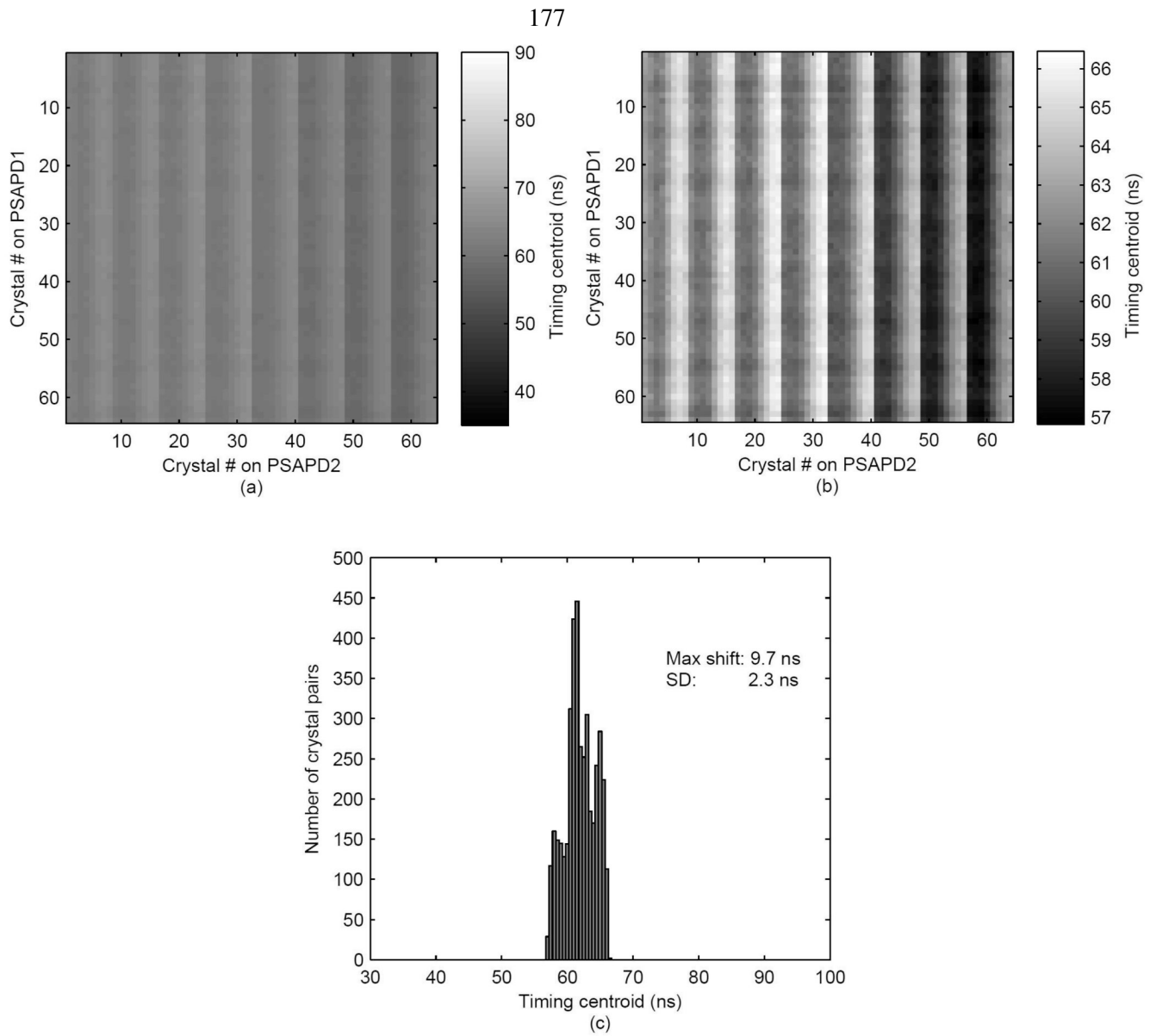


Figure 7. Crystal-crystal map of timing centroids plotted (a) on same scale as Figure 5a and (b) on expanded scale, and (c) histogram of timing centroids after time alignment correction with Method 1.

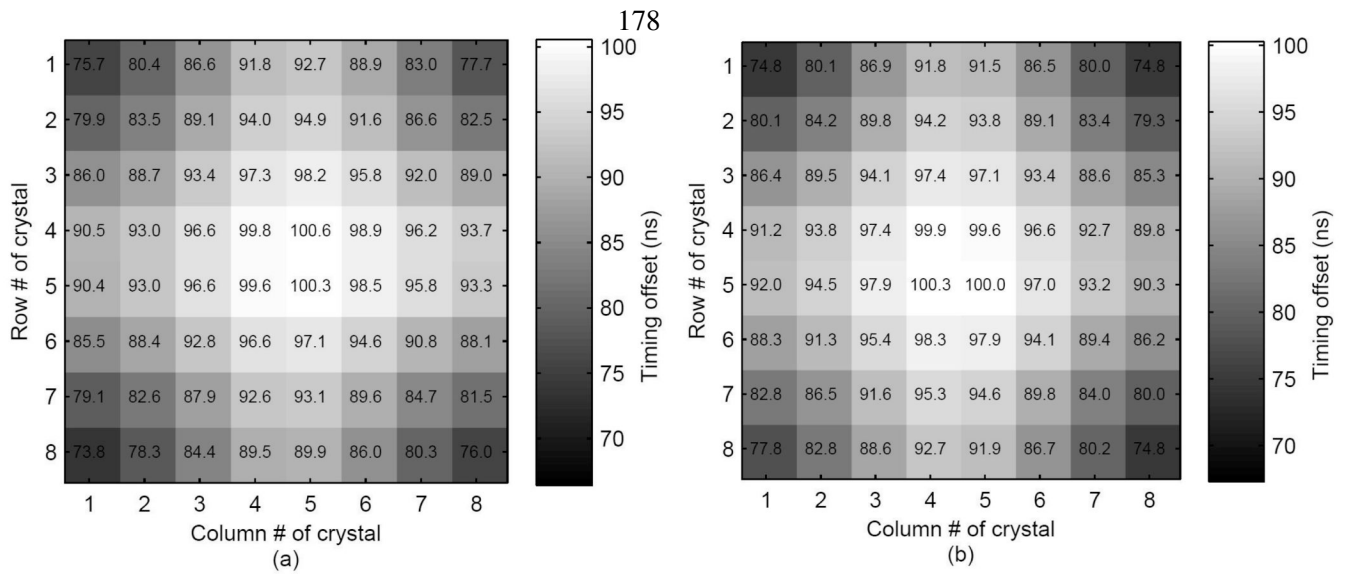


Figure 8. Timing offset LUTs of (a) PSAPD1 and (b) PSAPD2 used for correction Method 2.

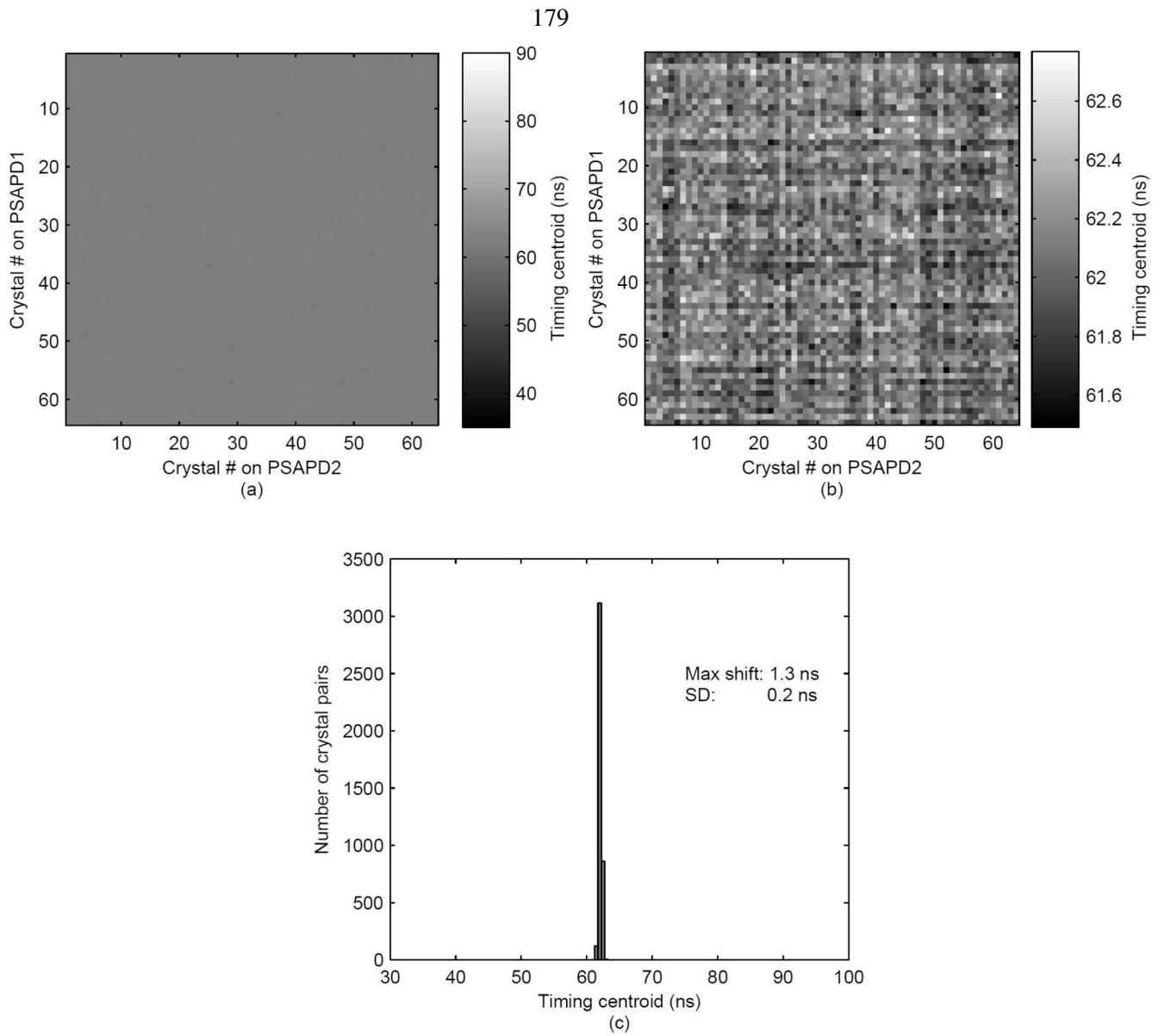


Figure 9. Crystal-crystal map of timing centroids plotted (a) on same scale as Figure 5a and (b) on expanded scale, and (c) histogram of timing centroids after time alignment correction with Method 2.

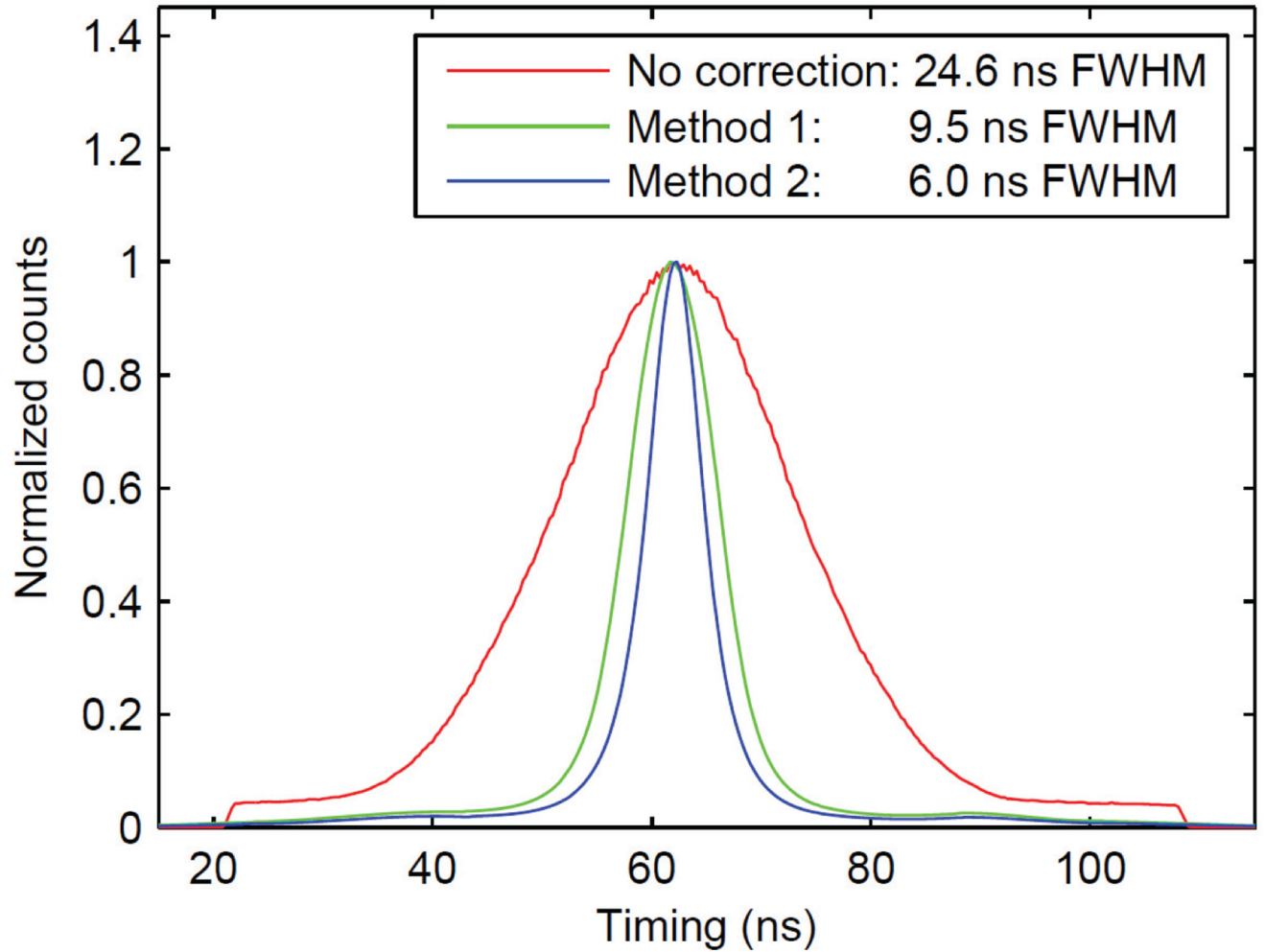


Figure 10. Measured averaged timing spectra (over all crystal pairs) without (red line) and with timing offset correction Method 1 (green line) and Method 2 (blue line).

181

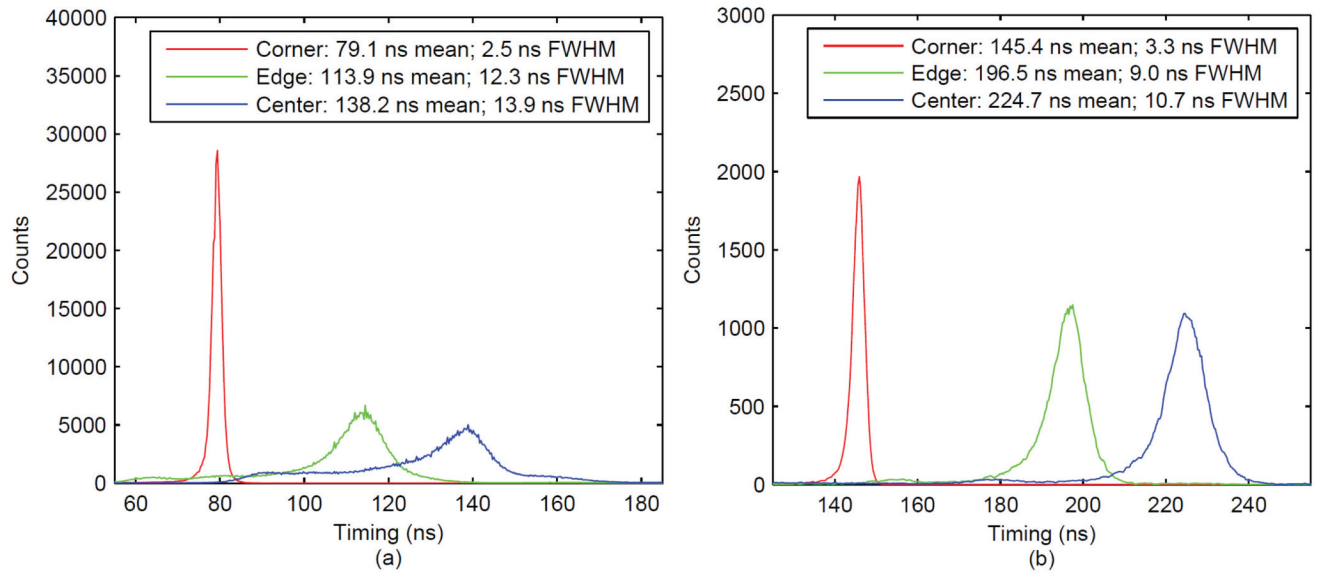


Figure 11. Timing spectra obtained from 20×20 mm² PSAPD with CFD delay of (a) 45 ns and (b) 125 ns.

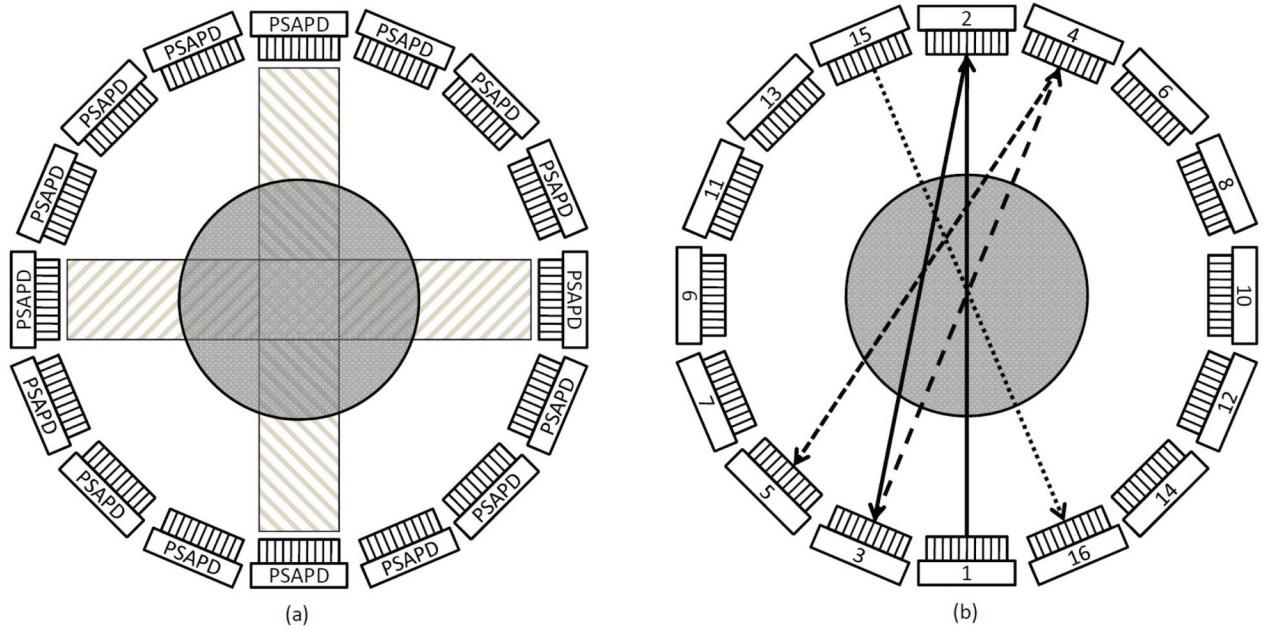


Figure 12.

Timing alignment scheme: to generate offset map for each individual PSAPD (a) and between PSAPDs (b). The cylinders in (a) and (b) represent the sources. The rectangles in (a) represent the regions covered by the opposing detector pairs. The lines with arrows in (b) show the calibration sequence, starting from PSAPD #1 and ending at #16. The lines from #5 to #15 are omitted for clarity.

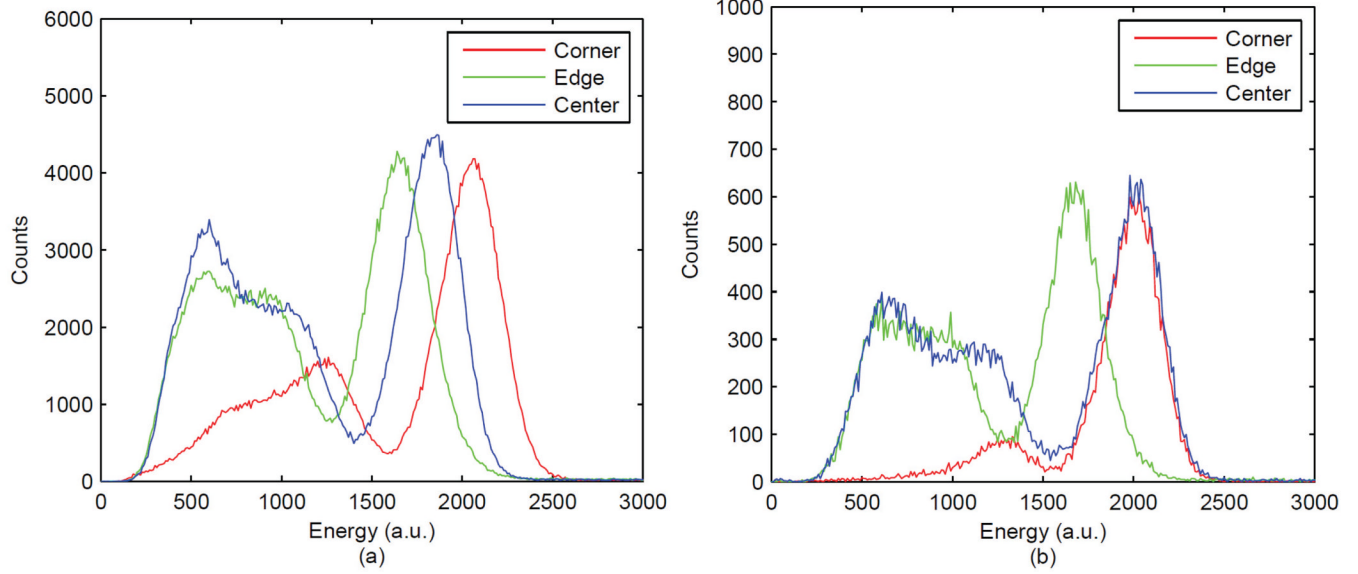


Figure 13. Energy spectra obtained from $20 \times 20 \text{ mm}^2$ PSAPD with CFD delay of (a) 45 ns and (b) 125 ns.

Table 1

Comparison of results (unit: ns)

	Individual crystal pairs						Whole arrays		
	Timing resolution (FWHM)			Timing centroid (mean of spectrum)			Timing resolution (FWHM)	Timing window (2 σ)	
	Mean	SD	Max	Min	SD	Max-Min			
No Correction	5.2	0.6	7.4	3.0	9.5	52.4	24.6	65.1	
Method 1	5.2	0.6	7.4	3.0	2.3	9.7	9.5	22.0	
Method 2	5.2	0.6	7.4	3.0	0.2	1.3	6.0	15.2	

Appendix B

Receptor-targeted Iron Oxide Nanoparticles for Molecular MR Imaging of Inflamed Atherosclerotic Plaques

This paper describes work done in collaboration with Angelique Louie's group at the University of California, Davis. The work involved the development of a novel iron-oxide based nanoparticle that targets macrophages in vulnerable atherosclerotic plaques. Improved chemistry and functionalization (via sulfation) of the particle surface enabled improved plaque targeting compared to a first generation particle. I was responsible for the design, acquisition and analysis of the *in vivo* studies.

This section is published in *Biomaterials*: Chuqiao Tu, Thomas S. C. Ng, Hargun Sohi, Heather A. Palko, Adrian House, Russell E. Jacobs, and Angelique Y. Louie (2011) Receptor-targeted iron oxide nanoparticles for molecular MR imaging of inflamed atherosclerotic plaques. *Biomaterials*, 32 (29). pp. 7209-7216.



Receptor-targeted iron oxide nanoparticles for molecular MR imaging of inflamed atherosclerotic plaques

Chuoqiao Tu^a, Thomas S.C. Ng^b, Hargun K. Sohi^b, Heather A. Palko^c, Adrian House^a, Russell E. Jacobs^b, Angelique Y. Louie^{a,*}

^a Department of Biomedical Engineering, University of California, Davis, CA 95616, USA

^b Beckman Institute, California Institute of Technology, Pasadena, CA 91125, USA

^c Department of Chemistry, University of California, Davis, CA 95616, USA

ARTICLE INFO

Article history:

Received 20 April 2011

Accepted 8 June 2011

Available online 13 July 2011

Keywords:

Nanoparticles

Imaging agents

MRI (magnetic resonance imaging)

Molecular imaging

Macrophages

Inflammation

ABSTRACT

In a number of literature reports iron oxide nanoparticles have been investigated for use in imaging atherosclerotic plaques and found to accumulate in plaques via uptake by macrophages, which are critical in the process of atheroma initiation, propagation, and rupture. However, the uptake of these agents is non-specific; thus the labeling efficiency for plaques *in vivo* is not ideal. We have developed targeted agents to improve the efficiency for labeling macrophage-laden plaques. These probes are based on iron oxide nanoparticles coated with dextran sulfate, a ligand of macrophage scavenger receptor type A (SR-A). We have sulfated dextran-coated iron oxide nanoparticles (DIO) with sulfur trioxide, thereby targeting our nanoparticle imaging agents to SR-A. The sulfated DIO (SDIO) remained mono-dispersed and had an average hydrodynamic diameter of 62 nm, an r_1 relaxivity of $18.1 \text{ mM}^{-1} \text{ s}^{-1}$, and an r_2 relaxivity of $95.8 \text{ mM}^{-1} \text{ s}^{-1}$ (37 °C, 1.4 T). Cell studies confirmed that these nanoparticles were nontoxic and specifically targeted to macrophages. *In vivo* MRI after intravenous injection of the contrast agent into an atherosclerotic mouse injury model showed substantial signal loss on the injured carotid at 4 and 24 h post-injection of SDIO. No discernable signal decrease was seen at the control carotid and only mild signal loss was observed for the injured carotid post-injection of non-sulfated DIO, indicating preferential uptake of the SDIO particles at the site of atherosclerotic plaque. These results indicate that SDIO can facilitate MRI detection and diagnosis of vulnerable plaques in atherosclerosis.

© 2011 Elsevier Ltd. All rights reserved.

1. Introduction

Cardiovascular disease (CVD) is the leading cause of death in the western world and its prevalence is expected to increase further during the next 3 decades [1]. Increasing evidence indicates that it is atherosclerotic plaque rupture rather than the severity of vessel occlusion that leads to major adverse events, such as stroke and myocardial infarction [2,3]. Early detection of unstable plaques would be of great value to guide treatment decisions, with the aim to decrease morbidity/mortality in affected patients. There is an intense focus in the field to identify specific biomarkers that indicate a plaque's risk for rupture and develop noninvasive methods to detect those markers [1,4,5]. Magnetic resonance imaging (MRI) has played a prominent role in anatomical and functional examinations of the major vessels; however, without signal enhancement, the technique

lacks sufficient sensitivity to directly detect and identify biomarkers of interest [6,7]

Recent advances in the development of MRI contrast agents (CAs), which specifically target relevant biomarkers and enhance images to generate sufficient contrast in tissues and organs of interest, allow MRI to visualize molecules and molecular events occurring at a cellular level [6,8]. However, the amount of biomarkers in the cardiovascular system is usually expressed in the low nanomolar range ($\leq 10^{-9}$ mol/g of tissue), which is below the detection sensitivity of routinely used gadolinium chelates (10^{-7} mol/g of tissue). Particle-based technologies provide an effective method to concentrate signal-generating materials into a relatively small entity, which can greatly improve their detectability (10^{-10} - 10^{-11} mol/g of tissue) *in vivo* [7,9,10]. Moreover, the particle CAs have a large surface areas, allowing them to display more targeting ligands, further enriching the CAs at the region of interest (ROI).

Non-toxic and biocompatible iron oxide nanoparticles (IO NPs) have been widely used as MRI CAs in the clinic [11]. IO NPs,

* Corresponding author. Tel.: +1 530 7527134; fax: +1 530 7527156.

E-mail address: aylouie@ucdavis.edu (A.Y. Louie).

however, are generally non-specific; they show a differential distribution in the body based primarily on relative tissue permeability. We are interested in the development of IO NP CAs that target biomarkers of atherosclerotic plaques. In the search for markers to identify high-risk plaque, macrophages have been found to correlate with plaque stability — plaques with high macrophage content tend to be more unstable, and the distribution pattern for the macrophages can be indicative of degree of stability [12,13]. IO NPs have been used for MRI detection of plaques in pre-clinical experiments using different animal models of atherosclerosis, and the results showed that these particles accumulate in plaque macrophages [14]. However, the uptake of IO NPs by macrophages is non-specific through phagocytosis. This is an inefficient process that provides relatively weak contrast between the plaque and surrounding tissues [15].

We have previously developed CAs based on the scavenger receptor type A (SR-A) targeting ligands maleylated BSA and dextran sulfate [16–18]. SR-A is highly expressed on activated macrophages and not found on normal vessel walls [19]. These probes labeled atherosclerotic plaques with improved efficiency over non-targeted probes. However, it was difficult to obtain mono-dispersed IO NPs by synthesizing them using either dextran sulfate, or a combination of dextran sulfate and dextran, as a starting materials to form the coating [20]. In this work, we introduce a new synthetic method in which we coated IO NPs with dextran (DIO), then sulfated the dextran coating of the particles to make dextran sulfate coated IO NPs (SDIO). The ability of SDIO to target macrophages *in vitro* and to detect and access macrophages in atherosclerotic plaque *in vivo* was evaluated by MRI.

2. Materials and methods

2.1. Materials

Materials were obtained from commercial suppliers and used directly, unless otherwise noted. Dextran (from leuconostoc, average mol. wt. 9000–11,000) and ferric chloride hexahydrate ($\text{FeCl}_3 \cdot 6\text{H}_2\text{O}$, Fw 270.29 g/mol) were purchased from Sigma-Aldrich. Ferrous chloride tetrahydrate ($\text{FeCl}_2 \cdot 4\text{H}_2\text{O}$, Fw 198.81 g/mol) and dextran sulfate (sodium salt, prepared from dextran from leuconostoc SSP, average mol. wt. 5000) were acquired from Fluka. Ammonium hydroxide (28–30%), sodium bicarbonate and sodium hydroxide were provided by Fisher Scientific. Sulfur trioxide (SO_3) pyridine complex, sulfur trioxide DMF complex and 2-methyl-2-butene (2M2B) were purchased from Acros. Anhydrous formamide was purchased from MP, Biomedicals, LLC. Spectra/por[®] dialysis membrane (mol. wt. cut-off 50,000) was purchased from Spectrum Laboratories, Inc. P388D1 cells and RPMI-1640 medium were obtained from American Type Culture Collection (ATCC). Fetal bovine serum (FBS), L-glutamine, PBS (1X) and C_{12} - Resazurin were provided by GIBCO. Lipoprotein deficient bovine serum (LPDS) was obtained from Biomedical Technologies, Inc. (Stoughton, MA). Water was purified using a Millipore Milli-Q Synthesis purifier (18.0 M Ω cm, Barnstead).

2.2. Synthesis of dextran sulfate coated iron oxide nanoparticles

Dextran coated iron oxide nanoparticles (DIO) were synthesized as previously reported [20]. The DIO (200 mg) was dissolved in 10 mL of dry formamide. After complete dissolution, 2-methyl-2-butene (2M2B) (1.6 mL, 15 mmol) was slowly added to the flask under argon atmosphere and magnetic stirring. A SO_3 -pyridine complex (0.32 g, 2 mmol) was rapidly added, and the reaction mixture was stirred at 30 °C under argon atmosphere for 2 h. The reaction was quenched by slowly pouring it into 7 mL of saturated sodium bicarbonate solution. After the final product was concentrated, the residue was dissolved in water and was dialyzed against deionized water in a dialysis bag with molecular weight (MW) cut-off of 50,000 Da for 72 h (8–10 changes of water). The solution was lyophilized to give a brown solid.

2.3. Characterization of SDIO

The iron oxide core size of SDIO and DIO were measured by transmission electron microscopy (TEM) on a Philips CM-12, operating at 80 kV. The average hydrodynamic particle size and size distribution of SDIO and DIO were measured using dynamic light scattering (DLS) with a Nanotracs 150 particle size analyzer (Microtrac, Inc., Montgomeryville, PA). The zeta potential (ζ) values of SDIO and DIO were measured by determining the electrophoretic mobility using a NICOMP[™] 380

ZLS device (Particle Sizing Systems, Inc., Santa Barbara, CA, USA) in deionized water at room temperature. Elemental analysis was performed by Columbia Analytical Services of Tucson, Arizona. FT-IR spectra were collected on a Shimadzu IR Prestige 21 spectrophotometer.

Longitudinal (T_1) and transverse (T_2) relaxation times were measured at 60 MHz (1.4 T) and 37 °C on a Bruker Minispec mq60 (Bruker, Billerica, MA). Three stock solutions of SDIO were prepared by dissolving appropriate amounts of particles in pH 7.0 deionized water. The concentration of iron was determined by ICP-MS. The stock solutions were diluted to give three series of aqueous solutions with decreasing iron concentration (0.3 mL each). All solutions were prepared by weight. Iron concentrations were calculated based on the concentration of the stock solution and appropriate dilution factors. T_1 values were measured using an inversion recovery sequence with 10–15 data points and T_2 values were measured using a Carr–Purcell–Meiboom–Gill (CPMG) sequence with $\tau = 1$ ms, and 200 data points. Each solution was incubated at 37 °C for 10 min before measurement. The longitudinal (r_1) and transverse (r_2) relaxivity were determined as the slope of the line for plots of $1/T_1$ or $1/T_2$, respectively, against increasing iron concentration with a correlation coefficient greater than 0.99 [21]. The relaxivity of DIO was measured by the same procedure. The T_1 and T_2 relaxation times of cell lysates containing SDIO or DIO were also measured with the method described above.

2.4. Cell experiments

2.4.1. Cell culture

The P388D1 cells were maintained in tissue culture flasks (75 cm²) in media (RPMI-1640 with 1% L-glutamine and 10% fetal bovine serum (FBS)) at 37 °C in a humidified environment of 5% CO_2 atmosphere. When the cells reached 80–90% confluence, the medium was removed. The cells were scraped down with a rubber policeman and used for either sub-culture or *in vitro* cell studies. All experiments were performed on cells that were passaged an equal number of times.

2.4.2. *In vitro* cellular uptake of SDIO and DIO

The P388D1 cells were plated to 60 mm diameter tissue culture dishes at 1×10^6 cells/mL of RPMI-1640 with 1% L-glutamine and 10% lipoprotein deficient bovine serum (LPDS) (2 mL per dish). The cells were maintained in media at 37 °C in a humidified environment of 5% CO_2 atmosphere overnight which allowed cells to adhere to the bottom of dishes.

Three stock solutions of SDIO or DIO were prepared by dissolving appropriate amount of particles in RPMI-1640 with 1% L-glutamine and 10% LPDS. The concentration of iron was determined by ICP-MS. The stock solutions were diluted with media to give series of three solutions with decreasing iron concentration. All solutions were prepared by weight and iron concentrations were calculated based on the concentration of the stock solution and appropriate dilution factors. The resultant media solutions of SDIO or DIO were incubated in 37 °C water bath for 20 min before use. After removal of maintenance media, the SDIO or DIO medium solutions were introduced to the cells and incubated at 37 °C in 5% CO_2 atmosphere for 2 h. After removal of the media, cells were washed with 1X PBS (37 °C) (3×2 mL for each dish, ~ 2 min for each washing). Deionized water was added in dishes (1.2 mL for each dish), and the freeze-thaw (30/20 min) method was repeated twice to lyse cells. The cell lysates were put into 1.5 mL conical tubes and lyophilized. Deionized water was added to the residue (0.3 mL each) to generate solutions for relaxation time measurement.

2.4.3. Specificity of uptake

To verify that cellular uptake was receptor-specific, competition experiments were conducted and characterized by relaxation times. The P388D1 cells were incubated with SDIO ($[\text{Fe}] = 5.0 \times 10^{-5}$ M) in the presence of competing dextran sulfate or non-competing dextran as control in 0, 0.02, 0.1, 0.4, 1, and 10-fold excess concentrations. Cells were incubated at 37 °C in a 5% CO_2 atmosphere for 2 h and then prepared for relaxation time measurement as described previously.

2.4.4. Cytotoxicity

Cytotoxicity of SDIO was evaluated with P388D1 cells using the C_{12} - Resazurin viability assays. P388D1 cells in RPMI-1640 were plated in 96-well dishes at a concentration of 1.1×10^4 cells per well. This places the cells at a density for linear growth rate which is optimal for the assay. After overnight incubation in 5% CO_2 atmosphere at 37 °C, the existing RPMI-1640 was replaced with fresh media containing varying amounts of SDIO. Cells were incubated with SDIO for either 4 or 24 h. The media were removed and cells were washed with 1X PBS three times, then media containing C_{12} - Resazurin (5 μM) was added. After incubation for 15 min for reduction of the compound, fluorescence was measured using a Safire² monochromator microplate reader (Tecan Austria G.M.B.H., Austria) with excitation of 563 nm and an emission of 587 nm. Samples were performed in triplicate to provide statistical significance.

2.5. Animal studies

2.5.1. Animal model

All animal experiments were performed under protocols approved by the Animal Care and Use Committee of the University of California, Davis and the

California Institute of Technology. Apo E^{-/-} mice (12 weeks old, Jax West Laboratories, West Sacramento, CA) were used for the experiments. Either the right or left carotid artery of each mouse was ligated two weeks before imaging. Subsequent to ligation, mice were placed on a high fat diet (TD.88137, Harlan Laboratories Inc., Madison, WI). To perform the ligation a medial incision was made between the mandible and clavicle, exposing the glands and vessels of the neck. The carotid artery was singled out from the surrounding tissue, with much attention given to protecting and excluding the parallel-running vagus nerve. A 6/0 silk suture was threaded under the dorsal side of the carotid artery and was tied off to cause injury to the site. The procedure was concluded with five to six discontinuous 4/0 ethilon sutures to reconnect the skin of the original ventral incision. The mice were monitored twice a day for approximately four days to check for irritation and to administer analgesics when appropriate.

2.5.2. In vivo MRI

All images were acquired on a 7T (Bruker Biospec) small animal magnet using a home-built birdcage coil. For all time points, the animal was anesthetized with an 1.5% isoflurane:air mixture, kept at 35–37 °C with warm air flowing through the bore and the respiration was monitored (MP150, Biopac, Goleta, CA). After localizing the ROI around the neck using a RARE spin echo sequence (TR/TE = 4000/22 ms, matrix size = 128 × 128, FOV = 35.35 × 35.35 mm², slice thickness = 0.754 mm), the common carotid arteries were located with a time-of-flight angiography sequence with venous saturation (FL2D_ANGIO method, Paravision 4.0: TR/TE = 13.7/3.5 ms, matrix size = 150 × 100; zero-filled to 256 × 100, FOV = 30 × 20 mm², slice thickness = 0.754 mm). A gradient echo sequence was then utilized to visualize the uptake of SDIO/DIO particles (TR/TE = 1000/5 ms, F.A. = 35°, matrix size = 200 × 200; zero-filled to 256 × 200, FOV = 35.35 × 35.35 mm², slice thickness = 0.754 mm) at the region of the common carotid arteries. A set of pre-injection images was acquired one day prior to injection. For particle injection, 30 mg/kg Fe content of SDIO (*n* = 3) or DIO (*n* = 2) particles dissolved in saline were injected via the tail vein. The imaging protocol was then repeated at 4 h and 24 h post-injection.

2.5.3. MR images analysis

To analyze the acquired images, all gradient echo images were first reconstructed such that the intensity scaling and offset of all images for each mouse were equivalent. To compare particle uptake between timepoints and subjects, we define a contrast ratio (CR) metric as:

$$CR = \frac{\frac{[I_{\text{ligated}}] - [I_{\text{brain}}]}{[I_{\text{control}}] - [I_{\text{brain}}]}}{\frac{[I_{\text{ligated}}] - [I_{\text{brain}}]}{[I_{\text{control}}] - [I_{\text{brain}}]}} \bigg|_{\text{prescan}} \quad (1)$$

Where I_{ligated} is the mean intensity of the region of interest (ROI) drawn around the ligated carotid artery, I_{control} is the mean intensity of the ROI drawn around the contra-lateral carotid. I_{brain} is the mean intensity of the ROI drawn in the spinal cord at the same image slice as the other ROIs and *i* is either 4 or 24 h post-injection timepoints.

ROIs were drawn manually at slice levels approximately located at the common carotid arteries. These were matched between timepoints. Angiography images were used to guide ROI delineation around the carotid arteries. Because previous reports noted that the carotid vessels along with the wall are ~1 mm in diameter [22], all arterial ROIs had diameters of 1.5 mm. CR for SDIO injected mice and DIO injected mice were compared using a two-sided *t*-test in Microsoft Excel.

3. Results and discussion

3.1. Synthesis of SDIO

The DIO were synthesized according to our previously reported procedure [20]. The sulfation of polysaccharides has been reported via both heterogeneous and homogeneous synthesis pathways. Heterogeneous sulfation reactions with chlorosulfonic acid are subject to major drawbacks such as multiple and non-reproducible side reactions, presence of hazardous and non-reproducible sulfation rates and patterns, and backbone degradation. Homogeneous sulfation of dextran with nitrogen base complexes of sulfur trioxide in aprotic solvents are the preferred method; however, homogeneous reactions are still accompanied by some non-reproducible side reactions such as cleavage of labile functional groups and backbone degradation [23]. Our first effort to sulfate DIO followed literature methods, which performed sulfation of dextran with sulfur trioxide pyridine complex in dry formamide at room temperature [24]. However, the resultant

188

particles showed 2 size peaks with an average hydrodynamic diameter of 122 ± 97 nm. The sulfation reaction was reassessed under different synthetic conditions including varying temperatures, using sulfur trioxide DMF complex as sulfating agent, or using DMF as reaction solvent, yielding similar results. This indicates that although sulfation of dextran with nitrogen base complexes of sulfur trioxide is well-known [23], successful translation to a dextran coat on a nanoparticle is not trivial. The larger-sized peak may have been due to the depolymerization of dextran followed by aggregation of incompletely coated iron oxide nanoparticles.

Sulfur trioxide pyridine complex is made by dripping chlorine sulfate acid into dry pyridine at -15 °C [24]. However, the presence of pyridine may only partially limit the highly acidic character of chlorosulfonic acid, which is known to be responsible for multiple, undesirable, and non-reproducible side reactions such as cleavage of acid labile functional groups and partial depolymerization [25]. We therefore introduced an acid scavenger of a neutral nature, 2-methyl-2-butene (2M2B), into the reaction before the addition of sulfation agent, hypothesizing that this would clear the free acid produced in the system in a timely fashion and lead to a more efficient reaction, with diminished side reactions in the sulfation of dextran coat on IO NPs (Scheme 1) [25,26]. The purified, sulfated DIO were turned out to be mono-dispersed nanoparticles.

3.2. Characterization of SDIO

3.2.1. SDIO formation verification

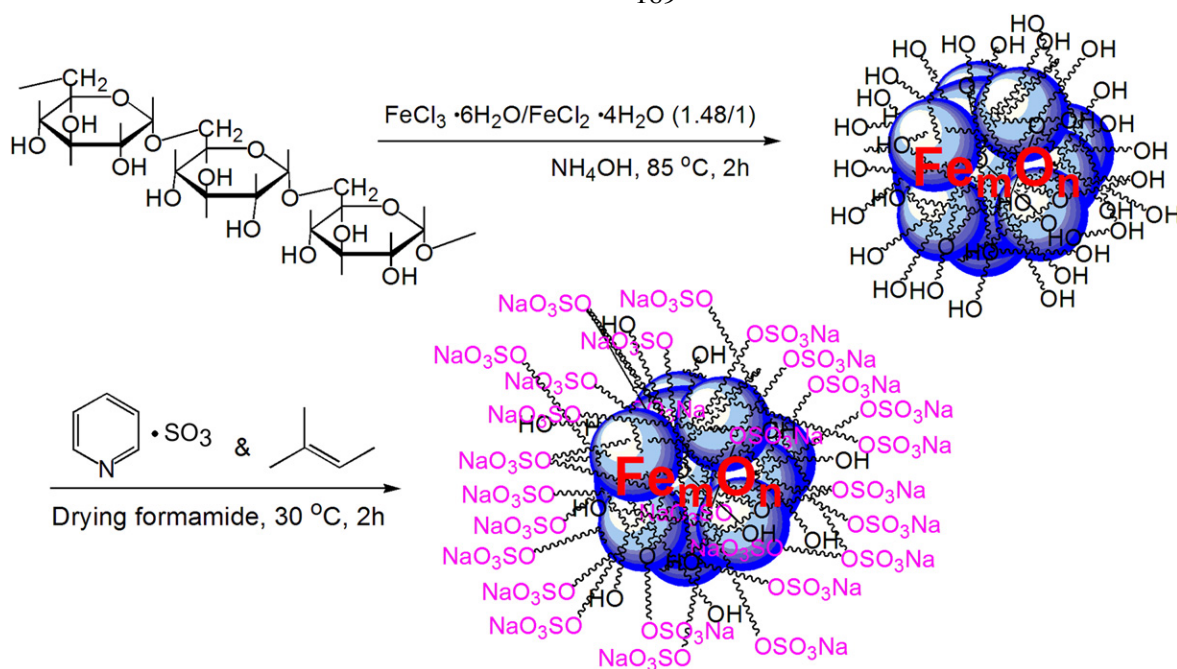
Successful sulfation was verified by infrared spectroscopy and elemental analysis of the purified particles. Compared to the infrared spectrum of DIO, new absorptions of S=O groups at 1234 cm⁻¹ (asymmetrical stretch), 1011 cm⁻¹ (symmetrical stretch), and 826 cm⁻¹ (symmetrical C–O–S stretch) were observed, while the absorptions at 3426 cm⁻¹ (O–H stretch) and 1026 cm⁻¹ (C–O stretch) were decreased in the infrared spectrum of SDIO [24]. The emergence of sulfur (9.74%) and decrease of iron content (from 17.7% in DIO to 11.34% in SDIO) in SDIO further verified successful sulfation of DIO. The results from elemental analysis of sulfur content also showed that a 2 h reaction time was sufficient for the sulfation of DIO; longer reaction time did not appear to increase sulfation.

3.2.2. SDIO size, relaxivity and surface charge

SDIO has an average core size of 7–8 nm (Fig. 1a) and an average hydrodynamic diameter of 62.4 nm (Fig. 1b), an r_1 relaxivity of 18.1 mM⁻¹ s⁻¹, and an r_2 relaxivity of 95.8 mM⁻¹ s⁻¹ (37 °C, 1.4 T) in pH 7.0 deionized water. The r_2 to r_1 ratio was 5.3, indicating that SDIO could be used, preferably, as a T_2 -weighted MRI contrast agent.

The measured zeta potential (ζ) values were -14.90 mV and -40.05 mV for DIO and SDIO, respectively. Typically the ζ value reflects the electric charge on the particle surface and indicates the physical stability of dispersions and emulsions in a colloidal system [27]. Double layers with high ζ values would create powerful electrostatic repulsion and, consequently, prevent aggregation resulting from collisions caused by Brownian motion. In comparison with DIO, the ζ value of SDIO decreased by 25.15 mV, indicating a more stable dispersion and emulsification of SDIO in water. In practice, we found SDIO to be very stable, with a long shelf life in aqueous solution. We have not observed any properties to change (e.g. aggregation, size, and magnetic property) after benchtop storage for over a year at room temperature.

Dextran in DIO is coated on the surface of iron oxide core. Due to decreased access for hydroxyl groups that lay deeper in the polymer layer, we estimate that the degree of sulfation of outer polymer layer is greater than that of the inner polymer layer. This should be



Scheme 1. Sulfation of dextran coated iron oxide nanoparticles.

ideal because the maximum sulfation of surface dextran can greatly increase the targeting ability of the nanoparticles to macrophages with less charge repulsion at the inner polymer layers that can affect size and MRI properties. Particle size was somewhat larger in comparison with that of non-sulfated DIO. This is likely due to the repulsion of negatively charged sulfate groups on the surface of SDIO. The r_1 and r_2 relaxivity values of SDIO were similar to those of DIO. This is not unexpected as the size of the iron oxide cores was similar for DIO and SDIO. Reproducibility of our method was validated by repeating the same reaction; running the reaction with a different scale of DIO; and using sulfur trioxide DMF complex as sulfation agent instead of sulfur trioxide pyridine complex. All of these reactions gave similar products, indicating that our sulfation procedure is reproducible and robust.

3.3. Cell experiments

3.3.1. SDIO targeting to macrophages P388D1

We selected SR-A as the target for our particles because it is highly expressed on activated macrophages in atheromas. SR-A

recognizes and binds a number of polyanionic molecules, such as oxidized LDL, that contribute to the involvement of macrophages in the formation of plaques [28]. For example, experiments conducted on Apo E knockout (Apo E^{-/-}) mice demonstrated that knocking out SR-A resulted in a significant decrease in atherosclerotic plaque size [29]. To demonstrate targeting of SDIO to macrophages, we performed *in vitro* studies using P388D1 murine macrophage cells. Uptake of DIO was also performed as a control for comparison; the properties of the DIO particles were similar to those of the commercially available MRI CA Sinerem (Table 1) [30].

The T_2 values of the lysates of macrophages incubated with increasing concentrations of SDIO or DIO for 2 h are shown in Fig. 2. In comparison with DIO, the mean T_2 values were significantly lower for cell lysates incubated with SDIO at all concentrations. In comparison with the lysates of blank macrophages, SDIO at 5.0×10^{-5} M Fe significantly decreased T_2 by 70% (p value = 0.002), compared to a 20% T_2 decrease (p value = 0.03) for the same iron concentration of DIO, indicating that there was limited uptake of DIO compared to SDIO under the same conditions. This result was as expected because DIO is not a ligand of SR-A so it is not recognized

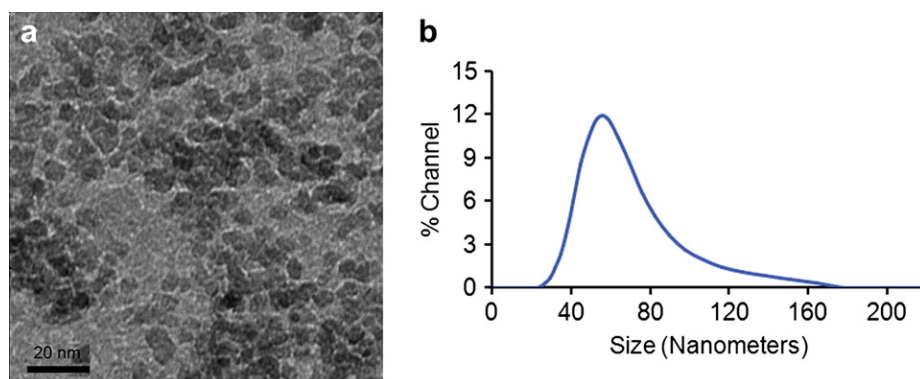


Fig. 1. (a) TEM, and (b) DLS of dextran sulfate coated iron oxide nanoparticles (SDIO).

Table 1

Characteristics of dextran sulfate coated iron oxide nanoparticles (SDIO), in comparison with dextran coated iron oxide nanoparticles (DIO) and commercially available dextran coated iron oxide nanoparticles (Sinerem).

Nanoparticles	Core size (nm)	Average hydrodynamic diameter (nm)	Relaxivity ($\text{mM}^{-1} \text{s}^{-1}$) (1.4 T, 37 °C)		% iron	ζ (mV)
			r_1	r_2		
SDIO	7–8	62.4	18.1	95.8	11.34	–40.05
DIO	7–8	42.4	15.7	89.2	17.7	–14.90
Sinerem	N/A	<50 nm	19.5 ^a	87.6 ^a	N/A	N/A

^a 1.5 T, 37 °C.

by the receptor. Our results demonstrate that sulfation of DIO facilitates SR-A targeting, and greatly improves accumulation of the particles in macrophages over the non-targeted, dextran coated particles.

3.3.2. Receptor-mediated uptake of SDIO by macrophages P388D1

Specificity for the cellular uptake of SDIO was confirmed by competition studies in which cells were incubated with a fixed concentration of SDIO and increasing excess of unlabeled dextran sulfate (ligand of SR-A) or dextran (not a ligand of SR-A). If uptake of the agents was receptor-mediated, the excess unlabeled ligand should compete for binding to the receptors. Nonspecific uptake is strictly concentration-dependent and would not be affected by additional ligands in the solution [16,31]. Receptor-mediated uptake of SDIO was confirmed by the results seen in Fig. 3: increasing amounts of competitor, from 0.02 to 10-fold excess, strongly reduce uptake, while increasing amounts of excess dextran had little influence on the uptake, indicating that the uptake of SDIO by SR-A is a receptor-mediated process. To exclude the possibility that the reduced uptake of SDIO in the presence of dextran sulfate is caused by toxicity or any other influence of dextran sulfate on the cells themselves, dextran sulfate alone, at the same concentrations, was applied to P388D1 cells in culture and the cell viability was evaluated by the C_{12} - Resazurin viability assay [32]. The average cell viability was above 96% after either 4 h or 24 h incubation of cells with the concentration of dextran sulfate varying from 0.04 to 10×10^{-3} M, indicating that the dextran sulfate is not toxic to mammalian cells (Supplementary Figure 1).

3.3.3. Cytotoxicity of SDIO to mammalian cells

As a preliminary assessment of SDIO's toxicity to cells, SDIO were applied to P388D1 cells in culture and the cell viability was evaluated by the C_{12} - Resazurin viability assay [32]. Untreated cells served as negative control. The average cell viability is above 96% or

94% after 4 h or 24 h incubation with the particles varying from 0.02 to 5×10^{-3} M iron, respectively (Fig. 4). The result showed that SDIO at concentrations relevant for biological imaging do not have observable toxicity to mammalian cells. This is similar to the results for most of the *in vitro* cytotoxicity studies on iron oxide nanoparticles reported in the literature [33–36].

A major concern that limits the use of nanomaterials in clinic is the potential toxicity. The iron oxide nanoparticles have been used in the clinic due to their biocompatibility. After injection the IO NPs are taken up in the liver and spleen where they are metabolized and broken down slowly to release free iron ions. The released iron ions are added to the body's iron stores and eventually incorporated by erythrocytes as hemoglobin [37]. Free iron ions could potentially be cytotoxic because of the catalytic function of iron in the production of reactive oxygen species (ROS), which in turn can cause lipid peroxidation, protein oxidation, and DNA damage. However, the body has the ability to process these released iron ions as indicated by iron's large median lethal dose (LD_{50}) of 450 mg/kg for oral ingestion in the rat model [10,14]. In fact, iron oxide nanoparticle MRI contrast agents have maintained an excellent safety record since they were approved for clinical use [37,38].

3.4. Animal studies

The Apo E^{-/-} mouse is a widely accepted model for atherosclerosis. In practice, we found that ligation of carotid arteries was an effective method to generate macrophage-laden plaques [18]. The carotid artery is relatively superficial and more amenable to surgical procedures than the coronary artery. Therefore, to evaluate the preliminary *in vivo* capabilities of SDIO we utilized a carotid ligation model. A single carotid artery in the Apo E^{-/-} mouse ($n = 5$) was ligated two weeks prior to the imaging study to induce atherosclerotic plaques. A T_2^* -weighted MRI with gradient echo sequence was utilized to visualize the uptake of SDIO and DIO

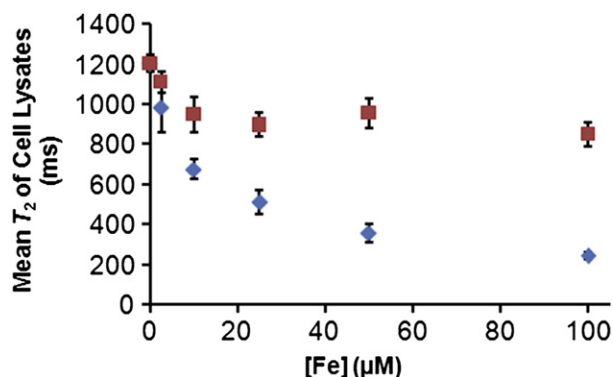


Fig. 2. Mean T_2 values of cell lysates incubated for 2 h with SDIO (◆) or DIO (■) of different iron concentrations.

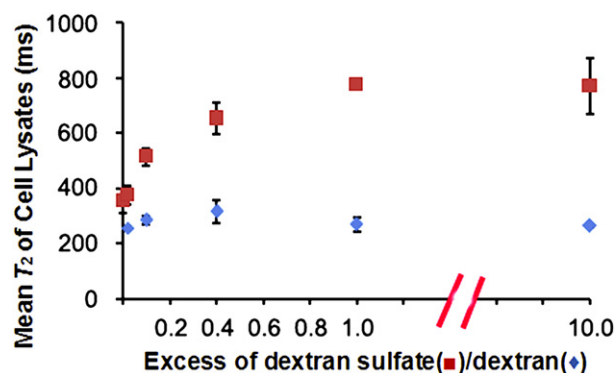


Fig. 3. Competitive uptake of SDIO ($[\text{Fe}] = 5.0 \times 10^{-5}$ M) and dextran sulfate (■), or dextran (◆) by P388D1 cells.

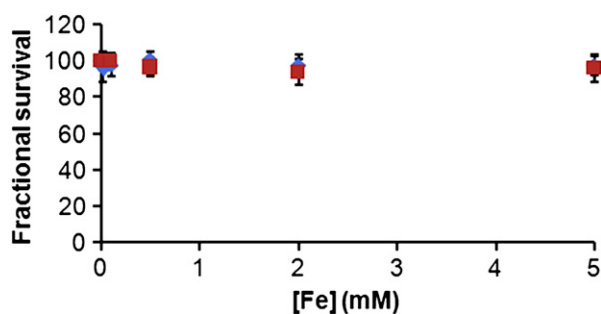


Fig. 4. Cell viability of P388D1 after 4- (◆), or 24 h (■) incubation with different concentrations of SDIO.

particles. Image slices from a representative mouse, matched at the same slice level of the mouse common carotid arteries over a 24-h time course are shown in Fig. 5a.

Because SDIO is a negative contrast agent, regions taking up SDIO produce a T_2 susceptibility effect, appearing darker than areas without SDIO. The MR images displayed a sizeable decrease in the signal of the ligated carotid artery at 4 and 24 h compared to the pre-injection image. The result parallels that from the *in vitro* particle incubation time study that showed that T_2 values of the lysates of macrophages incubated with SDIO decreased substantially after a 4 h incubation time with little subsequent change (Supplementary Figure 2). No discernible signal decrease was seen on the control carotid artery. This suggests preferential uptake of the SDIO particles at the sites of atherosclerotic plaque. Image slices from a representative mouse injected with DIO particles is shown in Fig. 5b. Compared to SDIO injected animals, less signal intensity decrease was seen over time for the DIO injected subjects. Visualization of the volume regions above and below each slice depicted in Fig. 5, shown in Supplementary Videos 1–6, confirmed that the signal decreases observed were due to localization of contrast agent, and not in homogeneities in endogenous signal between slices.

Supplementary video related to this article can be found at doi:10.1016/j.qdy.2009.12.006.

To compare the relative uptake between SDIO and DIO particles in a more quantitative manner, we define a contrast ratio (CR) metric to measure the magnitude of signal decrease at the arterial

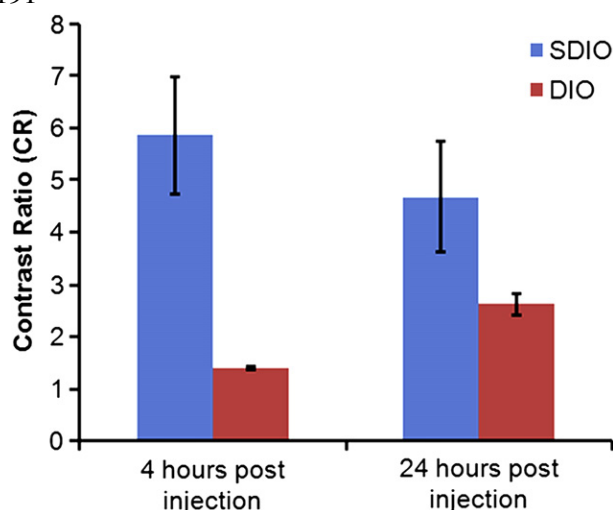


Fig. 6. Contrast Ratio between SDIO and DIO particle accumulation *in vivo*.

site. As seen in Fig. 6, the CR of SDIO injected mice were significantly higher than those of the DIO injected mice by 4 h post-injection (p value = 0.03). This suggests that at the same injected iron dose, SDIO accumulated preferentially compared to DIO particles at the site of atherosclerotic plaque. It should be noted that the ROIs delineated included the signal contribution of particles in the blood. We normalize for this effect by comparing between the left and right carotids, which factors out the signal contribution due to blood borne particles.

Iron oxide nanoparticle-enhanced MRI has been reported to be able to identify atherosclerotic plaques in both *in vivo* animal and human studies [14]. However, the non-specific contrast agents are taken up by activated macrophages in vulnerable plaques via phagocytosis, pinocytosis or fluid-phase transport, which are inefficient processes [15]. As a result, direct visualization of atherosclerotic plaques often required relatively large amounts of nanoparticles [14,39]. A tissue-specific contrast agent would allow for an improved identification of these lesions [38,40]. Active targeting of nanoparticles can be achieved by decorating them with a ligand against a known marker associated with lesions. Our *in vivo* MRI images revealed that at 4 h post-injection, targeted SDIO

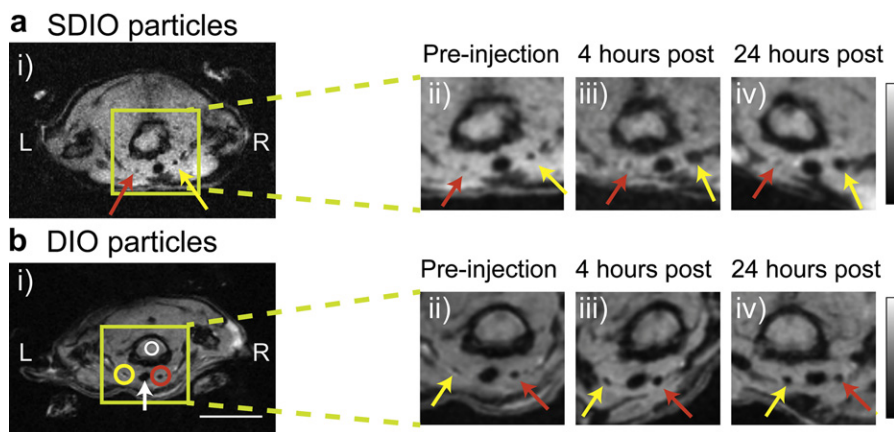


Fig. 5. Signal change in MRI over time after SDIO (a) or DIO (b) injection. The ligated carotid artery is denoted by the yellow arrow and the control carotid artery is denoted by the red arrow. Circles indicate the ROI measures used to derive the contrast ratio (CR) metric. To facilitate comparison, the magnified images in carotid areas were first rotated in plane so all timepoints in the orientation. They were then zero-filled by a factor of 2 and then smoothed with a 2×2 Gaussian filter. (Scale bar = 10 mm, both scale bar and intensity bar apply to the whole animal images only. L = left, R = right, green box shows magnification area, white arrow denotes the trachea). (For interpretation of the references to colour in this figure legend, the reader is referred to the web version of this article.)

provided a 4-fold increase in the contrast ratio compared to non-targeted DIO. The contrast ratio metric was used to account for differences in anatomy and physiology between subjects. Comparing the signal decrease between the ligated and control artery region normalizes the metric and allows cross comparisons over timepoints and between subjects. It should be noted that the ROIs delineated included the signal contribution of particles in the blood. We normalize for this effect by comparing between the left and right carotids, which factors out the signal contribution due to blood borne particles. Comparison between the CR of SDIO versus DIO injected mice (Fig. 6) suggests a time-dependence for optimal SDIO uptake. This is likely to be a function of the degree of vulnerability of the plaque at the local site as well as the general pharmacokinetics of the particles. Future studies will aim to correlate this with *ex-vivo* assays to further understand the mechanism of particle accumulation.

We have previously shown the SR-A is a viable target for labeling macrophages and atherosclerotic plaques [16,17]. Recently, micelles containing gadolinium chelates and antibodies against SR-A have been synthesized and applied to MRI of aortic plaques in Apo E^{-/-} mice. *In vivo* MRI revealed that at 24 h post-injection, targeted micelles provided a 79% increase in signal intensity of atherosclerotic aortas compared with 34% using non-targeted micelles, and no enhancement occurred using Gd-DTPA. Uptake of the micelles was shown, through competition experiments, to be a receptor-mediated process [41]. However, the potential immunogenicity of antibodies and cost to generate them in a quantity may limit the use of immunomicelles clinically [10]. Small molecules or polymers are alternatives to antibodies [42]. SR-A recognizes a wide range of ligands that are polyanionic, though not all polyanionic molecules. Our results show that sulfation of dextran coated IO NPs greatly increased the negative charges on the particle surface (high negative ζ value); this allowed the particles to be recognized by SR-A and accumulate at the injured carotid artery *in vivo*. Competition studies support that the particles were taken up by a receptor-mediated uptake and not merely due to non-specific electrostatic association.

Macrophages and macrophage scavenger receptors play a key role in the pathogenesis of atherosclerosis. Macrophages are present through all stages of atherosclerosis development, from the initiation of plaques through the formation of complex plaques containing foam cells, necrotic debris, and thrombi, and have been specifically associated with plaque stability—high densities of macrophages correlate with vulnerability to rupture [5,13]. Our results show that SDIO can be recognized and specifically taken up by macrophages via scavenger receptor. Their specific accumulation at the injured carotid, but not the control carotid, suggests the potential to use SDIO with MRI to detect and distinguish inflamed atherosclerotic plaques.

4. Conclusion

The use of MRI is a well-established means for injury and disease diagnosis on the anatomic scale. Current advances in targeted contrast agents allow researchers to gather *in vivo* anatomic and molecular information simultaneously. IO NPs modified to target various moieties in atherosclerotic plaques have demonstrated their utility as an important tool for enhancing magnetic resonance detection of atherosclerosis at the anatomical, cellular and molecular levels [43]. However, to date, reports of targeted MRI of macrophages, a key component in the formation and development of vulnerable plaques, are relatively rare. In this paper, we sulfated dextran coated IO NPs and therefore targeted the nanoparticles to scavenger receptors on macrophages. SDIO has a high r_2 value of 95.8 mM⁻¹ s⁻¹ and an r_2/r_1 ratio of 5.3 (37 °C, 1.4 T),

therefore acts as an efficient T₂-weighted MRI contrast agent. We demonstrate that SDIO nanoparticles are specifically and avidly taken up by macrophages via a receptor-mediated process that labels macrophages much more efficiently than non-sulfated analogues, and produces distinct contrast in both *in vitro* and *in vivo* T₂-weighted MRI images. High macrophage density has been associated with atherosclerotic plaques vulnerable to rupture. Thus, the specific targeting of macrophages with the MR nanoparticle imaging agent SDIO demonstrates the potential for SDIO to facilitate detection and diagnosis plaque stability with *in vivo* MRI.

Acknowledgements

The authors wish to acknowledge the National Institute of Health (EB008576-01, and EB000993), the Beckman Institute at Caltech, the Center for Molecular and Genomic Imaging at UC Davis (U24 CA 110804), and the NMR award of the University of California, Davis for support of this work. We thank Dr. Xuchu Ma, Dr. Jai Woong Seo, and Bitu Alaghebandan for help in IR spectroscopy, zeta potential, and animal handling, respectively.

Appendix. Supplementary material

Supplementary data associated with this article can be found, in the online version, at doi:10.1016/j.biomaterials.2011.06.026 .

References

- [1] Fuster V, Lois F, Franco M. Early identification of atherosclerotic disease by noninvasive imaging. *Nat Rev Cardiol* 2010;7:327–33.
- [2] Wickline SA, Neubauer AM, Winter PM, Caruthers SD, Lanza GM. Molecular imaging and therapy of atherosclerosis with targeted nanoparticles. *J Magn Reson Imaging* 2007;25:667–80.
- [3] Cyrus T, Lanza GM, Wickline SA. Molecular imaging by cardiovascular MR. *J Cardiovasc Magn Reson* 2007;9:827–43.
- [4] Rudd JHF, Hyafil F, Fayad ZA. Inflammation imaging in atherosclerosis. *Arterioscler Thromb Vasc Biol* 2009;29:1009–16.
- [5] Shaw SY. Molecular imaging in cardiovascular disease: targets and opportunities. *Nat Rev Cardiol* 2009;6:569–79.
- [6] Winter PM, Caruthers SD, Lanza GM, Wickline SA. Quantitative cardiovascular magnetic resonance for molecular imaging. *J Cardiovasc Magn Reson* 2010;12. Article Number: 62.
- [7] Sosnovik DE, Nahrendorf M, Weissleder R. Molecular magnetic resonance imaging in cardiovascular medicine. *Circulation* 2007;115:2076–86.
- [8] Terreno E, Castelli DD, Viale A, Aime S. Challenges for molecular magnetic resonance imaging. *Chem Rev* 2010;110:3019–42.
- [9] Galdes C, Laurent S. Classification and basic properties of contrast agents for magnetic resonance imaging. *Contrast Media Mol Imaging* 2009;4:1–23.
- [10] Cormode DP, Skajaa T, Fayad ZA, Mulder WJM. Nanotechnology in medical imaging probe design and applications. *Arterioscler Thromb Vasc Biol* 2009;29:992–1000.
- [11] Qiao RR, Yang CH, Gao MY. Superparamagnetic iron oxide nanoparticles: from preparations to *in vivo* MRI applications. *J Mater Chem* 2009;19:6274–93.
- [12] Croons V, Martinet W, De Meyer GRY. Selective removal of macrophages in atherosclerotic plaques as a pharmacological approach for plaque stabilization: benefits vs. potential complications. *Curr Vasc Pharmacol* 2010;8:495–508.
- [13] Osborn EA, Jaffer FA. Advances in molecular imaging of atherosclerotic vascular disease. *Curr Opin Cardiol* 2008;23:620–8.
- [14] Tang TY, Muller KH, Graves MJ, Li ZY, Walsh SR, Young V, et al. Iron oxide particles for atheroma imaging. *Arterioscler Thromb Vasc Biol* 2009;29:1001–8.
- [15] Sadat U, Li ZY, Graves MJ, Tang TY, Gillard JH. Noninvasive imaging of atheromatous carotid plaques. *Nat Clin Pract Cardiovasc Med* 2009;6:200–9.
- [16] Gustafsson B, Youens S, Louie AY. Development of contrast agents targeted to macrophage scavenger receptors for MRI of vascular inflammation. *Bioconjug Chem* 2006;17:538–47.
- [17] Tu CQ, Ma XC, Pantazis P, Kaulzarich SM, Louie AY. Paramagnetic, silicon quantum dots for magnetic resonance and two-photon imaging of macrophages. *J Am Chem Soc* 2010;132:2016–23.
- [18] Jarrett BR, Correa C, Ma KL, Louie AY. *In vivo* mapping of vascular inflammation using multimodal imaging. *PLoS One* 2010;5. Article Number: e13254.
- [19] de Winther MPJ, van Dijk KW, Havekes LM, Hofker MH. Macrophage scavenger receptor class A - A multifunctional receptor in atherosclerosis. *Arterioscler Thromb Vasc Biol* 2000;20:290–7.

- [20] Jarrett BR, Frendo M, Vogan J, Louie AY. Size-controlled synthesis of dextran sulfate coated iron oxide nanoparticles for magnetic resonance imaging. *Nanotechnology* 2007;18. Article Number: 035603.
- [21] Tu CQ, Louie AY. Photochromically-controlled, reversibly-activated MRI and optical contrast agent. *Chem Commun*; 2007:1331–3.
- [22] Kumar A, Hoover JL, Simmons CA, Lindner V, Shebuski RJ. Remodeling and neointimal formation in the carotid artery of normal and P-selectin-deficient mice. *Circulation* 1997;96:4333–42.
- [23] Heinze T, Liebert T, Heublein B, Hornig S. Functional polymers based on dextran. *Adv Polym Sci* 2006;205:199–291.
- [24] Mahner C, Lechner MD, Nordmeier E. Synthesis and characterisation of dextran and pullulan sulphate. *Carbohydr Res* 2001;331:203–8.
- [25] Papy-Garcia D, Barbier-Chassefiere V, Rouet V, Kerros ME, Klochendler C, Tournaire MC, et al. Nondegradative sulfation of polysaccharides. synthesis and structure characterization of biologically active heparan sulfate mimetics. *Macromolecules* 2005;38:4647–54.
- [26] Wondraczek H, Pfeifer A, Heinze T. Synthetic photocrosslinkable polysaccharide sulfates. *Eur Polym J* 2010;46:1688–95.
- [27] Obeidat WM, Schwabe K, Muller RH, Keck CM. Preservation of nanostructured lipid carriers (NLC). *Eur J Pharm Biopharm* 2010;76:56–67.
- [28] Greaves DR, Gordon S. The macrophage scavenger receptor at 30 years of age: current knowledge and future challenges. *J Lipid Res* 2009;50:S282–6.
- [29] Babaev VR, Gleaves LA, Carter KJ, Suzuki H, Kodama T, Fazio S, et al. Reduced atherosclerotic lesions in mice deficient for total or macrophage-specific expression of scavenger receptor-A. *Arterioscler Thromb Vasc Biol* 2000;20:2593–9.
- [30] Gossuin Y, Gillis P, Hocq A, Vuong QL, Roch A. Magnetic resonance relaxation properties of superparamagnetic particles. *Wiley Interdiscip Rev Nanomed Nanobiotechnol* 2009;1:299–310.
- [31] Tu C, Nagao R, Louie AY. Multimodal magnetic-resonance/optical-imaging contrast agent sensitive to NADH. *Angew Chem Int Ed Engl* 2009;48:6547–51.
- [32] O'Brien J, Wilson I, Orton T, Pognan F. Investigation of the Alamar Blue (resazurin) fluorescent dye for the assessment of mammalian cell cytotoxicity. *Eur J Biochem* 2000;267:5421–6.
- [33] Muller K, Skepper JN, Posfai M, Trivedi R, Howarth S, Corot C, et al. Effect of ultrasmall superparamagnetic iron oxide nanoparticles (Ferumoxtran-10) on human monocyte-macrophages in vitro. *Biomaterials* 2007;28:1629–42.
- [34] Metz S, Bonaterra G, Rudelius M, Settles M, Rummeny EJ, Daldrup-Link HE. Capacity of human monocytes to phagocytose approved iron oxide MR contrast agents in vitro. *Eur Radiol* 2004;14:1851–8.
- [35] Schulze E, Ferrucci JT, Poss K, Lapointe L, Bogdanova A, Weissleder R. Cellular uptake and trafficking of a prototypical magnetic iron-oxide label in-vitro. *Invest Radiol* 1995;30:604–10.
- [36] Mailander V, Lorenz MR, Holzapfel V, Musyanovych A, Fuchs K, Wiesneth M, et al. Carboxylated superparamagnetic iron oxide particles label cells intracellularly without transfection agents. *Mol Imaging Biol* 2008;10:138–46.
- [37] Sun C, Lee JSH, Zhang MQ. Magnetic nanoparticles in MR imaging and drug delivery. *Adv Drug Deliv Rev* 2008;60:1252–65.
- [38] Sosnovik DE, Caravan P. Molecular MRI of atherosclerotic plaque with targeted contrast agents. *Curr Cardiovasc Imaging Rep* 2009;2:87–94.
- [39] Nahrendorf M, Zhang HW, Hembador S, Panizzi P, Sosnovik DE, Aikawa E, et al. Nanoparticle PET-CT imaging of macrophages in inflammatory atherosclerosis. *Circulation* 2008;117:379–87.
- [40] Uppal R, Caravan P. Targeted probes for cardiovascular MRI. *Future Med Chem* 2010;2:451–70.
- [41] Amirbekian V, Lipinski MJ, Briley-Saebo KC, Amirbekian S, Aguinaldo JGS, Weinreb DB, et al. Detecting and assessing macrophages in vivo to evaluate atherosclerosis noninvasively using molecular MRI. *Proc Natl Acad Sci U S A* 2007;104:961–6.
- [42] Choudhury RP, Fisher EA. Molecular imaging in atherosclerosis, thrombosis, and vascular inflammation. *Arterioscler Thromb Vasc Biol* 2009;29:983–91.
- [43] Thorek DLJ, Chen A, Czupryna J, Tsourkas A. Superparamagnetic iron oxide nanoparticle probes for molecular imaging. *Ann Biomed Eng* 2006;34:23–38.

Receptor-targeted Iron Oxide Nanoparticles for Molecular MR

Imaging of Inflamed Atherosclerotic Plaques

Chuqiao Tu ^a, Thomas S.C. Ng ^b, Hargun Sohi ^b, Heather Palko ^c, Adrian House ^a,

Russell E. Jacobs ^b, and Angelique Y. Louie ^{a,*}

^a Department of Biomedical Engineering, ^c Department of Chemistry, University of California, Davis, CA 95616, USA. ^b Beckman Institute, California Institute of Technology, Pasadena, CA 91125, USA.

Supporting Information

Table of Contents

Caption of supplementary video 1: pre-injection MRI of neck/carotid region prior to the administration of SDIO contrast agent.	S2
Caption of supplementary video 2: MRI of neck/carotid region 4 hours post injection of SDIO contrast agent.	S2
Caption of supplementary video 3: MRI of neck/carotid region 24 hours post injection of SDIO contrast agent.	S2, S3
Caption of supplementary video 4: pre-injection MRI of neck/carotid region prior to the administration of DIO contrast agent.	S3
Caption of supplementary video 5: MRI of neck/carotid region 4 hours post injection of DIO contrast agent.	S3
Caption of supplementary video 6: MRI of neck/carotid region 24 hours post injection of DIO contrast agent.	S3, S4
Supplementary figure 1	S4
Supplementary figure 2	S5
Six videos for MRI of neck/carotid region pre-injection and 4h, 24h post-injection of SDIO or DIO contrast agents	Attachments

Captions of videos 1-6*Supplementary video 1.*

Pre-injection MRI of neck/carotid region prior to the administration of SDIO probes. Slices above and below the plane of Figure 5ai are provided in the video clip. Figure 5ai is the center slice of the volume set, denoted by frames containing white borders. Arrows are present to denote the ligated (yellow) right carotid artery and the non-ligated (red) left carotid artery. Video frames are zero-filled by a factor of 4 in plane and by a factor of 8 across slices to facilitate visualization of the volume.

Supplementary video 2

MRI of neck/carotid region 4 hours post injection of SDIO probes. Slices above and below the plane of Figure 5aiii are provided in the video clip. Slices matching Figure 5aiii are framed by white borders. As per Figure 5ai, the central slice of this volume is matched to the central slice Supplementary video 2. Arrows are present to denote the ligated (yellow) right carotid artery and the non-ligated (red) left carotid artery. Video frames are zero-filled by a factor of 4 in plane and by a factor of 8 across slices to facilitate visualization of the volume.

Supplementary video 3

MRI of neck/carotid region 24 hours post injection of SDIO probes. Slices above and below the plane of Figure 5aiv are provided in the video clip. Slices matching Figure 5aiv are framed by white borders. As per Figure 5ai, the central slice of this volume is matched to the central slice Supplementary video 3. Arrows are present to denote the

ligated (yellow) right carotid artery and the non-ligated (red) left carotid artery. Video frames are zero-filled by a factor of 4 in plane and by a factor of 8 across slices to facilitate visualization of the volume.

Supplementary video 4

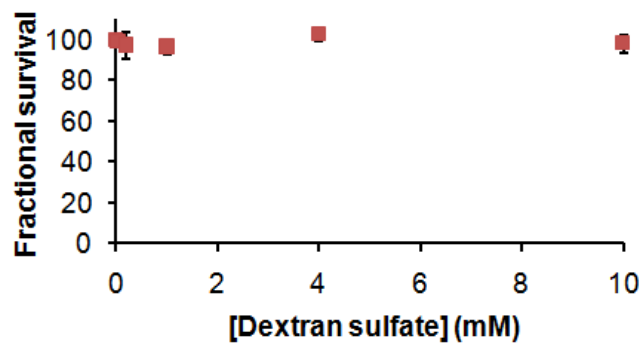
Pre-injection MRI of neck/carotid region prior to the administration of DIO probes. Slices above and below the plane of Figure 5bi are provided in the video clip. Figure 5bi is the center slice of the volume set, denoted by frames containing white borders. Arrows are present to denote the ligated (yellow) right carotid artery and the non-ligated (red) left carotid artery. Video frames are zero-filled by a factor of 4 in plane and by a factor of 8 across slices to facilitate visualization of the volume.

Supplementary video 5

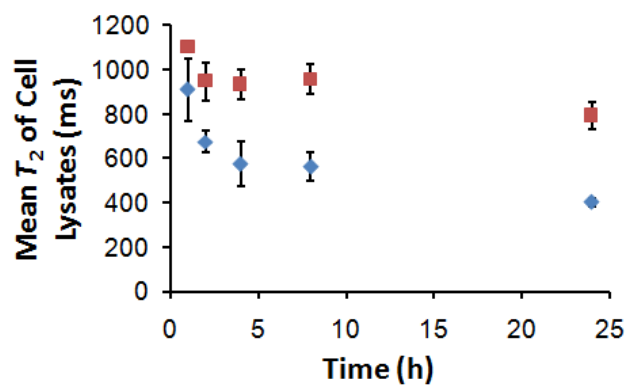
MRI of neck/carotid region 4 hours post injection of DIO probes. Slices above and below the plane of Figure 5biii are provided in the video clip. Slices matching Figure 5biii are framed by white borders. As per Figure 5bi, the central slice of this volume is matched to the central slice Supplementary video 5. Arrows are present to denote the ligated (yellow) right carotid artery and the non-ligated (red) left carotid artery. Video frames are zero-filled by a factor of 2 in plane and by a factor of 8 across slices to facilitate visualization of the volume.

Supplementary video 6

MRI of neck/carotid region 24 hours post injection of DIO probes. Slices above and below the plane of Figure 5biv are provided in the video clip. Slices matching Figure 5biv are framed by white borders. As per Figure 5bi, the central slice of this volume is matched to the central slice Supplementary video 5. Arrows are present to denote the ligated (yellow) right carotid artery and the non-ligated (red) left carotid artery. Video frames are zero-filled by a factor of 2 in plane and by a factor of 8 across slices to facilitate visualization of the volume.



Supplementary Fig. 1. Cell viability of P388D1 after 24-h incubation with different concentrations of dextran sulfate.



Supplementary Fig. 2. Mean T_2 values of cell lysates incubated with 1.0×10^{-5} M iron of SDIO (♦) or DIO (■) for different incubation times.

Appendix C

Cooccurrence Matrices to Compare Multimodal Image Datasets: Further Considerations

A cooccurrence matrix method was proposed in section 3.4 to compare multimodal imaging datasets voxel-by-voxel. Here we explored the effects of image spatial resolution disparity (as is present between PET and MRI images) on analysis made using this method and compared it with the direct voxel-by-voxel comparison method by simulation.

C.1 Methods

ADC maps derived from diffusion MRI data acquired for studies described in chapter 5 were used as the baseline *high-resolution* scans. For simulation purposes, we consider only the two-dimensional case and only for the tumor ROI.

C.1.1 Effects of Spatial Resolution on Voxel-by-voxel Analysis

Datasets that simulate those encountered in PET were generated by applying two-dimensional Gaussian filters of varying FWHM on the baseline dataset. In the first condition, we applied a spatially invariant filter on the baseline image. The effect of increasing FWHM (i.e. PSF, FWHM = 0–5 mm) on voxel-by-voxel comparison metrics were examined. Next, we filtered the image with a spatially variant filter to simulate spatially varying PSFs usually encountered in PET. FWHM as a function of radial distance from the center was determined from measurements made with the PET/MRI scanner [198]. FWHM at radial distances of <10 mm, the outer limit of the measurements,

were calculated from a quadratic fit from the data. The maximum FWHM from this fit was applied to radial distances of >10 mm. This represented a best case scenario as spatial resolution typically worsens farther away from the system's center [291]. Gaussian filtering was applied voxel-by-voxel using a nonlinear sliding window algorithm available as part of the MATLAB image processing package.

There are instances where we are interested in comparing regions of low signal in one modality with high signal in the other modality. To investigate this scenario, we generated blurred images from baseline images that have been inverted. An inverted baseline image, $Baseline_{inverted}$ was generated from the original baseline image $Baseline_{original}$ by

$$Baseline_{inverted}(i, j) = [Max(Baseline_{original}) - Baseline_{original}(i, j)] + Min(Baseline_{original}), \quad (C.1)$$

i, j are voxels indices within the tumor ROI.

Two metrics, the Pearson's correlation coefficient (PCC) and the concordance correlation coefficient (CCC) were calculated for voxel-by-voxel comparisons between baseline and Gaussian filtered images.

C.1.2 Cooccurrence Matrix Analysis

The cooccurrence matrix method was described in detail in section 3.4.3.4. Here, we examined how two variables present in this method may affect analysis.

C.1.2.1 PSF Window

One variable that may affect analysis is the PSF window considered around each voxel. cooccurrence matrices were calculated with different PSF windows ($|\Delta x|, |\Delta y| = 0-5$ mm), comparing the baseline image with four datasets:

1. The baseline image itself, as control (control matrix).
2. Baseline image blurred with static Gaussian filter (FWHM = 1.5 mm) to simulate the PET/MRI system.

3. Baseline image blurred with static Gaussian filter (FWHM = 2.2 mm) to simulate the microPET system.
4. Baseline image blurred with the spatially variant Gaussian filter to simulate actual PET systems.

Cooccurrence matrices were compared to the control matrix using CCC to evaluate the method's ability to compare data with different spatial resolutions. We repeated the analysis by comparing baseline images with inverted blurred images.

C.1.2.2 Binning method

The cooccurrence matrix is based on joint 2D histograms. Thus, an important parameter for this method is the choice of bins. We explored the robustness of the technique by comparing CCC values returned from matrices calculated with the following bin locations:

1. Minimum value = 0, maximum value = 65th percentile of tumor ADC values.
2. Minimum value = 0, maximum value = 75th percentile of tumor ADC values.
3. Minimum value = 0, maximum value = 85th percentile of tumor ADC values.
4. Minimum value = 0, maximum value = 95th percentile of tumor ADC values.
5. Minimum value = 0, maximum value = 100th percentile of tumor ADC values.

The number of histogram bins was set at 22. This was the average number returned from an optimal binning algorithm applied to the ADC data [292].

All simulations were performed in MATLAB. ADC images from three different animals acquired during different imaging sessions were used for the simulations.

C.2 Results and Discussion

C.2.1 Direct Voxel-by-voxel Comparison of PET and MRI Images is not Ideal

Voxel-by-voxel comparisons between baseline images and images blurred with a static and spatially varying Gaussian filter (which forms the ideal case) are shown in figure C.1. Image details, such

as the shape of the central fluid region in the tumor were lost upon filtering. Less details were lost when a spatially varying filter was used compared to the static filter. Visual inspection of the voxel-by-voxel plots did not show any obvious correlation between the baseline and blurred datasets. This was reflected in the correlation metrics. PCC and CCCs from the blurred to baseline comparisons decreased significantly from unity (PCC: -30%–50%, CCC: -60%–70%). This indicated that direct voxel-by-voxel comparisons of PET and MRI data is not optimal and can mask structures that may be correlated between the two modalities.

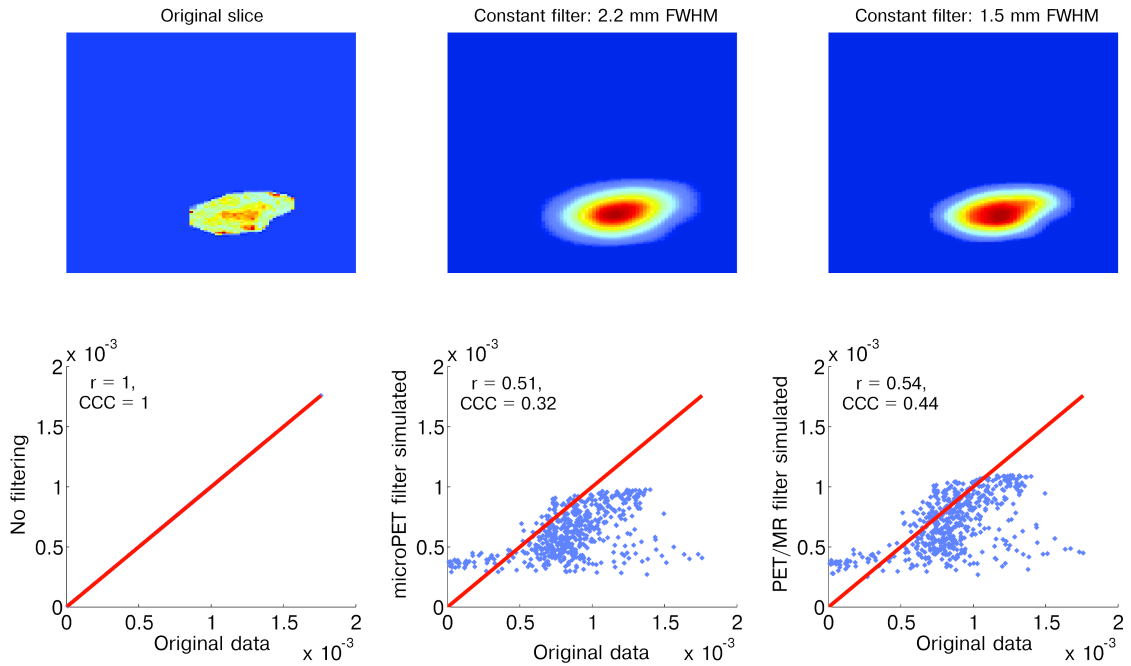
The effect of PSF size was examined by varying the filter FWHM (figure C.2). For the positive contrast comparison, PCC and CCC were dramatically reduced when FWHM >1 mm, the nominal resolution achievable by PET. The correlation drop off is more dramatic in the inverted comparison case: PCC and CCC were already attenuated for mouse 2 and mouse 3 with a filter of FWHM = 0.01 mm. This is expected, since Gaussian filters cause spillover of high voxel intensities into areas of lower voxel intensities.

C.2.2 Cooccurrence Matrix Comparison Provides an Reasonable Alternative to Direct Voxel Comparison

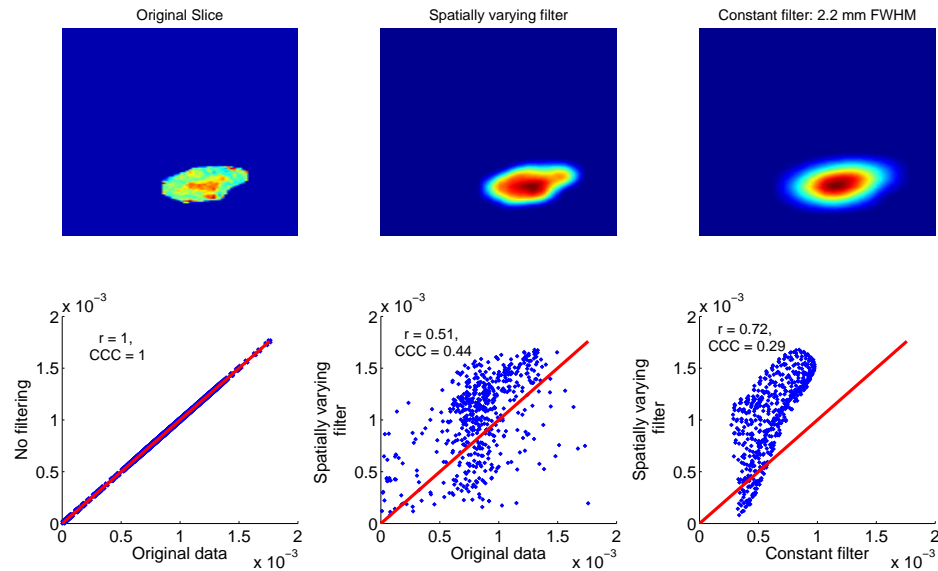
Example cooccurrence matrices for baseline-baseline and baseline-spatially variant filtered datasets are shown in figure C.3. The general pattern between the two matrices are similar. Slight differences between the two matrices are present. For example, a small portion of the lower ADC voxels on the blurred image cooccur with high ADC voxels on the baseline image. We quantified this difference by calculating the CCC for different binning methods at different PSF windows. The results for baseline/positive contrast and baseline/inverted contrast are shown in figure C.4.

A few trends were observed. Firstly, at the optimal PSF window and binning condition (~1 mm window, bin location condition 2), *Baseline_{original}* vs. *Baseline_{original}-blurred* matrices were consistently similar to *Baseline_{original}* vs. *Baseline_{original}* matrices for different animals. This was demonstrated by the high (>0.7) CCC values at the optimal condition. This suggests that cooccurrence matrices are able to recover image patterns that are obscured by blurring.

Secondly, cooccurrence matrices calculated for *Baseline_{original}* vs. *Baseline_{original}-blurred* images showed consistently higher CCC values compared to *Baseline_{original}* vs. *Baseline_{inverted}-blurred*

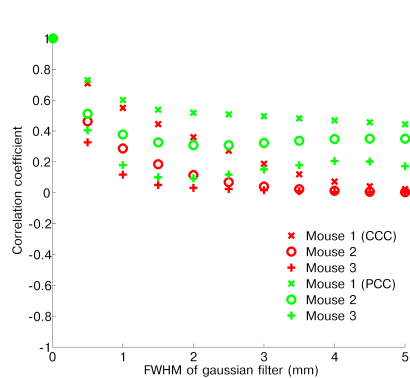


(a) Voxel-by-voxel comparisons of images filtered by spatially invariant Gaussian functions. Scatterplots do not reveal any obvious correlation between the datasets.

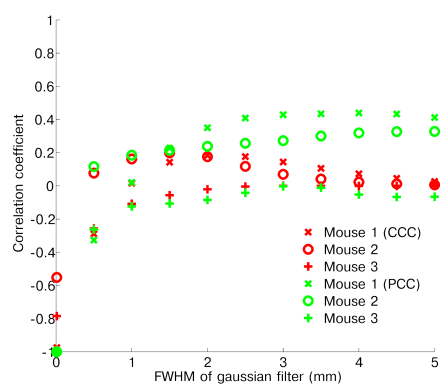


(b) Voxel-by-voxel comparisons of images filtered by spatially variant Gaussian functions. Although tumor details were less obscured, scatterplots still do not reveal any obvious correlation between the datasets.

Figure C.1: Voxel-by-voxel comparisons between images with different spatial resolutions for a single ADC dataset. Gaussian blurring drastically reduces image detail and obscures correlation by direct voxel analysis.

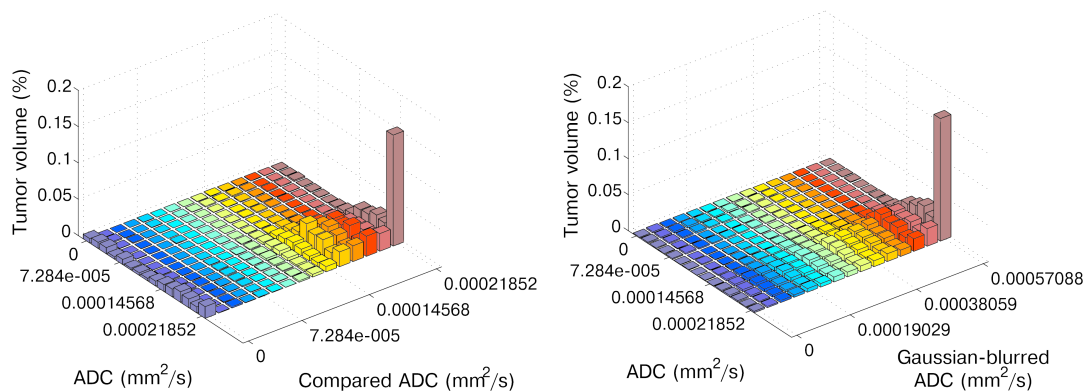


(a) Correlation of baseline and blurred data. A coefficient of 1 would indicate exact matching.



(b) Correlation of baseline and blurred data: comparison with inverted blurred data. A coefficient of -1 would indicate exact matching.

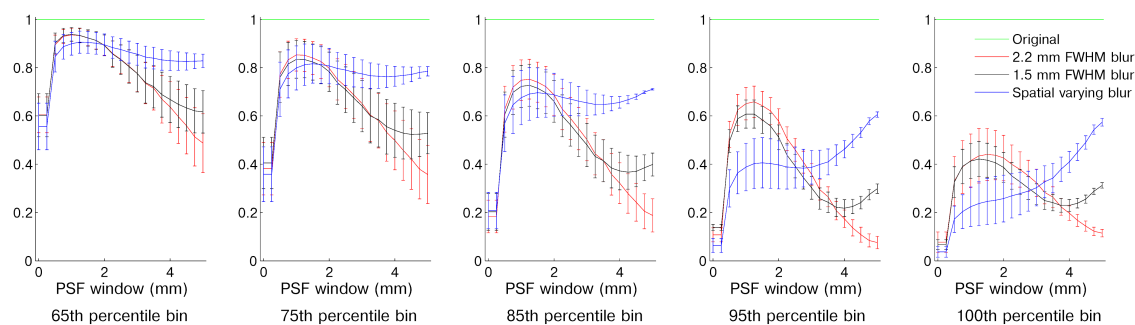
Figure C.2: Correlation of baseline and blurred data at different FWHM.



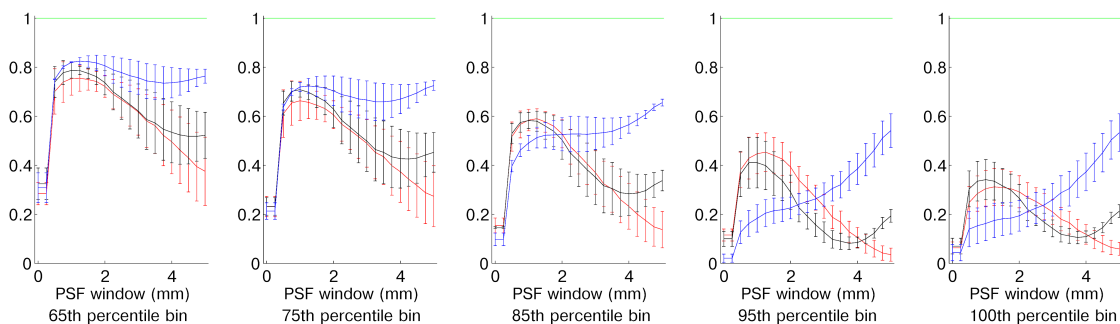
(a) Cooccurrence matrix calculated by comparing the baseline image with itself.

(b) Cooccurrence matrix calculated by comparing the baseline image with the spatially variant blurred image.

Figure C.3: Cooccurrence matrices were generated by binning from ADC values between 0 and the 75th percentile value within the tumor ROI. The PSF window used is 1.75 mm.



(a) Concordance correlation for different PSF windows with different binning conditions. Baseline images were compared to blurred baseline images.



(b) Concordance correlation for different PSF windows with different binning conditions. Baseline images were compared to blurred inverted baseline images.

Figure C.4: Concordance correlation coefficients for cooccurrence matrices compared to the control matrix. Matrices were calculated using different bin locations (percentile bin denotes the maximum histogram bin value) and PSF windows. Error bars denote standard error.

images. This makes sense, since Gaussian filters tend to cause spillover of high intensity voxels into low intensity regions and hence low intensity structures in the *Baseline_{inverted}*-blurred images are masked to a greater extent compared to the high intensity structures observed in the *Baseline_{original}*-blurred images.

Thirdly, the highest CCC was achieved in general for all binning conditions was observed with a PSF window ~ 1 mm. For images blurred with a spatially variant filter, a secondary high CCC peak was observed as the PSF window approached 5 mm. 1 mm is approximately half the FWHM of the Gaussian filters applied to the PET datasets. Thus, this should be the approximate radius which we expect a cooccurring voxel to lie compared to the voxel of interest. This relationship between structure resolvability and PSF window is supported by Valckx and Thijssen, who found that altering the PSF window as a function of speckle size in echographic images can affect the cooccurrence matrix method's ability to resolve structures [293].

The trend towards high CCC for spatially variant filtered images is due to the fact that the tumors being considered were ~ 5 mm. Thus, most of the tumor ROI voxels would cooccur with each other with a large PSF window.

Finally, we observed that the highest CCC are obtained using the 1 mm PSF window for maximal bin values at the 65th–85th percentile range. Maximal bin values above this resulted in reduced CCC values. The choice of optimal bin size and binning methods for cooccurrence matrix analysis is a subject of active investigation [294, 295, 296]. Both Handrick *et al.* [295] and Kim *et al.* [296] reported that nonlinear binning methods which adjust bin sizes depending on the histogram data were better than linear binning methods at tissue classification of CT images. This is reflected in our results, as linear binning (minimum value = 0, maximum value = maximum ADC value) showed the worst CCC with the baseline-baseline cooccurrence matrix. The 65th–85th percentile binning performed better, possibly because higher intensity values are clustered into a smaller number of bins. The optimal binning method may be dependent on the question being asked. For example, in section 3.4 we wanted to correlate voxels with high ADC values with voxels with high ^{64}Cu -antibody uptake. Thus, a binning method that clustered high PET intensities above a threshold value into a subset of matrix bins that was used is suitable for this purpose. Further investigations are required to identify more generalized guidelines for choosing the optimal binning method for cooccurrence

matrix generation.

C.3 Conclusion

We explored the effects of PSF window and binning method on cooccurrence matrices generated between images with different spatial resolutions. The optimal PSF window is dependent on the spatial resolution of the imaging modality being considered. For PET-like images, we found the optimal PSF window to be approximately half the FWHM of the image. The choice of histogram bins can also affect cooccurrence matrix results. Cooccurrence matrices are being increasingly applied to PET and MRI images [297, 298, 299]. Further studies are needed to refine this method for the analysis of PET/MRI datasets.

Appendix D

Synchronous PET/MRI Software Code

D.1 MRI Code Implemented in Paravision Environment

D.1.1 PET_FLASH.ppg, a Modified Bruker FLASH Sequence to Include Syncing Modules

```

,*****
;
; Copyright (c) 2001 - 2003
; Bruker BioSpin MRI GmbH
; D-76275 Ettlingen, Germany
;
; All Rights Reserved
;
; PET_FLASH - a gradient echo imaging method
;
; Set for Synchronised PET/MR
;
,*****
;
; d0 - TR padding
; d1 - T1 padding

```

Modifications in italics.

```

; d2 - T2 padding
; d3 = PVM_RiseTime
; d4 = PVM_RampTime
; d8 = CONFIG_amplifier_enable
#include<Avance.incl>
#include <DBX.include>
preset off
define delay denab
define delay d4d10u
define delay d5d20u
define delay d0d40u
define delay d4d2
"denab = d3 - de + depa"
"d4d10u = d4 +10u"
"d5d20u = d5 +20u"
"d0d40u = d0 -40u"
"d4d2 = d4 + d2"
"l3 = l1 + ds"
#include <PrepModulesHead.mod>
#include <FlowSatinit.mod>
#include <MEDSPEC.include>
lgrad r2d<2d> = L[1]
zgrad r2d
lgrad r3d<3d> = L[2]
zgrad r3d
#include <PET_MR_SYNC_A.mod>
;MR sequence started and trigger sent to the PET system,
;we now initiate pre-pulse sequence setup
lo to decr times DS

```

```

lgrad slice = NSLICES
zslice
10u recph ph1
; By now, the PET module should be ready. We then start the MR sequence and
; tell the PET system to start acquisition simultaneously.
#include <PET_MR_SYNC_B.mod>
start, 10u
if(PVM_BIBloodOnOff)
{
#include <TriggerPerPhaseStep.mod>
}
#include <blblood.mod>
#include <TriggerPerPhaseStep.mod>
#include <SelSliceIr.mod>
#include <tagging.mod>
;-----start of the main loop-----
slice, 10u fq8b:f1
#include <TriggerPerSlice.mod>
;-----preparation modules-----
#include <FlowSat.mod>
subr SatSlices()
#include <MagTrans.mod>
#include <FatSup.mod>
d6 grad{(0)|(0)|(t9)}
;-----slice selection-----
d3 grad{(0)|(0)|(t0)} fq1:f1
d8 gatepulse 1
p0:sp0 ph0
d4d10u groff

```

```

if(PVM_ppgFlag1) ;long TE mode
{
;-----slice rephase-----
d10 grad{(0)|(0)|(t1)}
d4d2 groff
;-----read dephase + phase encoding-----
d11 grad{(t2)|r2d(t3)|r3d(t4)}
d4d10u groff
}
if(!PVM_ppgFlag1) ;short TE mode
{
;-----slice rephase, read dephase, phase encoding-----
d10 grad{(t2)|r2d(t3)|(t1)+r3d(t4)}
d4d2 groff
}
;-----frequency encoding-----
denab REC_ENABLE grad{(t5)|(0)|(0)}
ADC_INIT_B(NOPH, ph2) ;ph1 is used (see recph)
aqq ADC_START
;-----read spoiler + phase encoding-----
d11 grad{(t6)|r2d(t7)|r3d(t8)} ; 2nd and 3rd dims
d12 grad{(t6)| (0) | (0) }
d3 groff
d0 ADC_END
;-----slice and movie loop-----
#include <FlowSatinc.mod>
if(NI > 1)
{
2.5u islice

```

```

lo to slice times NI
}
d20
;-----averaging loop-----
if(NA > 1)
{
2.5u ipp1 ipp2
2.5u recph ph1
lo to start times NA
2.5u rpp1 rpp2
}
;-----2d loop-----
igrad r2d
lo to start times l3
"l3=l1"
;-----3d loop-----
igrad r3d
lo to start times l2
2.5u
lo to start times NAE
2.5u
#include <Evolution.mod>
2.5u
lo to start times NR
SETUP_GOTO(start)
exit
ph0 = 0
ph1 = 0 2 1 3
ph2 = 0 2 3 1

```

D.1.2 PET_MR_SYNC_A.mod

```

;*****
;
; Caltech/ UC Davis PET/MR
;
; (c) 2010
;
;
; PET_MR_SYNC_A.mod - PET/MR Synchronous start module
;
;
;*****
; Need to link to the methods
;Initialise
TTL4_HIGH
;
;Wait for the start signal from the PET program to begin
trignl4
TTL4_HIGH

```

D.1.3 PET_MR_SYNC_B.mod

```

;*****
;
; Caltech/ UC Davis PET/MR
;
; (c) 2010
;
;
; PET_MR_SYNC_B.mod - PET/MR Synchronous start module

```

```
;  
;  
;*****  
; Need to link to the methods  
; Now Other prep stuff done, we start the sequence  
TTL4_LOW  
trigne4  
TTL4_HIGH
```

Appendix E

MATLAB Implementation of an Unique Identifier for Multimodal Data Linkage

```

%% Make a Multimodal imaging header extension
% Define ecode = 30 Need to register with NIFTI
clear all
% Multimodal ID self first
ecodeA = 30;
% Modalities
%{
PET : standard positron emission tomography dataset
MRI : standard magnetic resonance imaging dataset
DCEMRI: dynamic contrast enhanced MRI dataset
DCEPET: dynamic contrast enhanced PET dataset
DWI :
CFM : Confocal microscopy
unique identifier is the same for all the datasets that belong together.
%}
uid = datestr(now, 30);
ext.section(1).ecode = ecodeA;
MODAL = unicode2native(fullfile('PET', 'MRI', uid)); % This would encode a PET image data
which has an associated standard MRI dataset linked to it.
ext.section(1).edata = MODAL;

```

```
verify_nii_ext(ext)
```

```
% To store this extension.
```

```
%nii.ext
```

Bibliography

- [1] Hanahan D, Weinberg RA. Hallmarks of cancer: the next generation. *Cell* 2011;144:646–674.
- [2] Hanahan D, Weinberg RA. The hallmarks of cancer. *Cell* 2000;100:57–70.
- [3] Allinen M, Beroukhi R, Cai L, et al. Molecular characterization of the tumor microenvironment in breast cancer. *Cancer Cell* 2004;6:17–32.
- [4] Cho RW, Clarke MF. Recent advances in cancer stem cells. *Curr Opin Genet Dev* 2008; 18:48–53.
- [5] Barkan D, Green JE, Chambers AF. Extracellular matrix: a gatekeeper in the transition from dormancy to metastatic growth. *Eur J Cancer* 2010;46:1181–1188.
- [6] Bergers G, Benjamin LE. Tumorigenesis and the angiogenic switch. *Nat Rev Cancer* 2003; 3:401–410.
- [7] Ruoslahti E, Bhatia SN, Sailor MJ. Targeting of drugs and nanoparticles to tumors. *J Cell Biol* 2010;188:759–768.
- [8] Society AC. *Cancer Facts & Figures 2012*, 2012.
- [9] Salaverria I, Siebert R. The gray zone between Burkitt's lymphoma and diffuse large B-cell lymphoma from a genetics perspective. *J Clin Oncol* 2011;29:1835–1843.
- [10] Freedman AS, Friedberg JW. Treatment of Burkitt leukemia/lymphoma in adults. In: *UpToDate*, Lister A, Park J, Connor RF, eds. Waltham, MA: UpToDate, 2012 .
- [11] Eisenhauer EA, Therasse P, Bogaerts J, et al. New response evaluation criteria in solid tumours: Revised RECIST guideline (version 1.1). *Eur J Cancer* 2009;45:228–247.

- [12] Weissleder R, Pittet MJ. Imaging in the era of molecular oncology. *Nature* 2008;452:580–589.
- [13] Ben-Haim S, Ell P. 18F-FDG PET and PET/CT in the Evaluation of Cancer Treatment Response. *J Nucl Med* 2009;50:88–99.
- [14] Cherry SR. Multimodality Imaging: Beyond PET/CT and SPECT/CT. *Semin Nucl Med* 2009;39:348–353.
- [15] Ramanujan S, Pluen A, McKee TD, Brown EB, Boucher Y, Jain RK. Diffusion and convection in collagen gels: implications for transport in the tumor interstitium. *Biophys J* 2002;83:1650–1660.
- [16] Thurber GM, Schmidt MM, Wittrup KD. Factors determining antibody distribution in tumors. *Trends Pharmacol Sci* 2008;29:57–61.
- [17] Schluep T, Hwang J, Cheng J, et al. Preclinical Efficacy of the Camptothecin-Polymer Conjugate IT-101 in Multiple Cancer Models. *Clin Cancer Res* 2006;12:1606–1614.
- [18] Chauhan VP, Lanning RM, Diop-Frimpong B, et al. Multiscale measurements distinguish cellular and interstitial hindrances to diffusion in vivo. *Biophys J* 2009;97:330–336.
- [19] Schluep T, Hwang J, Hildebrandt IJ, et al. Pharmacokinetics and tumor dynamics of the nanoparticle IT-101 from PET imaging and tumor histological measurements. *P Natl Acad Sci Usa* 2009;106:11394–11399.
- [20] Thurber GM, Weissleder R. Quantitating antibody uptake in vivo: conditional dependence on antigen expression levels. *Mol Imaging Biol* 2011;13:623–632.
- [21] Blanco E, Hsiao A, Mann AP, Landry MG, Meric-Bernstam F, Ferrari M. Nanomedicine in cancer therapy: innovative trends and prospects. *Cancer Sci* 2011;102:1247–1252.
- [22] Davis ME, Chen ZG, Shin DM. Nanoparticle therapeutics: an emerging treatment modality for cancer. *Nat Rev Drug Discov* 2008;7:771–782.
- [23] Davis ME. The first targeted delivery of siRNA in humans via a self-assembling, cyclodextrin polymer-based nanoparticle: from concept to clinic. *Mol Pharmaceut* 2009;6:659–668.

- [24] Davis ME. Design and development of IT-101, a cyclodextrin-containing polymer conjugate of camptothecin. *Adv Drug Deliv Rev* 2009;61:1189–1192.
- [25] Bianco A, Kostarelos K, Prato M. Applications of carbon nanotubes in drug delivery. *Curr Opin Chem Biol* 2005;9:674–679.
- [26] Hofheinz RD, Gnad-Vogt SU, Beyer U, Hochhaus A. Liposomal encapsulated anti-cancer drugs. *Anti-Cancer Drug* 2005;16:691–707.
- [27] Singh P, Destito G, Schneemann A, Manchester M. Canine parvovirus-like particles, a novel nanomaterial for tumor targeting. *J Nanobiotechnology* 2006;4:2.
- [28] Johnson EE, Lum HD, Rakhmilevich AL, et al. Intratumoral Immunocytokine Treatment Results in Enhanced Antitumor Effects. *J Immunother* 2006;29:635
10.1097/01.cji.0000211343.73588.59.
- [29] Johnson EE, Lum HD, Rakhmilevich AL, et al. Intratumoral immunocytokine treatment results in enhanced antitumor effects. *Cancer Immunol Immunother* 2008;57:1891–1902.
- [30] Schluep T, Cheng J, Khin K, Davis M. Pharmacokinetics and biodistribution of the camptothecin-polymer conjugate IT-101 in rats and tumor-bearing mice. *Cancer Chemoth Pharm* 2006;57:654–662.
- [31] Choi CH, Alabi CA, Webster P, Davis ME. Mechanism of active targeting in solid tumors with transferrin-containing gold nanoparticles. *P Natl Acad Sci Usa* 2010;107:1235–1240.
- [32] Leamon CP, Reddy JA. Folate-targeted chemotherapy. *Adv Drug Deliv Rev* 2004;56:1127–1141.
- [33] Reddy GR, Bhojani MS, McConville P, et al. Vascular Targeted Nanoparticles for Imaging and Treatment of Brain Tumors. *Clin Cancer Res* 2006;12:6677–6686.
- [34] Yatvin MB, Kreutz W, Horwitz BA, Shinitzky M. pH-sensitive liposomes: possible clinical implications. *Science* 1980;210:1253–1255.

- [35] Olson ES, Jiang T, Aguilera TA, et al. Activatable cell penetrating peptides linked to nanoparticles as dual probes for in vivo fluorescence and MR imaging of proteases. *P Natl Acad Sci Usa* 2010;.
- [36] Gottesman MM, Fojo T, Bates SE. Multidrug resistance in cancer: role of ATP-dependent transporters. *Nat Rev Cancer* 2002;2:48–58.
- [37] Wong JYC, Chu DZ, Williams LE, et al. A phase I trial of (90)Y-DOTA-anti-CEA chimeric T84.66 (cT84.66) radioimmunotherapy in patients with metastatic CEA-producing malignancies. *Cancer Biol Ther* 2006;21:88–100.
- [38] Jain RK, Stylianopoulos T. Delivering nanomedicine to solid tumors. *Nat Rev Clin Oncol* 2010;7:653–664.
- [39] Gordon AN, Fleagle JT, Guthrie D, Parkin DE, Gore ME, Lacave AJ. Recurrent epithelial ovarian carcinoma: a randomized phase III study of pegylated liposomal doxorubicin versus topotecan. *J Clin Oncol* 2001;19:3312–3322.
- [40] Hobbs SK, Monsky WL, Yuan F, et al. Regulation of transport pathways in tumor vessels: role of tumor type and microenvironment. *P Natl Acad Sci Usa* 1998;95:4607–4612.
- [41] Padera TP, Stoll BR, Tooredman JB, Capen D, di Tomaso E, Jain RK. Pathology: cancer cells compress intratumour vessels. *Nature* 2004;427:695.
- [42] Thorne RG, Lakkaraju A, Rodriguez-Boulan E, Nicholson C. In vivo diffusion of lactoferrin in brain extracellular space is regulated by interactions with heparan sulfate. *P Natl Acad Sci Usa* 2008;105:8416–8421.
- [43] Jain RK. Normalization of tumor vasculature: an emerging concept in antiangiogenic therapy. *Science* 2005;307:58–62.
- [44] Monsky WL, Fukumura D, Gohongi T, et al. Augmentation of transvascular transport of macromolecules and nanoparticles in tumors using vascular endothelial growth factor. *Cancer Res* 1999;59:4129–4135.

- [45] Tseng JC, Granot T, DiGiacomo V, Levin B, Meruelo D. Enhanced specific delivery and targeting of oncolytic Sindbis viral vectors by modulating vascular leakiness in tumor. *Cancer Gene Ther* 2010;17:244–255.
- [46] McKee TD, Grandi P, Mok W, et al. Degradation of fibrillar collagen in a human melanoma xenograft improves the efficacy of an oncolytic herpes simplex virus vector. *Cancer Res* 2006;66:2509–2513.
- [47] Jarver P, Mager I, Langel U. In vivo biodistribution and efficacy of peptide mediated delivery. *Trends Pharmacol Sci* 2010;31:528–535.
- [48] Sugahara KN, Teesalu T, Karmali PP, et al. Tissue-penetrating delivery of compounds and nanoparticles into tumors. *Cancer Cell* 2009;16:510–520.
- [49] Sugahara KN, Teesalu T, Karmali PP, et al. Coadministration of a tumor-penetrating peptide enhances the efficacy of cancer drugs. *Science* 2010;328:1031–1035.
- [50] Teesalu T, Sugahara KN, Kotamraju VR, Ruoslahti E. C-end rule peptides mediate neuropilin-1-dependent cell, vascular, and tissue penetration. *P Natl Acad Sci Usa* 2009;106:16157–16162.
- [51] Phelps ME. *PET : molecular imaging and its biological applications*. New York: Springer, 2004.
- [52] Cherry SR, Sorenson JA, Phelps ME. *Physics in nuclear medicine*. 3rd ed. Philadelphia, PA: Saunders, 2003.
- [53] Bading JR, Shields AF. Imaging of cell proliferation: status and prospects. *J Nucl Med* 2008;49:64S–80.
- [54] Buerkle A, Weber WA. Imaging of tumor glucose utilization with positron emission tomography. *Cancer Metast Rev* 2008;27:545–554.
- [55] Ashworth S, Rabiner EA, Gunn RN, et al. Evaluation of ¹¹C-GSK189254 as a novel radioligand for the H3 receptor in humans using PET. *J Nucl Med* 2010;51:1021–1029.

- [56] Otsuka T, Ito H, Halldin C, et al. Quantitative PET analysis of the dopamine D2 receptor agonist radioligand 11C-(R)-2-CH₃O-N-n-propylnorapomorphine in the human brain. *J Nucl Med* 2009;50:703–710.
- [57] Wu AM. Antibodies and antimatter: the resurgence of immuno-PET. *J Nucl Med* 2009; 50:2–5.
- [58] Ray P, Tsien R, Gambhir SS. Construction and validation of improved triple fusion reporter gene vectors for molecular imaging of living subjects. *Cancer Res* 2007;67:3085–3093.
- [59] Hoffend J, Mier W, Schuhmacher J, et al. Gallium-68-DOTA-albumin as a PET blood-pool marker: experimental evaluation in vivo. *Nucl Med Biol* 2005;32:287–292.
- [60] Qi J, Leahy RM. Resolution and noise properties of MAP reconstruction for fully 3-D PET. *IEEE T Med Imaging* 2000;19:493–506.
- [61] Qi J, Leahy RM, Cherry SR, Chatzioannou A, Farquhar TH. High-resolution 3D Bayesian image reconstruction using the microPET small-animal scanner. *Phys Med Biol* 1998; 43:1001–1013.
- [62] Al-Nahhas A, Win Z, Szyszko T, et al. Gallium-68 PET: a new frontier in receptor cancer imaging. *Anticancer Res* 2007;27:4087–4094.
- [63] Wadas TJ, Wong EH, Weisman GR, Anderson CJ. Coordinating radiometals of copper, gallium, indium, yttrium, and zirconium for PET and SPECT imaging of disease. *Chem Rev* 2010;110:2858–2902.
- [64] Haacke EM. *Magnetic resonance imaging : physical principles and sequence design*. New York: J. Wiley & Sons, 1999.
- [65] Deese AJ, Dratz EA, Hymel L, Fleischer S. Proton NMR T₁, T₂, and T₁ rho relaxation studies of native and reconstituted sarcoplasmic reticulum and phospholipid vesicles. *Biophys J* 1982;37:207–216.
- [66] Bernstein MA, King KF, Zhou ZJ. *Handbook of MRI pulse sequences*. Burlington, MA: Elsevier Academic Press, 2004.

- [67] Liang ZP, Lauterbur PC, IEEE Engineering in Medicine and Biology Society. Principles of magnetic resonance imaging a signal processing perspective. Bellingham, Wash. New York: SPIE Optical Engineering Press ; IEEE Press,, 2000.
- [68] Stejskal EO, Tanner JE. Spin diffusion measurements: spin echoes in the presence of a time-dependent field gradient. *J Chem Phys* 1965;42:288–292.
- [69] Le Bihan D, Breton E. {Imagerie de diffusion in vivo par Résonance Magnétique Nucléaire.}. XXX CR Académie des Sciences de Paris 1985;301:1109–1112.
- [70] Colvin DC, Loveless ME, Does MD, Yue Z, Yankeelov TE, Gore JC. Earlier detection of tumor treatment response using magnetic resonance diffusion imaging with oscillating gradients. *Magn Reson Imaging* 2010;.
- [71] Colvin DC, Yankeelov TE, Does MD, Yue Z, Quarles C, Gore JC. New insights into tumor microstructure using temporal diffusion spectroscopy. *Cancer Res* 2008;68:5941–5947.
- [72] Gore JC, Yankeelov TE, Peterson TE, Avison MJ. Molecular imaging without radiopharmaceuticals? *J Nucl Med* 2009;50:999–1007.
- [73] Hagmann P, Jonasson L, Maeder P, Thiran JP, Wedeen VJ, Meuli R. Understanding diffusion MR imaging techniques: from scalar diffusion-weighted imaging to diffusion tensor imaging and beyond. *Radiographics* 2006;26:S205–S223.
- [74] Hoff BA, Chenevert TL, Bhojani MS, et al. Assessment of multiexponential diffusion features as MRI cancer therapy response metrics. *Magnet Reson Med* 2010;64:1499–1509.
- [75] Hara N, Okuizumi M, Koike H, Kawaguchi M, Bilim V. Dynamic contrast-enhanced magnetic resonance imaging (DCE-MRI) is a useful modality for the precise detection and staging of early prostate cancer. *The Prostate* 2005;62:140–147.
- [76] Padhani AR. Dynamic contrast-enhanced MRI in clinical oncology: Current status and future directions. *J Magn Reson Imaging* 2002;16:407–422.
- [77] Yankeelov TE, Avison MJ, Damon BM, Manning HC, Peterson TE, Gore JC. Frontiers of

- biomedical imaging science 2009: workshop report and research opportunities. *Cancer Res* 2009;69:7902–7904.
- [78] Daldrup-Link HE, Golovko D, Ruffell B, et al. MRI of tumor-associated macrophages with clinically applicable iron oxide nanoparticles. *Clin Cancer Res* 2011;17:5695–5704.
- [79] Perles-Barbacaru TA, Procissi D, Demyanenko AV, Hall FS, Uhl GR, Jacobs RE. Quantitative pharmacologic MRI: mapping the cerebral blood volume response to cocaine in dopamine transporter knockout mice. *Neuroimage* 2011;55:622–628.
- [80] Tofts PS. Modeling tracer kinetics in dynamic Gd-DTPA MR imaging. *J Magn Reson Imaging* 1997;7:91–101.
- [81] Tofts PS, Kermode AG. Measurement of the blood-brain barrier permeability and leakage space using dynamic MR imaging. 1. Fundamental concepts. *Magnet Reson Med* 1991; 17:357–367.
- [82] Yankeelov TE, Gore JC. Dynamic contrast enhanced magnetic resonance imaging in oncology: theory, data acquisition, analysis, and examples. *Curr Med Imaging Rev* 2009; 3:91–107.
- [83] Li X, Huang W, Yankeelov TE, Tudorica A, Rooney WD, Springer Jr CS. Shutter-speed analysis of contrast reagent bolus-tracking data: Preliminary observations in benign and malignant breast disease. *Magnet Reson Med* 2005;53:724–729.
- [84] Yankeelov TE, Cron GO, Addison CL, et al. Comparison of a reference region model with direct measurement of an AIF in the analysis of DCE-MRI data. *Magnet Reson Med* 2007; 57:353–361.
- [85] Yankeelov TE, Luci JJ, DeBusk LM, Lin PC, Gore JC. Incorporating the effects of transcytolemmal water exchange in a reference region model for DCE-MRI analysis: theory, simulations, and experimental results. *Magnet Reson Med* 2008;59:326–335.
- [86] Yankeelov TE, Rooney WD, Huang W, et al. Evidence for shutter-speed variation in CR bolus-tracking studies of human pathology. *NMR Biomed* 2005;18:173–185.

- [87] Catana C, van der Kouwe A, Benner T, et al. Toward implementing an MRI-based PET attenuation-correction method for neurologic studies on the MR-PET brain prototype. *J Nucl Med* 2010;51:1431–1438.
- [88] Hofmann M, Pichler B, Schölkopf B, Beyer T. Towards quantitative PET/MRI: a review of MR-based attenuation correction techniques. *Eur J Nucl Med Mol I* 2009;36:93–104.
- [89] Catana C, van der Kouwe A, Benner T, et al. Rigid-body MR-assisted PET motion correction. *J Nucl Med* 2009;50:592.
- [90] Frullano L, Catana C, Benner T, Sherry AD, Caravan P. Bimodal MR-PET agent for quantitative pH imaging. *Angew Chem Int Ed Engl* 2010;49:2382–2384.
- [91] Cho ZH, Son YD, Kim HK, et al. A hybrid PET-MRI: An integrated molecular-genetic imaging system with HRRT-PET and 7.0-T MRI. *Int J Imag Syst Tech* 2007;17:252–265.
- [92] Zaidi H, Ojha N, Morich M, et al. Design and performance evaluation of a whole-body Ingenuity TF PET/MRI system. *Phys Med Biol* 2011;56:3091.
- [93] Bindseil GA, Gilbert KM, Scholl TJ, Handler WB, Chronik BA. First image from a combined positron emission tomography and field-cycled MRI system. *Magnet Reson Med* 2011; 66:301–305.
- [94] Lucas AJ, Hawkes RC, Ansorge RE, et al. Development of a combined microPET-MR system. *Technol Cancer Res Treat* 2006;5:337–341.
- [95] Delso G, Fürst S, Jakoby B, et al. Performance measurements of the Siemens mMR integrated whole-body PET/MR scanner. *J Nucl Med* 2011;.
- [96] Mackewn JE, Halsted P, Charles-Edwards G, et al. Performance evaluation of an MRI-compatible pre-clinical PET system using long optical fibers. *IEEE T Nucl Sci* 2010; 57:1052–1062.
- [97] Raylman RR, Majewski S, Velan SS, et al. Simultaneous acquisition of magnetic resonance spectroscopy (MRS) data and positron emission tomography (PET) images with a prototype MR-compatible, small animal PET imager. *J Magn Reson* 2007;186:305–310.

- [98] Tatsumi M, Yamamoto S, Imaizumi M, et al. Simultaneous PET/MR body imaging in rats: initial experiences with an integrated PET/MRI scanner. *Ann Nucl Med* 2012;.
- [99] Yiping S, Simon RC, Keyvan F, et al. Simultaneous PET and MR imaging. *Phys Med Biol* 1997;42:1965.
- [100] Catana C, Benner T, van der Kouwe A, et al. MRI-assisted PET motion correction for neurologic studies in an integrated MR-PET scanner. *J Nucl Med* 2011;52:154–161.
- [101] Maramraju SH, al E, Smith SD, et al. Small animal simultaneous PET/MRI: initial experiences in a 9.4 T microMRI. *Phys Med Biol* 2011;56:2459–2480.
- [102] Judenhofer MS, Wehrl HF, Newport DF, et al. Simultaneous PET-MRI: a new approach for functional and morphological imaging. *Nat Med* 2008;14:459–465.
- [103] Seiichi Y, Tadashi W, Hiroshi W, et al. Simultaneous imaging using Si-PM-based PET and MRI for development of an integrated PET/MRI system. *Phys Med Biol* 2012;57:N1.
- [104] Yoon HS, Ko GB, Kwon SI, et al. Initial results of simultaneous PET/MRI experiments with an MRI-compatible silicon photomultiplier PET scanner. *J Nucl Med* 2012;53:608–614.
- [105] Catana C, Procissi D, Wu Y, et al. Simultaneous in vivo positron emission tomography and magnetic resonance imaging. *P Natl Acad Sci Usa* 2008;105:3705–3710.
- [106] Catana C. Development of an integrated multi-slice PET-MRI scanner using fiber optically coupled LSO/PSAPD detectors. Ph.D. thesis, University of California, Davis, 2007.
- [107] Herrmann K, Wieder HA, Buck AK, et al. Early response assessment using 3'-deoxy-3'-[18F]fluorothymidine-positron emission tomography in high-grade non-Hodgkin's lymphoma. *Clin Cancer Res* 2007;13:3552–3558.
- [108] Humm JL, Ballon D, Hu YC, et al. A stereotactic method for the three-dimensional registration of multi-modality biologic images in animals: NMR, PET, histology, and autoradiography. *Med Phys* 2003;30:2303–2314.

- [109] Zhao S, Kuge Y, Mochizuki T, et al. Biologic correlates of intratumoral heterogeneity in 18F-FDG distribution with regional expression of glucose transporters and hexokinase-II in experimental tumor. *J Nucl Med* 2005;46:675–682.
- [110] Johnston RF, Pickett SC, Barker DL. Autoradiography using storage phosphor technology. *Electrophoresis* 1990;11:355–360.
- [111] Yaghoubi SS, Berger F, Gambhir SS. Studying the biodistribution of positron emission tomography reporter probes in mice. *Nat Protocols* 2007;2:1752–1755.
- [112] Christian N, Lee JA, Bol A, De Bast M, Gallez B, Gregoire V. Immobilization device for in vivo and in vitro multimodality image registration of rodent tumors. *Radiother Oncol* 2008;87:147–151.
- [113] Baker JH, Lindquist KE, Huxham LA, Kyle AH, Sy JT, Minchinton AI. Direct visualization of heterogeneous extravascular distribution of trastuzumab in human epidermal growth factor receptor type 2 overexpressing xenografts. *Clin Cancer Res* 2008;14:2171–2179.
- [114] Loomis K, McNeeley K, Bellamkonda RV. Nanoparticles with targeting, triggered release, and imaging functionality for cancer applications. *Soft Matter* 2011;7:839–856.
- [115] Bading J, Ng T, Jacobs R, Raubitschek A, Colcher D. [Cu-64]-DOTA-Herceptin: radiosynthesis and initial evaluation in vivo. *J Nucl Med* 2009;50:1912–.
- [116] Li L, Bading J, Yazaki PJ, et al. A versatile bifunctional chelate for radiolabeling humanized anti-CEA antibody with In-111 and Cu-64 at either thiol or amino groups: PET imaging of CEA-positive tumors with whole antibodies. *Bioconjugate Chem* 2008;19:89–96.
- [117] Wong JYC, Raubitschek A, Yamauchi D, et al. A pretherapy biodistribution and dosimetry study of indium-111-radiolabeled trastuzumab in patients with human epidermal growth factor receptor 2-overexpressing breast cancer. *Cancer Biol Ther* 2010;25:387–394.
- [118] Wu Y, Ng TSC, Yang Y, Shah K, Farrell R, Cherry SR. A study of the timing properties of position-sensitive avalanche photodiodes. *Phys Med Biol* 2009;54:5155.

- [119] Sun C, Lee JS, Zhang M. Magnetic nanoparticles in MR imaging and drug delivery. *Adv Drug Deliv Rev* 2008;60:1252–1265.
- [120] Artemov D, Mori N, Ravi R, Bhujwala ZM. Magnetic resonance molecular imaging of the HER-2/neu receptor. *Cancer Res* 2003;63:2723–2727.
- [121] Rapoport N, Nam KH, Gupta R, et al. Ultrasound-mediated tumor imaging and nanotherapy using drug loaded, block copolymer stabilized perfluorocarbon nanoemulsions. *J Control Release* 2011;153:4–15.
- [122] Fidarova EF, El-Emir E, Boxer GM, et al. Microdistribution of targeted, fluorescently labeled anti-Carcinoembryonic antigen antibody in metastatic colorectal cancer: implications for radioimmunotherapy. *Clin Cancer Res* 2008;14:2639–2646.
- [123] Kobayashi H, Shirakawa K, Kawamoto S, et al. Rapid accumulation and internalization of radiolabeled herceptin in an inflammatory breast cancer xenograft with vasculogenic mimicry predicted by the contrast-enhanced dynamic MRI with the macromolecular contrast agent G6-(1B4M-Gd)₂₅₆. *Cancer Res* 2002;62:860–866.
- [124] Thurber GM, Weissleder R. A systems approach for tumor pharmacokinetics. *PLoS ONE* 2011;6:e24696.
- [125] Lippens RJ. Liposomal daunorubicin (daunoxome) in children with recurrent or progressive brain tumors. *Pediatr Hemat Oncol* 1999;16:131–139.
- [126] Valle JW, Armstrong A, Newman C, et al. A phase 2 study of sp1049c, doxorubicin in p-glycoprotein-targeting pluronics, in patients with advanced adenocarcinoma of the esophagus and gastroesophageal junction. *Invest New Drug* 2011;29:1029–1037.
- [127] Amadori D, Milandri C, Comella G, et al. A phase I/II trial of non-pegylated liposomal doxorubicin, docetaxel and trastuzumab as first-line treatment in HER-2-positive locally advanced or metastatic breast cancer. *European journal of cancer (Oxford, England : 1990)* 2011;47:2091–2098.

- [128] Kobrinsky B, Andreopoulou E, Mourtzikos K, Muggia F. Documentation of complete response in metastatic breast cancer to liver and bone achieved with trastuzumab and pegylated liposomal Doxorubicin. *Clin Med Oncol* 2008;2:469–470.
- [129] Link J, Waisman J, Nguyen B, Jacobs C. Bevacizumab and Albumin-Bound Paclitaxel Treatment in Metastatic Breast Cancer. *Clin Breast Cancer* 2007;7:779–783.
- [130] Hamstra DA, Galbán CJ, Meyer CR, et al. Functional diffusion map as an early imaging biomarker for high-grade glioma: correlation with conventional radiologic response and overall survival. *J Clin Oncol* 2008;26:3387–3394.
- [131] Padhani AR. Dynamic contrast-enhanced MRI in clinical oncology: Current status and future directions. *J Magn Reson Imaging* 2002;16:407–422.
- [132] Ellingson BM, LaViolette PS, Rand SD, et al. Spatially quantifying microscopic tumor invasion and proliferation using a voxel-wise solution to a glioma growth model and serial diffusion MRI. *Magnet Reson Med* 2011;65:1131–1143.
- [133] Yankeelov TE, Atuegwu NC, Deane NG, Gore JC. Modeling tumor growth and treatment response based on quantitative imaging data. *Integr Biol (Camb)* 2010;2:338–345.
- [134] Jubb AM, Harris AL. Biomarkers to predict the clinical efficacy of bevacizumab in cancer. *Lancet Oncol* 2010;11:1172–1183.
- [135] Zhang F, Zhu L, Liu G, et al. Multimodality imaging of tumor response to doxil. *Theranostics* 2011;1:302–309.
- [136] Sun X, Yan Y, Liu S, et al. ¹⁸F-FPPRGD2 and ¹⁸F-FDG PET of response to abraxane therapy. *J Nucl Med* 2011;52:140–146.
- [137] Weber H, Paul D, Elverfeldt DV, Hennig J, Zaitsev M. Extended multi-flip-angle B1 mapping: A 3D mapping method for inhomogeneous B1 fields. *Concept Magn Reson B* 2010;37B:203–214.
- [138] Wehrl HF, Judenhofer MS, Thielscher A, Martirosian P, Schick F, Pichler BJ. Assessment

of MR compatibility of a PET insert developed for simultaneous multiparametric PET/MR imaging on an animal system operating at 7 T. *Magnet Reson Med* 2011;65:269–279.

- [139] Cheng HLM, Wright GA. Rapid high-resolution T1 mapping by variable flip angles: accurate and precise measurements in the presence of radiofrequency field inhomogeneity. *Magnet Reson Med* 2006;55:566–574.
- [140] Metzger GJ, Snyder C, Akgun C, Vaughan T, Ugurbil K, Van de Moortele PF. Local B1+ shimming for prostate imaging with transceiver arrays at 7T based on subject-dependent transmit phase measurements. *Magnet Reson Med* 2008;59:396–409.
- [141] Vaughan JT, Garwood M, Collins CM, et al. 7T vs. 4T: RF power, homogeneity, and signal-to-noise comparison in head images. *Magnet Reson Med* 2001;46:24–30.
- [142] Peng B. Studies of the Interactions of the MRI System with the PET insert in the Bore of a 7T Magnet and its Applications. Ph.D. thesis, University of California, Davis, 2010.
- [143] Doubrovina M, Serganova I, Mayer-Kuckuk P, Ponomarev V, Blasberg RG. Multimodality in vivo molecular-genetic imaging. *Bioconjugate Chem* 2004;15:1376–1388.
- [144] Ottobriani L, Ciana P, Biserni A, Lucignani G, Maggi A. Molecular imaging: a new way to study molecular processes in vivo. *Mol Cell Endocrinol* 2006;246:69–75.
- [145] Rehemtulla A, Hall DE, Stegman LD, et al. Molecular imaging of gene expression and efficacy following adenoviral-mediated brain tumor gene therapy. *P Soc Photo-Opt Ins* 2002; 1:43–55.
- [146] Stell A, Belcredito S, Ramachandran B, et al. Multimodality imaging: novel pharmacological applications of reporter systems. *Q J Nucl Med Mol Im* 2007;51:127–138.
- [147] Deroose CM, De A, Loening AM, et al. Multimodality imaging of tumor xenografts and metastases in mice with combined small-animal PET, small-animal CT, and bioluminescence imaging. *J Nucl Med* 2007;48:295–303.
- [148] la Fougere C, Hundt W, Brockel N, et al. Value of PET/CT versus PET and CT performed

as separate investigations in patients with Hodgkin's disease and non-Hodgkin's lymphoma. *Eur J Nucl Med Mol I* 2006;33:1417–1425.

- [149] Pichler BJ, Judenhofer MS, Pfannenber C. Multimodal imaging approaches: PET/CT and PET/MRI. *Handb Exp Pharmacol* 2008;109–132.
- [150] Roldan-Valadez E, Ortega-Lopez N, Cervera-Ceballos E, Valdivieso-Cardenas G, Vega-Gonzalez I, Granados-Garcia M. Whole-body (18)F-FDG PET/CT in primary non-Hodgkin's lymphoma of the thyroid associated with Hashimoto's thyroiditis and bilateral kidney infiltration. *Rev Esp Med Nucl* 2008;27:34–39.
- [151] Jan ML, Ni YC, Chen KW, Liang HC, Chuang KS, Fu YK. A combined micro-PET/CT scanner for small animal imaging. *Nucl Instrum Meth A* 2006;569:314–318.
- [152] Slomka PJ, Baum RP. Multimodality image registration with software: state-of-the-art. *Eur J Nucl Med Mol I* 2008;.
- [153] Chow PL, Stout DB, Komisopoulou E, Chatziioannou AF. A method of image registration for small animal, multi-modality imaging. *Phys Med Biol* 2006;379.
- [154] Rodriguez-Ruano A, Pascau J, Chamorro J, et al. PET/CT alignment for small animal scanners based on capillary detection. In: *Nuclear Science Symposium Conference Record, 2008. NSS '08. IEEE*. 2008 3832–3835.
- [155] Ogawa S, Lee TM, Kay AR, Tank DW. Brain magnetic resonance imaging with contrast dependent on blood oxygenation. *P Natl Acad Sci Usa* 1990;87:9868–9872.
- [156] Hamstra DA, Rehemtulla A, Ross BD. Diffusion magnetic resonance imaging: A biomarker for treatment response in oncology. *J Clin Oncol* 2007;25:4104–4109.
- [157] Gillies RJ, Morse DL. In vivo magnetic resonance spectroscopy in cancer. *Annu Rev Biomed Eng* 2005;7:287–326.
- [158] Jacobs RE, Cherry SR. Complementary emerging techniques: high-resolution PET and MRI. *Curr Opin Neurobiol* 2001;11:621–629.

- [159] Bindseil G, Handler W, Scholl T, Gilbert K, Peng H, Chronik B. Design of a combined PET and field-cycled MRI system for small animal imaging. In: Proceedings 16th Scientific Meeting, International Society for Magnetic Resonance in Medicine. Toronto, 2008 351.
- [160] Catana C, Wu Y, Judenhofer MS, Qi J, Pichler BJ, Cherry SR. Simultaneous acquisition of multislice PET and MR images: initial results with a MR-compatible PET scanner. *J Nucl Med* 2006;47:1968–1976.
- [161] Zhang Z, Ramirez NE, Yankeelov TE, et al. $\alpha_2\beta_1$ integrin expression in the tumor microenvironment enhances tumor angiogenesis in a tumor cell-specific manner. *Blood* 2008; 111:1980–1988.
- [162] Judenhofer MS, Pichler BJ, Cherry SR. Evaluation of high performance data acquisition boards for simultaneous sampling of fast signals from PET detectors. *Phys Med Biol* 2005; 50:29–44.
- [163] Goshtasby A. Image registration by local approximation methods. *Image Vision Comput* 1988;6:255–261.
- [164] Witz IP, Levy-Nissenbaum O. The tumor microenvironment in the post-PAGET era. *Cancer Lett* 2006;242:1–10.
- [165] Zhang M, Huang M, Le C, et al. Accuracy and reproducibility of tumor positioning during prolonged and multi-modality animal imaging studies. *Phys Med Biol* 2008;53:5867–5882.
- [166] Pfluger T, Vollmar C, Wismuller A, et al. Quantitative comparison of automatic and interactive methods for MRI-SPECT image registration of the brain based on 3-dimensional calculation of error. *J Nucl Med* 2000;41:1823–1829.
- [167] Jupp B, O'Brien TJ. Application of coregistration for imaging of animal models of epilepsy. *Epilepsia* 2007;48 Suppl 4:82–89.
- [168] Rowland DJ, Garbow JR, Laforest R, Snyder AZ. Registration of [18F]FDG microPET and small-animal MRI. *Nucl Med Biol* 2005;32:567–572.

- [169] Slomka PJ. Software approach to merging molecular with anatomic information. *J Nucl Med* 2004;45 Suppl 1:36S–45S.
- [170] Twieg DB. The k-trajectory formulation of the NMR imaging process with applications in analysis and synthesis of imaging methods. *Med Phys* 1983;10:610–621.
- [171] Bowtell R, Mansfield P. Gradient coil design using active magnetic screening. *Magnet Reson Med* 1991;17:15–21.
- [172] Barmet C, De Zanche N, Wilm BJ, Pruessmann KP. A transmit/receive system for magnetic field monitoring of in vivo MRI. *Magnet Reson Med* 2009;62:269–276.
- [173] Barmet C, Zanche ND, Pruessmann KP. Spatiotemporal magnetic field monitoring for MR. *Magnet Reson Med* 2008;60:187–197.
- [174] Papadakis NG, Smponias T, Berwick J, Mayhew JEW. k-space correction of eddy-current-induced distortions in diffusion-weighted echo-planar imaging. *Magnet Reson Med* 2005; 53:1103–1111.
- [175] Blümer P. Spatially resolved magnetic resonance : methods, materials, medicine, biology, rheology, geology, ecology, hardware. Weinheim ; New York: Wiley-VCH, 1998.
- [176] Montagner J, Barra V, Boire JY. A geometrical approach to multiresolution management in the fusion of digital images. In: *Pixelization Paradigm*. 2008 121–136.
- [177] Reveillès JP. The geometry of the intersection of voxel spaces. *Electron Notes Theor Comput Sci* 2001;46:285–308.
- [178] Agrawal G, Chen JH, Baek HM, et al. MRI features of breast cancer: a correlation study with HER-2 receptor. *Ann Oncol* 2007;18:1903–1904.
- [179] Brindle K. New approaches for imaging tumour responses to treatment. *Nat Rev Cancer* 2008;8:94–107.
- [180] Gatenby RA, Gillies RJ. Why do cancers have high aerobic glycolysis? *Nat Rev Cancer* 2004;4:891–899.

- [181] Guo J, Higashi K, Yokota H, et al. In vitro proton magnetic resonance spectroscopic lactate and choline measurements, 18F-FDG uptake, and prognosis in patients with lung adenocarcinoma. *J Nucl Med* 2004;45:1334–1339.
- [182] Zhou R, Pickup S, Yankeelov TE, Springer Jr CS, Glickson JD. Simultaneous measurement of arterial input function and tumor pharmacokinetics in mice by dynamic contrast enhanced imaging: effects of transcytolemmal water exchange. *Magnet Reson Med* 2004;52:248–257.
- [183] Cho H, Ackerstaff E, Carlin S, et al. Noninvasive multimodality imaging of the tumor microenvironment: registered dynamic magnetic resonance imaging and positron emission tomography studies of a preclinical tumor model of tumor hypoxia. *Neoplasia* 2009;11:247–259.
- [184] Gee MS, Upadhyay R, Bergquist H, et al. Human breast cancer tumor models: molecular imaging of drug susceptibility and dosing during HER2/neu-targeted therapy. *Radiology* 2008;248:925–935.
- [185] Serganova I, Blasberg R. Reporter gene imaging: potential impact on therapy. *Nucl Med Biol* 2005;32:763–780.
- [186] Jarrett BR, Gustafsson B, Kukis DL, Louie AY. Synthesis of ⁶⁴Cu-labeled magnetic nanoparticles for multimodal imaging. *Bioconjugate Chem* 2008;19:1496–1504.
- [187] Thayer D, Unlu MB, Lin Y, Yan K, Nalcioglu O, Gulsen G. Dual-contrast dynamic MRI-DOT for small animal imaging. *Technol Cancer Res Treat* 2010;9:61–70.
- [188] Horn BKP. Closed-form solution of absolute orientation using unit quaternions. *J Opt Soc Am A* 1987;4:629–642.
- [189] Bebis G, Boyle R, Koracin D, et al. *Advances in Visual Computing* (vol. # 4292) Second International Symposium, ISVC 2006, Lake Tahoe, NV, USA, November 6-8, 2006, Proceedings, Part II, 2006.
- [190] Sauter AW, Wehrl HF, Kolb A, Judenhofer MS, Pichler BJ. Combined PET/MRI: one step further in multimodality imaging. *Trends Mol Med* 2010;16:508–515.

- [191] Choyke PL, Dwyer AJ, Knopp MV. Functional tumor imaging with dynamic contrast-enhanced magnetic resonance imaging. *J Magn Reson Imaging* 2003;17:509–520.
- [192] Galbán CJ, Bhojani MS, Lee KC, et al. Evaluation of treatment-associated inflammatory response on diffusion-weighted magnetic resonance imaging and 2-[18F]-fluoro-2-deoxy-D-glucose-positron emission tomography imaging biomarkers. *Clin Cancer Res* 2010;16:1542–1552.
- [193] Li X, Yankeelov TE, Peterson TE, Gore JC, Dawant BM. Automatic nonrigid registration of whole body CT mice images. *Med Phys* 2008;35:1507–1520.
- [194] Yang Y, Tai YC, Siegel S, et al. Optimization and performance evaluation of the microPET II scanner for in vivo small-animal imaging. *Phys Med Biol* 2004;49:2527–2545.
- [195] Metz S, Ganter C, Lorenzen S, et al. Phenotyping of tumor biology in patients by multimodality multiparametric imaging: relationship of microcirculation, alpha-v-beta3 expression, and glucose metabolism. *J Nucl Med* 2010;51:1691–1698.
- [196] NEMA. Performance measurements of small-animal positron emission tomographs. Tech. rep., National Electrical Manufacturers Association., Rosslyn, VA, 2008.
- [197] Coe RA. Quantitative whole-body autoradiography. *Regul Toxicol Pharm* 2000;31:S1–3.
- [198] Wu Y, Catana C, Farrell R, et al. PET performance evaluation of an MR-Compatible PET insert. *IEEE T Nucl Sci* 2009;56:574–580.
- [199] Clarke P, Mann J, Simpson JF, Rickard-Dickson K, Primus FJ. Mice transgenic for human Carcinoembryonic antigen as a model for immunotherapy. *Cancer Res* 1998;58:1469–1477.
- [200] Knoess C, al E, Siegel S, et al. Performance evaluation of the microPET R4 PET scanner for rodents. *Eur J Nucl Med Mol I* 2003;30:737.
- [201] Ng TSC, Procissi D, Wu Y, Jacobs RE. A robust coregistration method for in vivo studies using a first generation simultaneous PET/MR scanner. *Med Phys* 2010;37:1995–2003.
- [202] Zhou W, Bovik AC, Sheikh HR, Simoncelli EP. Image quality assessment: from error visibility to structural similarity. *IEEE T Med Imaging* 2004;13:600–612.

- [203] Sampat MP, Zhou W, Gupta S, Bovik AC, Markey MK. Complex Wavelet Structural Similarity: A New Image Similarity Index. *IEEE T Image Process* 2009;18:2385–2401.
- [204] Disselhorst JA, Brom M, Laverman P, et al. Image-Quality Assessment for Several Positron Emitters Using the NEMA NU 4-2008 Standards in the Siemens Inveon Small-Animal PET Scanner. *J Nucl Med* 2010;51:610–617.
- [205] Laforest R, Longford D, Siegel S, Newport DF, Yap J. Performance Evaluation of the microPET-FOCUS-F120. *Nuclear Science, IEEE Transactions on* 2007;54:42–49.
- [206] Christian N, Lee JA, Bol A, De Bast M, Jordan B, Grégoire V. The limitation of PET imaging for biological adaptive-IMRT assessed in animal models. *Radiother Oncol* 2009;91:101–106.
- [207] Chow PL, Rannou FR, Chatziioannou AF. Attenuation correction for small animal PET tomographs. *Phys Med Biol* 2005;50:1837–1850.
- [208] Atuegwu NC, Gore JC, Yankeelov TE. The integration of quantitative multi-modality imaging data into mathematical models of tumors. *Phys Med Biol* 2010;55:2429–2449.
- [209] York D, Evensen NM, Martinez ML, Delgado JD. Unified equations for the slope, intercept, and standard errors of the best straight line. *Am J Phys* 2004;72:367–375.
- [210] Christian N, Lee JA, Bol A, De Bast M, Gallez B, Grégoire V. Immobilization device for in vivo and in vitro multimodality image registration of rodent tumors. *Radiother Oncol* 2008; 87:147–151.
- [211] Weirich C, Brenner D, Tellmann L, Herzog H, Shah N. Systematic investigation and correction of MR influences on simultaneous PET measurements. In: *Proceedings 19th Scientific Meeting, International Society for Magnetic Resonance in Medicine*. 2011 3796.
- [212] Vandembroucke A, Lee J, Spanoudaki V, Lau F, Reynolds PD, Levin CS. Temperature and bias voltage studies of a large area position sensitive Avalanche Photodiode. In: *Nuclear Science Symposium Conference Record (NSS/MIC), 2009 IEEE*. 2009 3664–3669.
- [213] Wu Y, Yang Y, Bec J, Cherry SR. A DOI-capable MR-compatible PET insert for simultaneous PET/MRI imaging. *Mol Imaging Biol* 2010;12:S603.

- [214] Cho K, Wang X, Nie S, Chen Z, Shin DM. Therapeutic nanoparticles for drug delivery in cancer. *Clin Cancer Res* 2008;14:1310–1316.
- [215] Gribben JG. How I treat indolent lymphoma. *Blood* 2007;109:4617–4626.
- [216] Kuruvilla J. Standard therapy of advanced Hodgkin lymphoma. *Hematology* 2009;2009:497–506.
- [217] Numbenjapon T, Wang J, Colcher D, et al. Preclinical results of Camptothecin-polymer conjugate (IT-101) in multiple human Lymphoma xenograft models. *Clin Cancer Res* 2009;15:4365–4373.
- [218] Armitage JO. Early-stage Hodgkin's Lymphoma. *New Engl J Med* 2010;363:653–662.
- [219] Yen Y, Coerver LA, Garmey EG, et al. Final phase 1/2a results evaluating the cyclodextrin-containing nanoparticle CRLX101 in patients with advanced solid tumor malignancies. *Mol Cancer Ther* 2011;10:Supplement 1.
- [220] Zhao B, Schwartz LH, Larson SM. Imaging surrogates of tumor response to therapy: anatomic and functional biomarkers. *J Nucl Med* 2009;50:239–249.
- [221] Marcus CD, Ladam-Marcus V, Cucu C, Bouché O, Lucas L, Hoeffel C. Imaging techniques to evaluate the response to treatment in oncology: current standards and perspectives. *Crit Rev Oncol Hemat* 2009;72:217–238.
- [222] Patterson DM, Padhani AR, Collins DJ. Technology insight: water diffusion MRI—a potential new biomarker of response to cancer therapy. *Nat Clin Pract Oncol* 2008;5:220–233.
- [223] Huang MQ, Pickup S, Nelson DS, et al. Monitoring response to chemotherapy of non-Hodgkin's lymphoma xenografts by T2-weighted and diffusion-weighted MRI. *NMR Biomed* 2008;21:1021–1029.
- [224] Lee KC, Moffat BA, Schott AF, et al. Prospective early response imaging biomarker for neoadjuvant breast cancer chemotherapy. *Clin Cancer Res* 2007;13:443–450.

- [225] Kim S, Loevner L, Quon H, et al. Diffusion-weighted magnetic resonance imaging for predicting and detecting early response to chemoradiation therapy of squamous cell carcinomas of the head and neck. *Clin Cancer Res* 2009;15:986–994.
- [226] Hamstra DA, Chenevert TL, Moffat BA, et al. Evaluation of the functional diffusion map as an early biomarker of time-to-progression and overall survival in high-grade glioma. *P Natl Acad Sci Usa* 2005;102:16759–16764.
- [227] Lazovic J, Jensen MC, Ferkassian E, Aguilar B, Raubitschek A, Jacobs RE. Imaging immune response in vivo: cytolytic action of genetically altered T cells directed to glioblastoma multiforme. *Clin Cancer Res* 2008;14:3832–3839.
- [228] Deisboeck TS, Wang Z, Macklin P, Cristini V. Multiscale cancer modeling. *Annu Rev Biomed Eng* 2011;13:127–155.
- [229] Yankeelov TE, Atuegwu NC, Deane NG, Gore JC. Modeling tumor growth and treatment response based on quantitative imaging data. *Integr Biol (Camb)* 2010;2:338–345.
- [230] Atuegwu NC, Colvin DC, Loveless ME, Xu L, Gore JC, Yankeelov TE. Incorporation of diffusion-weighted magnetic resonance imaging data into a simple mathematical model of tumor growth. *Phys Med Biol* 2012;57:225.
- [231] Rockne R, Rockhill JK, Mrugala M, et al. Predicting the efficacy of radiotherapy in individual glioblastoma patients in vivo: a mathematical modeling approach. *Phys Med Biol* 2010; 55:3271.
- [232] Wang CH, Rockhill JK, Mrugala M, et al. Prognostic significance of growth kinetics in newly diagnosed glioblastomas revealed by combining serial imaging with a novel biomathematical model. *Cancer Res* 2009;69:9133–9140.
- [233] Xinjian C, Summers R, Jianhua Y. FEM-Based 3-D tumor growth prediction for kidney tumor. *IEEE T Biomed Eng* 2011;58:463–467.
- [234] Swanson KR, Rockne RC, Claridge J, Chaplain MAJ, Alvord EC, Anderson ARA. Quantifying the role of angiogenesis in malignant progression of gliomas: In silico modeling integrates imaging and histology. *Cancer Res* 2011;.

- [235] Brown CE, Wright CL, Naranjo A, et al. Biophotonic cytotoxicity assay for high-throughput screening of cytolytic killing. *J Immunol Methods* 2005;297:39–52.
- [236] Thomas DL, Lythgoe MF, Pell GS, Calamante F, Ordidge RJ. The measurement of diffusion and perfusion in biological systems using magnetic resonance imaging. *Phys Med Biol* 2000;45:R97–138.
- [237] Hutchings M, Loft A, Hansen M, et al. FDG-PET after two cycles of chemotherapy predicts treatment failure and progression-free survival in Hodgkin lymphoma. *Blood* 2006;107:52–59.
- [238] Mikhaeel NG, Hutchings M, Fields PA, O’Doherty MJ, Timothy AR. FDG-PET after two to three cycles of chemotherapy predicts progression-free and overall survival in high-grade non-Hodgkin lymphoma. *Ann Oncol* 2005;16:1514–1523.
- [239] Brepoels L, Stroobants S, Verhoef G, De Groot T, Mortelmans L, De Wolf-Peeters C. 18F-FDG and 18F-FLT uptake early after cyclophosphamide and mTOR inhibition in an experimental lymphoma model. *J Nucl Med* 2009;50:1102–1109.
- [240] Graf N, Herrmann K, den Hollander J, et al. Imaging proliferation to monitor early response of lymphoma to cytotoxic treatment. *Mol Imaging Biol* 2008;10:349–355.
- [241] van Waarde A, Cobben DCP, Suurmeijer AJH, et al. Selectivity of 18F-FLT and 18F-FDG for differentiating tumor from Inflammation in a rodent model. *J Nucl Med* 2004;45:695–700.
- [242] Fazel R, Krumholz HM, Wang Y, et al. Exposure to low-dose ionizing radiation from medical imaging procedures. *New Engl J Med* 2009;361:849–857.
- [243] Jubb AM, Strickland LA, Liu SD, Mak J, Schmidt M, Koeppe H. Neuropilin-1 expression in cancer and development. *J Pathol* 2012;226:50–60.
- [244] Pan Q, Chantry Y, Liang WC, et al. Blocking neuropilin-1 function has an additive effect with anti-VEGF to inhibit tumor growth. *Cancer Cell* 2007;11:53–67.
- [245] Liu Z, Li ZB, Cao Q, Liu S, Wang F, Chen X. Small-animal PET of tumors with 64Cu-labeled RGD-bombesin heterodimer. *J Nucl Med* 2009;50:1168–1177.

- [246] Bernatchez PN, Rollin S, Soker S, Sirois MG. Relative effects of VEGF-A and VEGF-C on endothelial cell proliferation, migration and PAF synthesis: Role of neuropilin-1. *Journal of Cellular Biochemistry* 2002;85:629–639.
- [247] Gray MJ, Wey JS, Belcheva A, et al. Neuropilin-1 Suppresses Tumorigenic Properties in a Human Pancreatic Adenocarcinoma Cell Line Lacking Neuropilin-1 Coreceptors. *Cancer Research* 2005;65:3664–3670.
- [248] Folkman J, Hanahan D. Switch to the angiogenic phenotype during tumorigenesis. *Princess Takamatsu Symp* 1991;22:339–347.
- [249] Folkman J. Angiogenesis in cancer, vascular, rheumatoid and other disease. *Nat Med* 1995; 1:27–30.
- [250] Huang W, Li X, Morris EA, et al. The magnetic resonance shutter speed discriminates vascular properties of malignant and benign breast tumors in vivo. *P Natl Acad Sci Usa* 2008; 105:17943–17948.
- [251] Hylton N. Dynamic Contrast-Enhanced Magnetic Resonance Imaging As an Imaging Biomarker. *J Clin Oncol* 2006;24:3293–3298.
- [252] Radjenovic A, Dall BJ, Ridgway JP, Smith MA. Measurement of pharmacokinetic parameters in histologically graded invasive breast tumours using dynamic contrast-enhanced MRI. *Brit J Radiol* 2008;81:120–128.
- [253] Matsumoto S, Yasui H, Batra S, et al. Simultaneous imaging of tumor oxygenation and microvascular permeability using Overhauser enhanced MRI. *P Natl Acad Sci Usa* 2009; 106:17898–17903.
- [254] Folkman J. Role of angiogenesis in tumor growth and metastasis. *Semin Oncol* 2002;29:15–18.
- [255] Ah-See MLW, Makris A, Taylor NJ, et al. Early changes in functional dynamic magnetic resonance imaging predict for pathologic response to neoadjuvant chemotherapy in primary breast cancer. *Clin Cancer Res* 2008;14:6580–6589.

- [256] Hirashima Y, Yamada Y, Tateishi U, et al. Pharmacokinetic parameters from 3-Tesla DCE-MRI as surrogate biomarkers of antitumor effects of bevacizumab plus FOLFIRI in colorectal cancer with liver metastasis. *Int J Cancer* 2011;.
- [257] Wedam SB, Low JA, Yang SX, et al. Antiangiogenic and Antitumor Effects of Bevacizumab in Patients With Inflammatory and Locally Advanced Breast Cancer. *J Clin Oncol* 2006; 24:769–777.
- [258] Su MY, Wang Z, Roth GM, Lao X, Samoszuk MK, Nalcioglu O. Pharmacokinetic changes induced by vasomodulators in kidneys, livers, muscles, and implanted tumors in rats as measured by dynamic Gd-DTPA-enhanced MRI. *Magnet Reson Med* 1996;36:868–877.
- [259] Wang Z, Su MY, Najafi A, Nalcioglu O. Effect of vasodilator hydralazine on tumor microvascular random flow and blood volume as measured by intravoxel incoherent motion (IVIM) weighted MRI in conjunction with Gd-DTPA-Albumin enhanced MRI. *Magn Reson Imaging* 2001;19:1063–1072.
- [260] Dafni H, Landsman L, Schechter B, Kohen F, Neeman M. MRI and fluorescence microscopy of the acute vascular response to VEGF165: vasodilation, hyper-permeability and lymphatic uptake, followed by rapid inactivation of the growth factor. *NMR Biomed* 2002;15:120–131.
- [261] Dafni H, Israely T, Bhujwala ZM, Benjamin LE, Neeman M. Overexpression of vascular endothelial growth factor 165 drives peritumor interstitial convection and induces lymphatic drain: magnetic resonance imaging, confocal microscopy, and histological tracking of triple-labeled albumin. *Cancer Res* 2002;62:6731–6739.
- [262] Cartwright L, Farhat WA, Sherman C, et al. Dynamic contrast-enhanced MRI to quantify VEGF-enhanced tissue-engineered bladder graft neovascularization: Pilot study. *J Biomed Mater Res A* 2006;77A:390–395.
- [263] Loveless ME, Halliday J, Liess C, et al. A quantitative comparison of the influence of individual versus population-derived vascular input functions on dynamic contrast enhanced-MRI in small animals. *Magnet Reson Med* 2012;67:226–236.

- [264] McGrath DM, Bradley DP, Tessier JL, Lacey T, Taylor CJ, Parker GJM. Comparison of model-based arterial input functions for dynamic contrast-enhanced MRI in tumor bearing rats. *Magnet Reson Med* 2009;61:1173–1184.
- [265] Gerlinger M, Rowan AJ, Horswell S, et al. Intratumor heterogeneity and branched evolution revealed by multiregion sequencing. *New Engl J Med* 2012;366:883–892.
- [266] Marusyk A, Polyak K. Tumor heterogeneity: Causes and consequences. *Biochimica et Biophysica Acta (BBA) - Reviews on Cancer* 2010;1805:105–117.
- [267] Sirois MG, Edelman ER. VEGF effect on vascular permeability is mediated by synthesis of platelet-activating factor. *Am J Physiol* 1997;272:H2746–56.
- [268] Kim KI, Park JJ, Lee YJ, et al. Gamma camera and optical imaging with a fusion reporter gene using human sodium/iodide symporter and monomeric red fluorescent protein in mouse model. *Int J Radiat Biol* 2011;87:1182–1188.
- [269] Balsa D, Merlos M, Giral M, Ferrando R, Garcia-Rafanell J, Forn J. Effect of endotoxin and platelet-activating factor on rat vascular permeability: role of vasoactive mediators. *J Lipid Mediat Cell* 1997;17:31–45.
- [270] Chen Q, Krol A, Wright A, Needham D, Dewhirst MW, Yuan F. Tumor microvascular permeability is a key determinant for antivascular effects of doxorubicin encapsulated in a temperature sensitive liposome. *Int J Hyperther* 2008;24:475–482.
- [271] Murohara T, Horowitz JR, Silver M, et al. Vascular endothelial growth factor/vascular permeability factor enhances vascular permeability via nitric oxide and prostacyclin. *Circulation* 1998;97:99–107.
- [272] Brkovic A, Sirois MG. Vascular permeability induced by VEGF family members in vivo: Role of endogenous PAF and NO synthesis. *Journal of Cellular Biochemistry* 2007;100:727–737.
- [273] Hudry-Clergeon H, Stengel D, Ninio E, Vilgrain I. Platelet-activating factor increases VE-cadherin tyrosine phosphorylation in mouse endothelial cells and its association with the PtdIns3'-kinase. *The FASEB Journal* 2005;19:512–520.

- [274] Grandclement C, Borg C. Neuropilins: A New Target for Cancer Therapy. *Cancers* 2011; 3:1899–1928.
- [275] Miao HQ, Lee P, Lin H, Soker S, Klagsbrun M. Neuropilin-1 expression by tumor cells promotes tumor angiogenesis and progression. *The FASEB Journal* 2000;14:2532–2539.
- [276] Acevedo LM, Barillas S, Weis SM, Göthert JR, Cheresh DA. Semaphorin 3A suppresses VEGF-mediated angiogenesis yet acts as a vascular permeability factor. *Blood* 2008; 111:2674–2680.
- [277] Becker PM, Waltenberger J, Yachechko R, et al. Neuropilin-1 regulates vascular endothelial growth factor-mediated endothelial permeability. *Circ Res* 2005;96:1257–1265.
- [278] Hu G, Schwartz DE, Shajahan AN, et al. Isoflurane, but not sevoflurane, increases transendothelial albumin permeability in the isolated rat lung: role for enhanced phosphorylation of caveolin-1. *Anesthesiology* 2006;104:777–785.
- [279] Zhu W, Kato Y, Artemov D. Effect of anesthesia on tumor vascular permeability measurements by DCE-MRI. In: *Proceedings 19th Scientific Meeting, International Society for Magnetic Resonance in Medicine*. 2011 3109.
- [280] Yankeelov TE, DeBusk LM, Billheimer DD, et al. Repeatability of a reference region model for analysis of murine DCE-MRI data at 7T. *J Magn Reson Imaging* 2006;24:1140–1147.
- [281] Lin MI, Yu J, Murata T, Sessa WC. Caveolin-1 deficient mice have increased tumor microvascular permeability, angiogenesis, and growth. *Cancer Res* 2007;67:2849–2856.
- [282] Cyran C, Sennino B, Chaopathomkul B, et al. Magnetic resonance imaging for monitoring the effects of thalidomide on experimental human breast cancers. *Eur Radiol* 2009;19:121–131.
- [283] Strijkers GJ, Hak S, Kok MB, Springer CS, Nicolay K. Three-compartment T1 relaxation model for intracellular paramagnetic contrast agents. *Magnet Reson Med* 2009;61:1049–1058.

- [284] Brisset JC, Desestret V, Marcellino S, et al. Quantitative effects of cell internalization of two types of ultrasmall superparamagnetic iron oxide nanoparticles at 4.7 T and 7 T. *Eur Radiol* ;20:275–285.
- [285] Zhang ZG, Zhang L, Jiang Q, et al. VEGF enhances angiogenesis and promotes blood-brain barrier leakage in the ischemic brain. *J Clin Invest* 2000;106:829–838.
- [286] Lee TH, Seng S, Sekine M, et al. Vascular endothelial growth factor mediates intracrine survival in human breast carcinoma cells through internally expressed VEGFR1/FLT1. *Plos Med* 2007;4:e186.
- [287] Liu Z, Yan Y, Liu S, Wang F, Chen X. (18)F, (64)Cu, and (68)Ga labeled RGD-bombesin heterodimeric peptides for PET imaging of breast cancer. *Bioconjugate Chem* 2009;20:1016–1025.
- [288] Bencherif B, Stumpf MJ, Links JM, Frost JJ. Application of MRI-based partial-volume correction to the analysis of PET images of μ -opioid receptors using statistical parametric mapping. *J Nucl Med* 2004;45:402–408.
- [289] Wang H, Fei B. An MR image-guided, voxel-based partial volume correction method for PET images. *Med Phys* 2012;39:179–195.
- [290] Ng T, Procissi D, Wu Y, Jacobs RE. MRI derived arterial input function for radionuclides using combined and simultaneous PET-MRI insert. *Mol Imaging Biol* 2010;12:S229–S230.
- [291] Knoess C, al E. Performance evaluation of the microPET R4 PET scanner for rodents. *Eur J Nucl Med Mol Imaging* 2003;30:737.
- [292] Shimazaki H, Shinomoto S. A method for selecting the bin size of a time histogram. *Neural Comput* 2007;19:1503–1527.
- [293] Valckx FMJ, Thijssen JM. Characterization of echographic image texture by cooccurrence matrix parameters. *Ultrasound in Medicine & Biology* 1997;23:559–571.
- [294] Bankman IN. *Handbook of medical imaging : processing and analysis*. San Diego: Academic, 2000.

- [295] Handrick S, Naimipour B, Raicu D, Furst J. Evaluation of binning strategies for tissue classification in computed tomography images. vol. 6144. San Diego, CA, USA: SPIE, 2006 61444L–11.
- [296] Kim N, Seo JB, Sung YS, et al. Effect of various binning methods and ROI sizes on the accuracy of the automatic classification system for differentiation between diffuse infiltrative lung diseases on the basis of texture features at HRCT. vol. 6914. San Diego, CA, USA: SPIE, 2008 69143N–7.
- [297] Asselin MC, O'Connor JPB, Boellaard R, Thacker NA, Jackson A. Quantifying heterogeneity in human tumours using MRI and PET. *Eur J Cancer* 2012;48:447–455.
- [298] Chen W, Giger ML, Li H, Bick U, Newstead GM. Volumetric texture analysis of breast lesions on contrast-enhanced magnetic resonance images. *Magnet Reson Med* 2007;58:562–571.
- [299] Risse F, Pesic J, Young S, Olsson LE. A texture analysis approach to quantify ventilation changes in hyperpolarised ^3He MRI of the rat lung in an asthma model. *NMR Biomed* 2012; 25:131–141.